SPRINGER BRIEFS IN
ELECTRICAL AND COMPUTER ENGINEERING

Chi-Seng Lam
Man-Chung Wong

Design and Control of Hybrid Active Power Filters

Springer

SpringerBriefs in Electrical and Computer Engineering

For further volumes:
http://www.springer.com/series/10059

Chi-Seng Lam · Man-Chung Wong

Design and Control of Hybrid Active Power Filters

Springer

Chi-Seng Lam
University of Macau
Macao
People's Republic of China

Man-Chung Wong
University of Macau
Macao
People's Republic of China

ISSN 2191-8112 ISSN 2191-8120 (electronic)
ISBN 978-3-642-41322-3 ISBN 978-3-642-41323-0 (eBook)
DOI 10.1007/978-3-642-41323-0
Springer Heidelberg New York Dordrecht London

Library of Congress Control Number: 2013950732

© The Author(s) 2014
This work is subject to copyright. All rights are reserved by the Publisher, whether the whole or part of the material is concerned, specifically the rights of translation, reprinting, reuse of illustrations, recitation, broadcasting, reproduction on microfilms or in any other physical way, and transmission or information storage and retrieval, electronic adaptation, computer software, or by similar or dissimilar methodology now known or hereafter developed. Exempted from this legal reservation are brief excerpts in connection with reviews or scholarly analysis or material supplied specifically for the purpose of being entered and executed on a computer system, for exclusive use by the purchaser of the work. Duplication of this publication or parts thereof is permitted only under the provisions of the Copyright Law of the Publisher's location, in its current version, and permission for use must always be obtained from Springer. Permissions for use may be obtained through RightsLink at the Copyright Clearance Center. Violations are liable to prosecution under the respective Copyright Law.
The use of general descriptive names, registered names, trademarks, service marks, etc. in this publication does not imply, even in the absence of a specific statement, that such names are exempt from the relevant protective laws and regulations and therefore free for general use.
While the advice and information in this book are believed to be true and accurate at the date of publication, neither the authors nor the editors nor the publisher can accept any legal responsibility for any errors or omissions that may be made. The publisher makes no warranty, express or implied, with respect to the material contained herein.

Printed on acid-free paper

Springer is part of Springer Science+Business Media (www.springer.com)

To my parents: Sio-Hong Lam
and In-Fong Lei
To my brothers: Chi-Kit Lam
and Chi-Man Lam
To my beloved one: Weng-Tong Cheong

Chi-Seng Lam

To my parents: Kok Kay and Yuk Ying
To my beloved wife: Ebbie Wong
To my naughty daughter: Oriana Wong

Man-Chung Wong

Preface

With the increased use of power electronics devices (nonlinear loads) and motor loadings, low cost, low loss and high performance shunt current quality compensators are highly in demand by power customers to solve current quality problems caused by those loadings. Undoubtedly, lower cost, lower loss, and better performances will be the development trends and goals in the coming decades. Among different current quality compensators, hybrid active power filter (HAPF) possesses high potential to get balance between cost, loss, and performance.

In this book, the content starts by overviewing the power quality issues, power quality standards, and comparing different HAPF topologies, etc. With the comprehensive consideration of the cost, loss, performance, and anti-resonance capability, the design and control of a HAPF topology are investigated as the prospective solution for the low cost, low loss, high performance current quality compensation. And the validity and effectiveness of the design and control techniques for the HAPF are verified by a 55 V, 1.65 kVA and a 220 V, 10 kVA HAPF experimental system. In addition, the system performance analysis method, design, and control techniques presented in this book can be extendable to other compensators, such as active power filter (APF), static synchronous compensator (STATCOM), etc.

The book is intended for researchers, Ph.D. students, postgraduates, and electrical power engineers specializing in power quality compensation, in which they can gain the specific knowledge of the design and control of the HAPF system. Moreover, it is intended for bachelor students and postgraduates specializing in electrical engineering, in which they can gain the basic knowledge of current quality problems and its different compensating methods, power electronics converters, pulse width modulation (PWM), etc.

Chi-Seng Lam
Man-Chung Wong

Acknowledgments

The research works presented in this book were carried out in the Power Electronics Laboratory (PELab), Department of Electrical and Computer Engineering (ECE), Faculty of Science and Technology (FST) of University of Macau (UM). We would like to express our gratitude to the Macao Science and Technology Development Fund (FDCT) and Research Committee (RC) of UM for funding this research work.

We would like to express our hearty and profound gratitude to Prof. Han Ying-Duo from Tsinghua University, China, for having opened our vision. We also appreciate him for this immensely inspirational guidance and precious advice.

An extraordinary word of thanks must be delivered to Mr. Choi Wai-Hei and Mr. Cui Xiao-Xi for their great assistance in implementing and testing the experimental prototypes.

Last, but certainly not least, we would like to send our heartfelt appreciation to our families, who endured our dedication to this book.

Contents

Abbreviations

A	Amperes
AC	Alternating current
A/D	Analog-to-digital
ADC	Analog-to-digital converter
APF	Active power filter
ASD	Adjustable speed drive
CB	Capacitor bank
CT	Coupling transformer
DC	Direct current
DPF	Displacement power factor
DSP	Digital signal processor
DVR	Dynamic voltage restorer
FFT	Fast fourier transform
HAPF	Hybrid active power filter
HPF	High pass filter
HVDC	High-voltage dc transmission
IEC	International Electro Technical Commission
IEEE	Institute of Electrical and Electronics Engineering
IGBT	Insulated gate bipolar transistor
IPM	Intelligent power module
L	Inductor
LC	Inductor and capacitor
LPF	Low pass filter
P	Proportional
PCB	Printed circuit board
PF	Power factor
PI	Proportional and integral
PPF	Passive power filter
PSCAD/EMTDC	Power system computer aided design/electro magnetic transient in dc system
PWM	Pulse width modulation
S/H	Sample and hold
STATCOM	Static synchronous compensator
SVC	Static var compensation

THD	Total harmonic distortion
UPQC	Unified power quality compensator
UPS	Uninterruptible power supplies
RMS	Root mean square
V	Volts
VSI	Voltage source inverter

Chapter 1
Introduction

Abstract This chapter initially presents an overview of the power quality issues. Then three common international standards relating to the voltage and current distortion are introduced. In order to provide a cost-effective three-phase shunt current quality compensator with resonances prevention capability, different hybrid active filter (HAPF) topologies have been compared and discussed in detail. Among them, one HAPF topology is chosen for in-depth investigation and further study in this book because it can offer the lowest cost, size, and weight, and has potential to provide dynamic reactive power compensation. Owning to the limitations of this HAPF, this book aims to provide their corresponding solutions. Finally, the organization of this book is introduced at the end of this chapter.

Keywords Active Power Filter · Hybrid Active Power Filter · Passive Power Filter · Power Quality · Power Quality Compensation · Pulse Width Modulation · Voltage Source Inverter

1.1 Power Quality Issues

Due to the advancement of science and technology, industrial structure reforming, and the development of smart grid technology recently, people have a higher demand for improved power quality. However, with the proliferation and increased use of power electronics devices (nonlinear loads) and motor loadings, such as converters, Adjustable Speed Drives (ASDs), arc furnaces, bulk rectifiers, power supplies, computers, fluorescent lamps, elevators, escalators, large air conditioning systems, compressors, etc. [1–25], it is becoming more and more difficult to achieve this goal. Table 1.1 lists power electronics and motor applications that cover a wide power range from a few tens of watts to several hundreds of megawatts in residential, commercial, industrial, and aerospace systems [26].

Although the widespread applications of power electronic devices enable the control and tuning of all power circuits for maximum performance, cost-

C.-S. Lam and M.-C. Wong, *Design and Control of Hybrid Active Power Filters*, SpringerBriefs in Electrical and Computer Engineering,
DOI: 10.1007/978-3-642-41323-0_1, © The Author(s) 2014

Table 1.1 Power electronics and motor applications

- (a) *Residential*
  - Refrigeration and freezes
  - Space heating
  - Air conditioning
  - Cooking
  - Lighting
  - Electronics (personal computers, Other entertainment equipments)
  - Elevators, escalators
- (b) *Commercial*
  - Heating, ventilating, and air conditioning
  - Central refrigeration
  - Lighting
  - Computers and office equipment
  - Uninterruptible power supplies (UPS)
  - Elevators, escalators
- (c) *Industrial*
  - Compressors
  - Blowers and fans
  - Machine tools (robots)
  - Arc furnaces, induction furnaces
  - Lighting
  - Industrial lasers
  - Induction heating
  - Welding
  - Elevators, escalators
- (d) *Telecommunications*
  - Battery chargers
  - Power supplies (dc and UPS)
- (e) *Transportation*
  - Traction control of electric vehicles
  - Battery charges for electric vehicles
  - Electric locomotives
  - Street cars, trolley buses
  - Subways
  - Automotive electronics including engine controls
- (f) *Utility systems*
  - High-voltage dc transmission (HVDC)
  - Static var compensation (SVC)
  - Supplemental energy sources (wind, photovoltaic), fuel cells
  - Energy storage systems
  - Induced-draft fans
  - Boiler feedwater pumps
- (g) *Custom power devices*
  - Active power filter (APF)
  - Dynamic voltage restorer (DVR)
  - Unified power quality compensator (UPQC)
  - Static synchronous compensators (STATCOM)
  - Uninterruptible power supply (UPS)
- (h) *Aerospace*
  - Space shuttle power supply systems
  - Satellite power systems
  - Aircraft power systems

effectiveness, and enhanced energy efficiency, they will increase the distortion and disturbances on the current and voltage signals in the power network. This is because the power electronic devices draw harmonic currents from the power utility and the harmonic voltage will then be generated, as harmonic currents cause nonlinear voltage drops across the power network impedance. The presence of current and voltage components at frequencies other than the fundamental one, and also the negative and zero sequences in three-phase systems are harmful to the equipments of the power supply utilities and those of the customers. Harmonic distortion causes various problems in both power network and consumer products, such as equipment overheating, capacitor fuse blowing, transformer overheating, maloperation of control devices, excessive neutral current, degrades the defection of accuracy in power meters, etc. [5].

On the other hand, the usage of induction motor loadings will cause a phase shift between the current and the voltage in the power network. This results in lowering the power factor of the loading. Loadings with low power factor draw more reactive current than those with high power factor. The larger the reactive current/power, the larger the system losses and the lower the power network stability. Moreover, the larger the reactive current, the thicker the cables required for power transmission, which will either increase the cost or lower the transmission capacity of the existing cables. Thus, electricity utilities usually charge industrial and commercial customers a higher electricity cost with low power factor situation.

All of these current and voltage phase shift and distortion phenomena are responsible for the deterioration of power quality in the transmission and distribution power systems. Clearly, there is a need from both utilities and customers for power quality improvement. Consequently, power quality has become an issue that is of increasing importance to electricity consumers at all levels of usage.

1.2 Standards of Power Quality Issues

There are three common international standards relating to voltage and current distortion.

- *IEEE 519:1992*. IEEE Recommended Practices and Requirements for Harmonic Control in Electrical Power Systems [27]
- *IEEE 1159:1995*. IEEE Recommended Practice for Monitoring Electric Power Quality [28]
- *IEC 61 000-3-2*. Electromagnetic Compatibility (EMC) —Part 3-2: Limits — Limits for Harmonic Current Emissions (Equipment Input Current <=16A per Phase) [29]

According to the above standards, Tables 1.2 and 1.3 summarize the voltage and current harmonics distortion limits, in which they are used to evaluate the compensating performances of the proposed HAPF system.

To solve the current harmonics and reactive power problems generated by the nonlinear and induction motor loadings, shunt current quality compensators can be implemented between the load and the power supply sides. In the following section, the different shunt current quality compensators and the development of hybrid active power filter in distribution power system will be introduced, compared, and discussed.

1.3 Development of Hybrid Active Power Filter

Shunt capacitor banks (CBs) as shown in Fig. 1.1 are used extensively in distribution power systems for power-factor correction and feeder voltage control. The principal advantages of CBs are their low cost and flexibility of installation and

Table 1.2 Voltage harmonic distortion limits

Standard	Bus voltage 69 kV and below	
	Individual voltage distortion (%)	Total voltage harmonic distortion THD_v (%)
IEEE 519:1992	3.0	5.0

Table 1.3 Current harmonic distortion limits

Standards	Total current harmonic distortion (%)
IEEE 1159:1995	20 (for small customers) 5 (for very large customers)
IEC 61 000-3-2	16 (for load smaller than 16 A per phase)

Fig. 1.1 Parallel capacitor bank (CB)

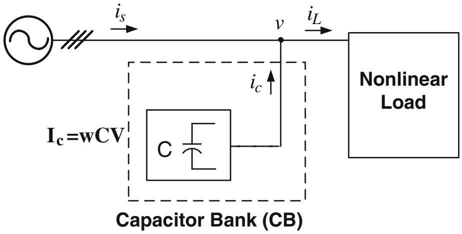

Fig. 1.2 Passive power filter (PPF)

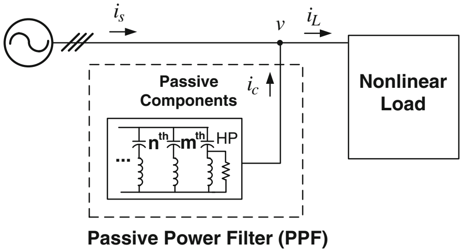

operation. However, the CB can easily be burnt if the current harmonics level is high. Moreover, the reactive power output is reduced at low load voltage as it is dependent on load voltage. In order to solve the current harmonics problem, power filters as shown in Fig. 1.2 can be employed. Since the first installation of passive power filters (PPFs) in the mid-1940s, PPFs have been widely used to suppress current harmonics and compensate reactive power in distribution power systems [14] due to their low cost, simplicity, and high efficiency characteristics. Unfortunately, they have many disadvantages such as low dynamic performance, filtering characteristic easily be affected by small variations of the system parameters, resonance problems, etc. [1–13, 16, 17, 22, 24, 25]. Since the concept "Active ac Power Filter" was first developed by L. Gyugyi in 1976 [4, 14], research studies on the active power filters (APFs) as shown in Fig. 1.3 for current quality compensation are prospering since then. APFs can overcome the

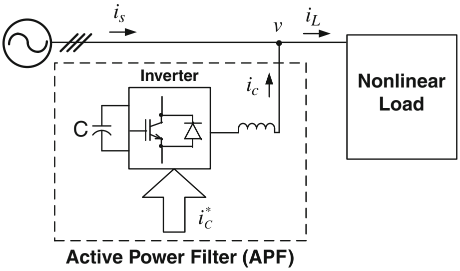

Fig. 1.3 Active power filter (APF)

disadvantages inherent in PPFs, but their initial and operational costs are relatively high [1–7, 9, 10, 13, 16, 22, 25] due to the costs of semiconductor switching devices with its drivers and digital controller. In addition, the dc-link operating voltage of APF should be higher than the load voltage, thus increasing the cost and switching loss of the switching devices [30]. This results in slowing down their large-scale application in distribution power networks.

Later, different HAPF topologies composed of active and passive components in series and/or parallel have been proposed [1–25], aiming to improve the compensation characteristics of PPFs and reduce the voltage and/or current ratings (costs) of the APFs, thus leading to the relative effectiveness in system cost and performances. But HAPFs usually have a smaller compensation range than pure APFs. In the following, different HAPF topologies will be introduced and compared.

In the past research, different HAPF topologies have been proposed [1–25], in which they can be classified into three general types: HAPF topology 1–series APF and shunt PPF [1–8], HAPF topology 2–shunt APF and shunt PPF [1, 2, 9–13], and HAPF topology 3–APF in series with shunt PPF [2, 3, 17–25] as shown in Fig. 1.4. Hereinafter, discussions and comparisons between these HAPF topologies are given.

1.3.1 HAPF Topology 1–Series APF and Shunt PPF [1–8]

The HAPF topology 1– series APF and shunt PPF circuit configuration is shown in Fig. 1.4a. Figure 1.5 shows this HAPF topology in three-phase three-wire power system presented by Peng et al. in 1988 [4] and three-phase four-wire power system presented by Salmeron and Litran in 2010 [8] respectively. The APF is usually connected in series with the distribution power system through filtering inductor and capacitor (LC) and coupling transformer (CT), while the shunt PPF can be a tuned LC filter or high pass filter or any combination of them.

Under this HAPF topology, the APF acts as a harmonic isolator between the system source and load sides by forcing the load harmonic current flow into the shunt PPF. At the fundamental frequency, the shunt PPF shows a high impedance while the series APF shows a low impedance. On the contrary, the shunt PPF

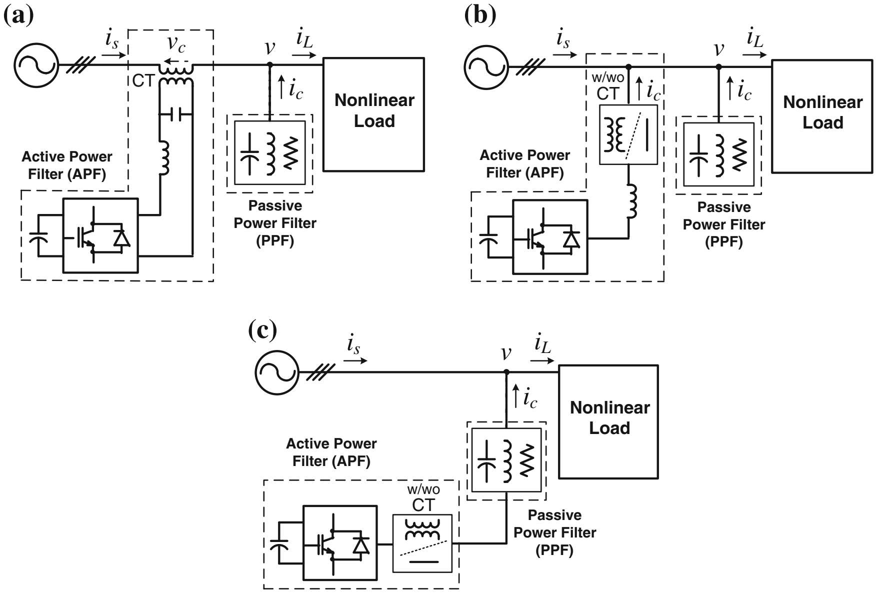

Fig. 1.4 Three general types of HAPF topology: **a** HAPF topology 1–series APF and shunt PPF, **b** HAPF topology 2–shunt APF and shunt PPF and **c** HAPF topology 3 –APF in series with shunt PPF

shows a low impedance while the series APF shows a high impedance at harmonic frequency. This HAPF topology aims to reduce the current rating of the APF. Moreover, it can prevent the series and parallel resonance phenomena.

However, the series APF requires adequate protection in case of malfunction of the APF because it is in series with the distribution power system. Moreover, as the series APF is connected to the power system through CT, its CT is capable to withstand full load current, thus increasing the system cost, size, and loss.

1.3.2 HAPF Topology 2–Shunt APF and Shunt PPF [1, 2, 9–13]

The HAPF topology 2–shunt APF and shunt PPF circuit configuration is shown in Fig. 1.4b. Figure 1.6 shows this HAPF topology with CT in three-phase three-wire power system presented by Khositkasame and Sangwongwanich in 1997 [9] and Corasaniti et al. in 2009 [12], and without CT in three-phase four-wire power system presented by Chiang et al. in 2005 [11] respectively. The shunt APF can be connected to the distribution power system through coupling inductor (L) with or without CT, while the shunt PPF can be a tuned LC filter or high pass filter or any combination of them.

Under this HAPF configuration, the PPF acts as the main compensator and the APF is used to compensate the remaining current harmonic contents, which have been filtered by the PPF, so as to improve the system filtering performances. Thus, this HAPF topology aims to reduce the current rating of the APF. In addition, the advantages of this topology are the shunt APF applicable if the shunt PPF already exists and reactive power controllable. Moreover, it can prevent the parallel resonance phenomenon.

However, the APF cannot change either the voltage across the PPF or the current through the PPF. Therefore, large circulating current will be generated by the PPF if the PPF impedance is low at the voltage distortion frequency. In order to prevent the harmonic current flows to the supply, the required APF current rating will still be high. If the APF is directly connected to the distribution power system without CT, its required voltage rating is also high. By adding CT, its voltage rating can be reduced; however, using CT will increase the system cost, size, and loss. By choosing the PPF as a high pass filter, this HAPF topology can avoid obtaining low PPF impedance at the voltage harmonic frequencies. However, high pass filters (with resistance) increase the filter loss and reduce the filtering effectiveness at the tuned frequency.

1.3.3 HAPF Topology 3–APF in Series with Shunt PPF [2, 3, 17–25]

The HAPF topology 3–APF in series with shunt PPF circuit configuration is shown in Fig. 1.4c. Figure 1.7 shows this HAPF topology with CT in three-phase three-wire power system presented by Fujita and Akagi in 1991 [3] and Rivas et al. in 2003 [17], and without CT in three-phase three-wire power system presented by Srianthumrong and Akagi in 2003 [20] respectively. The APF and PPF are connected in series with or without CT, and this HAPF is then shunted to the distribution power system. The PPF can be a tuned LC filter or high pass filter or any combination of them.

Under this HAPF configuration, the APF aims to change the impedance of the PPF so that the PPF has a nearly zero impedance to load-side current harmonics and infinite impedance to system-side voltage harmonics, so as to improve the compensation characteristics of the PPF. When a PPF and an APF are connected in series, the fundamental system voltage mainly drops on the capacitor of the PPF, but not the APF. Thus, this HAPF topology aims to reduce the voltage rating of the APF. Moreover, it can prevent the series and parallel resonance phenomena.

Table 1.4 shows the characteristics and comparisons for these three general HAPF topologies. From Table 1.4, HAPF topology 3 can be considered as the best among the three general topologies because (i) it can effectively prevent series and parallel resonances, (ii) it has potential to generate less switching noise into the distribution power system as it requires a low dc-link voltage, and (iii) it does not contain large circulating current problem and can easily bypass the system in case of malfunction of APF or PPF.

In addition, the comparisons between the HAPF topology 3 [3, 17, 20] as shown in Fig. 1.7 are summarized in Table 1.5.

1.4 Research Objectives

In this book, the research objective aims to investigate and develop a low cost three-phase four-wire HAPF for dynamic reactive power and current harmonics

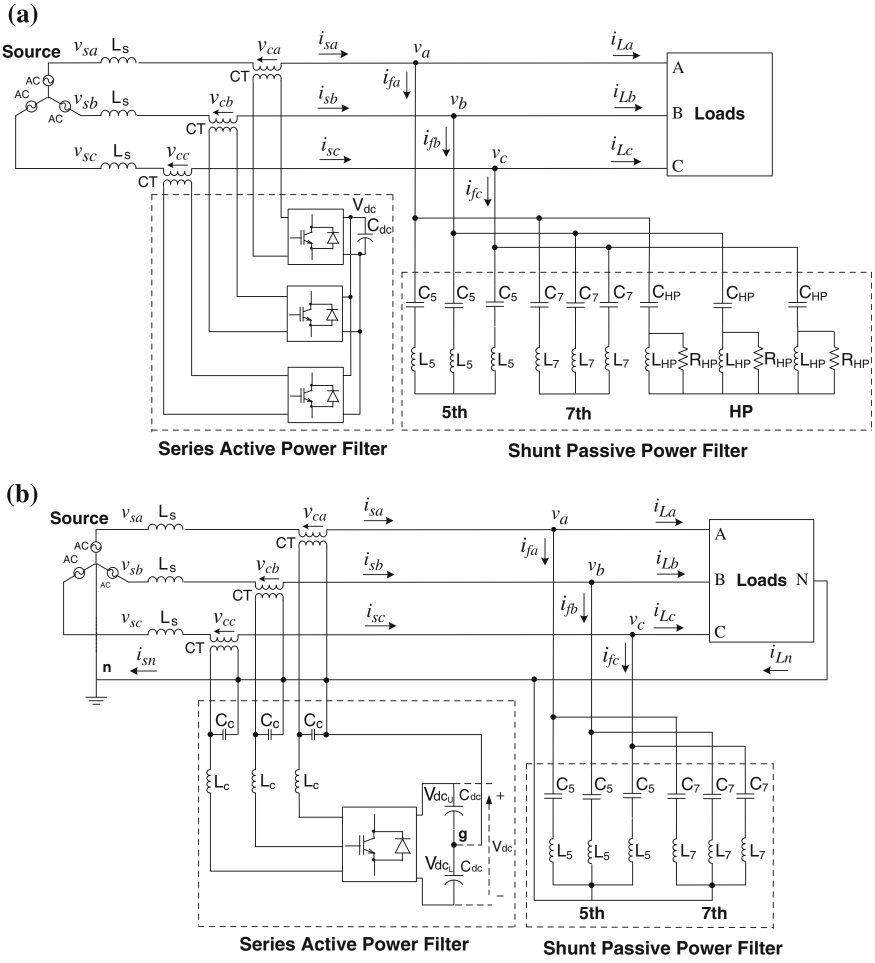

Fig. 1.5 HAPF topology 1–series APF and shunt PPF presented by: **a** Peng et al. in 1988 [4] and **b** Salmeron and Litran in 2010 [8]

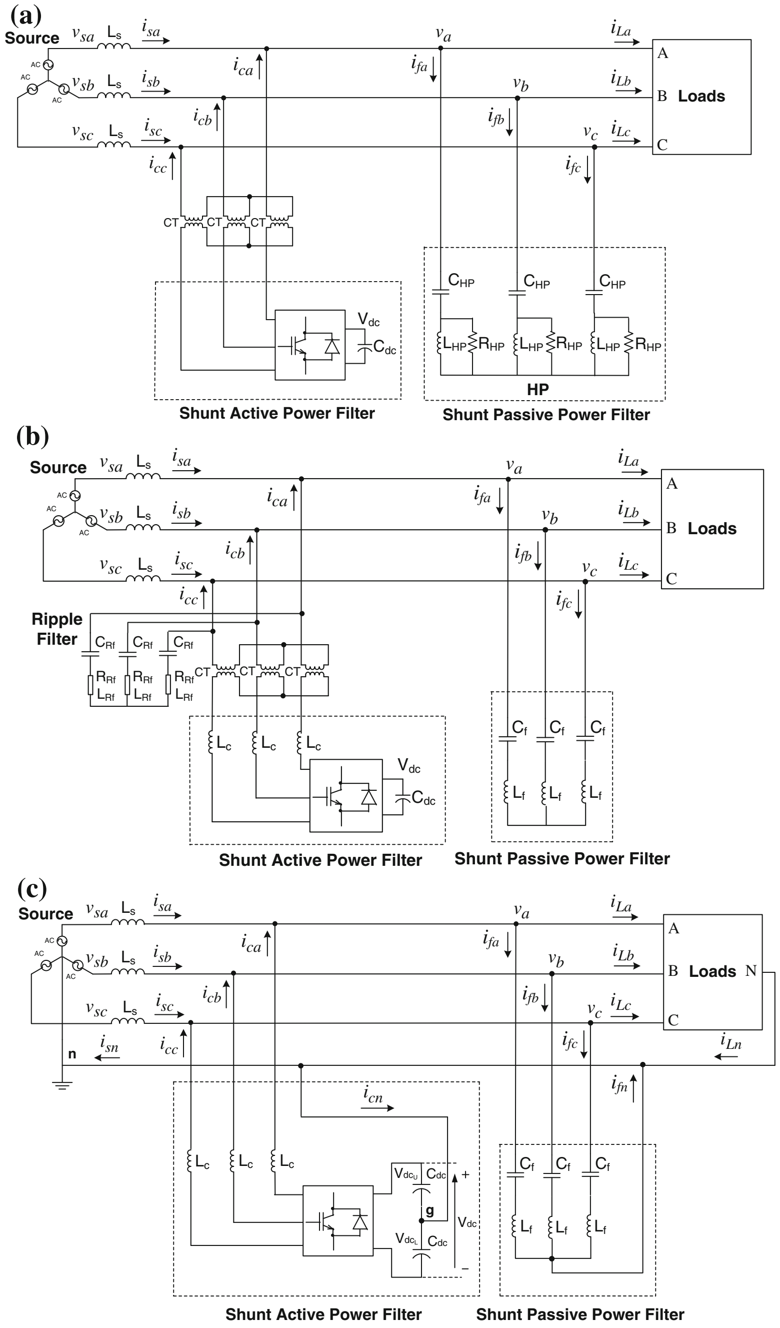

Fig. 1.6 HAPF topology 2–shunt APF and shunt PPF presented by: **a** Khositkasame and Sangwongwanich in 1997 [9], **b** Corasaniti et al. in 2009 [12] and **c** Chiang et al. in 2005 [11]

compensation in distribution power system, which can also minimize the switching loss and switching noise purposes. Moreover, the HAPF is capable to prevent the resonance phenomena inherent in the pure PPF part and enhances the system robustness. From Table 1.5, the three-phase HAPF topology as shown in Fig. 1.7c is chosen for in-depth investigation and further study because it can offer the lowest initial cost, size, and weight. Moreover, it has potential to provide the best dynamic reactive power compensation capability among the topologies shown in Fig. 1.7. In addition, its coupling LC functions not only as a harmonic filter but also as a switching ripple filter. As a result, the research works presented in this book will be focused on this HAPF topology in three-phase four-wire distribution power system applications.

1.4.1 Circuit Configuration of a Three-Phase Four-Wire Center-Split HAPF

When this conventional HAPF topology (Fig. 1.7c) is applied to three-phase four-wire power systems, either center-split or four-leg voltage source inverter (VSI) can be used. Compared with the four-leg VSI configuration, with just slight increase in the dc-link operating voltage and an additional low cost dc capacitor for the three-leg center-split VSI, it can save two costly power electronic switches and driver circuits [22]. Thus, the three-leg center-split VSI structure is chosen for the active inverter part of this HAPF. Figure 1.8 illustrates the system configuration of a three-phase four-wire center-split HAPF, where the subscript 'x' denotes phase $a,\ b,\ c,\ n$. v_{sx} is the system voltage, v_x is the load voltage, L_s is the system inductance normally neglected due to its low value relatively, thus $v_{sx} \approx v_x$. i_{sx}, i_{Lx} and i_{cx} are the system, load, and inverter current for each phase. C_{c1} and L_{c1} are the coupling capacitor and inductor of the HAPF, in which C_{c1} and L_{c1} are designed based on the reactive power consumption and the dominant harmonic current of the inductive loading as presented in Chap. 6. C_{dc1}, V_{dc1_U} and V_{dc1_L} are the dc capacitor, upper, and lower dc capacitor voltages of the HAPF with $V_{dc1_U} = V_{dc1_L} = 0.5\ V_{dc1}$. The dc-link midpoint is assumed to be ground reference (g). From Fig. 1.8, the inverter line-to-ground voltages $v_{invjx-g}$ will be equal to the inverter line-to-neutral voltages $v_{invjx-n}$ because the neutral point n is connected to the dc-link midpoint$g$. The load can be a nonlinear load, a linear load, or their combination. The nonlinear loads are composed of three single-phase diode bridge rectifiers, which act as harmonic producing loads. In this book, the research study will be mainly focused on this three-phase four-wire HAPF system.

Fig. 1.7 HAPF topology 3–APF in series with shunt PPF presented by: **a** Fujita and Akagi in 1991 [3], **b** Rivas et al. in 2003 [17] and **c** Srianthumrong and Akagi in 2003 [20]

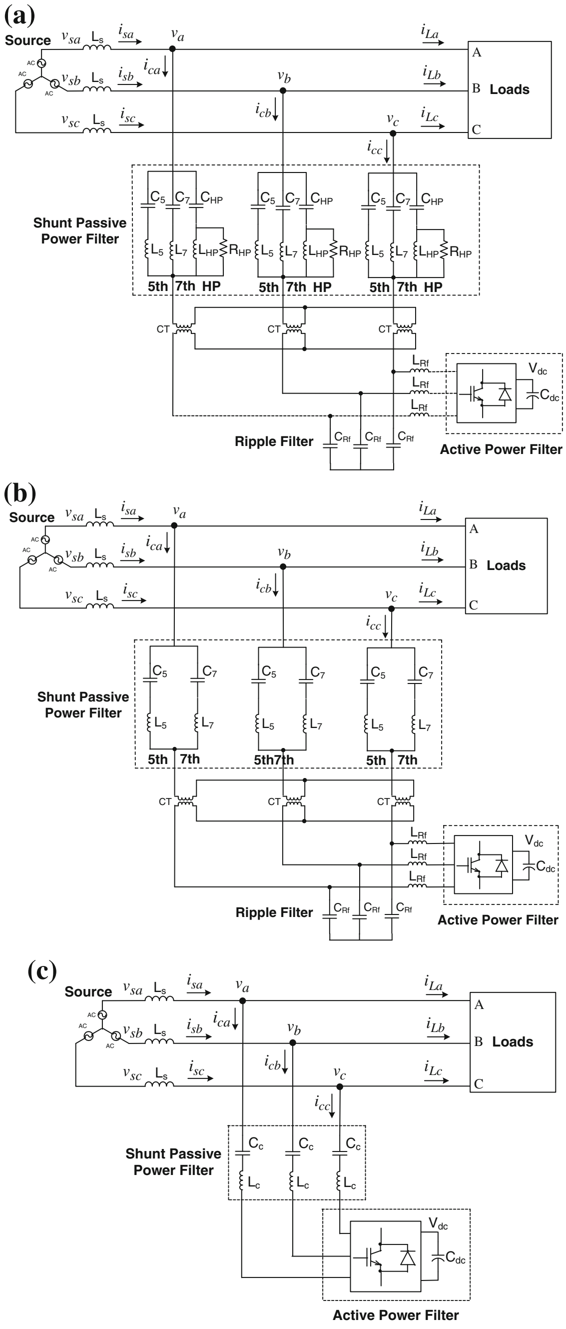

Table 1.4 Characteristics and comparisons of three general HAPF topologies

	HAPF topology 1 [1–8]	HAPF topology 2 [1, 2, 9–13]	HAPF topology 3 [2, 3, 17–25]
Function of APF	Harmonic isolator	Harmonic compensator	To improve the filtering characteristics of PPF
Series and parallel resonance preventing capability	Effective on both	Effective on parallel resonance	Effective on both
Advantages	- Current capacity reduction of APF - Applicable even PPF already exists	- Current capacity reduction of APF - Applicable even PPF already exists	- Voltage capacity reduction of APF
Disadvantages	- Special isolation and protection during series APF is malfunction - Extra loss due to CT	- Extra loss–with CT - Large circulating current generated during low PPF impedance at harmonic voltage	- Extra loss–with CT Need modification if PPF already exists
Cost	High due to CT	Lower–without CT High–with CT	Lower–without CT High–with CT
Size and weight	Bulky due to CT	Bulky–with CT Lighter–without CT	Bulky–with CT Lighter–without CT
Harmonic current compensation	Mainly support	Mainly support	Mainly support
Dynamic reactive power compensation	Possible to support	Possible to support	Possible to support

Table 1.5 Comparisons between HAPF topology 3 presented by: Fujita and Akagi in 1991 [3], Rivas et al. in 2003 [17], and Srianthumrong and Akagi in 2003 [20]

	Fig. 1.7a Fujita and Akagi in 1991 [3]	Fig. 1.7b Rivas et al. in 2003 [17]	Fig. 1.7c Srianthumrong and Akagi in 2003 [20]
Cost	Highest	High	Lowest
Size and weight	Bulky	Bulky	Lightest
Coupling transformer	3	3	0
AC inductor	12	9	3
AC capacitor	12	9	3
Resistor	3	0	0
Harmonic current compensation	Best	Good	Medium
Dynamic reactive power compensation	Not available	Not available	Not available

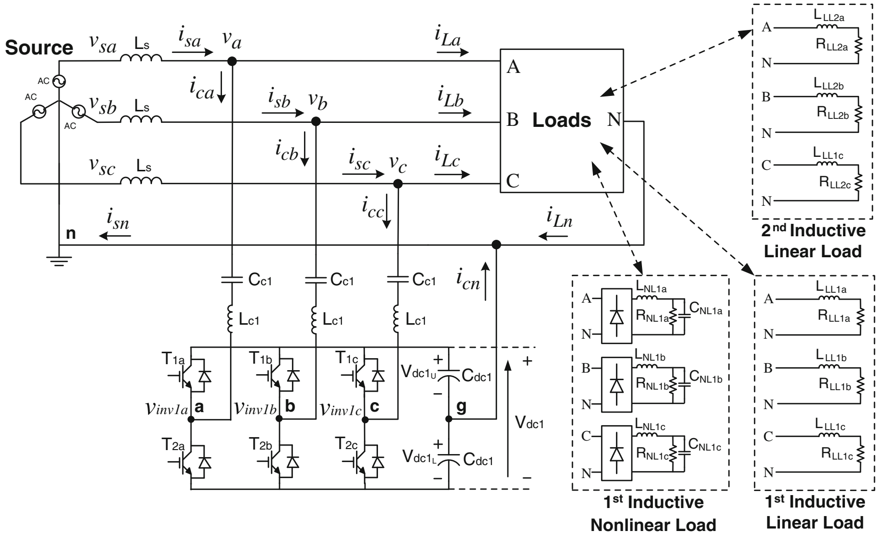

Fig. 1.8 System configuration of a three-phase four-wire center-split HAPF

1.4.2 Conventional and Proposed Compensating Current Generation Method for HAPF

To generate the compensating current as its reference value, the HAPF should be controlled and acted as a current source. The HAPF usual method for generating compensating current by a VSI is indirect current (voltage reference) control [19–25], in which the final reference compensating current is transformed into a voltage reference. Then the voltage reference is compared with a triangular carrier in order to produce pulse width modulation (PWM) gate signals for switching devices of the VSI. To enhance the compensation performance, the authors in [19–21] even combine the feedback control and feedforward control by detecting both the system source currents and load currents respectively. Actually, in order to calculate the exact voltage reference from the reference compensating current for HAPF, a modeling including the coupling LC and load voltage is necessary. However, as the coupling LC is a second-order circuit, which might be complicated to deduce the exact modeling, therefore, the authors in [19–24] just use an approximation model (multiplying the reference current by a gain) to calculate the voltage reference. This approximation will induce errors to the reference signal. Moreover, the system parameters are necessary in the voltage reference calculation process, thus their variation by environmental factors will influence the system compensating performance.

Actually, the direct current (current reference) control [31] can also be applied to the HAPF system. This control method treats the VSI as a current-controlled source, which adopts current PWM techniques such as: hysteresis, ramp comparison, etc., [31] for generating the calculated compensating current. In addition, the direct current (current reference) control method can yield a faster response than the indirect (voltage reference) one. A comparison between indirect current control and direct current control is also summarized in Table 1.6.

With faster dynamic response and higher robustness than the indirect current control method, the direct current (current reference) control technique is applied to the HAPF system in this book. There are mainly two PWM methods to achieve the direct current control: hysteresis band PWM and ramp comparison PWM [31], in which their details will be discussed in the following.

1.4.2.1 Hysteresis Band PWM

Among the various PWM techniques, the hysteresis band PWM is one of the most popular PWM strategies and widely applied in current quality compensation, owing to its advantages such as ease of implementation, fast dynamic response, current limiting capability, etc. Besides, it does not need any knowledge of system parameters for operation. However, the switching frequency using hysteresis PWM

Table 1.6 Comparison between indirect current control and direct current control

Characteristics	Indirect current control (voltage reference) [19–24]	Direct current control (current reference) [31]
Reference signal	Voltage	Current
Knowledge of system parameters	Required	Not required
Influence by the variations of system parameters	More	Less
Response time	Slower	Faster
Control scheme	Feedback control/Feedback control and Feedforward control	Feedback control

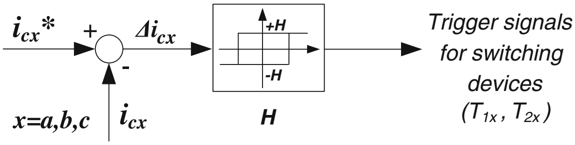

Fig. 1.9 Control block diagram of hysteresis band PWM control

is not fixed and varies with the magnitude and frequency of the reference. The basic implementation of hysteresis PWM is based on deriving the switching signals from the comparison of the current error Δi_{cx} between the reference compensating current i^*_{cx} and the actual compensating current i_{cx} with a fixed hysteresis band H, the subscript 'x' denotes phase a, b, c. The trigger signals will drive the switching devices of the VSI in order to let i_{cx} tracks with its reference i^*_{cx}. A typical hysteresis band PWM control block diagram is shown in Fig. 1.9. For the i_{cx} direction as shown in Fig. 1.8, the hysteresis band PWM working principle is described as shown in Fig. 1.10, in which T_{1x} is ON and T_{2x} is OFF when the compensating current error Δi_{cx} is smaller than the hysteresis band $-H$ ($\Delta i_{cx} < -H$), and T_{1x} is OFF and T_{2x} is ON when Δi_{cx} is larger than $+H$ ($\Delta i_{cx} > +H$). If i_{cx} is within the band H, the trigger signal will maintain until the next reverse operation. If the i_{cx} direction as shown in Fig. 1.8 is in reverse, T_{1x} is OFF and T_{2x} is ON when $\Delta i_{cx} < -H$, and T_{1x} is ON and T_{2x} is OFF when $\Delta i_{cx} > +H$.

1.4.2.2 Ramp Comparison PWM

The ramp comparison PWM is initially computing the current error signal Δi_{cx} by subtracting the reference compensating current $i_{cx}{}^*$ by the actual compensating current i_{cx}, Δi_{cx} will be inputted into a proportional (P)/proportional and integral (PI)

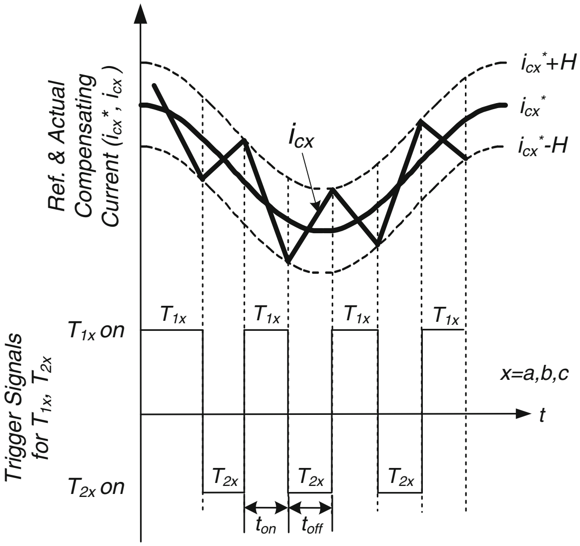

Fig. 1.10 Working principle waveforms of hysteresis band PWM control

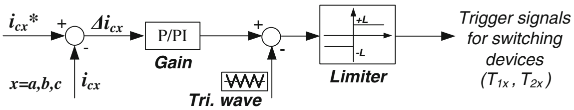

Fig. 1.11 Control block diagram of ramp comparison PWM control

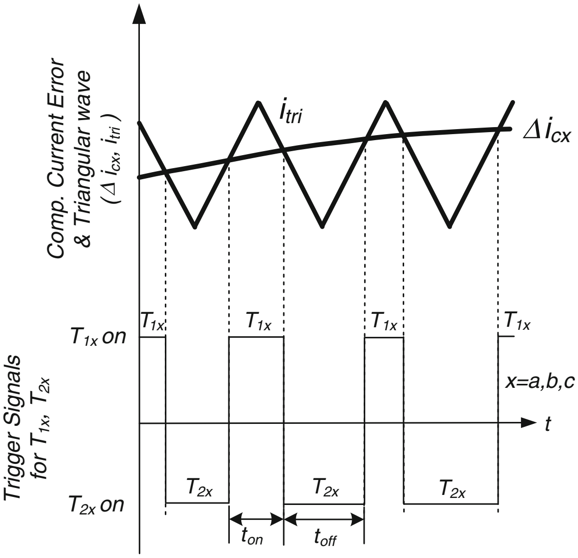

Fig. 1.12 Working principle waveforms of ramp comparison PWM control

controller. Then its corresponding output will be compared with a fixed frequency triangular carrier wave i_{tri} in order to generate the trigger signals for the switching devices. By using the ramp comparison PWM, the switching devices of the VSI operate at an approximately fixed frequency as the triangular wave, however, there exists an inherent magnitude and phase errors of the generated compensating current compared with its reference. The errors can be reduced by increasing the controller gain, where the gain can be adjusted by either adjusting the amplitude of triangular wave or the current error signal [31]. The ramp comparison PWM control block diagram is shown in Fig. 1.11. For the i_{cx} direction as shown in Fig. 1.8, the ramp comparison PWM working principle is described as shown in Fig. 1.12, in which T_{1x} is ON and T_{2x} is OFF when Δi_{cx} is smaller than the triangular wave i_{tri} $(\Delta i_{cx} < i_{tri})$, and T_{1x} is OFF and T_{2x} is ON when Δi_{cx} is larger than i_{tri} $(\Delta i_{cx} > i_{tri})$. Similar to the hysteresis band PWM control case, the reverse T_{1x} and T_{2x} results are obtained if the i_{cx} direction as shown in Fig. 1.8 is in reverse.

In addition, both the hysteresis and ramp comparison PWM [31] were traditionally developed based on linear concept. They can be applied on the conventional linear inductive-coupling VSIs for different applications, such as ac motor drives, APF, DVR, etc.

1.4.3 Limitations of Conventional Three-Phase HAPF

The limitations of the conventional three-phase HAPF as shown in Fig. 1.7c are listed below:

(1) There is less detailed study on the HAPF resonance phenomena prevention capability, filtering performance, and system robustness when it is operating in standalone.
(2) As the coupling LC of the HAPF yields a nonlinear inverter current slope, this can affect the controllability of using the conventional linear PWM control methods, and its linear operation requirement should be investigated. Unfortunately, there is still no research work examining or discussing the minimum operating requirement for this HAPF [19–25] if the linear hysteresis or ramp comparison control strategy is applied.
(3) The active inverter part of the HAPF is solely responsible for current harmonics compensation [19–25] and the HAPF can only inject a fixed amount of reactive power which is provided by coupling LC. In the practical case, the load-side reactive power consumption varies from time to time, as a result, the HAPF cannot perform satisfactory dynamic reactive power compensation.
(4) The HAPFs are operating at a fixed dc-link voltage level [19–25]. Without adding any extra soft-switching hardware components, the HAPF cannot reduce its switching loss and switching noise during operation.
(5) The minimum dc-link operating voltage requirement for the HAPF in reactive power and current harmonics compensation has not been mathematically deduced. Moreover, without adding extra LC branches to the HAPF, the solution to further reduce its minimum dc-link voltage requirement is lack of investigation.

1.5 Organization of the Book

This book is organized into seven chapters and one appendix as shown in Fig. 1.13. This chapter presents an overview of the power quality issues. Then three common international standards relating to the voltage and current distortion are introduced. In order to provide a cost-effective three-phase shunt current quality compensator with resonances prevention capability, different HAPF topologies have been compared and discussed. Among them, the HAPF topology as shown in Fig. 1.8, is chosen for further investigation in this book because it can offer the lowest cost, size, and weight, and has the potential to provide dynamic reactive power compensation.

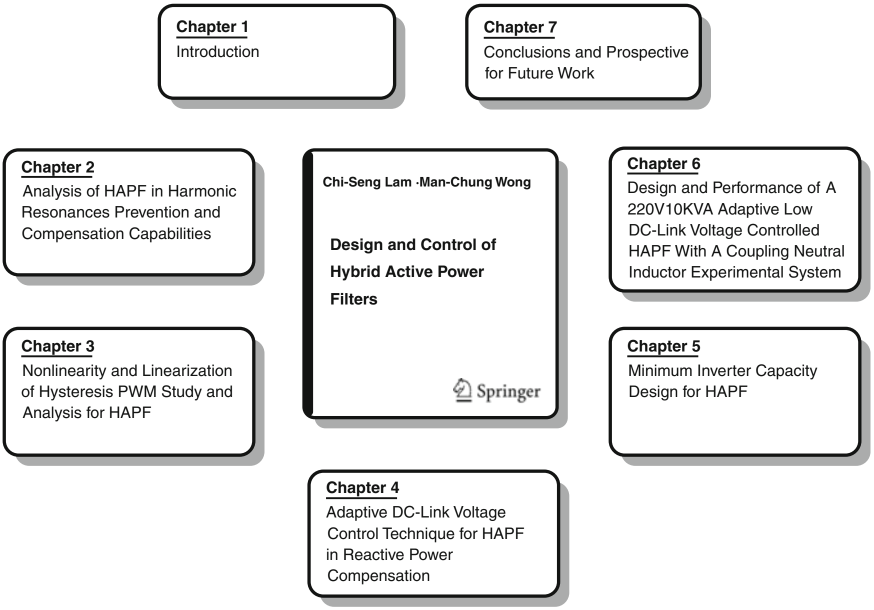

Fig. 1.13 Organization of the book

Chapter 2 analyzes and discusses the details of the HAPF resonance phenomena prevention capability, filtering performance, and system robustness when it is operating in standalone. Simulation results are provided to verify the analysis.

Chapter 3 presents and analyzes the approximately linear operation requirement of the hysteresis PWM control for the HAPF, in comparison with the linear APF. Simulation and experimental results are provided to show the validity of the HAPF linearization analysis.

Chapter 4 proposes an adaptive dc-link voltage control technique for HAPF in dynamic reactive power compensation, so that the switching loss and switching noise can be reduced, in comparison with the traditional fixed dc-link voltage controlled HAPF. Moreover, the proposed dc-link control method can work for the initial start-up dc-link self-charging process. Simulation and experimental results are provided to verify the validity and effectiveness of the proposed adaptive dc control technique.

Chapter 5 deduces and analyzes the required minimum dc-link voltage expression for the HAPF in reactive power and current harmonics compensation. Through the analysis of the HAPF equivalent circuit models in d-q-0 coordinate, by adding a tuned coupling neutral inductor to the HAPF, it is possible to further reduce its minimum dc-link voltage requirement and its inverter capacity. Simulation and experimental results are provided to verify the minimum inverter capacity design for HAPF.

Chapter 6 presents the design and performance of a 220 V, 10 kVA adaptive low dc-link voltage controlled HAPF with a coupling neutral inductor experimental prototype. The design procedures of the adaptive dc-link voltage controller are discussed. Then the design of the PPF and APF parts are introduced. The general design procedures for the adaptive dc voltage controlled HAPF with neutral inductor are also given. The validity and effectiveness of the adaptive dc-link voltage controlled HAPF with neutral inductor experimental system are confirmed by experimental results compared with the conventional fixed and adaptive dc-link voltage controlled HAPFs without neutral inductor. The compensated results meet the requirements of the international standards.

Chapter 7 finally draws the relevant concluding remarks and proposes prospective future research works.

Appendix presents the algorithms for HAPF reference reactive and harmonic compensating calculation based on both three-single instantaneous *pq* theory (Appendix A.1) and single-phase instantaneous *pq* theory (Appendix A.2), which are necessary complementary parts for Chaps. 2–6. Appendix also includes the determination process of the quasi-linear limit and linear limit for HAPF inverter current slope (Appendix A.3) and its corresponding hysteresis band value (Appendix A.4). They are complementary parts of the linearization of hysteresis PWM study and analysis for HAPF described in Chap. 3. Appendix also presents the photo and system parameters of a 55 V, 1.65 kVA three-phase four-wire HAPF experimental prototype (Appendix A.5), in which the experimental results presented in Chaps. 3 and 4 are all obtained by this experimental prototype. The key originalities of this research have led to these publications [32–37].

References

1. H. Akagi, Trends in active power line conditioners. IEEE Trans. Power Electron. **9**(3), 263–268 (1994)
2. H. Akagi, New trends in active filters for power conditioning. IEEE Trans. Ind. Appl. 32(6), 1312–1322 (1996)
3. H. Fujita, H. Akagi, A practical approach to harmonic compensation in power systems–series connection of passive and active filters. IEEE Trans. Ind. Applicat. 27(6), 1020–1025 (1991)
4. F.Z. Peng, H. Akagi, A. Nabae, A new approach to harmonic compensation in power systems–a combined system of shunt passive and series active filters, IEEE Trans. Ind. Applicat. 26(6), 983–990 (1990)
5. L. Chen, A.V. Jouanne, A comparison and assessment of hybrid filter topologies and control algorithms, in *Proceedings of IEEE 32nd Annual Power Electronics Specialists Conference, PESC 01*, vol. 2, 2001, pp. 565–570
6. F.Z. Peng, H. Akagi, A. Nabae, Compensation characteristics of the combined system of shunt passive and series active filters. IEEE Trans. Ind. Applicat. 29(1), 144–152 (1993)
7. P. Salmerón, S.P. Litrán, A control strategy for hybrid power filter to compensate four-wires three-phase systems. IEEE Trans. Power Electron. **25**(7), 1923–1931 (2010)
8. P. Salmeron, S.-P. Litran, Improvement of the electric power quality using series active and shunt passive filters. IEEE Trans. Power Del. **25**(2), 1058–1067 (2010)

9. S. Khositkasame, S. Sangwongwanich, Design of harmonic current detector and stability analysis of a hybrid parallel active filter. in *Proceedings of Power Conversion Conference*, vol. 1, 1997, pp. 181–186
10. Z. Chen, F. Blaabjerg, J.K. Pedersen, Harmonic resonance damping with a hybrid compensation system in power systems with dispersed generation, in *IEEE 35th Annual Power Electronics Specialists Conference, PESC 04*, vol. 4, 2004, pp. 3070–3076
11. H.-K. Chiang, B.-R. Lin, K.-T. Yang, K.-W. Wu, Hybrid active power filter for power quality compensation, in *International Conference on Power Electronics and Drives Systems*, *PEDS 2005*, vol. 2, 2005, pp. 949–954
12. V.F. Corasaniti, M.B. Barbieri, P.L. Arnera, M.I. Valla, Hybrid active filter for reactive and harmonics compensation in a distribution network. IEEE Trans. Ind. Electron. **56**(3), 670–677 (2009)
13. R. Khanna, S.T. Chacko, N. Goel, Performance and investigation of hybrid filters for Power Quality Improvement, in *5th International Power Engineering and Optimization Conference*, *PEOCO*, 2011, pp. 93–97
14. S.T. Senini, P.J. Wolfs, Systematic identification and review of hybrid active filter topologies, in *Proceedings of. IEEE 33rd Annual Power Electronics Specialists Conference, PESC. 02*, vol. 1, 2002, pp. 394–399
15. S. Senini, P.J. Wolfs, Analysis and design of a multiple-loop control system for a hybrid active filter. IEEE Trans. Ind. Electron. **49**(6), 1283–1292 (2002)
16. J.-H. Sung, S. Park, K. Nam, New hybrid parallel active filter configuration minimising active filter size, IEEE Proc. Electr. Power Applicat. 147(2), 93–98 (2000)
17. D. Rivas, L. Moran, J.W. Dixon et al., Improving passive filter compensation performance with active techniques. IEEE Trans. Ind. Electron. **50**(1), 161–170 (2003)
18. H. Fujita, T. Yamasaki, H. Akagi, A hybrid active filter for damping of harmonic resonance in industrial power systems. IEEE Trans. Power Electron. **15**(2), 215–222 (2000)
19. H. Akagi, S. Srianthumrong, Y. Tamai, Comparisons in circuit configuration and filtering performance between hybrid and pure shunt active filters, in *Conference. Record of IEEE-IAS Annual Meeting,* vol. 2, 2003, pp. 1195–1202
20. S. Srianthumrong, H. Akagi, A medium-voltage transformerless AC/DC Power conversion system consisting of a diode rectifier and a shunt hybrid filter. IEEE Trans. Ind. Applicat. 39(3), 874–882 (2003)
21. W. Tangtheerajaroonwong, T. Hatada, K. Wada, H. Akagi, Design and performance of a transformerless shunt hybrid filter integrated into a three-phase diode rectifier. IEEE Trans. Power Electron. **22**(5), 1882–1889 (2007)
22. H.-L. Jou, K.-D. Wu, J.-C. Wu, C.-H. Li, M.-S. Huang, Novel power converter topology for three phase four-wire hybrid power filter, IET Power Electron. (1)1 164–173 (2008)
23. R. Inzunza, H. Akagi, A 6.6-kV transformerless shunt hybrid active filter for installation on a power distribution system. IEEE Trans. Power Electron. **20**(4), 893–900 (2005)
24. V.-F. Corasaniti, M.-B. Barbieri, P.-L. Arnera, M.-I. Valla, Hybrid power filter to enhance power quality in a medium voltage distribution. IEEE Trans. Ind. Electron. **56**(8), 2885–2893 (2009)
25. S. Rahmani, A. Hamadi, N. Mendalek, K. Al-Haddad, A new control technique for three-phase shunt hybrid power filter. IEEE Trans. Ind. Electron. **56**(8), 2904–2915 (2009)
26. N.-Yi Dai, A generalized 3D pulse width modulator for multi-level voltage source inverters in three-phase four-wire power systems, Ph.D. thesis, University of Macau, 2007
27. IEEE Standard, IEEE Recommended Practices and Requirements for Harmonic Control in Electrical Power Systems, 1992, pp. 519–1992
28. IEEE Standard, IEEE Recommended Practice on Monitoring Electric Power Quality, 1995, 1159:1995
29. IEC Standard, Electromagnetic Compatibility (EMC), Part 3: limits, Section 2: limits for Harmonics Current Emissions (Equipment Input Current $\leq$ 16 A Per Phase), 61000-3-2, 1997

30. M.-C. Wong, J. Tang, Y.-D. Han, Cylindrical coordinate control of three-dimensional PWM technique in three-phase four-wired trilevel inverter. IEEE Trans. Power Electron. **18**(1), 208–220 (2003)
31. D.M. Brod, D.W. Novotny, Current control of VSI-PWM inverters. IEEE Trans. Ind. Applicat. (21)3, 562–570 (1985)
32. C.-S. Lam, M.-C. Wong, Y.-D. Han, Investigation of LC-hybrid active power filters in resonances prevention and compensation capabilities, in *IEEE Asia Pacific Conference on Postgraduate Research in Micro-Electronics (PrimeAsia)*, Oct. 2011, pp. 21–24
33. C.-S. Lam, M.-C. Wong, Y.-D. Han, Hysteresis current control of hybrid active power filters. IET Power Electron. **5**(7), 1175–1187 (2012)
34. C.-S. Lam, W.-H. Choi, M.-C. Wong, Y.-D. Han, Adaptive dc-link voltage controlled hybrid active power filters for reactive power compensation. IEEE Trans. Power Electron. **27**(4), 1758–1772 (2012)
35. W.-H. Choi, C.-S. Lam, M.-C. Wong, Y.-D. Han, Analysis of dc-link voltage controls in three-phase four-wire hybrid active power filters. IEEE Trans. Power Electron. **28**(5), 2180–2191 (2013)
36. C.-S. Lam, X–.X. Cui, W.-H. Choi, M.-C. Wong, Y.-D. Han, Minimum inverter capacity design for three-phase four-wire LC-hybrid active power filters. IET Power Electron. **5**(7), 956–968 (2012)
37. C.-S. Lam, M.-C. Wong, W.-H. Choi, X.-X. Cui, H.-M. Mei, J.-Z. Liu, Design and performance of an adaptive low dc voltage controlled LC-hybrid active power filter with a neutral inductor in three-phase four-wire power systems *IEEE Trans. Ind. Electron.*, in press

Chapter 2
Analysis of HAPF in Harmonic Resonances Prevention and Compensation Capabilities

Abstract This chapter aims to investigate the harmonic resonances prevention and compensation capabilities of the three-phase four-wire hybrid active power filter (HAPF). First, a single-phase harmonic equivalent circuit model of the HAPF is deduced and built. Based on this circuit model, the HAPF compensating characteristics are studied and evaluated by four indexes: capability to prevent parallel resonance between the passive power filter (PPF) and the impedance of power system, capability to prevent series resonance of the PPF, capability to improve the filtering performances of the PPF, and capability to enhance the system robustness, in which it shows superior compensating characteristics compared with its pure PPF part. Lastly, simulation results for both the pure PPF part and the HAPF are given to verify all the analyses.

Keywords Filtering Performances · Hybrid Active Power Filter · Parallel Resonance · Passive Power Filter · Series Resonance · System Robustness

2.1 Introduction

In this chapter, the steady-state compensating performances for the HAPF will be discussed, analyzed, and compared with its pure PPF part by four evaluation indexes, capability to prevent the parallel resonance between the PPF and the impedance of the power system, capability to prevent the series resonance of the PPF, capability to improve the filtering performances of the PPF, and capability to enhance the system robustness. First of all, a single-phase harmonic circuit model of the three-phase four-wire HAPF as shown in Fig. 1.8 will be deduced and built in this chapter. Based on the harmonic circuit model, the steady-state compensation performances for both pure PPF part and HAPF will be presented and discussed. Then the corresponding simulation results for pure PPF and HAPF will be given to verify all the deduced and analyzed results. In the following, all the analyses are based on sufficient dc-link voltage assumption.

C.-S. Lam and M.-C. Wong, *Design and Control of Hybrid Active Power Filters*,
SpringerBriefs in Electrical and Computer Engineering,
DOI: 10.1007/978-3-642-41323-0_2,

2.2 HAPF Single-Phase Harmonic Circuit Model

Under opposite i_{cx} direction consideration of the HAPF as in Fig. 1.8, provided that the inverter of the HAPF is controlled by hysteresis PWM with hysteresis error band $H \approx 0$ and is responsible for compensate harmonic components only,

when $(i_{cxh}{}^{*} - i_{cxh}) \geq H$, i.e., $(i_{cxh}{}^{*} - i_{cxh}) \geq 0$, the inverter harmonic output voltage v_{invx1h} can be expressed as:

$$v_{invx1h} = 0.5V_{dc1} = K_1 \cdot (i_{cxh}{}^{*} - i_{cxh}),\ K_1 > 0 \tag{2.1}$$

when $(i_{cxh}{}^{*} - i_{cxh}) < H$, i.e., $(i_{cxh}{}^{*} - i_{cxh}) < 0$, v_{invx1h} can be expressed as:

$$v_{invx1h} = -0.5V_{dc1} = K_2 \cdot (i_{cxh}{}^{*} - i_{cxh}),\ K_2 > 0 \tag{2.2}$$

where the subscript 'x' denotes phase $x = a, b, c$ and the subscript 'h' denotes the harmonic component, $i_{cxh}{}^{*}$ represents the reference compensating harmonic current while i_{cxh} represents the actual compensating harmonic current. As K_1 and K_2 are both in positive, v_{invx1h} can be expressed into a general form as:

$$v_{invx1h} = K \cdot (i_{cxh}{}^{*} - i_{cxh}),\ K > 0 \tag{2.3}$$

In ideal case, $i_{cxh}{}^{*}$ should be equal to the load harmonic current i_{Lxh}, that is $i_{cxh}{}^{*} = i_{Lxh}$. As $i_{sxh} + i_{cxh} = i_{Lxh}$, the inverter harmonic output voltage can be expressed as:

$$v_{inv1xh} = K \cdot i_{sxh},\ K > 0 \tag{2.4}$$

From (2.4), the inverter can be modeled as a current control voltage source in the following harmonic circuit analysis. Figure 2.1 shows the HAPF single-phase harmonic circuit model, in which the nonlinear load and the active inverter part are modeled as a harmonic current source I_{Lxh} and harmonic voltage source V_{invx1h} $(V_{inv1xh} = K \cdot I_{sxh})$. V_{sxh} and V_{xh} are the system and load harmonic voltages, I_{sxh}, I_{Lxh}, and I_{cxh} are the system, load, and inverter compensating harmonic currents. Z_{sh} and $Z_{\mathrm{PPF}h}$ are the harmonic impedance of the power system and PPF, respectively. Figures 2.2 and 2.3 show the HAPF single-phase harmonic circuit models due to load harmonic current I_{Lxh} or system harmonic voltage V_{sxh} component.

2.2.1 HAPF Single-Phase Harmonic Circuit Model Due to I_{Lxh} Only

For the system voltage contains no harmonic components, that is $V_{sxh} = 0$, the HAPF single-phase harmonic circuit model due to load harmonic current I_{Lxh} is shown in Fig. 2.2a. From Fig. 2.2a,

$$I_{sxh} + I_{cxh} = I_{Lxh} \tag{2.5}$$

$$K \cdot I_{sxh} = I_{cxh}Z_{\mathrm{PPF}h} - I_{sxh}Z_{sh} \tag{2.6}$$

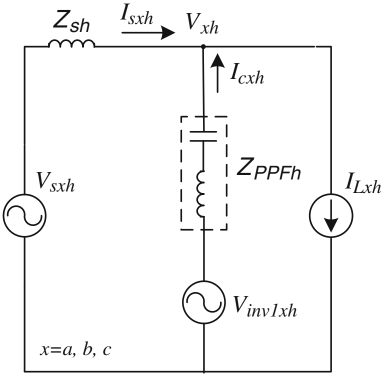

Fig. 2.1 HAPF single-phase harmonic circuit model

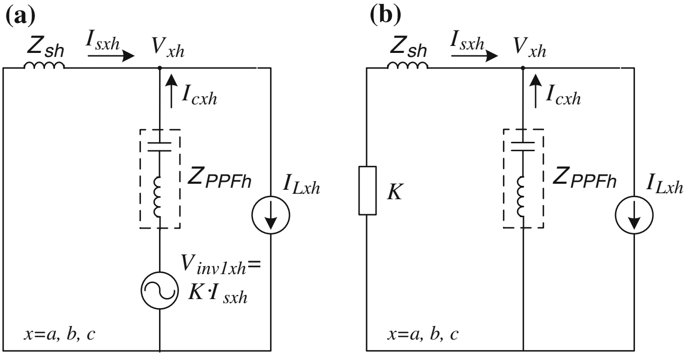

Fig. 2.2 HAPF single-phase harmonic circuit model: **a** $V_{sxh} = 0$ and I_{Lxh} is considered only and **b** a harmonic equivalent circuit model due to I_{Lxh} only

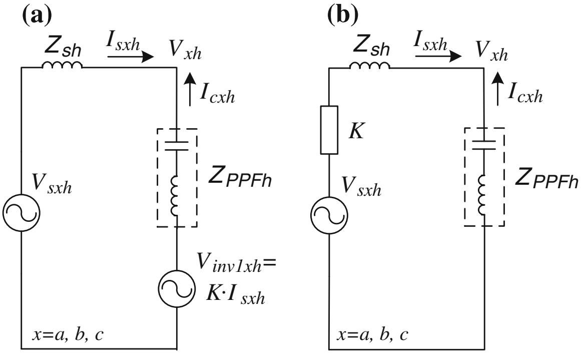

Fig. 2.3 HAPF single-phase harmonic circuit model: **a** $I_{Lxh} = 0$ and V_{sxh} is considered only and **b** a harmonic equivalent circuit model due to V_{sxh} only

From (2.5) and (2.6), the harmonic currents flow into the power system I_{sxh} and the HAPF I_{cxh} due to I_{Lxh} can only be expressed as:

$$K_{sxh\_i} = \frac{I_{sxh}}{I_{Lxh}} = \frac{Z_{\mathrm{PPFh}}}{K + Z_{sh} + Z_{\mathrm{PPF}h}} \tag{2.7}$$

$$K_{cxh\_i} = \frac{I_{cxh}}{I_{Lxh}} = \frac{K + Z_{sh}}{K + Z_{sh} + Z_{\mathrm{PPF}h}} \tag{2.8}$$

In a perfect HAPF compensation, $K_{sxh\_i} = 0$ and $K_{cxh\_i} = 1$ should be achieved so that the load harmonic current flows into the HAPF $(I_{cxh} = I_{Lxh})$ and the power system side does not contain any harmonic current $(I_{sxh} = 0)$. To achieve this objective, K should be very large. Figure 2.2b shows a harmonic equivalent circuit model due to I_{Lxh} only. From Fig. 2.2b, it seems that the inverter is equivalent as a large harmonic impedance which is connected in series with the harmonic impedance of the power system, so that it blocks the harmonic current flowing into the power system and forces it to flow into the HAPF as deduced by (2.7) and (2.8). Therefore, the power system harmonic current I_{sxh} can be significantly reduced if K is significantly large.

2.2.2 HAPF Single-Phase Harmonic Circuit Model Due to V_{sxh} Only

For the load current contains no harmonic components, that is $I_{Lxh} = 0$, the HAPF single-phase harmonic circuit model due to system harmonic voltage V_{sxh} is shown in Fig. 2.3a. From Fig. 2.3a,

$$I_{sxh} = -I_{cxh} \tag{2.9}$$

$$K \cdot I_{sxh} = I_{cxh}(Z_{\mathrm{PPF}h} + Z_{sh}) + V_{sxh} \tag{2.10}$$

From (2.9) and (2.10), the harmonic currents flow into the power system I_{sxh} and the HAPF I_{cxh} due to V_{sxh} can be expressed as:

$$K_{sxh\_v} = \frac{I_{sxh}}{V_{sxh}} = \frac{1}{K + Z_{sh} + Z_{\mathrm{PPF}h}} \tag{2.11}$$

$$K_{cxh\_v} = \frac{I_{cxh}}{V_{sxh}} = -\frac{1}{K + Z_{sh} + Z_{\mathrm{PPF}h}} \tag{2.12}$$

To lessen the effect of V_{sxh} to the harmonic current contents in the power system and the HAPF, $K_{sxh\_v} = 0$ and $K_{cxh\_v} = 0$ should be achieved. To achieve this objective, K should be very large. Figure 2.3b shows a harmonic equivalent circuit model due to V_{sxh} only. From Fig. 2.3b, it seems that the inverter is equivalent as a large harmonic impedance which is connected in series with the harmonic impedance of the power system, so that the effect of V_{sxh} to the power system and the HAPF can be significantly reduced if K is significantly large.

From (2.7), (2.8), (2.11), and (2.12), with superposition theorem, the power system harmonic current I_{sxh} and the HAPF compensating harmonic current I_{cxh} due to V_{sxh} and I_{Lxh} can be expressed as:

$$I_{sxh} = \frac{1}{K + Z_{sh} + Z_{\mathrm{PPF}h}} V_{sxh} + \frac{Z_{\mathrm{PPF}h}}{K + Z_{sh} + Z_{\mathrm{PPF}h}} I_{Lxh} \tag{2.13}$$

$$I_{cxh} = -\frac{1}{K + Z_{sh} + Z_{\mathrm{PPF}h}} V_{sxh} + \frac{K + Z_{sh}}{K + Z_{sh} + Z_{\mathrm{PPF}h}} I_{Lxh} \tag{2.14}$$

When only its pure PPF part is used, that is $K = 0$ in (2.3) and (2.4), (2.13) and (2.14) become:

$$I_{sxh} = \frac{1}{Z_{sh} + Z_{\mathrm{PPF}h}} V_{sxh} + \frac{Z_{\mathrm{PPF}h}}{Z_{sh} + Z_{\mathrm{PPF}h}} I_{Lxh} \tag{2.15}$$

$$I_{cxh} = -\frac{1}{Z_{sh} + Z_{\mathrm{PPF}h}} V_{sxh} + \frac{Z_{sh}}{Z_{sh} + Z_{\mathrm{PPF}h}} I_{Lxh} \tag{2.16}$$

Comparing with (2.13) and (2.14), as $K > 0$, it is obvious that when the HAPF is operating, its harmonic current compensating capability is better than the case when only its pure PPF is used. Equation (2.13) also illustrates that the HAPF can compensate the harmonic current components caused by both the nonlinear load and the distorted system voltage. Moreover, it has the capability to suppress the parallel resonance between the PPF and the impedance of the power system, and also the series resonance of the PPF. In addition, the robustness of the system may also be improved when the HAPF is adopted. In the following, the capabilities of the HAPF to prevent parallel and series resonance phenomena, improve filtering effects of the PPF, and enhance the system robustness will be analyzed, discussed, and verified.

2.3 Investigation of HAPF Steady-State Compensating Performances

In this section, the HAPF steady-state compensating performances are studied and discussed with four evaluation indexes, capability to prevent the parallel and series resonances, capability to improve the filtering performances of the PPF, and capability to enhance the system robustness. Then, the corresponding simulation results for the three-phase four-wire HAPF as shown in Fig. 1.8 will be presented to illustrate and verify the PPF and HAPF steady-state compensating performance analyses. The nonlinear load as shown in Fig. 1.8 is composed of three balanced single-phase diode bridge rectifiers, which acts as harmonic producing load in this

Table 2.1 HAPF simulated system parameters for its steady-state compensating performance analysis

System parameters	Values
v_x $(x = a, b, c), f$	220 V, 50 Hz
L_s, L_{c1}, C_{c1}	1 mH, 5 mH, 80 μF
V_{dc1U}, V_{dc1L}	50 V
L_{NLx}, C_{NLx}, R_{NLx}	30 mH, 200 μF, 26 Ω

chapter. Simulation studies were carried out by using Power System Computer Aided Design (PSCAD)/Electro Magnetic Transient in DC System (EMTDC). Table 2.1 shows a set of three-phase four-wire HAPF simulated system parameters for analyzing its steady-state compensating performances compared with its PPF part, where the coupling inductor L_{c1} and capacitor C_{c1} are designed basing on the reactive power consumption and the fifth-order harmonic frequency of the inductive loading. To simplify the verification, the dc-link is supported by external dc voltage source and the simulated three-phase loadings are balanced.

In addition, the HAPF reference compensating current can be determined by using either the three-phase or single-phase instantaneous *pq* theory as discussed in Appendix A.1 and A.2. Then the corresponding control block diagram of the three-phase four-wire HAPF is also illustrated in Appendix A.1 or A.2. And hysteresis PWM is applied for generating the required compensating current. Thus, the compensating current error Δi_{cx} together with hysteresis band H will be sent to the current PWM control part for generating the trigger signals to the switching devices, insulated gate bipolar transistors (IGBTs) of the VSI.

2.3.1 HAPF Capability to Prevent Parallel Resonance

The parallel resonance between the PPF and the power system impedance may occur when the operating conditions of the power system change, which results in a harmonic current amplification phenomenon at the power system side. The magnitude diagrams of $K_{sxh\_i} = \frac{I_{sxh}}{I_{Lxh}}$ (2.7) with respect to different operating frequency f and power system inductance L_s when only PPF is employed or the HAPF is employed are shown in Fig. 2.4, in which Fig. 2.4 can help to analyze the HAPF capability to prevent parallel resonance. From Fig. 2.4a, when only pure PPF is used, $K = 0$ in (2.7), the harmonic current amplification phenomenon will occur from the f range of 177–250 Hz with L_s range from 0.1 to 5 mH, respectively. When the HAPF is employed, the harmonic current amplification phenomenon disappears, as shown in Fig. 2.4b. As a result, Fig. 2.4 clearly illustrates that the HAPF has the capability to prevent the parallel resonance phenomenon, in which the pure PPF cannot avoid this phenomenon.

Figure 2.5 shows the corresponding simulation results for the parallel resonance prevention capability: (a) when only PPF is utilized and (b) HAPF is employed. When L_s increases from 1 to 5 mH, the parallel resonance between the PPF and

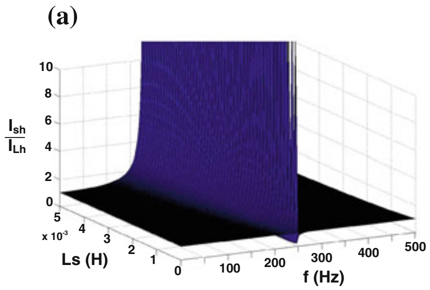

Fig. 2.4 Capability to prevent the parallel resonance between the PPF and the impedance of the power system: **a** when only PPF is utilized (*K* = *0*) and **b** HAPF is employed (*K* = *50*)

power system impedance can occur close to the third-order harmonic frequency. This results in a third-order harmonic current amplification phenomenon at the system side. Figure 2.5a shows that the pure PPF compensation will enlarge the third-order harmonic current from 2.01 to 4.59 A. This phenomenon deteriorates the compensation results as shown in Table 2.2, in which the total harmonic distortion of the system current ($THD_{i_{sx}} = 54.5\ \%$) and load voltage ($THD_{v_x} = 10.5\ \%$) do not satisfy the international standards ($THD_{\mathrm{i_{sx}}} < 20\ \%$ for IEEE, $THD_{\mathrm{i_{sx}}} < 16\ \%$ for IEC, $THD_{v_x} < 5\ \%$ for IEEE) [1–3]. Moreover, the system neutral current i_{sn} has been increased from 5.84 to 13.83 A after PPF compensation.

When the HAPF is employed, Fig. 2.5b shows that the HAPF can obtain better compensation results without the occurrence of the parallel resonance phenomenon. The amplitudes of system current fundamental, third harmonic, and other harmonic contents have been significantly reduced. The nonlinear system current and system displacement power factor (DPF) after HAPF compensation becomes sinusoidal ($THD_{i_{sx}} = 5.6\ \%$) and unity, and the THD_{v_x} of load voltage is 4.8 %, in which the HAPF compensation results as summarized in Table 2.2 satisfy the international standards [1–3]. Moreover, i_{sn} has been reduced from 8.56 to 1.16 A after HAPF compensation.

Figure 2.5 and Table 2.2 clearly illustrate that the HAPF has the capability to prevent the parallel resonance, in which the pure PPF cannot avoid this phenomenon. These simulation results verify the previous PPF and HAPF parallel resonance prevention analyses as shown in Fig. 2.4.

2.3.2 HAPF Capability to Prevent Series Resonance

The PPF may fall into series resonance when the system harmonic voltage produces excessive harmonic current flowing into the PPF. The magnitude diagrams of $K_{cxh\_v} = \frac{I_{cxh}}{V_{sxh}}$ (2.12) with respect to different *f* and L_s when only PPF is employed

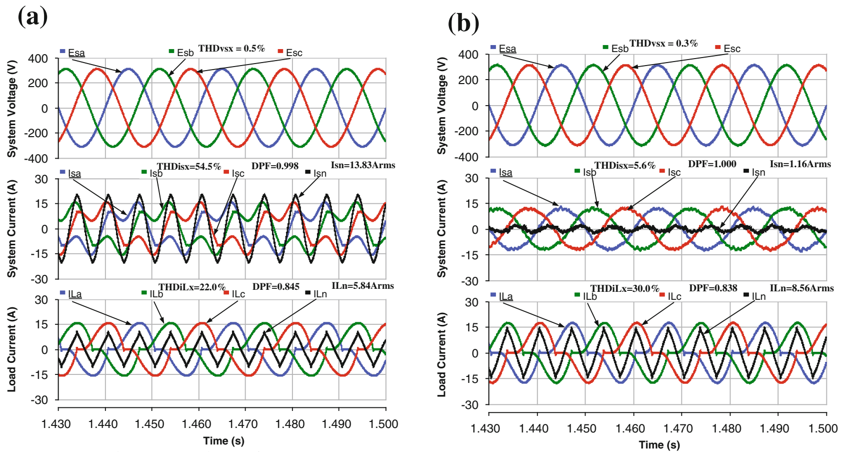

(i) Compensation performances

(i) Compensation performances

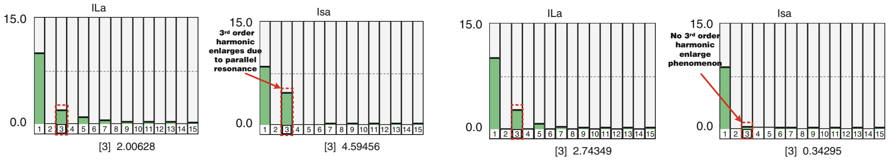

(ii) Frequency spectrum of phase *a* load current i_{Lx} and system current i_{sx} after compensation

(ii) Frequency spectrum of phase *a* load current i_{Lx} and system current i_{sx} after compensation

Fig. 2.5 Simulation results for the parallel resonance prevention capability: **a** when only PPF is utilized and **b** HAPF is employed

Table 2.2 Simulation results before and after PPF and HAPF compensation

Before compensation					After compensation			
Capabilities		THD_{isx} (%)	i_{sn} (A)	DPF	THD_{isx} (%)	i_{sn} (A)	DPF	THD_{vx} (%)
Prevent parallel resonance	PPF	22.0	5.84	0.845	54.5	13.83	0.998	10.5
	HAPF	30.0	8.56	0.838	5.6	1.16	1.000	4.8
Prevent series resonance	PPF	30.0	8.10	0.838	> 75.0	9.25	0.999	5.2
	HAPF	30.0	8.56	0.838	8.5	1.17	1.000	4.6
Improve filtering performances	PPF	30.0	8.10	0.838	37.0	9.30	1.000	2.1
	HAPF	30.0	8.56	0.838	5.0	0.90	1.000	2.2
Enhance system robustness	PPF	25.4	6.86	0.837	44.0	10.20	0.999	5.5
	HAPF	30.0	8.56	0.838	5.2	1.05	1.000	4.0

or HAPF is employed are shown in Fig. 2.6, in which Fig. 2.6 can help to analyze the HAPF capability to prevent series resonance.

From Fig. 2.6a, when only pure PPF is used, $K = 0$ in (2.12), the PPF harmonic current amplification phenomenon due to the distorted system voltage V_{sxh} will occur from f range of 177–250 Hz with the L_s range from 0.1 to 5 mH respectively.

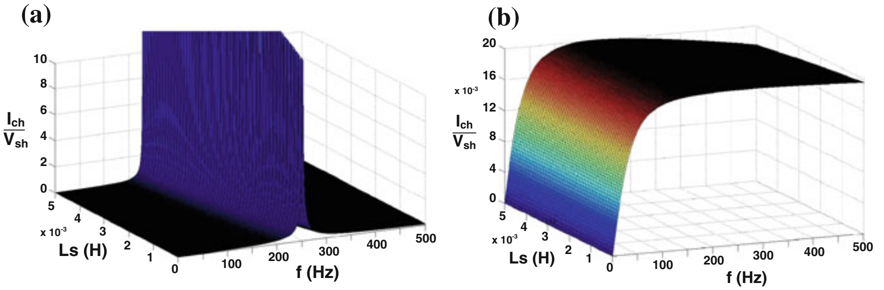

Fig. 2.6 Capability to prevent the series resonance between the PPF and the impedance of the power system: **a** when only PPF is utilized (*K* = *0*) and **b** HAPF is employed (*K* = *50*)

When the HAPF is employed, the PPF harmonic current amplification phenomenon disappears, as shown in Fig. 2.6b. As a result, Fig. 2.6 clearly illustrates that the HAPF has capability to prevent the series resonance as well, in which the pure PPF cannot prevent this phenomenon.

Figure 2.7 shows the corresponding simulation results for the series resonance prevention capability: (a) when only PPF is utilized and (b) HAPF is employed. As the coupling inductor L_{c1} and capacitor C_{c1} are tuned at fifth-order harmonic frequency as shown in Table 2.1, when 4 % of fifth-order harmonic voltage is added to the system voltage, the series resonance of the PPF can occur close to the fifth-order harmonic frequency. This results in a fifth-order harmonic current amplification phenomenon at the system side. Figure 2.7a shows that the pure PPF compensation will enlarge the fifth-order harmonic current at the system side from 0.74 to 5.94 A. This phenomenon deteriorates the compensation results as shown in Table 2.2, in which the total harmonic distortion of the system current $(THD_{i_{sx}} > 75.0\ \%)$ and load voltage $(THD_{v_x} = 5.2\ \%)$ do not satisfy the international standards [1–3]. Moreover, i_{sn} has been increased from 8.10 to 9.25 A after PPF compensation.

When the HAPF is employed, Fig. 2.7b shows that the HAPF can obtain better compensation results without the occurrence of the series resonance phenomenon. The amplitudes of system current fundamental, fifth harmonic and other harmonic contents have been significantly reduced. The nonlinear system current and system DPF after HAPF compensation becomes sinusoidal $(THD_{i_{sx}} = 8.5\ \%)$ and unity, and the THD_{v_x} of load voltage is 4.6 %, in which the HAPF compensation results as summarized in Table 2.2 satisfy the international standards [1–3]. Moreover, i_{sn} has been reduced from 8.56 to 1.17 A after HAPF compensation. Figure 2.7 and Table 2.2 clearly illustrate that the HAPF has the capability to prevent the series resonance, in which the pure PPF cannot avoid this phenomenon. These simulation results verify the previous PPF and HAPF series resonance prevention analyses as shown in Fig. 2.6.

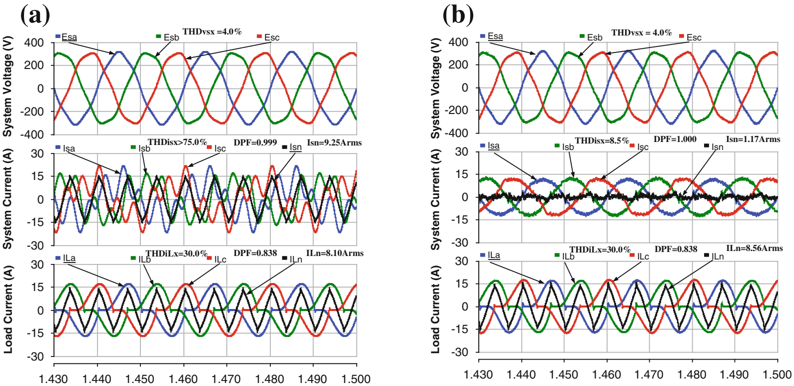

(i) Compensation performance

(i) Compensation performance

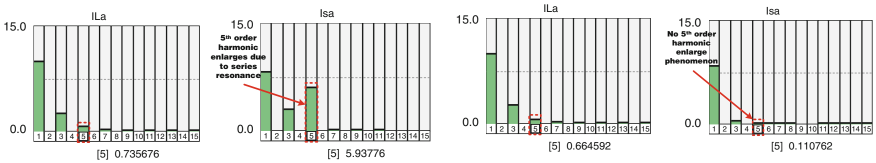

(ii) Frequency spectrum of phase a load current i_{Lx} and system currents i_{sx} after compensation

(ii) Frequency spectrum of phase a load current i_{Lx} and system currents i_{sx} after compensation

Fig. 2.7 Simulation results for the series resonance prevention capability: **a** when only PPF is utilized and **b** HAPF is employed

2.3.3 HAPF Capability to Improve Filtering Performances

From Table 2.1, Fig. 2.8a shows a bode diagram of $K_{sxh\_i} = \frac{I_{sxh}}{I_{Lxh}}$ (2.7) with respect to different K values due to the effect of I_{Lxh}. And Fig. 2.8b shows a bode diagram of $K_{sxh\_v} = \frac{I_{sxh}}{V_{sxh}}$ (2.11) with respect to different K values due to the effect of V_{sxh}. When only PPF is utilized, $K = 0$ in (2.7) and (2.11), the harmonic current amplification phenomenon occurs at $\omega = 1120$ rad/s. However, when the HAPF is employed ($K = 25$ or 50), all the harmonic current components can be significantly decreased as shown in Fig. 2.8a, b. And the harmonic current amplification phenomenon also disappears. In addition, the larger the K value, the better the filtering performances can be obtained and vice versa. These results verify that the active inverter part of the HAPF is capable to improve the filtering performances of the PPF and compensate the harmonic current caused by both I_{Lxh} and V_{sxh}.

Figure 2.9 shows the corresponding simulation results for the filtering capability: (a) when only PPF is utilized and (b) HAPF is employed. From Fig. 2.9a, when only pure PPF is employed, the amplitudes of the system current fundamental and fifth harmonic have been reduced. The system DPF becomes unity and the fifth harmonic current at the power system side reduces from 0.74 to 0.26 A. However, a larger $THD_{i_{sx}}$ is obtained after PPF compensation, from 30.0 to 37.0 %,

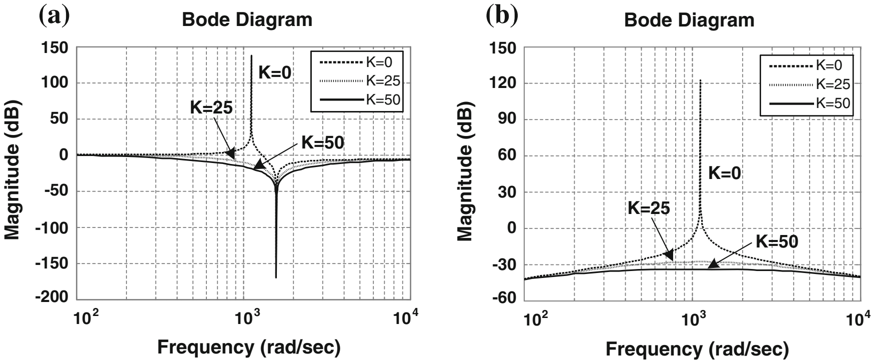

Fig. 2.8 Capability to improve the filtering performances of the PPF ($K = 0$, $K = 25$, $K = 50$) due to: **a** I_{Lxh} and **b** V_{sxh}

which is due to the decrease of the system current fundamental component and the increase of the third-order harmonic current at the system side. The THD_{v_x} of load voltage after PPF compensation is 2.1 %, in which the compensation results are summarized in Table 2.2. The $THD_{i_{sx}}$after PPF compensation does not satisfy the international standards [1, 2]. Moreover, i_{sn} has been increased from 8.10 to 9.30 A after PPF compensation.

When the HAPF is employed, Fig. 2.9b shows that the amplitudes of the system current fundamental, fifth harmonic and other harmonic contents have been significantly reduced. The nonlinear system current and system DPF after HAPF compensation becomes sinusoidal ($THD_{i_{sx}} = 5.0\ \%$) and unity, and the THD_{v_x} of load voltage is 2.2 %, in which the HAPF compensation results as summarized in Table 2.2 satisfy the international standards [1–3]. Moreover, i_{sn} has been reduced from 8.56 to 0.90 A after HAPF compensation. Figure 2.9 and Table 2.2 clearly illustrate that the HAPF has the capability to improve the filtering performances of the PPF. These simulation results verify the previous PPF and HAPF filtering performance analyses as shown in Fig. 2.8.

2.3.4 HAPF Capability to Enhance System Robustness

Due to the effect of I_{Lxh}, Fig. 2.10 shows a bode diagram of $K_{sxh\_i} = \frac{I_{sxh}}{I_{Lxh}}$ (2.7) with respect to different $L_s$values when only PPF is employed or HAPF is employed. When only the PPF is utilized, the harmonic current amplification point will move to the lower frequency side as the increase of L_s value and vice versa, as shown in Fig. 2.10a. Moreover, L_s value affects the system filtering performances. When the HAPF is employed, the harmonic current amplification point disappears no matter what the L_s value is. Moreover, the harmonic current compensation characteristic of the HAPF does not vary at all, as shown in Fig. 2.10b.

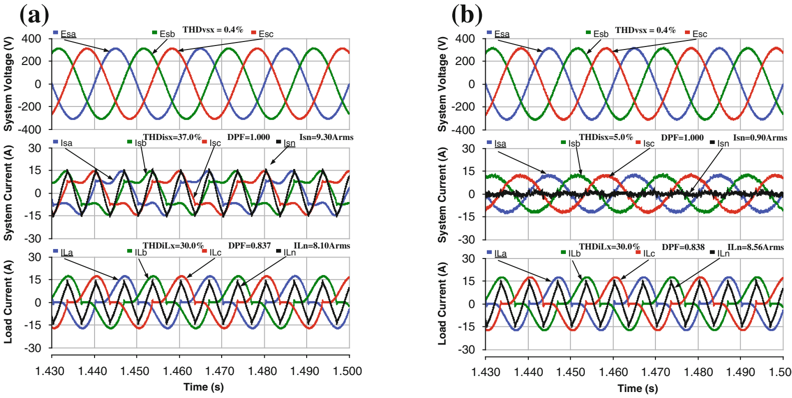

(i) Compensation performance

(i) Compensation performance

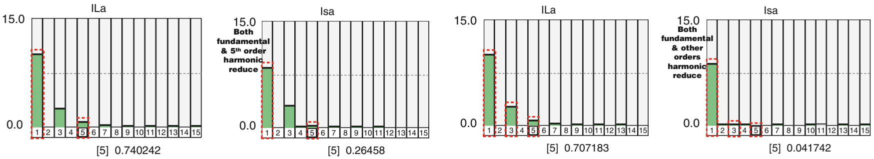

(ii) Frequency spectrum of phase *a* load current i_{Lx} and system currents i_{sx} after compensation

(ii) Frequency spectrum of phase *a* load current i_{Lx} and system currents i_{sx} after compensation

Fig. 2.9 Simulation results for improving the filtering effects of the PPF: **a** when only PPF is utilized and **b** HAPF is employed

Due to the effect of V_{sxh}, Fig. 2.11 shows a bode diagram of $K_{sxh\_v} = \frac{I_{sxh}}{V_{sxh}}$ (2.11) with respect to different L_s values when only PPF is employed or HAPF is employed. Similar as Fig. 2.10, when only the PPF is utilized, harmonic current amplification point will move to the lower frequency side as the increase of L_s value and vice versa, as shown in Fig. 2.11a. When the HAPF is employed, the

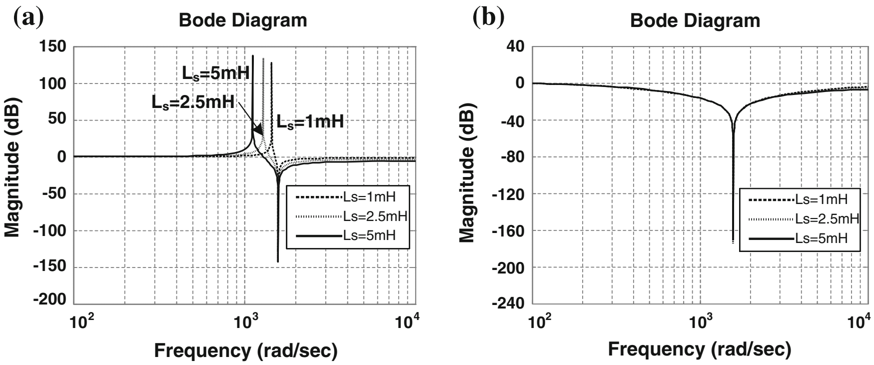

Fig. 2.10 Capability to enhance the system robustness due to I_{Lxh}: **a** when only PPF is utilized ($K = 0$) and **b** HAPF is employed ($K = 50$)

harmonic current amplification point disappears no matter what the L_s value is. Moreover, the harmonic current compensation characteristic of the HAPF does not vary at all, as shown in Fig. 2.11b. And it has also a large attenuation of more than –34 dB, which reflects the power system harmonic current content caused by V_{sxh} can be significantly reduced when the HAPF is adopted.

Both results in Figs. 2.10 and 2.11 verify that the HAPF has capability to enhance the system robustness even though L_s is varying.

Figure 2.12 shows the corresponding simulation results for the system robustness enhancement capability: (a) when only PPF is utilized and (b) HAPF is employed. When L_s increases from 1 to 3 mH, the harmonic current amplification point of the pure PPF will move to the lower frequency side. This results in enlarging the third-order harmonic current at the power system side as shown in Fig. 2.12a. Though the amplitudes of the system current fundamental and fifth harmonic contents have been reduced, a larger $THD_{i_{sx}}$ is obtained after PPF compensation, from 25.4 to 44.0 %. The increase of $THD_{i_{sx}}$ is due to the decrease of the system current fundamental component and the increase of the third-order harmonic current. Compared with Fig. 2.9a, Fig. 2.12a yields a larger $THD_{i_{sx}}$ after PPF compensation because increasing L_s to 3 mH moves the current amplification point closer to the third-order harmonic frequency, thus amplifying the amplitude of the third-order harmonic current more and deteriorating the compensation results. The THD_{v_x} of load voltage after PPF compensation is 5.5 %, in which the compensation results are summarized in Table 2.2. Both $THD_{i_{sx}}$ and THD_{v_x} after PPF compensation do not satisfy the international standards [1–3]. Moreover, i_{sn} has been increased from 6.86 to 10.20 A after PPF compensation.

When the HAPF is employed, Fig. 2.12b shows that even though L_s increases from 1 to 3 mH, the HAPF can still obtain similar and good compensation results compared with Fig. 2.9b. The amplitudes of system current fundamental, fifth harmonic and other harmonic contents have been significantly reduced. The nonlinear system current and system DPF after HAPF compensation becomes

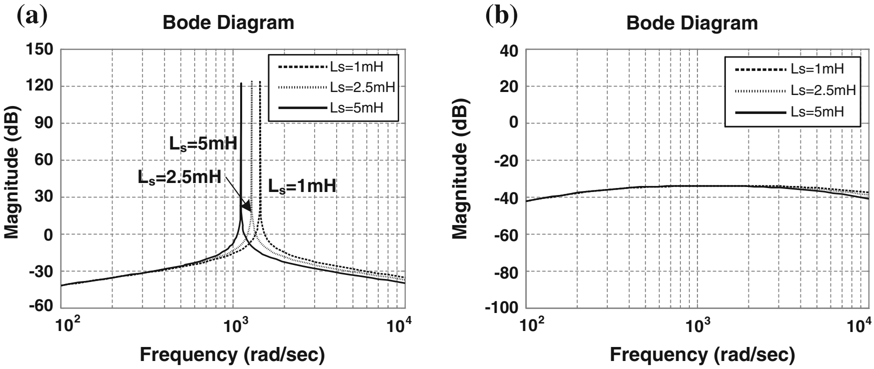

Fig. 2.11 Capability to enhance the system robustness due to V_{sxh}: **a** when only PPF is utilized ($K = 0$) and **b** HAPF is employed ($K = 50$)

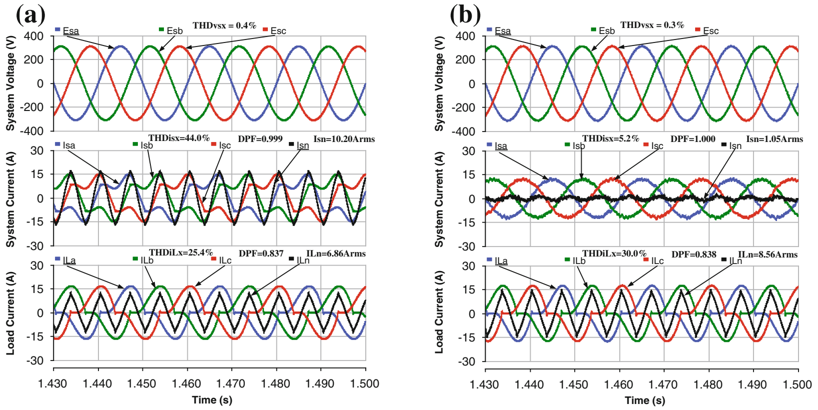

(i) Compensation performance

(i) Compensation performance

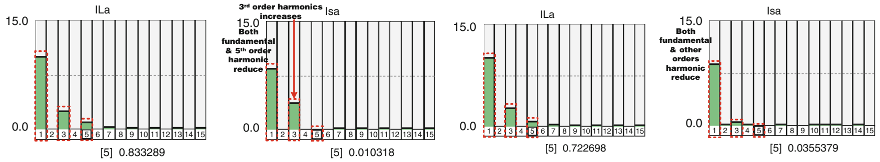

(ii) Frequency spectrum of phase a load current i_{Lx} and system currents i_{sx} after compensation

(ii) Frequency spectrum of phase a load current i_{Lx} and system currents i_{sx} after compensation

Fig. 2.12 Simulation results for enhancing the system robustness: **a** when only PPF is utilized and **b** HAPF is employed

sinusoidal $(THD_{i_{sx}} = 5.2\ \%)$ and unity, and the THD_{v_x} of load voltage is 4.0 %, in which the HAPF compensation results as summarized in Table 2.2 satisfy the international standards [1–3]. Moreover, i_{sn} has been reduced from 8.56 to 1.05 A after HAPF compensation. Figure 2.12 and Table 2.2 clearly illustrate that the HAPF has the capability to enhance the system robustness. These simulation results verify the previous PPF and HAPF in enhancing system robustness analyses as shown in Figs. 2.10 and 2.11.

From the above simulation results and Table 2.2, they clearly illustrate that the HAPF is capable to prevent the parallel resonance between the PPF and the power system impedance, series resonance of the PPF, to improve the filtering characteristic of the PPF, and to enhance the system robustness. Moreover, they verify the PPF and HAPF steady-state compensating performance analyses.

2.4 Summary

In this chapter, a single-phase harmonic circuit model of the three-phase four-wire center-split HAPF is deduced and built. Based on the harmonic circuit model, the steady-state compensating performances for pure PPF and HAPF are deduced, discussed, and analyzed with four evaluation indexes, capability to prevent the parallel resonance between the PPF and the impedance of the power system (2.7), capability to prevent the series resonance of the PPF (2.12), capability to improve the filtering performances (2.7), (2.11) and capability to enhance the system robustness (2.7), (2.11). It is found that the HAPF has the capability to prevent parallel and series resonance phenomena inherent in pure PPF, to improve the filtering effects of the PPF, and to enhance the system robustness, in which all the deduced and analyzed results are verified by simulation results.

References

1. IEEE Standard 519-1992, *IEEE recommended practices and requirements for harmonic control in electrical power systems*, (1992)
2. IEC Standard 61000-3-2, *Electromagnetic compatibility (EMC), Part 3: Limits, Section 2: Limits for harmonics current emissions* (*equipment input current ≤16 A per phase*) (1997)
3. IEEE Standard 1159:1995, *IEEE recommended practice on monitoring electric power quality*, (1995)

Chapter 3
Nonlinearity and Linearization of Hysteresis PWM Study and Analysis for HAPF

Abstract This chapter presents a hysteresis pulse width modulation (PWM) study for three-phase four-wire hybrid active power filter (HAPF). As the coupling inductor and capacitor (LC) impedance yields a nonlinear inverter current slope, this can affect the controllability of using the conventional hysteresis control method and generate unexpected trigger signals to the switching devices. This results in deteriorating the system operating performances. Based on the proposed modeling, the linearization of the hysteresis control for the HAPF is first studied, investigated, and compared with the linear active power filter (APF). Two limits are proposed in this work that divides the HAPF into nonlinear, quasi-linear, and linear operation regions. The design criteria of hysteresis band and sampling time can then be derived. Single-phase simulation and experimental results are given to verify the hysteresis control study of HAPF compared with APF. Finally, representative simulation and experimental results of a three-phase four-wire center-split HAPF for power quality compensation are presented to demonstrate the validity of the hysteresis linearization study.

Keywords Active Power Filter · Coupling LC · Hybrid Active Power Filter · Hysteresis PWM · Linearization · Nonlinear Inverter Current Slope

3.1 Introduction

Pulse width modulation (PWM) techniques such as: hysteresis, ramp comparison, space vector, etc. were traditionally developed based on linear concept [1]. They are usually applied on the conventional linear inductive-coupling voltage source inverters (L coupling VSIs) for different applications [1–9], such as: ac motor drives, active power filter (APF), dynamic voltage restorer (DVR), etc. Among different PWM methods, hysteresis is one of the most popular PWM strategies [2–5] and widely applied in APF for current quality compensation, owing to its

C.-S. Lam and M.-C. Wong, *Design and Control of Hybrid Active Power Filters*,
SpringerBriefs in Electrical and Computer Engineering,
DOI: 10.1007/978-3-642-41323-0_3,

advantages such as ease of implementation, fast dynamic response, current limiting capability, etc.

In recent research studies, the design principles and filtering characteristics for the HAPF have been presented and discussed [10]. An optimal design of its dc-link voltage has been introduced based on the vector trajectory method [11]. In order to enhance the HAPF system response, a novel control technique has also been proposed [12]. As the coupling LC of the HAPF yields a nonlinear inverter current slope, this can affect the controllability of using the conventional hysteresis control method and generate unexpected trigger signals to the switching devices, thus deteriorating the system operating performances. However, there is still no research work neither examining nor discussing the hysteresis margin constraints for this HAPF (i.e., LC coupling VSI) if the linear hysteresis control strategy is applied.

Due to the limitations among the existing literatures, the modeling of the HAPF will be first presented in this chapter. Via its modeling, the linearization work of hysteresis PWM control for the HAPF will be studied in comparison to the linear APF. Two limits: quasi-linear limit and linear limit which divide the HAPF into nonlinear, quasi-linear, and linear regions are proposed. With respect to different coupling LC values, this chapter aims to define the corresponding requirements for hysteresis band and sampling time, such that the inverter current slope of the HAPF can be approximately treated as linear using the hysteresis method. Otherwise, unexpected trigger signals will be generated to the switching devices and strongly affect the HAPF compensating performances. Finally, simulation and experimental results for single-phase and three-phase systems are presented to verify the hysteresis control study for the HAPF compared with that of linear APF.

3.2 Modeling of a Three-Phase Four-Wire Center-Split HAPF and APF

3.2.1 Circuit Configuration of a Three-Phase Four-Wire Center-Split HAPF and APF

Figures 3.1 and 3.2 illustrate the circuit configuration of a three-phase four-wire HAPF and APF, where the subscript 'x' denotes phase $a, b, c,$ and n. v_{sx} is the system voltage, v_x is the load voltage, and L_s is the system inductance normally neglected due to its low value relatively, thus $v_{sx} \approx v_x$. i_{sx}, $i_{L\mathrm{x}}$, and $i_{c\mathrm{x}}$ are the system, load, and inverter current for each phase. C_{c1} and L_{c1} are the coupling capacitor and inductor of the HAPF, in which C_{c1} and L_{c1} are designed basing on the reactive power consumption and the dominant harmonic current of the inductive loading. L_{c2} is the coupling inductor of the APF, in which L_{c2} is designed basing on the switching frequency, switching ripple, and dc-link voltage level consideration. C_{dc1}, V_{dc1_U}, and V_{dc1_L} are the dc capacitor, upper, and lower dc capacitor voltages of the HAPF, while C_{dc2}, V_{dc2_U}, and V_{dc2_L} are the dc capacitor,

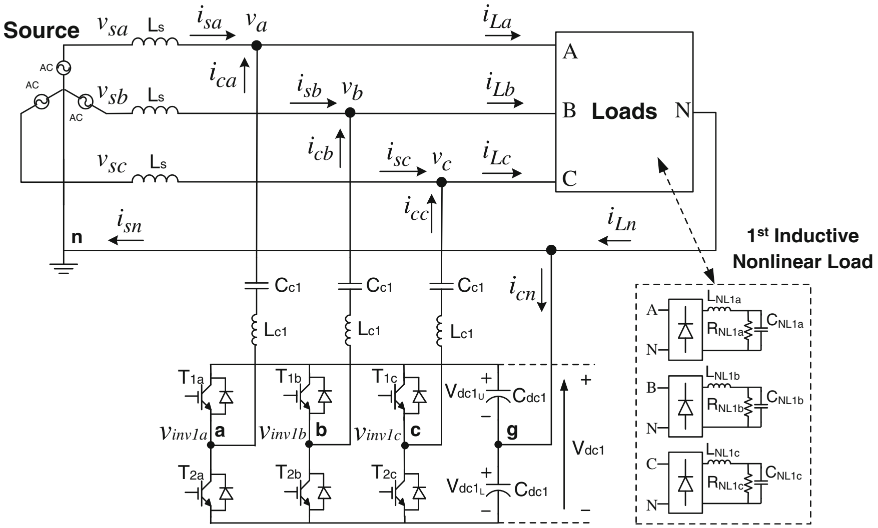

Fig. 3.1 A hybrid active power filter (HAPF)

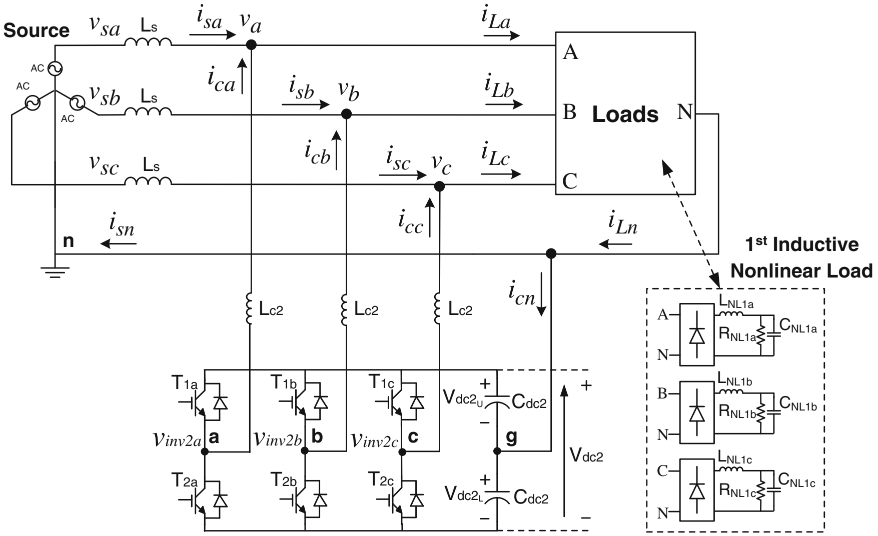

Fig. 3.2 An active power filter (APF)

upper, and lower dc capacitor voltages of the APF. The dc-link midpoint is assumed to be ground reference (g). From Figs. 3.1 and 3.2, the inverter line-to-ground voltages $v_{invjx-g}$ will be equal to the inverter line-to-neutral voltages $v_{invjx-n}$ because the neutral point n is connected to the dc-link midpoint g, where subscript

$j = 1$ represents the HAPF and $j = 2$ represents the APF. The nonlinear loads are composed of three single-phase diode bridge rectifiers, which act as harmonic producing loads in this chapter. In the following, all the analyses are based on sufficient dc-link voltage assumption. Moreover, the internal resistance of the coupling part is assumed to be small and can be neglected.

3.2.2 Mathematical Modeling of a Three-Phase Four-Wire Center-Split HAPF and APF

From Figs. 3.1 and 3.2, the switching functions S_x for each inverter leg of the HAPF and APF can be given as:

$$S_x = \begin{cases} 1 \text{ when } T_{1x} \textit{ is ON} \text{ and } T_{2x} \textit{ is OFF} \\ -1 \text{ when } T_{2x} \textit{ is ON} \text{ and } T_{1x} \textit{ is OFF} \end{cases} \tag{3.1}$$

For $V_{dcj_U} = V_{dcj_L} = 0.5V_{dcj}$, the output voltage for each inverter leg can be expressed as:

$$v_{invjx} = S_x \times 0.5V_{dcj} \tag{3.2}$$

The inverter line-to-neutral voltage $v_{invjx-n}$ can be expressed as:

$$v_{invjx-n} = v_{invjx} - v_n = v_{invjx} \tag{3.3}$$

where the neutral line voltage $v_n = 0$, the switching state of an inverter leg is independent of the switching states of the other two legs, the inverter line-to-neutral voltage v_{invjx} for each leg is either equal to $-0.5V_{dcj}$ or $+0.5V_{dcj}$.

From Fig. 3.1, the relationship among the inverter current i_{cx}, load voltage v_x, coupling capacitor voltage v_{Cc1x}, and inverter line-to-neutral voltage v_{inv1x} of the HAPF is:

$$L_{c1}\frac{di_{cx}(t)}{dt} = v_{inv1x}(t) - v_x(t) - v_{Cc1x}(t) \tag{3.4}$$

From (3.2), the modeling for each inverter leg of the HAPF can be expressed as:

$$L_{c1}\frac{di_{cx}(t)}{dt} = S_x \times 0.5V_{dc1} - v_x(t) - v_{Cc1x}(t) \tag{3.5}$$

$$C_{c1}\frac{dv_{Cc1x}(t)}{dt} = i_{cx}(t) \tag{3.6}$$

From Fig. 3.2, the relationship among the inverter current i_{cx}, load voltage v_x, and inverter line-to-neutral voltage v_{inv2x} of the APF is:

$$L_{c2}\frac{di_{cx}(t)}{dt} = v_{inv2x}(t) - v_x(t) \tag{3.7}$$

From (3.2), the modeling for each inverter leg of the APF can be expressed as:

$$L_{c2}\frac{di_{cx}(t)}{dt} = S_x \times 0.5V_{dc2} - v_x(t) \tag{3.8}$$

Via (3.4)–(3.8), the linearization study of hysteresis control for the HAPF in comparison to the linear APF will be presented in the following.

3.3 Hysteresis PWM Control for HAPF

3.3.1 Nonlinearity of HAPF Inverter Current Slope

As the coupling LC of the HAPF yields a nonlinear inverter current slope, this can affect the controllability of using the conventional hysteresis PWM, the linearization of the hysteresis control for the HAPF should be investigated. In this section, the slope of the HAPF inverter current i_{cx} is categorized into three operation regions: (i) nonlinear region (ii) quasi-linear region, and (iii) linear region, in which their corresponding definitions and diagrams under hysteresis control are given below:

(1) *Nonlinear region*: The slope of the HAPF inverter current i_{cx} is defined as 'nonlinear' if its slope polarity has interchanged from positive to negative or vice versa before i_{cx} touches the top or bottom hysteresis band H (within each switching on t_{on} or off t_{off} interval), as shown in Fig. 3.3a. i_{cx}^* is the reference inverter current.

(2) *Quasilinear region*: The slope of the HAPF inverter current i_{cx} is defined as 'quasi-linear' if its slope polarity changes only when i_{cx} touches the top or bottom hysteresis band H. Within each switching on or off interval, the absolute percentage error of its current slope compared with a linear one is larger than $\varepsilon\%$ ($|di_{cx}/dt|_{error} > \varepsilon\%$), as shown in Fig. 3.3b. The current slope error limit ε can be determined in Appendix A.3.

(3) *Linear region*: The slope of the HAPF inverter current i_{cx} can be treated as 'linear' if its slope polarity changes only when i_{cx} touches the top or bottom hysteresis band H. Within each switching on or off interval, the absolute percentage error of its current slope compared with a linear one is less than or equal to $\varepsilon\%$ ($|di_{cx}/dt|_{error} \leq \varepsilon\%$), as shown in Fig. 3.3c.

In addition, these three operation regions are separated by two limits: quasi-linear limit T_{limit} and linear limit T_{linear}, in which their values are determined based on a constant reference inverter current i_{cx}^*assumption as given in Appendix A.3. After that, the corresponding quasi-linear limit H_{limit} and linear limit H_{linear} for the hysteresis band can be obtained in Appendix A.4. In the following, these three definitions and two limits will be used for the HAPF inverter current slope linearity justification under hysteresis control method.

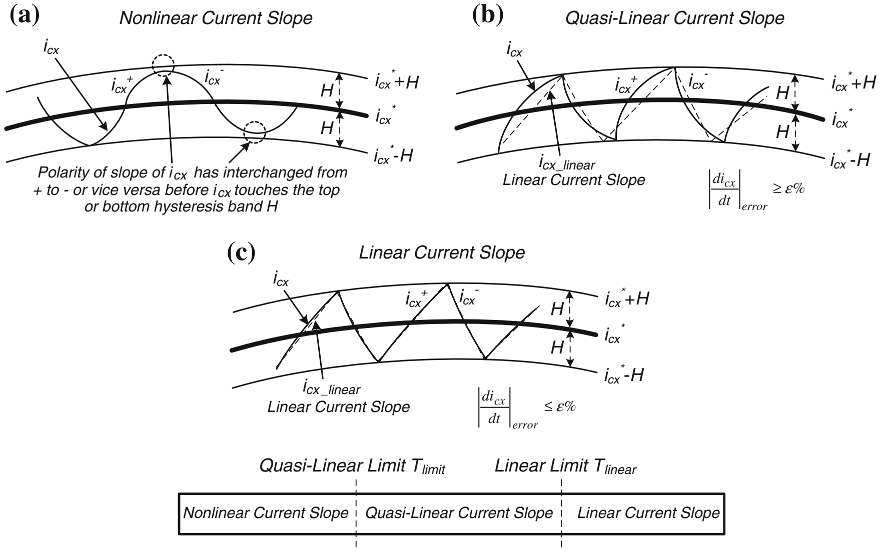

Fig. 3.3 Slope of the HAPF inverter current i_{cx} under hysteresis PWM control: **a** nonlinear region **b** quasi-linear region and **c** linear region

In practical case, as different loading situations may require different coupling C_{c1} and L_{c1} values, thus yielding different $T_{\text{limit}}\ (H_{\text{limit}})$ and $T_{\text{linear}}\ (H_{\text{linear}})$ values (Appendix A.3–A.4), it is important and necessary to carry out this linearity analysis, so that the linear operation region for each HAPF system can be achieved. To simplify the verification, the coupling part internal resistance for the HAPF and APF are approximately treated as zero in the following simulations and experiments because their values are usually small in practical situation.

3.3.2 Single-Phase Simulation and Experimental Results for HAPF Inverter Current Slope Linearization Analysis

Under constant reference inverter current i_{cx}^* assumption, Fig. 3.4a and b illustrate the HAPF and APF single-phase inverter current slope linearization study models for upper switch T_{1x} at different switching on interval ($t = t_{\text{on}}$), in which the upper switch is an IGBT. E_1 and E_2 represent the instantaneous peak voltage difference between the inverter output voltage and load voltage. Reversing the polarity of E_1 and E_2 will yield their models for lower switch $T_{2x}\ (t = t_{\text{off}})$. As the only difference between upper and lower switches is the opposite current polarity, the results for T_{2x} will not be included. In short, E_1 and E_2 can be treated as dc voltage inputs. In addition, the load voltage is treated as a constant value for the following

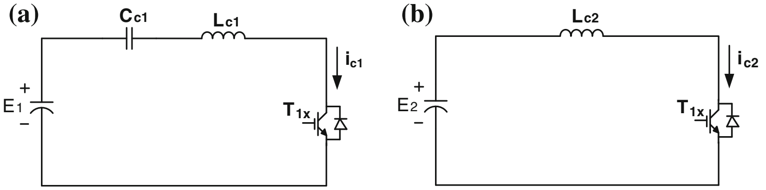

Fig. 3.4 Single-phase model for upper switch T_{1x} at different t_{on} interval: **a** HAPF and **b** APF

analysis. Table 3.1 lists the system parameters of HAPF and APF single-phase models. When the internal resistance of the coupling part is small and can be neglected, the current slope for APF will be linear no matter what the switching interval is, as verified by (3.7), (3.8). Since E_1 and E_2 values do not affect the determination results of the quasi-linear limit and linear limit, E_1 and E_2 are chosen as 20 V in this work. From Table 3.1, the quasi-linear limit and linear limit for HAPF can be determined as: $T_{\text{limit}} = 1{,}000\,\mu\text{s}$ and $T_{\text{linear}} = 200\,\mu\text{s}$, respectively, (Appendix A.3). Simulation studies were carried out by using PSCAD/EMTDC. In the following, simulation and experimental results for Fig. 3.4a and b will be given to verify the HAPF inverter current slope linearization analysis compared with the linear APF. Figures 3.5 and 3.8 illustrate the simulated and experimental inverter current i_{c1} and i_{c2} for their single-phase models at different switching on interval.

In order to satisfy the linear region definition $|di_{cx}/dt|_{\text{error}} \leq 5\,\%$ (Appendix A.3–A.4), the slope error of HAPF inverter current i_{c1} compared with the APF one i_{c2} should be less than 5 %. From Fig. 3.5a, when $t_{\text{on}} > 1{,}000\,\mu\text{s}$, which is larger than the quasi-linear limit ($T_{\text{limit}} = 1,000\,\mu\text{s}$), the rising slope of i_{c1} as in Fig. 3.5a is nonlinear compared with that of i_{c2} as shown in Fig. 3.6a. However, even when $t_{\text{on}} = 1{,}000\,\mu\text{s}$ and $t_{\text{on}} = 500\,\mu\text{s}$ satisfy the quasi-linear limit, they do not satisfy the linear limit. It is obvious that Fig. 3.5b and c contain current slope errors (35.3, 10.0 %) compared with that of APF as shown in Fig. 3.6b and c. These errors have the potential of deteriorating the system operating performance significantly. When $t_{\text{on}} = 200\,\mu\text{s}$, which satisfies the linear limit ($T_{linear} = 200\,\mu\text{s}$), the current slope error decreases to 1.5 % (within the linear region definition $|di_{cx}/dt|_{\text{error}} \leq 5\,\%$), i_{c1} in Fig. 3.5d is approximately the same as i_{c2} in Fig. 3.6d.

The experimental current i_{c1} and i_{c2} for their single-phase models at different switching on interval ($t = t_{\text{on}}$) are shown in Figs. 3.7 and 3.8, in which the experimental results are consistent with the simulation results as shown in Figs. 3.5 and 3.6. When $t_{\text{on}} > 1{,}000\,\mu\text{s}$, the rising slope of i_{c1} as shown in Fig. 3.7a

Table 3.1 System parameters of HAPF and APF single-phase models

System parameters	Physical values
L_{c1}, L_{c2}	6 mH
C_{c1}	70 μF
E_1, E_2	20 V (dc)

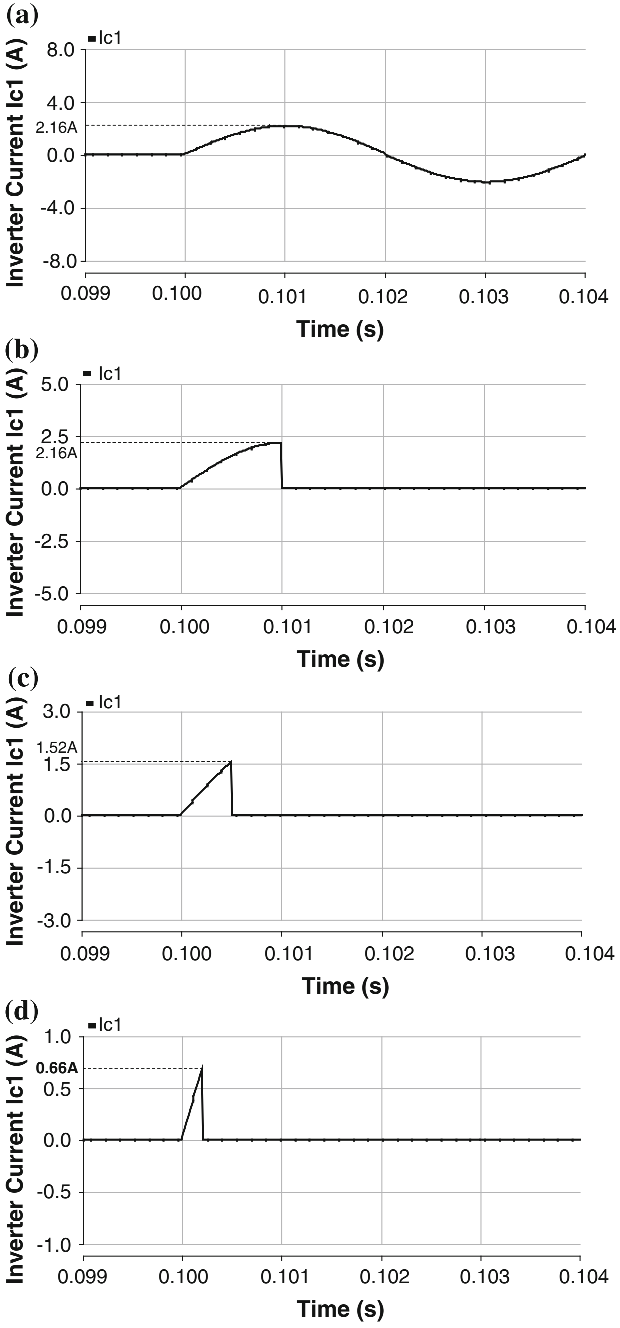

Fig. 3.5 Simulated i_{c1} of HAPF single-phase model at different t_{on} interval and $E_1 = 20\,\mathrm{V}$: **a** $t_{\mathrm{on}} = 2{,}000$ µs (Nonlinear), **b** $t_{\mathrm{on}} = 1{,}000$ µs (Quasi-linear), **c** $t_{\mathrm{on}} = 500$ µs (Quasi-linear), and **d** $t_{\mathrm{on}} = 200$ µs (Linear)

Fig. 3.6 Simulated i_{c2} of APF single-phase model at different t_{on} interval and $E_2 = 20$ V: **a** $t_{\mathrm{on}} = 2{,}000$ μs (Linear), **b** $t_{\mathrm{on}} = 1{,}000$ μs (Linear), **c** $t_{\mathrm{on}} = 500$ μs (Linear), and **d** $t_{\mathrm{on}} = 200$ μs (Linear)

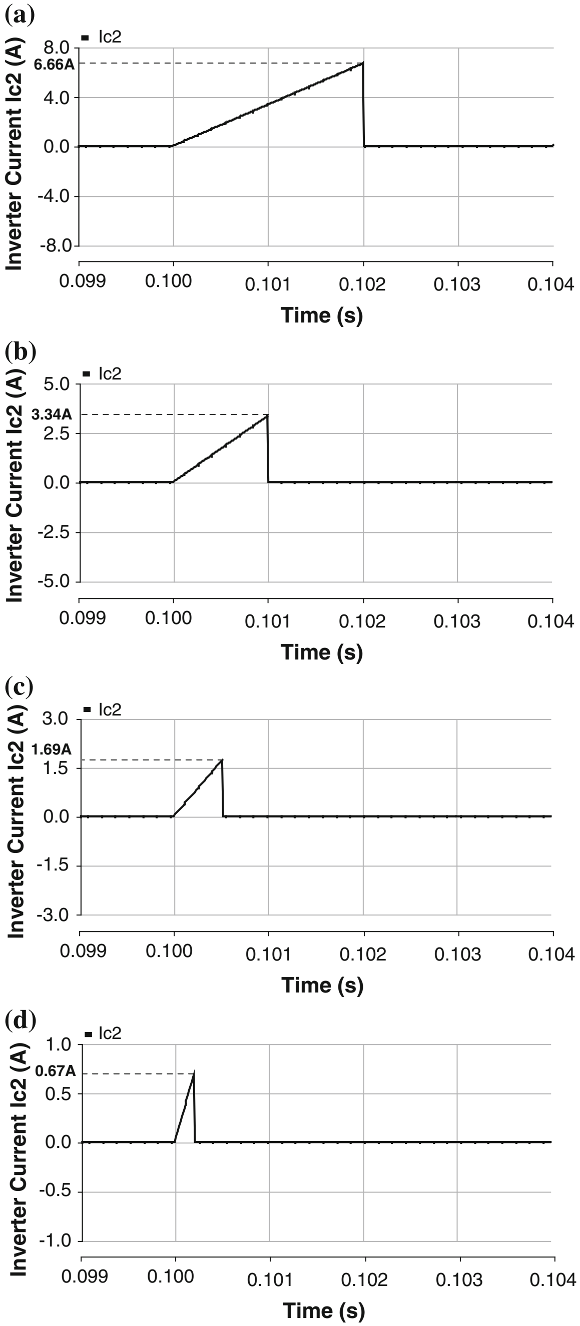

Fig. 3.7 Experimental i_{c1} of HAPF single-phase model at different t_{on} interval and $E_1 = 20$ V: **a** $t_{\mathrm{on}} = 2{,}000$ μs (Nonlinear), **b** $t_{\mathrm{on}} = 1{,}000$ μs (Quasi-linear), **c** $t_{\mathrm{on}} = 500$ μs (Quasi-linear), and **d** $t_{\mathrm{on}} = 200$ μs (Linear)

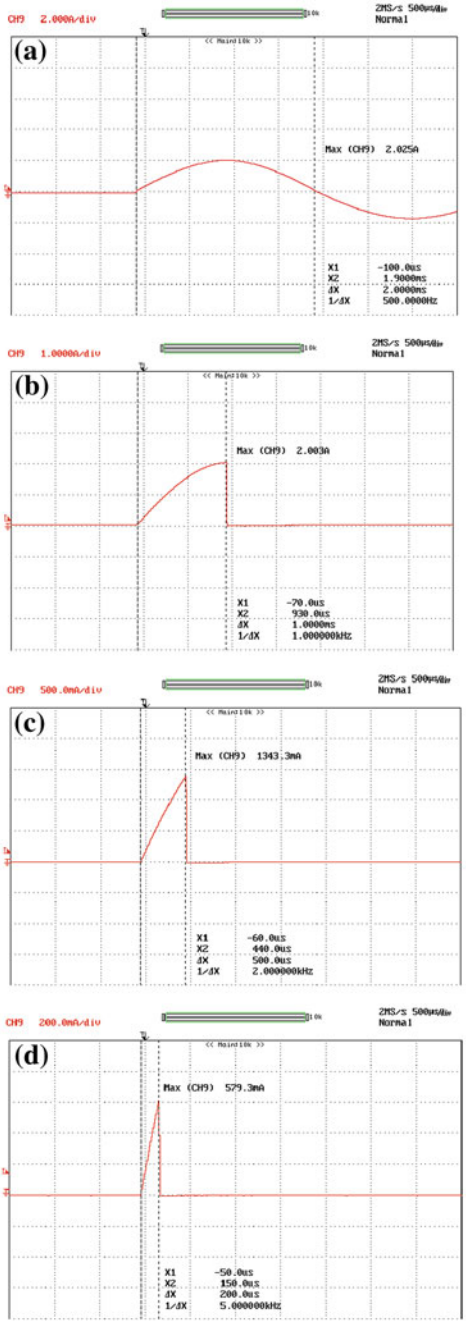

Fig. 3.8 Experimental i_{c2} of APF single-phase model at different t_{on} interval and $E_2 = 20$ V: **a** $t_{on} = 2{,}000$ μs (Linear), **b** $t_{on} = 1{,}000$ μs (Linear), **c** $t_{on} = 500$ μs (Linear), and **d** $t_{on} = 200$ μs (Linear)

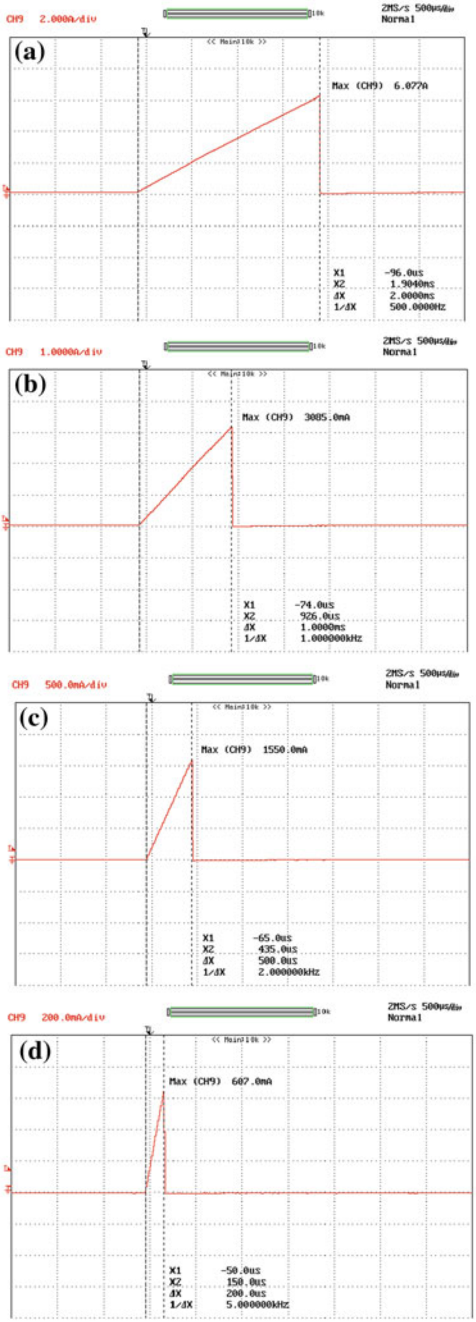

is nonlinear compared with that of i_{c2} as shown in Fig. 3.8a. Even when $t_{\mathrm{on}} = 1{,}000\,\mu\mathrm{s}$ and $t_{\mathrm{on}} = 500\,\mu\mathrm{s}$ satisfy the quasi-linear limit ($T_{\mathrm{limit}} = 1{,}000\,\mu\mathrm{s}$), it is obvious that Fig. 3.7b and c contain current slope errors (35.1, 13.4 %) compared with that of APF as in Fig. 3.8b and c. When $t_{\mathrm{on}} = 200\,\mu\mathrm{s}$, which satisfies the linear limit ($T_{\mathrm{linear}} = 200\,\mu\mathrm{s}$), the current slope error decreases to 4.6 % (within the linear region definition), i_{c1} in Fig. 3.7d is approximately the same as i_{c2} in Fig. 3.8d.

As the load voltage is treated as a constant value in the analysis, its inconstant effect to the HAPF nonlinearity analysis can be neglected. From Figs. 3.5, 3.6, 3.7, and 3.8, APF always obtains a linear current slope, whereas HAPF can obtain a nonlinear current slope due to its inherent nonlinear characteristic. The single-phase simulation and experimental results verify the hysteresis linearization study of HAPF compared with that of linear APF.

3.3.3 Summary for Determining Quasi-Linear Limit T_{limit} and Linear Limit T_{linear}

In summary, the quasi-linear limit T_{limit}, linear limit T_{linear}, and their corresponding hysteresis bands (H_{limit}, H_{linear}) for the HAPF can be determined in the following steps:

(1) Input system parameters L_{c1} and C_{c1}, by setting $A = \cos \omega_r t = 0$, T_{limit} is the minimum value among all t values when $A = 0$(excluding $t = 0$), where $\omega_r = 1/\sqrt{L_{c1}C_{c1}}$. H_{limit} can then be obtained by (A.19) in Appendix A.4.

(2) Finding T_{linear} value by setting $\left|\frac{di_{cx}}{dt}\right|_{\mathrm{error}} = |1 - \cos \omega_r t| = \varepsilon\,\%$(A.16), ε is set to 5 % in this work (Appendix A.3). H_{linear} can then be obtained by (A.19).

3.4 HAPF Linearization Study Verification Under Three-Phase Four-Wire Power Quality Compensator Application

The previous linearization analyses and verifications are based on constant reference inverter current i_{cx}^{*} assumption (Appendix A.3), which yields a fixed switching frequency as verified by (A.19) and illustrated in Fig. 3.9a. However, i_{cx}^{*} is not a constant value and unpredictable in practical three-phase four-wire power quality compensator application, thus the switching frequency of the practical HAPF system under a fixed hysteresis band value is not fixed as verified by (A.18) and illustrated in Fig. 3.9b. From Fig. 3.9b, when the slope of the inverter current i_{cx} keeps the same as Fig. 3.9a, it is obvious that $\mathrm{t_{on1}}$, $\mathrm{t_{on2}} > T_{\mathrm{linear}}$, and $\mathrm{t_{off1}}$, $t_{\mathrm{off2}} < T_{\mathrm{linear}}$ due to the variation of reference inverter current i_{cx}^{*}. In addition, when

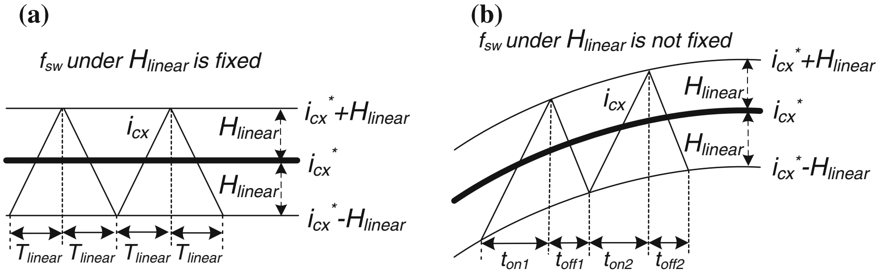

Fig. 3.9 Hysteresis PWM control under H_{linear} based on: **a** previous constant $i_{cx}{}^{*}$ assumption and **b** inconstant $i_{cx}{}^{*}$ consideration

the slope of i_{cx} is the same polarity as the reference i_{cx}^{*}, t_{on1}, $t_{\text{on2}} > T_{\text{linear}}$ and vice versa. Owing to H_{linear} is set under a small slope error of $\varepsilon = 5\,\%$ in this work, it can also be treated as the linear hysteresis band limit during practical case.

In practical, three-phase four-wire power quality compensator application, by setting the hysteresis band H significantly smaller than the quasi-linear limit H_{limit} or linear limit H_{linear}, it is possible to keep the HAPF operates in quasi-linear region or linear region.

3.4.1 Determination of Final Sampling Time T_{final} and Hysteresis Band H_{final}

The final sampling time T_{final} and hysteresis band H_{final} for the HAPF can be determined in the following steps:

(1) For the fastest sampling time by AD converter is T_{fastest}, the final sampling time T_{final} can be chosen as: $T_{\text{fastest}} \leq T_{\text{final}} \leq T_{\text{linear}}$.

(2) For the switching frequency limitation of the switching devices is $f_{\text{swlimit(SD)}}$, the hysteresis band $H_{\text{swlimit(SD)}}$ based on $f_{\text{swlimit(SD)}}$ can be obtained via (A.19). Then the final hysteresis band can be chosen as $H_{\text{swlimit(SD)}} \leq H_{\text{final}} \leq H_{\text{linear}}$ in order to obtain a linear hysteresis control for the HAPF.

3.4.2 Simulation and Experimental Verifications for HAPF Linearization Study Under Three-Phase Four-Wire Power Quality Compensator Application

In this section, the HAPF linearization study under three-phase four-wire power quality compensator application as shown in Fig. 3.1 will be investigated by both simulations and experiments. To simplify the verification, the dc-link is supported by external dc voltage source and the simulated and experimental three-phase

Table 3.2 HAPF simulated and experimental system parameters for power quality compensation

System parameters	Physical values
v_x ($x = a,b,c$), f	55 V, 50 Hz
L_s	0.5 mH
L_{c1}, C_{c1}	6 mH, 70 μF
C_{dc1}	5 mF
V_{dc1U}, V_{dc1L}	30 V
L_{NL1x}, C_{NL1x}, R_{NL1x}	30 mH, 202 μF, 25 Ω

loadings are approximately balanced. Simulation studies were carried out by using PSCAD/EMTDC. In order to verify the simulation results, a 55 V, 1.65kVA three-phase four-wire center-split HAPF experimental prototype is also implemented in the laboratory. The control system of the prototype is a digital signal processor (DSP) TMS320F2407 and the sampling time is chosen as 50 μs (20 kHz). Moreover, the Mitsubishi IGBT intelligent power modules (IPMs) PM300DSA060 are employed as the switching devices for the inverter. The switching frequency limitation of the switching devices $f_{\text{swlimit(SD)}}$ is 20 kHz and the corresponding $H_{\text{swlimit(SD)}} = 0.0625\text{A}$. The photo of the experimental prototype is shown in Appendix A.5. Table 3.2 lists the HAPF simulated and experimental system parameters for power quality compensation. From Table 3.2, the quasi-linear limit and linear limit for HAPF can be calculated as $T_{\text{limit}} = 1{,}000\,\mu\text{s}$ ($H_{\text{limit}} = 1.25\text{A}$) and $T_{\text{linear}} = 200\,\mu\text{s}$ ($H_{\text{linear}} = 0.25\text{A}$), respectively.

The HAPF reference compensating current can be determined by using either the three-phase or single-phase instantaneous *pq* theory as discussed in Appendix A.1 and A.2. Then, the corresponding control block diagram of the three-phase four-wire HAPF is illustrated in Appendix A.1 or A.2. And hysteresis PWM is applied for generating the required compensating current. Thus, the compensating current error Δi_{cx} together with hysteresis band H will be sent to the current PWM control part for generating the trigger signals to the IGBTs of the VSI. In the following, representative simulation and experimental results are included to illustrate and verify the HAPF inverter current slope linearization study under three-phase power quality compensator application.

3.4.3 Simulation Results

Figure 3.10a shows the simulated reference inverter current i^*_{cx}, and Fig. 3.10b–d depict the simulated inverter current i_{cx} when the HAPF is operating at nonlinear region, quasi-linear region, and linear region. Table 3.3 summarizes their corresponding simulation results before and after compensation.

(1) *Nonlinear region*: As $T_{\text{limit}} = 1{,}000\,\mu\text{s}$ ($H_{\text{limit}} = 1.25\text{A}$), the hysteresis band $H = 1.25\text{A}$ will keep the HAPF operating at nonlinear region The polarity of the inverter current slope has interchanging before i_{cx} touches the band H at

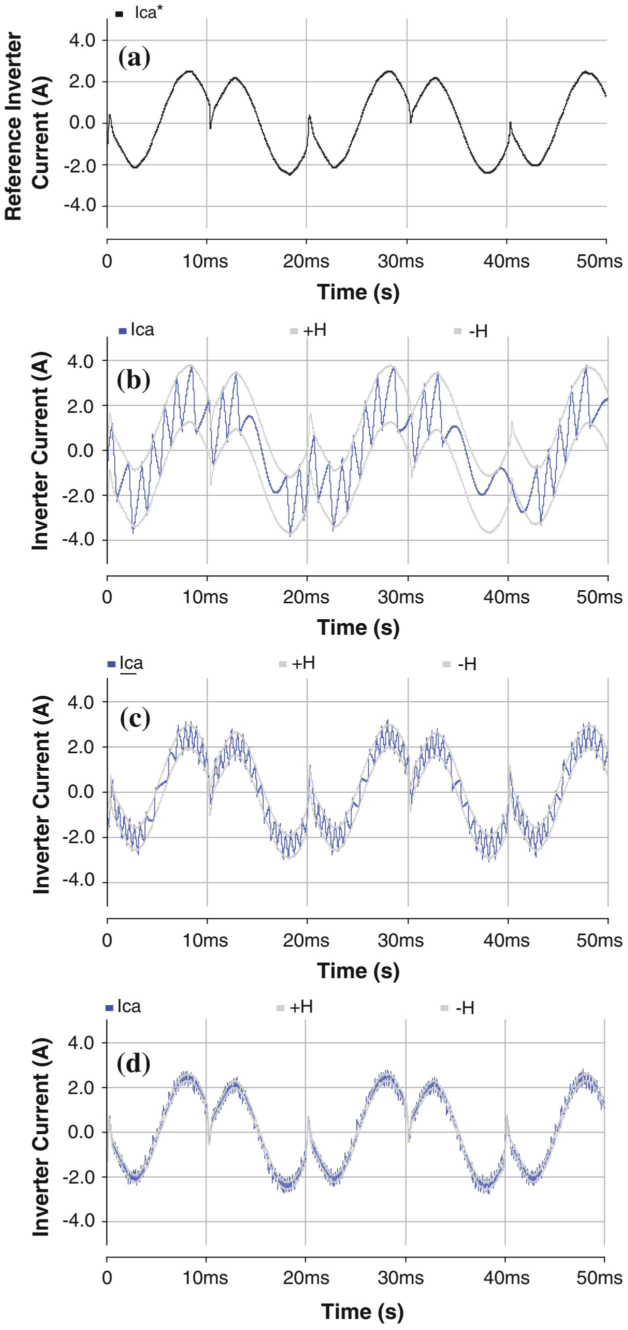

Fig. 3.10 Simulated i_{cx}^{*} and i_{cx} for HAPF at different operation regions: **a** reference inverter current i_{cx}*, **b** nonlinear region ($H = 1.25$A), **c** quasi-linear region ($H = 0.50$A), and **d** linear region ($H = 0.156$A)

Table 3.3 Simulation results for hysteresis PWM-controlled HAPF before and after compensation at different operation regions

	HAPF with V_{dc1U}, $V_{dc1L} = 30$ V, $C_{c1} = 70$ μF, $L_{c1} = 6$ mH			
	Before comp.	After comp.		
		(a) $H = 1.25$A (Nonlinear)	(b) $H = 0.50$A (Quasi-linear)	(c) $H = 0.156$A (Linear)
RMS of system current i_{sx} (A)	2.67	2.36	2.17	2.12
System displacement power factor (DPF)	0.83	1.00	1.00	1.00
Total harmonic distortion of system current THD_{isx} (%)	28.0	31.2	17.3	6.2
Total harmonic distortion of load voltage THD_{Vx} (%)	2.1	7.2	6.6	2.8
RMS of system neutral current i_{sn} (A)	2.18	1.40	0.68	0.32
Average operating switching frequency f_{sw} (Hz)	–	0.6 k	1.7 k	5.1 k

some instances, which can be verified by Fig. 3.10b. Table 3.3 illustrates that the HAPF can compensate the system displacement power factor (DPF) from 0.83 into unity. However, the nonlinear slope of i_{cx} deteriorates the compensation results ($THD_{i_{sx}} = 31.2\,\%$, $THD_{V_x} = 7.2\,\%$, root mean square (RMS) of the system neutral current $i_{sn} = 1.40$A) by generating unexpected trigger signals to the switching devices. Moreover, both compensated $THD_{i_{sx}}$ and THD_{V_x} do not satisfy the international standards ($THD_{\mathrm{i_{sx}}} < 20\,\%$ for IEEE, $THD_{\mathrm{i_{sx}}} < 16\,\%$ for IEC, $THD_{v_x} < 5\,\%$ for IEEE) [13–15]. From Table 3.3, the system average operating switching frequency is 0.6 kHz.

(2) *Quasi-linear region*: Setting the band $H = 0.50$A can keep the HAPF operating at quasi-linear region. The polarity of the inverter current slope changes only when i_{cx} touches the band H, as shown in Fig. 3.10c. The system DPF has been compensated into unity and $i_{sn} = 0.68$A. When HAPF is operating at quasi-linear region, the current slope error is significant, which affects the system performances. This phenomenon can be verified by showing compensated $THD_{i_{sx}} = 17.3\,\%$ and $THD_{V_x} = 6.6\,\%$ as shown in Table 3.3, in which both of them do not satisfy the international standards [13–15]. From Table 3.3, the system average operating switching frequency is 1.7 kHz.

(3) *Linear region*: As $T_{\mathrm{linear}} = 200$ μs ($H_{\mathrm{linear}} = 0.25$A) and $H_{\mathrm{swlimit(SD)}} = 0.0625$A, the hysteresis band $H = 0.156$A can satisfy both the linear limit and the switching frequency limitation of the switching devices. This band value can keep the HAPF operating at linear region as verified by Fig. 3.10d. Table 3.3 illustrates that $H = 0.156$A yields the best compensation performances among the three operation regions. The system current, system neutral current, and system DPF after compensation become sinusoidal ($THD_{i_{sx}} = 6.2\,\%$), less (0.32A), unity and $THD_{V_x} = 2.8\,\%$, in which all the results satisfy the

international standards [13–15]. From Table 3.3, the system average operating switching frequency is 5.1 kHz. When H is further decreased, the HAPF can obtain better compensation results as the slope error can be reduced.

3.4.4 Experimental Results

Figure 3.11a shows the experimental reference inverter current i_{cx}^{*} in DSP, and Fig. 3.11b–d depict the experimental inverter current i_{cx} when the HAPF is operating at nonlinear region, quasi-linear region, and linear region. Table 3.4 summarizes their experimental results before and after compensation.

1. *Nonlinear region*: As $T_{\mathrm{limit}} = 1{,}000\,\mu\mathrm{s}$ ($H_{\mathrm{limit}} = 1.25\mathrm{A}$), the hysteresis band $H = 1.25\mathrm{A}$ will keep the HAPF operating at nonlinear region. The polarity of the inverter current slope has interchanging before i_{cx} touches the band H at some instances, as shown in Fig. 3.11b. Table 3.4 illustrates that the HAPF can compensate the system DPF close to unity. However, the nonlinear slope of i_{cx} deteriorates the compensation results ($THD_{i_{sx}} = 27.3\,\%$, $THD_{V_x} = 5.6\,\%$ for the worst phase, $i_{sn} = 1.46\mathrm{A}$) by generating unexpected trigger signals to the switching devices. Moreover, both compensated $THD_{i_{sx}}$ and THD_{V_x} do not satisfy the international standards [13–15]. From Table 3.4, the system average operating switching frequency is 0.5 kHz.
2. *Quasi-linear region*: Setting the band $H = 0.50\mathrm{A}$ can keep the HAPF operating at quasi-linear region. The polarity of the inverter current slope changes only when i_{cx} touches the band H, as shown in Fig. 3.11c. The system DPF has been compensated close to unity. When HAPF is operating at quasi-linear region, the current slope error is significant, which affects the operating performances ($THD_{i_{sx}} = 16.4\%$ and $THD_{V_x} = 4.3\%$ for the worst phase, $i_{sn} = 0.98\mathrm{A}$) as shown in Table 3.4, and the compensated $THD_{i_{sx}}$does not satisfy the international standards [13–15]. From Table 3.4, the system average operating switching frequency is 1.1 kHz.
3. *Linear region*: As $T_{\mathrm{linear}} = 200\,\mu\mathrm{s}$ ($H_{\mathrm{linear}} = 0.25\mathrm{A}$) and $H_{\mathrm{swlimit(SD)}} = 0.0625\ \mathrm{A}$, the hysteresis band $H = 0.156\ \mathrm{A}$ can satisfy both the linear limit and the switching frequency limitation of the switching devices. This band value can keep the HAPF operating at linear region as verified by Fig. 3.11d. Table 3.4 illustrates that $H = 0.156\ \mathrm{A}$ yields the best compensation performance among the three operation regions. The system DPF has been compensated close to unity, $THD_{i_{sx}} = 9.8\,\%$ and $THD_{V_x} = 3.0\,\%$ for the worst phase, $i_{sn} = 0.64\mathrm{A}$, in which all the compensated results satisfy the international standards [13–15]. From Table 3.4, the system average operating switching frequency is 3.1 kHz.

Comparing Table 3.4 with Table 3.3, there are differences between simulation and experimental results, which are actually due to the difference of component parameters, the resolution of the transducers, the digital computation error, and the noise in the experiment. Moreover, those factors will affect the HAPF

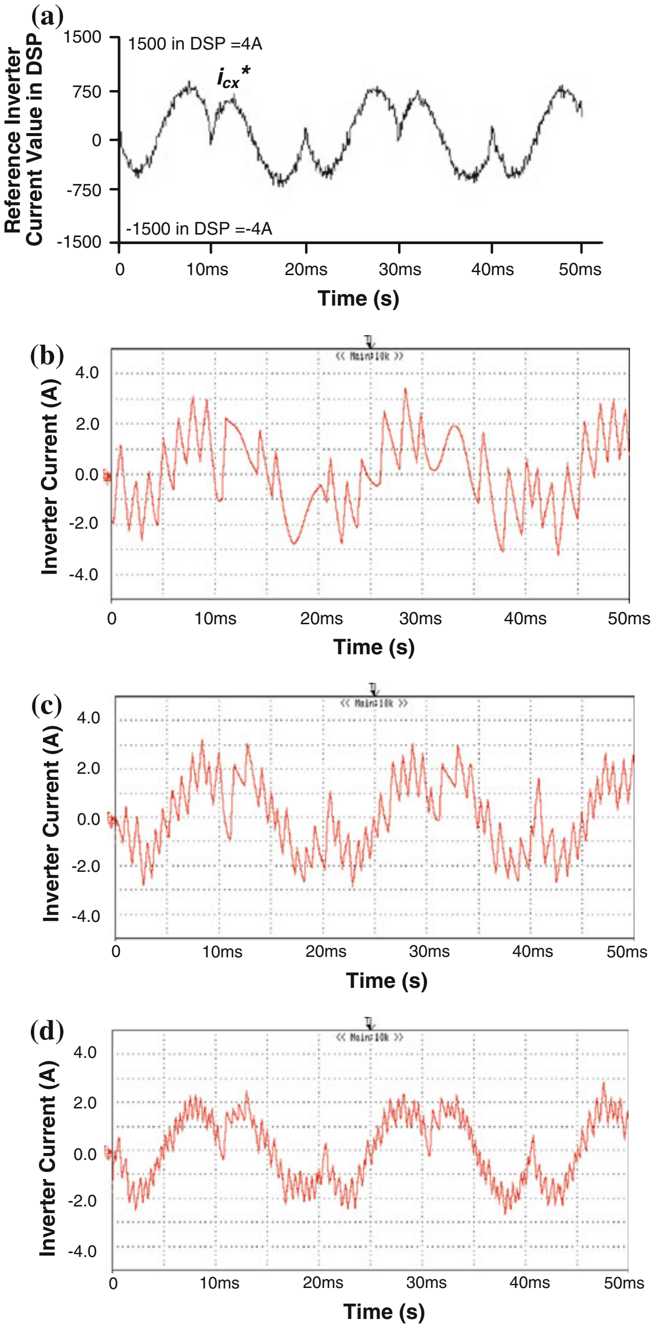

Fig. 3.11 Experimental $i_{cx}^{*}$and i_{cx} for HAPF at different operation regions: **a** reference inverter current $i_{cx}*$ in DSP, **b** nonlinear region ($H = 1.25$A), **c** quasi-linear region ($H = 0.50$A), and **d** linear region ($H = 0.156$A)

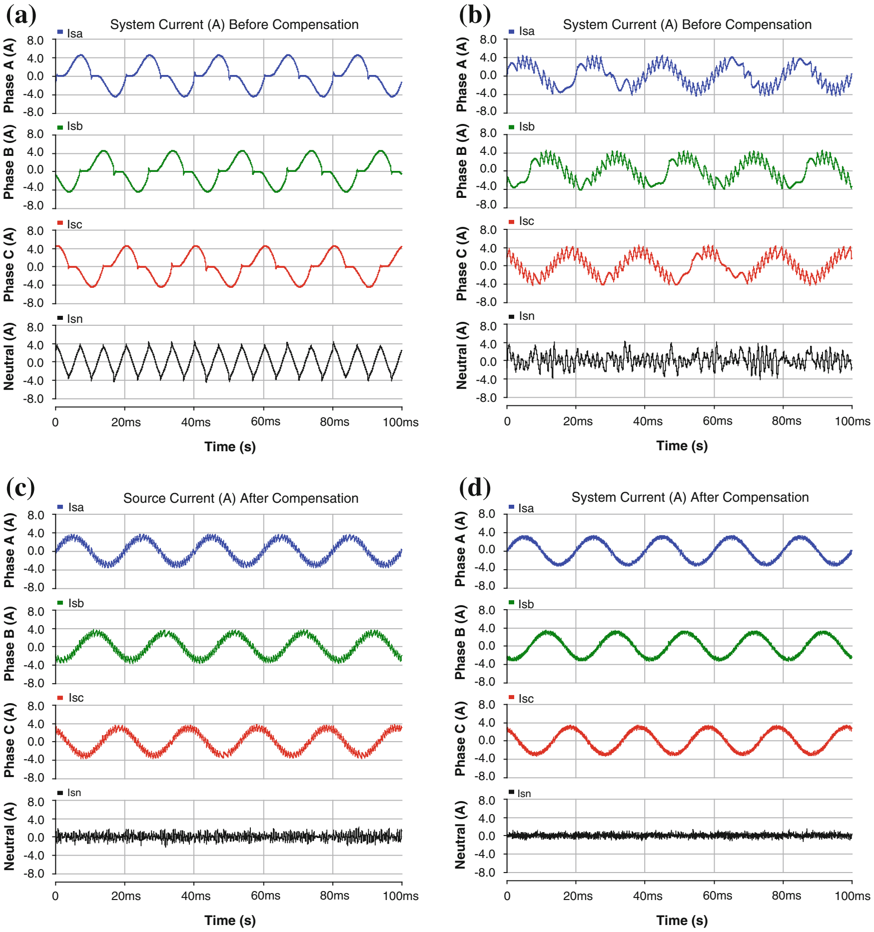

Fig. 3.12 Simulated i_{sx} before and after HAPF compensation at different operation regions: **a** before compensation, **b** nonlinear region ($H = 1.25$A), **c** quasi-linear region ($H = 0.50$A), and **d** linear region ($H = 0.156$A)

compensation performances significantly in linear region operation because more precise A/D signals, computation and control for the HAPF are required. To improve the performances (reduce the slope error) of the HAPF experimental prototype, the hysteresis band H value can be further reduced.

The experimental results as shown in Fig. 3.11 and Table 3.4 agreed with the simulation results as shown in Fig. 3.10 and Table 3.3, which verifies the hysteresis linearization study for HAPF under three-phase four-wire power quality compensator application. In addition, the HAPF can compensate the system DPF to unity among the three operation regions. However, only when the HAPF is

Table 3.4 Experimental results for hysteresis PWM controlled HAPF before and after compensation at different operation regions

		HAPF with V_{dc1U}, $V_{dc1L} = 30$ V, $C_{c1} = 70$ μF, $L_{c1} = 6$ mH			
		Before comp.	After comp.		
			(a) $H = 1.25$A (Nonlinear)	(b) $H = 0.50$A (Quasi-linear)	(c) $H = 0.156$A (Linear)
RMS of system current i_{sx} (A)	A	2.42	2.21	2.13	2.10
	B	2.42	2.20	2.14	2.11
	C	2.35	2.07	1.96	1.94
System displacement power factor (DPF)	A	0.86	1.00	1.00	1.00
	B	0.89	1.00	1.00	1.00
	C	0.86	1.00	1.00	1.00
Total harmonic distortion of system current THD_{isx} (%)	A	23.2	27.3	16.1	9.5
	B	22.4	25.9	16.4	9.2
	C	23.4	26.2	16.0	9.8
Total harmonic distortion of load voltage THD_{Vx} (%)	A	2.5	5.6	4.3	2.8
	B	2.4	5.2	4.2	3.0
	C	2.5	5.1	4.2	2.9
RMS of system neutral current i_{sn} (A)	N	1.57	1.46	0.98	0.64
Average operating switching frequency f_{sw} (Hz)	A	–	0.5 k	1.1 k	3.1 k
	B				
	C				

operating at linear operation region, the compensated $THD_{i_{sx}}$and THD_{V_x}can satisfy the international standards [13–15].

Figure 3.13 depicts the experimental three-phase system current i_{sx} before and after compensation, in which the results are consistent with the simulation results as shown in Fig. 3.12. And the current harmonics and neutral current can only be significantly compensated at HAPF linear operation region. When the HAPF operates at linear region, it can obtain acceptable current quality compensation performances (Tables 3.3 and 3.4) with an average power loss of about 4.0 % of the loading power consumption and a fast response time of less than 10 ms.

3.5 Summary

In this chapter, the characteristic and linear requirement of hysteresis PWM control for a HAPF are investigated and discussed. Based on the modelings, the nonlinear phenomenon and linearization process for the HAPF inverter current slope are studied, explored, and compared with that of the linear APF. According to the designed coupling C_{c1} and L_{c1} for HAPF, two limits: quasi-linear limit and linear limit are proposed, which separate the HAPF into nonlinear, quasi-linear, and linear operation regions. In order to ensure the controllability of using the conventional hysteresis control and to avoid obtaining unexpected trigger signals for the switching devices, the hysteresis band, and sampling time should satisfy the

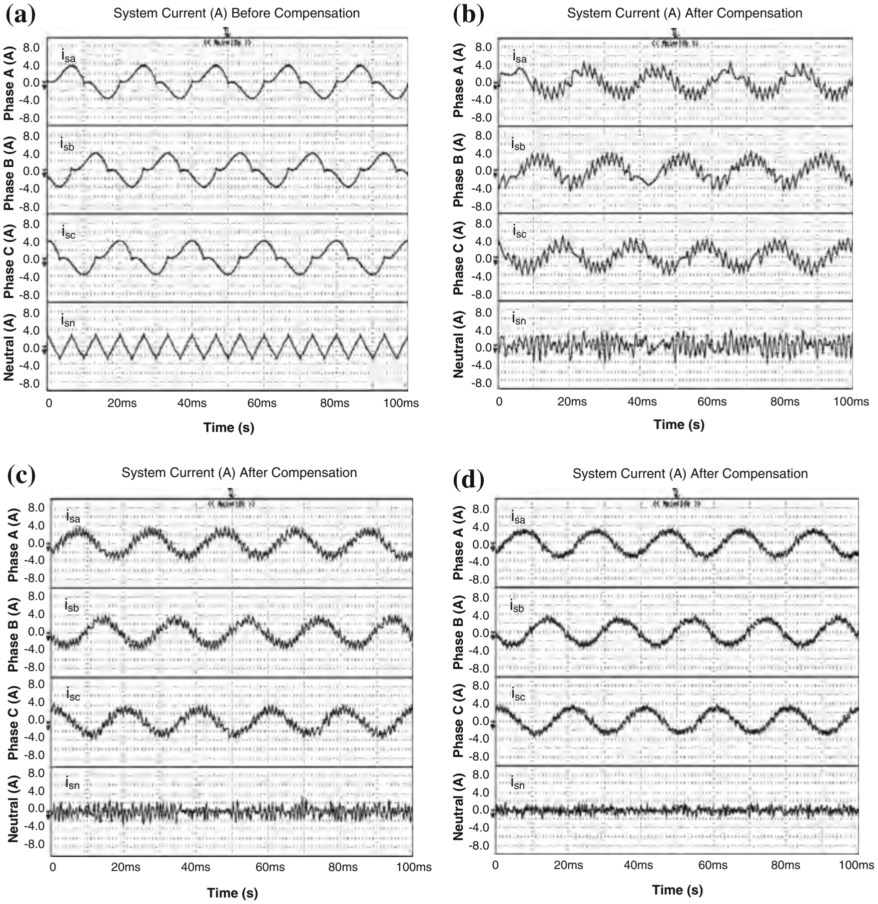

Fig. 3.13 Experimental i_{sx} before and after HAPF compensation at different operation regions: **a** before compensation, **b** nonlinear region ($H = 1.25$A), **c** quasi-linear region ($H = 0.50$A), and **d** linear region ($H = 0.156$A)

linear limit requirement. Single-phase simulation and experimental results are presented to verify the hysteresis linearization study of the HAPF and compared with that of the APF. Finally, representative simulation and experimental results of HAPF under three-phase power quality compensation system are given to prove the validity of the hysteresis linearization study.

References

1. B. Bose, *Power electronics and variable frequency drives: technology and applications* (IEEE Press, New York, 1997)
2. D.M. Brod, D.W. Novotny, Current control of VSI-PWM inverters. IEEE Trans. Ind. Appl. **21**(3), 562–570 1985
3. B.K. Bose, An adaptive hysteresis-band current control technique of a voltage-fed PWM inverter for machine drive system. IEEE Trans. Ind. Appl. **37**(5), 402–408 (1990)
4. B.-J. Kang, C.-M. Law, A robust hysteresis current-controlled PWM inverter for linear PMSM driven magnetic suspended positioning system. IEEE Trans. Ind. Appl. **48**(5), 956–967 (2001)
5. L. Malesami, P. Mattavelli, P. Tomasin, High-performance hysteresis modulation technique for active filters. IEEE Trans. Power Electron. **12**(5), 876–884 (1997)
6. D. Casadei, G. Serra, A. Tani, L. Zarri, Theoretical and experimental analysis for the RMS current ripple minimization in induction motor drives controlled by SVM technique. IEEE Trans. Ind. Electron. **51**(5), 1056–1065 (2004)
7. D. Shen, P.W. Lehn, Fixed-frequency space-vector-modulation control for three-phase four-leg active power filters. IEEE Proc–Electr. Power Appl. **149**(4), 268–274 2002
8. R. Zhang, V.H. Prasad, D. Boroyevich, F.C. Lee, Three-dimensional space vector modulation for four-leg voltage-source converters. IEEE Trans. Power Electron. **17**(3), 314–326 (2002)
9. C.J. Zhan, A. Arulampalam, N. Jenkins, Four-wire dynamic voltage restorer based on a three-dimensional voltage space vector PWM algorithm. IEEE Trans. Power Electron. **18**(4), 1093–1102 (2003)
10. S. Srianthumrong, H. Akagi, A medium-voltage transformerless AC/DC power conversion system consisting of a diode rectifier and a shunt hybrid filter. IEEE Trans. Ind. Appl. **39**(3), 874–882 2003
11. W. Tangtheerajaroonwong, T. Hatada, K. Wada, H. Akagi, Design and performance of a transformerless shunt hybrid filter integrated into a three-phase diode rectifier. IEEE Trans. Power Electron. **22**(5), 1882–1889 (2007)
12. S. Rahmani, A. Hamadi, N. Mendalek, K. Al-Haddad, A new control technique for three-phase shunt hybrid power filter. IEEE Trans. Ind. Electron. **56**(8), 2904–2915 (2009)
13. IEEE recommended practices and requirements for harmonic control in electrical power systems, 1992, IEEE Standards 519–1992
14. Electromagnetic Compatibility (EMC), Part 3: Limits, Section 2: Limits for Harmonics Current Emissions (Equipment Input Current $\leq$ 16A Per Phase), IEC Standards 61000–3–2, 1997
15. IEEE Recommended Practice on Monitoring Electric Power Quality, 1995, IEEE Standards 1159:1995

Chapter 4
Adaptive DC-Link Voltage Control Technique for HAPF in Reactive Power Compensation

Abstract This chapter presents a novel adaptive dc-link voltage control technique for hybrid active power filter (HAPF) in reducing switching loss and switching noise under reactive power compensation. The mathematical relationship between HAPF dc-link voltage and reactive power compensation range is initially deduced and presented. Based on the compensation range analysis, the required minimum dc-link voltage with respect to different loading reactive power is deduced. Then an adaptive dc-link voltage controller for the three-phase four-wire HAPF is proposed, in which the dc-link voltage as well as the reactive power compensation range can be adaptively changed according to different inductive loading situations. Therefore, the compensation range, switching loss, and switching noise of the HAPF can be determined and reduced correspondingly. In this chapter, the reference dc-link voltage is classified into certain levels for selection in order to alleviate the problem of dc voltage fluctuation caused by its reference frequent variation, and hence reducing the fluctuation impact on the compensation performances. Finally, representative simulation and experimental results of a three-phase four-wire center-split HAPF are presented to verify the validity and effectiveness of the proposed adaptive dc-link voltage controlled HAPF in dynamic reactive power compensation.

Keywords Active Power Filter · Adaptive DC-Link Voltage Control · Hybrid Active Power Filter · Passive Part · Reactive Power Control · Switching Loss · Switching Noise

4.1 Introduction

Traditionally, the active inverter part of the existing HAPF is solely responsible for the current harmonics compensation [1–7] and the HAPF can only inject a fixed amount of reactive power which is provided by its coupling LC. In a practical case, the load-side reactive power consumption varies from time to time, as a result, the HAPF [1–7] cannot perform satisfactory dynamic reactive power compensation. The larger the reactive power compensation difference between the load-side and the

C.-S. Lam and M.-C. Wong, *Design and Control of Hybrid Active Power Filters*,
SpringerBriefs in Electrical and Computer Engineering,
DOI: 10.1007/978-3-642-41323-0_4,

coupling LC, the larger the system current loss, and it will lower the network stability. In addition, if the loading is dominated by a centralized air-conditioning system, its reactive power consumption will be much higher than the harmonic power consumption [8, 9]. Therefore, it is important and necessary for the HAPF to possess dynamic reactive power compensation capability under this loading situation.

Besides, the HAPF [1–7] and other HAPF topologies are all operating at a fixed dc-link voltage level. As the switching loss is directly proportional to the dc-link voltage [10], the system will obtain a larger switching loss if a higher dc-link voltage is used, and vice versa. Therefore, if the dc-link voltage can be adaptively changed according to different loading reactive power situations, the system can obtain better performances and operational flexibility.

To achieve the above two functionalities of the HAPF, which are lacking among the existing literatures, this chapter proposes an adaptive dc-link voltage control technique for the three-phase four-wire HAPF in dynamic reactive power compensation. Compared with the traditional fixed dc-link voltage HAPF, the adaptive control technique for the HAPF will experience less switching loss, switching noise and improve the compensation performances.

In the following, the single-phase fundamental equivalent circuit model of the HAPF will be initially illustrated. Based on the circuit model, the relationship between the HAPF dc-link voltage and reactive power compensation range can be obtained. Then the required minimum dc-link voltage with respect to different loading reactive power will be deduced. Then the main contribution of this chapter on the adaptive dc-link voltage controller for three-phase four-wire HAPF in dynamic reactive power compensation will be described. Finally, simulation and experimental verification of the adaptive dc-link voltage controlled HAPF will be presented and discussed. Given that most of the loads in the distribution power systems are inductive, the following analysis and discussion will only focus on inductive loads [11]. Moreover, as this chapter mainly focuses on HAPF reactive power compensation, hence only the HAPF reactive power compensation analysis, simulation, and experimental results are included in this chapter.

4.2 Single-Phase Fundamental Equivalent Circuit Model of HAPF

From the HAPF circuit configuration as shown in Fig.1.8, its single-phase fundamental equivalent circuit model is shown in Fig. 4.1, where the subscript 'f' denotes the fundamental frequency component. In the following analysis, all the parameters are in RMS values.

For simplicity, v_{sx} and v_x are assumed to be pure sinusoidal without harmonic components (i.e., $\vec{V}_x = \vec{V}_{xf} = \left|\vec{V}_x\right| = V_x$). From Fig. 4.1, the inverter fundamental voltage phasor $\vec{V}_{\mathrm{inv}1x_f}$ can be expressed as

$$\vec{V}_{\mathrm{inv}1x_f} = \vec{V}_x - \vec{Z}_{\mathrm{PPF}_f} \cdot \vec{I}_{cx_f} \tag{4.1}$$

Fig. 4.1 HAPF single-phase fundamental equivalent circuit model

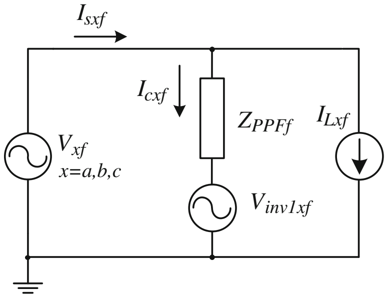

Here, $\vec{Z}_{\mathrm{PPF}_f}$ is the fundamental impedance of the coupling passive part, the fundamental compensating current phasor $\vec{I}_{cx_f}$ of the HAPF can be expressed as $\vec{I}_{cx_f} = I_{cx_{fp}} + jI_{cx_{fq}}$, where the subscripts '*p*' and '*q*' denote the active and reactive components. $I_{cx_{fp}}$ is the fundamental active current for compensating loss and dc-link voltage control while $I_{cx_{fq}}$ is the fundamental reactive current for compensating reactive power of the loading. Simplifying (4.1) yields,

$$\vec{V}_{\mathrm{inv1}x_f} = V_{\mathrm{inv1}x_{fp}} + jV_{\mathrm{inv1}x_{fq}} \tag{4.2}$$

where

$$\begin{aligned} V_{\mathrm{inv1}x_{fp}} &= \vec{V}_x + I_{cx_{fq}} X_{\mathrm{PPF}_f} \\ V_{\mathrm{inv1}x_{fq}} &= -I_{cx_{fp}} X_{\mathrm{PPF}_f} \end{aligned} \tag{4.3}$$

X_{PPF_f} is the fundamental reactance of the coupling passive part. From (4.3), the fundamental compensating active current $I_{cx_{fp}}$ and reactive current $I_{cx_{fq}}$ are

$$I_{cx_{fp}} = -\frac{V_{\mathrm{inv1}x_{fq}}}{X_{\mathrm{PPF}_f}} \tag{4.4}$$

$$I_{cx_{fq}} = \frac{V_{\mathrm{inv1}x_{fp}} - V_x}{X_{\mathrm{PPF}_f}} \tag{4.5}$$

As the HAPF aims to compensate fundamental reactive power, the steady-state active fundamental current $I_{cx_{fp}}$ from the inverter is small $\left(I_{cx_{fp}} \approx 0\right)$ provided that the dc-link voltage control is implemented. Thus, $V_{\mathrm{inv1}x_{fq}} \approx 0$. Therefore, the effect of dc-link voltage control for the HAPF system can be simply neglected during steady-state situation.

For a fixed dc-link voltage level $V_{\mathrm{dc1}_U} = V_{\mathrm{dc1}_L} = 0.5\, V_{\mathrm{dc1}}$ and modulation index m is assumed as $m \approx 1$, $R_{V_{dc}}$ represents the ratio between the dc-link voltage V_{dc1_U}, V_{dc1_L} and load voltage V_x reference to neutral n, which can be expressed as

$$R_{V_{\mathrm{dc}}} = \frac{\pm V_{\mathrm{inv1}xf}}{V_x} = \frac{\pm 0.5\, V_{\mathrm{dc1}}/\sqrt{2}}{V_x} = \pm \frac{V_{\mathrm{dc1}}}{2\sqrt{2}\, V_x} \tag{4.6}$$

where $V_{\mathrm{inv}1xf}$ is the inverter fundamental RMS voltage.

For the HAPF system, the coupling passive part is composed of a series connection of an inductor $(L_{\mathrm{c}1})$ and a capacitor $(C_{\mathrm{c}1})$, and $C_{\mathrm{c}1}$ dominates the passive part at fundamental frequency. However, if the coupling passive part is replaced by a pure inductor $(L_{\mathrm{c}2})$, the original HAPF system will become an APF. With the effect of dc-link voltage control being neglected $\left(I_{cx_{fp}} = 0\right)$ at steady-state, substituting $X_{PPF_f} = X_{Lc2_f}$ for APF and $X_{\mathrm{PPF}_f} = -|X_{\mathrm{Cc}1_f} - X_{\mathrm{Lc}1_f}|$ for HAPF, their corresponding fundamental reactive power injection range Q_{cx_f} per square of the load voltage level V_x^2 with respect to different $R_{V_{\mathrm{dc}}}$ can be shown in Fig. 4.2.

Since Q_{cx_f} should be negative for inductive loading compensation, from Fig. 4.2, the ratio $R_{V_{\mathrm{dc}}}$ for APF must be at least >1, while the ratio $R_{V_{\mathrm{dc}}}$ for HAPF is possible to be smaller than 1 within a specific operational range. This means that the required dc-link voltage $V_{\mathrm{dc}2_U}$, $V_{\mathrm{dc}2_U}$ for APF as shown in Fig. 3.2 must be larger than the peak of load voltage V_x regardless of the coupling inductance $L_{\mathrm{c}2}$, while the required dc-link voltage $V_{\mathrm{dc}1_U}$, $V_{\mathrm{dc}1_U}$ for HAPF can be smaller than the peak of V_x within that operational range. When $R_{V_{\mathrm{dc}}} = 0$, it means that both the APF and HAPF are operating at pure passive filter mode, in which the APF at $R_{V_{\mathrm{dc}}} = 0$ cannot support inductive loading compensation while the HAPF can support a fixed Q_{cx_f}. Moreover, this fixed Q_{cx_f} depends on the passive part parameters. Figure 4.2 clearly illustrates the main advantage of HAPF over the traditional APF under inductive loading reactive power compensation. Under the same dc-link voltage consideration in Fig. 4.2b, when the coupling capacitor $C_{\mathrm{c}1}$ or inductor $L_{\mathrm{c}1}$ of the HAPF increases, the upper limit of $|Q_{cx_f}|$ for inductive loading compensation region increases, however, the lower limit of $|Q_{cx_f}|$ for that region decreases and vice versa. In the following section, the mathematical deduction details of the HAPF fundamental reactive power compensation range with respect to the dc-link voltage under $I_{cx_{fp}} = 0$ assumption will be given. After that, the required minimum dc-link voltage with respect to different loading reactive power can be deduced.

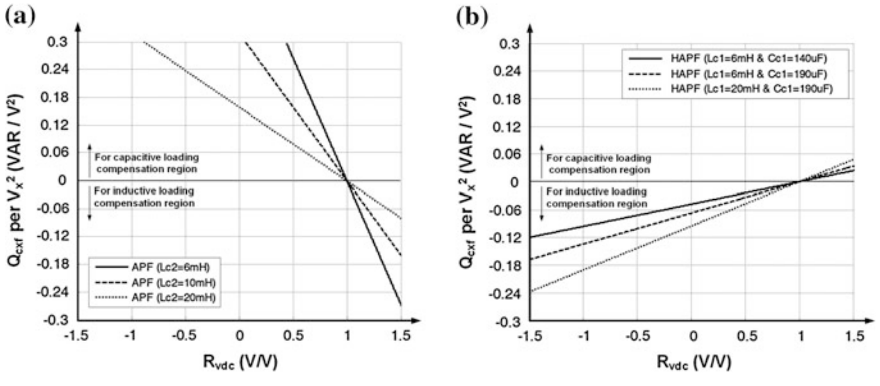

Fig. 4.2 Q_{cxf} per V_x^2 with respect to different R_{Vdc} for **a** APF and **b** HAPF

4.3 HAPF Required Minimum DC-Link Voltage with Respect to Loading Reactive Power

Based on the previous assumption that the active fundamental current $I_{cx_{fp}}$ is very small $\left(I_{cx_{fp}} \approx 0\right)$ at steady state, the inverter injects pure reactive fundamental current $\vec{I}_{cx_f} = jI_{cx_{fq}}$. Therefore, the $\vec{V}_{\mathrm{inv}1x_f}$ in (4.2) contains pure active part as $V_{inv1x_{fp}} = V_x - I_{cx_{fq}}\left(X_{Cc1_f} - X_{Lc1_f}\right)$ only. Then the HAPF single-phase fundamental phasor diagram under inductive loading can be shown in Fig. 4.3. The vertical y-axis can be considered as the HAPF active power (P/W) when locating $\vec{V}_x$ onto the HAPF horizontal reactive power (Q/VAR) x-axis. The circle and its radius of $V_{\mathrm{inv}1x_{f\_\mathrm{dc}}} = \left(0.5\,V_{\mathrm{dc}1}/\sqrt{2}\right)$ represent the HAPF fundamental compensation range and maximum compensation limit under a fixed dc-link voltage. $\vec{V}_{PPFx_f}$ is the fundamental voltage phasor of the coupling passive part. $\vec{I}_{Lx_f}$ is the fundamental load current phasor, where $I_{Lx_{fp}}$ and $I_{Lx_{fq}}$ are the fundamental load active and reactive current.

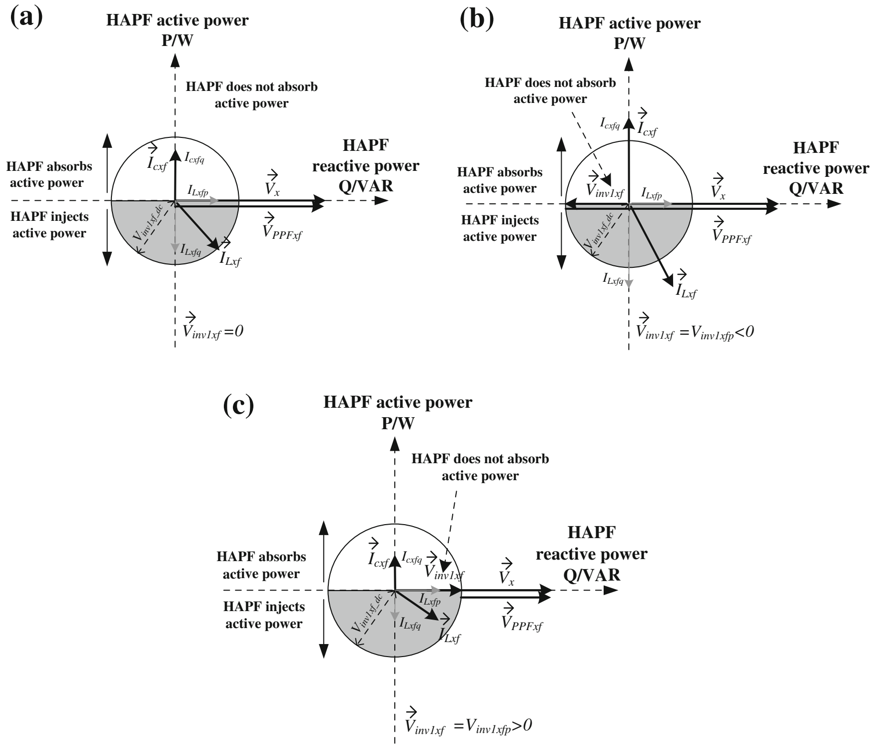

Fig. 4.3 HAPF single-phase fundamental phasor diagram under inductive loading during, **a** full-compensation, **b** under-compensation, and **c** over-compensation by coupling passive part

In Fig. 4.3, the white semi-circle area represents HAPF active power absorption region, whereas the shaded semi-circle area represents HAPF active power injection region. When $\vec{V}_{inv1x_f}$ is located inside the white semi-circle area, the HAPF is absorbing active power, on the other hand, the HAPF is injecting active power when $\vec{V}_{inv1x_f}$ is located inside the shaded semi-circle area. When $\vec{V}_{inv1x_f}$ is located onto the Q/VAR X-axis, the HAPF does not absorb active power. From Fig. 4.3, the HAPF reactive power compensation range with respect to different dc-link voltage can be deduced.

4.3.1 Full-Compensation by Coupling Passive Part

When the loading reactive power Q_{Lx_f} is full-compensation by coupling passive part $\left(Q_{Lx_f} = \left|Q_{cx_f\_\mathrm{PPF}}\right|\right)$ as shown in Fig. 4.3a, the inverter does not need operation and output voltage $\left(V_{\mathrm{inv}1x_{fp}} = 0\right)$. Thus, the switching loss and switching noise will be minimized in this situation. The HAPF compensating reactive power Q_{cx_f} is equal to the reactive power provided by the passive part $Q_{cx_f\_\mathrm{PPF}}$:

$$Q_{cx_f} = Q_{cx_f\_\mathrm{PPF}} = -\frac{V_x^2}{\left|X_{Cc1_f} - X_{Lc1_f}\right|} < 0 \tag{4.7}$$

where $Q_{cx_f\_\mathrm{PPF}} < 0$ means injecting reactive power or providing leading reactive power.

4.3.2 Under-Compensation by Coupling Passive Part

When the loading reactive power Q_{Lx_f} is under-compensated by coupling passive part ($Q_{Lx_f} > \left|Q_{cx_f\_\mathrm{PPF}}\right|$) as shown in Fig. 4.3b, in order to generate a larger $I_{cx_{fq}}$, the inverter should output a negative inverter fundamental active voltage ($V_{\mathrm{inv}1x_{fp}} < 0$) as indicated by (4.5). With a fixed V_{dc1}, the HAPF maximum compensating reactive power limit $Q_{cx_f\_\max}$ can be deduced through the under-compensation by coupling passive part case, which can be expressed as

$$Q_{cx_f\_\max} = -\frac{V_x^2(1 + |R_{V_{\mathrm{dc}}}|)}{\left|X_{Cc1_f} - X_{Lc1_f}\right|} = Q_{cx_f\_\mathrm{PPF}}(1 + |R_{V_{\mathrm{dc}}}|) < 0 \tag{4.8}$$

4.3.3 Over-Compensation by Coupling Passive Part

When the loading reactive power Q_{Lx_f} is over-compensated by coupling passive part ($Q_{Lx_f} < \left|Q_{cx_f\_\mathrm{PPF}}\right|$) as shown in Fig. 4.3c, in order to generate a smaller $I_{cx_{fq}}$, the inverter should output a positive inverter fundamental active voltage ($V_{\mathrm{inv}1x_{fp}} > 0$) as indicated by (4.5). With a fixed $V_{\mathrm{dc}1}$, the HAPF minimum compensating reactive power limit $Q_{cx_f\_\min}$ can be deduced through the over-compensation by coupling passive part case, which can be expressed as

$$Q_{cx_f\_\min} = -\frac{V_x^2(1-|R_{V_{\mathrm{dc}}}|)}{|X_{Cc1_f} - X_{Lc1_f}|} = Q_{cx_f\_\mathrm{PPF}}(1-|R_{V_{\mathrm{dc}}}|) < 0 \tag{4.9}$$

From (4.8) and (4.9), the larger the dc-link voltage $V_{\mathrm{dc}1}$ or ratio $R_{V_{\mathrm{dc}}}$, the larger the HAPF compensation range obtained, and vice versa. However, a larger dc-link voltage will increase the HAPF switching loss and generate a larger switching noise into the system, while a smaller dc-link will deteriorate the compensating performances if Q_{Lx_f} is outside the HAPF compensation range. When $V_{\mathrm{dc}1}$ is designed, the HAPF reactive power compensating range for loading Q_{Lx_f} can be expressed as

$$|Q_{cx_f\_\min}| \le Q_{Lx_f} \le |Q_{cx_f\_\max}| \tag{4.10}$$

Table 4.1 summarizes the HAPF reactive power compensating range deduction steps under a fixed dc-link voltage $V_{\mathrm{dc}1_U} = V_{\mathrm{dc}1_L} = 0.5\,V_{\mathrm{dc}1}$. When Q_{Lx_f} is perfectly compensated by the coupling passive part, the minimum dc-link voltage requirement ($V_{\mathrm{dc}1_U} = V_{\mathrm{dc}1_L} = 0$) can be achieved. In addition, the larger the reactive power compensation differences between the loading and the coupling passive part, the larger the dc-link voltage requirement and vice versa. From Table 4.1, the required minimum dc-link voltage $V_{\mathrm{dc}1\_\mathrm{minx}}$ in each phase can be found by setting $Q_{Lx_f} \approx |Q_{cx_f\_\min}| \approx |Q_{cx_f\_\max}|$ in (4.10),

$$V_{\mathrm{dc}1\_\mathrm{minx}} = 2\sqrt{2}\,V_x\left|1 - \frac{Q_{Lx_f}}{|Q_{cx_f\_\mathrm{PPF}}|}\right| \tag{4.11}$$

in which (4.11) can be applied for the adaptive dc-link voltage control algorithm. Once the Q_{Lx_f} is calculated, the corresponding $V_{\mathrm{dc}1\_\mathrm{min}x}$ in each phase can be

Table 4.1 HAPF reactive power compensation range deduction steps under a fixed dc-link voltage $V_{\mathrm{dc}1_U} = V_{\mathrm{dc}1_L} = 0.5\,V_{\mathrm{dc}1}$

1	With a fixed dc-link voltage $V_{\mathrm{dc}1_U} = V_{\mathrm{dc}1_L} = 0.5\,V_{\mathrm{dc}1}$:	
	$Q_{cx_f\_PPF} = -\frac{V_x^2}{\lvert X_{Cc1_f} - X_{Lc1_f}\rvert} < 0$	(4.7)
	$Q_{cx_f\_max} = Q_{cx_f\_PPF}(1+\lvert R_{V_{dc}}\rvert) < 0$	(4.8)
	$Q_{cx_f\_\min} = Q_{cx_f\_PPF}(1-\lvert R_{V_{dc}}\rvert) < 0$	(4.9)
	Where $\lvert R_{V_{\mathrm{dc}}}\rvert = \left\lvert\frac{V_{\mathrm{dc}1}}{2\sqrt{2}\,V_x}\right\rvert$	(4.6)
2	HAPF reactive power compensating range for loading Q_{Lx_f}:	
	$\lvert Q_{cx_f\_min}\rvert \le Q_{Lx_f} \le \lvert Q_{cx_f\_max}\rvert$	(4.10)

obtained. Then the final three-phase required minimum dc-link voltage $V_{\mathrm{dc1\_min}}$ can be chosen as follows:

$$V_{\mathrm{dc1\_min}} = \max(V_{\mathrm{dc1\_min}a}, V_{\mathrm{dc1\_min}b}, V_{\mathrm{dc1\_min}c}) \tag{4.12}$$

In the next section, the proposed adaptive dc-link voltage controller for the three-phase four-wire HAPF will be introduced so that the HAPF reactive power compensation range can be determined, switching loss and switching noise can be reduced compared with the traditional fixed dc-link voltage HAPF.

4.4 Adaptive DC-link Voltage Controller for A Three-Phase Four-Wire HAPF

Figure 4.4 shows the adaptive dc-link voltage control block diagram for the three-phase four-wire HAPF in dynamic reactive power compensation, which consists of three main control blocks: instantaneous power compensation control block, adaptive dc-link voltage control block, and final reference compensating current and PWM control block. And their details will be introduced in the following.

4.4.1 Instantaneous Power Compensation Control Block

For the instantaneous power compensation control block, the reference compensating currents for HAPF (i_{cx_q}, the subscript $x = a, b, c$ for three phases) are determined by the three-phase instantaneous *pq* theory as discussed in Appendix A.1. Actually, i_{cx_q} can also be determined by the single-phase instantaneous *pq* theory as discussed in Appendix A.2.

4.4.2 Adaptive DC-Link Voltage Control Block

The adaptive dc-link voltage control block consists of three parts: (i) determination of adaptive minimum dc-link voltage V_{dc1_min}, (ii) determination of final reference dc-link voltage level V^*_{dc1}, and (iii) dc-link voltage feedback P/PI controller.

1. *Determination of Adaptive Minimum DC-link Voltage.* Initially, the loading instantaneous fundamental reactive power in each phase q_{Lx_f} ($x = a, b, c$) are calculated by using single-phase instantaneous *pq* theory as discussed in Appendix A.2 and low-pass filters. Usually, $-q_{Lx_f}/2$ can keep as a constant value for more than one cycle, thus Q_{Lx_f} can be approximately treated as $Q_{Lx_f} \approx -q_{Lx_f}/2$. Then the required minimum dc-link voltage $V_{\mathrm{dc1\_min}x}$ for

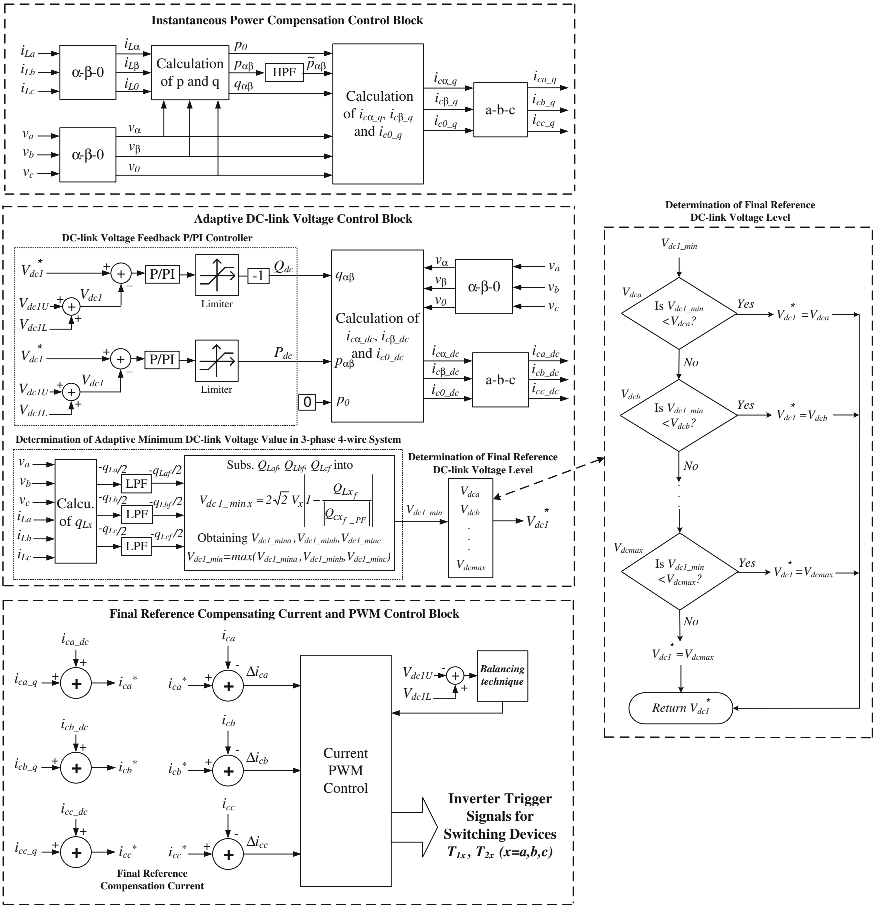

Fig. 4.4 Adaptive dc-link voltage control block diagram for the three-phase four-wire HAPF in reactive power compensation

compensating each phase $\left(Q_{Lx_f}\right)$ can then be calculated by using (4.11), where V_x is the RMS load voltage and $Q_{cx_f\_\mathrm{PPF}}$ can be obtained according to (4.7). The adaptive minimum dc-link voltage will be equal to $V_{\mathrm{dc1\_min}}$, which can be determined by (4.12). During balanced loading case, the three-phase fundamental reactive power consumptions are the same $\left(Q_{La_f} = Q_{Lb_f} = Q_{Lc_f}\right)$, therefore, $V_{\mathrm{dc1\_min}} = V_{\mathrm{dc1\_min}a} = V_{\mathrm{dc1\_min}b} = V_{\mathrm{dc1\_min}c}$. In order to implement the adaptive dc-link voltage control function for the three-phase four-wire HAPF, $V_{\mathrm{dc1\_min}}$ can be simply treated as the final reference dc-link voltage $V_{\mathrm{dc1}}{}^{*}$. It is obvious that when the loading reactive power consumption $\left(Q_{Lx_f}\right)$ is changing, the system will adaptively yield different $V_{\mathrm{dc1\_min}x}$ and $V_{\mathrm{dc1\_min}}$ values.

2. *Determination of Final Reference DC-Link Voltage Level.* However, this adaptive control scheme may frequently change the dc voltage reference V_{dc1}^{*} in

practical situations, as the loading is randomly determined by electric users (different Q_{Lx_f}). Then this frequent change would cause a rapid dc voltage fluctuation, resulting in deterioration of the HAPF operational performances [12]. To alleviate this problem, a final reference dc-link voltage level determination process is added as shown in Fig. 4.4. The final reference dc-link voltage V_{dc1}^{*} is classified into certain levels ($V_{\mathrm{dc}a}$, $V_{\mathrm{dc}b}$, $\ldots V_{\mathrm{dc\,max}}$, $V_{\mathrm{dc}a} < V_{\mathrm{dc}b} \ldots < V_{\mathrm{dc\,max}}$) for selection, so that V_{dc1}^{*}can be maintained as a constant value within a specific compensation range. From Fig. 4.4, when the input $V_{\mathrm{dc1\_min}}$ is less than the lowest dc voltage level $V_{\mathrm{dc}a}$, the final reference dc-link voltage will be $V_{\mathrm{dc1}}^{*} = V_{\mathrm{dc}a}$. If not, repeat the steps until $V_{\mathrm{dc1\_min}}$ is found to be less than a dc-link voltage level. However, if $V_{\mathrm{dc1\_min}}$ is greater than the maximum voltage level $V_{\mathrm{dc\,max}}$, the final reference dc-link voltage will be $V_{\mathrm{dc1}}{}^{*} = V_{\mathrm{dc\,max}}$. In this way, the dc-link voltage fluctuation problem under the adaptive dc voltage control method can be lessened.

3. *DC-Link Voltage Feedback P/PI Controller*. The HAPF can effectively control the dc-link voltage and reactive power by feedback the dc-link voltage error signal as both reactive and active current reference components (Q_{dc}, P_{dc}) [13, 14]:

$$Q_{\mathrm{dc}} = -K_q \cdot (V_{\mathrm{dc1}^*} - V_{\mathrm{dc1}}) \tag{4.13}$$

$$P_{\mathrm{dc}} = K_p \cdot (V_{\mathrm{dc1}^*} - V_{\mathrm{dc1}}) \tag{4.14}$$

where Q_{dc} aims to change the dc-link voltage level due to adaptive dc voltage control and start-up dc-link self-charging function, while P_{dc} aims to maintain the dc-link voltage due to the system loss. K_q and K_p are the positive proportional gains of the controller. In this chapter, *P* controller is chosen because it is simpler and has less operational machine cycles in the DSP, therefore it can yield a faster response than the PI controller. If the dc-link voltage with zero steady-state error is taken into consideration, PI controller is appreciated. A limiter is also applied to avoid the overflow problem of the controller.

With the help of the three-phase instantaneous *pq* theory as discussed in Appendix A.1, (4.13) and (4.14), the three-phase dc voltage control reference compensating currents in α-β-0 coordinates can be calculated as below:

$$\begin{bmatrix} i_{c0\_\mathrm{dc}} \\ i_{c\alpha\_\mathrm{dc}} \\ i_{c\beta\_\mathrm{dc}} \end{bmatrix} = \frac{1}{v_0 v_{\alpha\beta}^2} \begin{bmatrix} v_{\alpha\beta}^2 & 0 & 0 \\ 0 & v_0 v_\alpha & -v_0 v_\beta \\ 0 & v_0 v_\beta & v_0 v_\alpha \end{bmatrix} \begin{bmatrix} 0 \\ P_{\mathrm{dc}} \\ Q_{\mathrm{dc}} \end{bmatrix} \tag{4.15}$$

where v_α, v_β and v_0 are the load voltages on the α-β-0 coordinate after the Clarke transformation in Appendix A.1, and $v_{\alpha\beta^2} = v_\alpha^2 + v_\beta^2$. By the inverse matrix of Clarke transformation in α-β-0 coordinates, the dc-link voltage V_{dc1} can trend its reference V_{dc1}^{*} by changing the dc voltage reference compensating currents (i_{cx_dc}).

$$\begin{bmatrix} i_{ca\_\mathrm{dc}} \\ i_{cb\_\mathrm{dc}} \\ i_{cc\_\mathrm{dc}} \end{bmatrix} = \sqrt{\frac{2}{3}} \begin{bmatrix} 1/\sqrt{2} & 1 & 0 \\ 1/\sqrt{2} & -1/2 & \sqrt{3}/2 \\ 1/\sqrt{2} & -1/2 & -\sqrt{3}/2 \end{bmatrix} \begin{bmatrix} i_{c0\_\mathrm{dc}} \\ i_{c\alpha\_\mathrm{dc}} \\ i_{c\beta\_\mathrm{dc}} \end{bmatrix} \tag{4.16}$$

Therefore, the adaptive dc-link voltage control scheme for the HAPF in reactive power compensation can then be implemented under various inductive linear loading conditions. In addition, the HAPF initial start-up dc-link self-charging function can also be carried out by the adaptive dc-link voltage control scheme.

4.4.3 Final Reference Compensating Current and PWM Control Block

Both the hysteresis PWM and the triangular carrier-based sinusoidal PWM method can be applied for the PWM control part. After the process of instantaneous power compensation and adaptive dc-link voltage control blocks as shown in Fig. 4.4, the final reference compensating current i_{cx}^* can be obtained by summing up the i_{cx_q} and i_{cx_dc}. Then the final reference and actual compensating currents i_{cx}^* and i_{cx} will be sent to the PWM control part, and the PWM trigger signals for the switching devices can then be generated. If the three-phase loadings are unbalanced, the dc capacitor voltage imbalance may occur, the dc capacitor voltage balancing concepts and techniques in [15, 16] can be applied to balance the $V_{\mathrm{dc}1_U}$ and V_{dc1_L} under the adaptive dc voltage control method. The adaptive dc-link voltage controlled HAPF can compensate the dynamic reactive power and reduce the switching loss and switching noise. In the following, the HAPF simulated and experimental compensation results using the adaptive dc-link voltage control algorithm will be given, compared with a fixed dc-link voltage controlled HAPF.

4.5 Simulation and Experimental Verifications of the Adaptive DC-Link Voltage Controller for the Three-Phase Four-Wire HAPF

In this section, the adaptive dc-link voltage controlled HAPF for reactive power compensation in three-phase four-wire power system will be verified by simulations and experiments. Table 4.2 lists the simulated and experimental system parameters for the HAPF. When the loading reactive power consumption is close to that provided by the coupling passive part at under-compensation and over-compensation situations, the dc-link voltage requirement can be low. To show this phenomenon, two sets of passive part parameters for the HAPF are chosen for testing. For (a) under-compensation case, $L_{c1} = 6$ mH, $C_{c1} = 140$ μF, the passive part supports a fixed reactive power of $Q_{cx_f\_\mathrm{PPF}} = -145.1$ var. For (b) over-

Table 4.2 HAPF system parameters for simulations and experiments

System parameters		Physical values
V_x, f		55 V, 50 Hz
L_s		0.5 mH
(a) Under-compensation: $L_{c1} = 6$ mH, $C_{c1} = 140$ µF	Resistor R_{LL1x} and inductor L_{LL1x} for 1st inductive loading	10 Ω, 30 mH
$Q_{cxf\_\mathrm{PPF}} = -145.1$ var	Resistor R_{LL2x} and inductor L_{LL2x} for 2nd inductive loading	22 Ω, 30 mH
(b) Over-compensation: $L_{c1} = 6$ mH, $C_{c1} = 190$ µF	Resistor R_{LL1x} and inductor L_{LL1x} for 1st inductive loading	10 Ω, 30 mH
$Q_{cxf\_\mathrm{PPF}} = -203.5$ var	Resistor R_{LL2x} and inductor L_{LL2x} for 2nd inductive loading	22 Ω, 30 mH

compensation case, $L_{c1} = 6$ mH, $C_{c1} = 190$ µF, the passive part supports a fixed $Q_{cx_f\_\mathrm{PPF}} = -203.5$ var. The L_{c1} is designed based on the switching frequency with switching ripple less than 0.5 A under a maximum dc-link voltage of V_{dc1_U}, $V_{\mathrm{dc1}_L} = 40$ V consideration. Then the two C_{c1} values are designed based on the reactive power consumption for the 1st inductive loading, and both 1st and 2nd inductive loadings as listed in Table 4.2.

The triangular carrier-based sinusoidal PWM method with current error limiter is applied in this chapter so that the compensating current error must be within the triangular wave. And the frequency of the triangular wave is set to $f_{\mathrm{tri}} = 7.5$ kHz. To simplify the verification, the simulated and experimental three-phase loadings are approximately balanced as shown in Fig. 4.5, so that the difference between V_{dc1_U} and V_{dc1_L} is small ($V_{\mathrm{dc1}_U} \approx V_{\mathrm{dc1}_L}$) during the adaptive dc-link voltage control. As discussed in the previous section, in order to alleviate the dc-link voltage fluctuation problem under the adaptive control method, the final reference dc-link voltage $V_{\mathrm{dc1}}{}^*$ can be classified into certain levels for selection, in which $V_{\mathrm{dc1}}{}^*$ is set to have four levels (V_{dc1_U}, $V_{\mathrm{dc1}_L} = 10$ V, 20 V, 30 V and 40 V) for the following simulation and experimental verification.

Simulation studies were carried out by using PSCAD/EMTDC. In order to verify the simulation results, a 55 V, 1.65 kVA three-phase four-wire HAPF

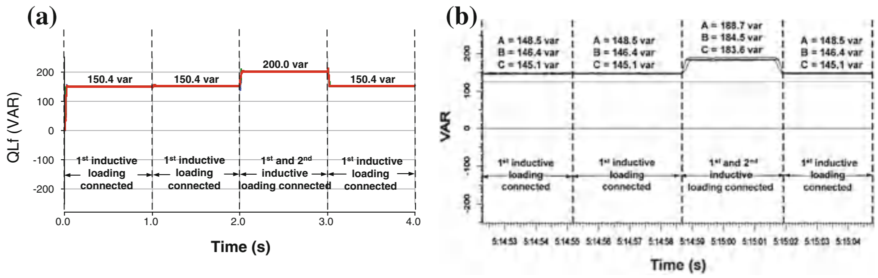

Fig. 4.5 Q_{Lxf} for both under-compensation and over-compensation by coupling passive part cases **a** simulated Q_{Lxf} and **b** experimental Q_{Lxf}

experimental prototype is also implemented in the laboratory. The control system of the prototype is a DSP TMS320F2407 and the sampling frequency is chosen as 50 μs (20 kHz). Moreover, the Mitsubishi IGBT IPMs PM300DSA060 are employed as the switching devices for the inverter. The photo of the experimental prototype is shown in Appendix A.5. Figure 4.4 shows the adaptive dc-link voltage controlled HAPF control block diagram for both simulations and experiments. Figure 4.5 shows the simulated and experimental reactive power at load-side Q_{Lx_f}. When the 1st inductive loading is connected, the three-phase simulated Q_{Lx_f} are 150.4 var with displacement power factor (DPF) = 0.729, while the three-phase experimental Q_{Lx_f} are 148.5 var, 146.4 var, and 145.1 var with DPF = 0.763, 0.742 and 0.746 respectively. When both the 1st and 2nd inductive loadings are connected, the three-phase simulated Q_{Lx_f} increase to 200.0 var with DPF = 0.810, while the three-phase experimental Q_{Lx_f} increase to 188.7 var, 184.5 var, and 183.6 var with DPF = 0.805, 0.815 and 0.822 respectively.

According to the designed four voltage levels (V_{dc1_U}, V_{dc1_L} = 10 V, 20 V, 30 V, and 40 V) for both simulations and experiments, from Table 4.3, the HAPF required minimum dc-link voltage level will be V_{dc1_U}, V_{dc1_L} = 10 V or V_{dc1_U}, V_{dc1_L} = 30 V for compensating the 1st loading or both 1st and 2nd loadings during (a) under-compensation case. During (b) over-compensation case, the HAPF required minimum dc-link voltage level will become V_{dc1_U}, V_{dc1_L} = 30 V or V_{dc1_U}, V_{dc1_L} = 10 V for compensating the same loadings. In the following, the corresponding simulation and experimental results after the adaptive dc-link voltage controlled HAPF compensation will be presented.

4.5.1 Under-Compensation by Coupling Passive Part Situation ($\mathbf{L}_{c1}$ = 6 mH, $\mathbf{C}_{c1}$ = 140 μF)

From Table 4.3, the required minimum dc-link voltage level for the HAPF is V_{dc1_U}, V_{dc1_L} = 10 V for the 1st loading and V_{dc1_U}, V_{dc1_L} = 30 V for the 1st and 2nd loadings. Therefore, the adaptive control method for the HAPF can reduce the switching loss and switching noise compared with a fixed V_{dc1_U}, V_{dc1_L} = 30 V case. For the simulated and experimental Q_{Lx_f} as shown in Figs. 4.5, 4.6 and 4.7 illustrate the HAPF simulated and experimental dynamic process of the adaptive dc-link voltage level and compensation performances during under-compensation by coupling passive part situation. Figures 4.6a and 4.7a show that the simulated and experimental dc-link voltage level (V_{dc1_U}, V_{dc1_L}) can be adaptively changed according to different reactive power consumption of the loading. As the simulated and experimental loadings are approximately balanced, only phase *b* compensation diagrams will be illustrated. From Figs. 4.6b and 4.7b, the simulated and experimental system-side reactive power Q_{sx_f} of phase *b* can be compensated close to zero regardless of whether it is only the 1st loading or both 1st and 2nd loadings are connected, compared with Fig. 4.5. Figures 4.6c and 4.7c show that the

Table 4.3 HAPF simulated and experimental minimum dc-link voltage level with respect to Q_{Lxf} within $V_{\mathrm{dc1}_U} = V_{\mathrm{dc1}_L} = 10\,\mathrm{V},\ 20\,\mathrm{V},\ 30\,\mathrm{V}$ and 40 V

Reactive power by coupling passive part Q_{cxf_PPF}	Simulated and experimental Q_{Lxf} for three phases (var)			Required $V_{\mathrm{dc1\_min}}/2$	Minimum Level $V_{\mathrm{dc1}_U} = V_{\mathrm{dc1}_L}$
(a) Under-compensation: $L_{c1} = 6$ mH, $C_{c1} = 140$ μF $Q_{cxf\_\mathrm{PPF}} = -145.1$ var	1st loading	Simulated	150.4, 150.4, 150.4	2.9 V	10 V
		Experimental	148.5, 146.4, 145.1	1.8 V	10 V
	1st and 2nd loadings	Simulated	200.0, 200.0, 200.0	29.5 V	30 V
		Experimental	188.7, 184.5, 183.6	23.4 V	30 V
(b) Over-compensation: $L_{c1} = 6$ mH, $C_{c1} = 190$ μF $Q_{cxf\_\mathrm{PPF}} = -203.5$ var	1st loading	Simulated	150.4, 150.4, 150.4	20.3 V	30 V
		Experimental	148.5, 146.4, 145.1	22.3 V	30 V
	1st and 2nd loadings	Simulated	200.0, 200.0, 200.0	1.4 V	10 V
		Experimental	188.7, 184.5, 183.6	7.6 V	10 V

simulated and experimental DPF of phase *b* can be compensated from 0.729 to 1.000 and 0.742 to 0.999 respectively once the HAPF starts operation during the 1st inductive loading situation. From Figs. 4.6d and 4.7d, the simulated and experimental DPF of phase *b* can be kept at 0.990 or above when the 2nd loading is connected. The simulation results as shown in Fig. 4.6 are consistent with the experimental results as shown in Fig. 4.7.

Tables 4.4 and 4.5 summarize the simulation and experimental compensation results of the adaptive dc-link voltage controlled HAPF during under-compensation case. Compared with Q_{Lx_f}, the three-phase simulated Q_{sx_f} (5.0 var or 22.0 var) and experimental Q_{sx_f} (0.8 var, −1.5 var, 3.5 var or 25.2 var, 15.3 var, 22.2 var) have been compensated close to zero when the 1st loading or both 1st and 2nd loadings are connected. These can be verified by showing three-phase simulated and experimental DPF = 0.990 or above and $\mathrm{THD}_{i_{sx}}$ are within 3.0 % and 5.0 % respectively. Moreover, the simulated and experimental i_{sx} can be significantly reduced after HAPF compensation. Figures 4.6, 4.7 and Tables 4.4, 4.5 verify the adaptive dc-link voltage controlled HAPF for reactive power compensation during under-compensation case.

4.5.2 *Over-Compensation by Coupling Passive Part Situation ($\mathbf{L}_{c1} = 6$ mH, $\mathbf{C}_{c1} = 190$ μF)*

From Table 4.3, the required minimum dc-link voltage level for the HAPF is V_{dc1_U}, $V_{\mathrm{dc1}_L} = 30$ V for the 1st loading and V_{dc1_U}, $V_{\mathrm{dc1}_L} = 10$ V for the 1st and 2nd loadings. Therefore, the adaptive control method for the HAPF can reduce the switching loss and switching noise compared with a fixed V_{dc1_U}, $V_{\mathrm{dc1}_L} = 30$ V case. For the simulated and experimental Q_{Lx_f} as shown in Figs. 4.5, 4.8, and 4.9 illustrate the HAPF simulated and experimental dynamic processes of the adaptive dc-link voltage level and compensation performances during over-compensation by coupling passive part situation. Figures 4.8a and 4.9a show that the simulated and experimental dc-link voltage level (V_{dc1_U}, V_{dc1_L}) can be adaptively changed

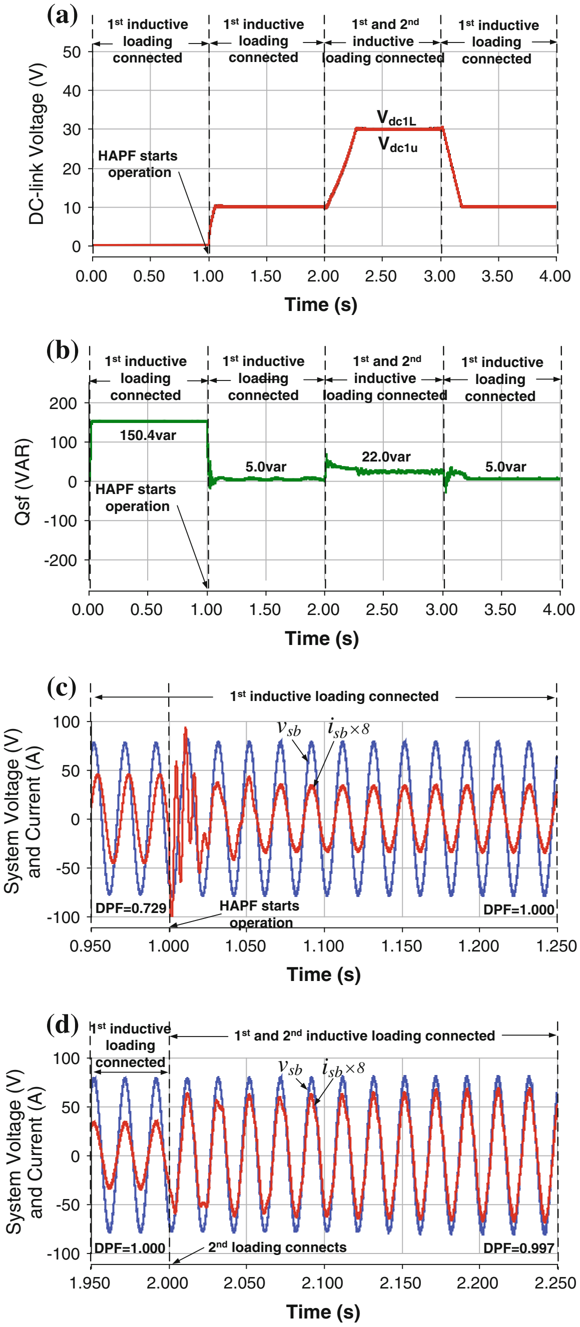

Fig. 4.6 HAPF simulated dynamic process during under-compensation by coupling passive part **a** adaptive $V_{\mathrm{dc1}_U} = V_{\mathrm{dc1}_L}$, **b** Q_{sxf} of phase *b*, **c** DPF of phase *b* before and after HAPF starts operation and **d** DPF of phase *b* before and after the 2nd loading is connected

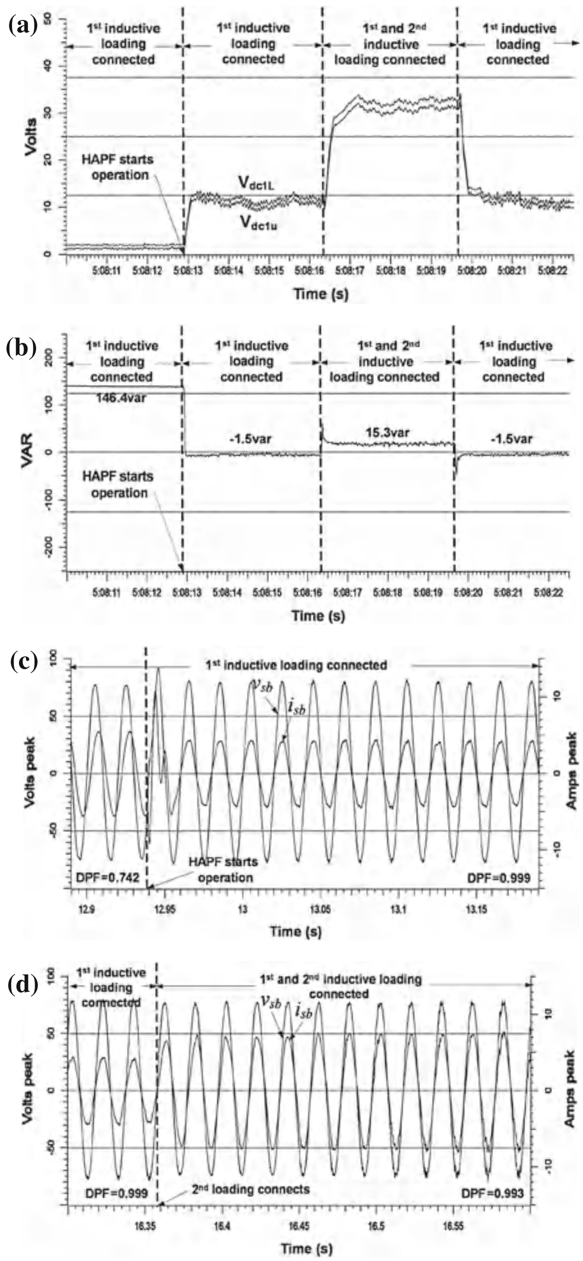

Fig. 4.7 HAPF experimental dynamic process during under-compensation by coupling passive part, **a** adaptive $V_{\mathrm{dc1}_U} = V_{\mathrm{dc1}_L}$, **b** Q_{sxf} of phase *b*, **c** DPF of phase *b* before and after HAPF starts operation and **d** DPF of phase *b* before and after the 2nd loading is connected

according to different reactive power consumption of the loading. From Figs. 4.8b and 4.9b, the simulated and experimental Q_{sx_f} of phase *b* can be compensated close to zero when the 1st loading or both 1st and 2nd loadings are connected.

Table 4.4 Simulation results before and after HAPF reactive power compensation with an adaptive dc-link voltage control (Under-compensation by coupling passive part, $L_{c1} = 6$ mH, $C_{c1} = 140$ µF)

Before compensation				After compensation			
Different cases	Q_{Lxf} (var)	DPF	i_{sx} (A)	Q_{sxf} (var)	DPF	i_{sx}(A)	THDi_{sx} (%)
1st inductive loading	150.4	0.729	4.01	5.0	1.000	2.95	2.4
1st and 2nd inductive loading	200.0	0.810	6.25	22.0	0.997	5.04	2.8

Table 4.5 Experimental results before and after HAPF reactive power compensation with an adaptive dc-link voltage control (Under-compensation by coupling passive part, $L_{c1} = 6$ mH, $C_{c1} = 140$ µF)

Before compensation					After compensation			
Different cases		Q_{Lxf} (var)	DPF	i_{sx} (A)	Q_{sxf} (var)	DPF	i_{sx} (A)	THDi_{sx} (%)
1st inductive loading	A	148.5	0.763	4.06	0.8	0.999	3.04	3.4
	B	146.4	0.742	3.90	-1.5	0.999	3.05	4.9
	C	145.1	0.746	4.01	3.5	0.999	3.02	4.7
1st and 2nd inductive loading	A	188.7	0.805	6.03	25.2	0.990	4.97	3.3
	B	184.5	0.815	5.87	15.3	0.993	4.96	4.1
	C	183.6	0.822	5.94	22.2	0.991	4.90	4.7

Figures 4.8c and 4.9c show that the simulated and experimental DPF of phase *b* can be compensated from 0.729 to 0.998 and 0.742 to 0.989, respectively, once the HAPF starts operation. From Figs. 4.8d and 4.9d, the simulated and experimental DPF of phase *b* can be kept at 0.999 or above when the 2nd loading is connected. The simulation results as shown in Fig. 4.8 are consistent with the experimental results as shown in Fig. 4.9.

Tables 4.6 and 4.7 summarize the simulation and experimental compensation results of the adaptive dc-link voltage controlled HAPF during over-compensation case. Compared with Q_{Lx_f}, the three-phase simulated Q_{sx_f} (−10.8 var or 3.2 var) and experimental Q_{sx_f} (−13.4 var, −16.8 var, −13.8 var or −3.4 var, −2.9 var, −0.8 var) have been compensated close to zero when the 1st loading or both the 1st and 2nd loadings are connected. These can be verified by showing three-phase simulated and experimental DPF = 0.990 or above and $\mathrm{THD}_{i_{sx}}$ are within 4.0 % and 6.0 % respectively. Figures 4.8, 4.9 and Tables 4.6, 4.7 verify the adaptive dc-link voltage controlled HAPF for reactive power compensation during over-compensation case.

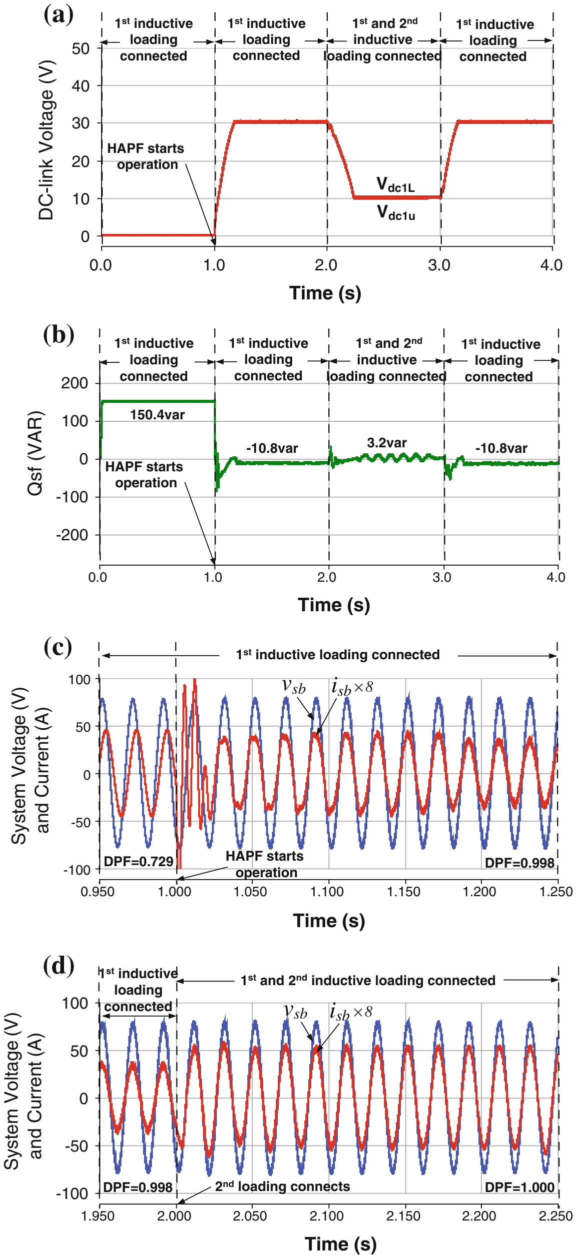

Fig. 4.8 HAPF simulated dynamic process during overcompensation by coupling passive part, **a** adaptive $V_{\mathrm{dc}1_U} = V_{\mathrm{dc}1_L}$, **b** Q_{sxf} of phase *b*, **c** DPF of phase *b* before and after HAPF starts operation and **d** DPF of phase *b* before and after the 2nd loading is connected

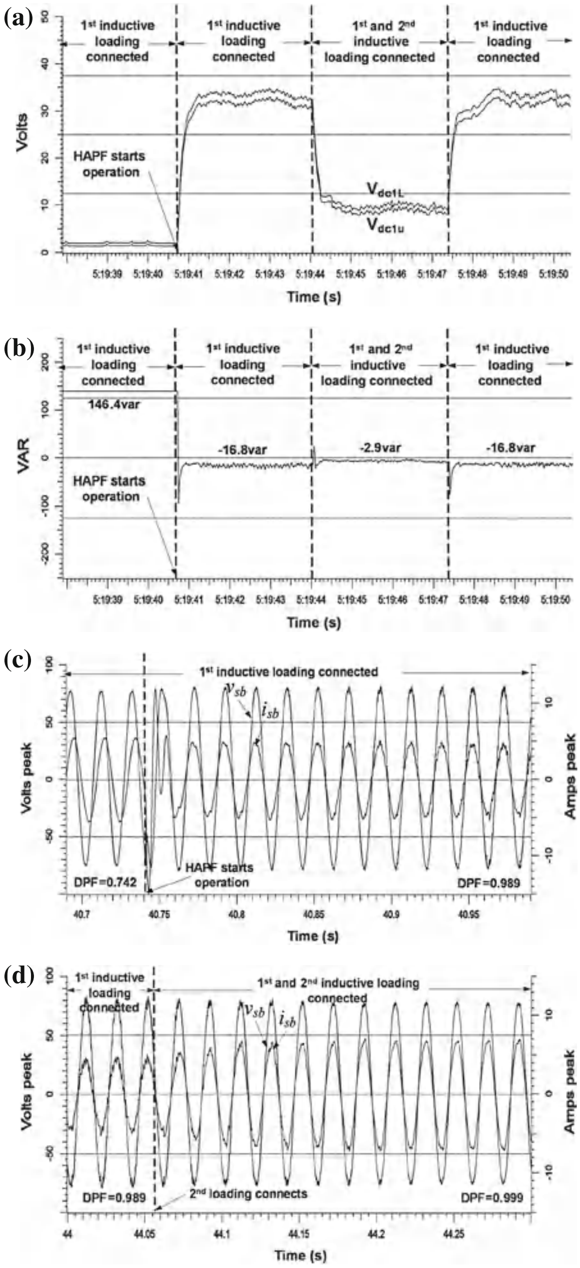

Fig. 4.9 HAPF experimental dynamic process during over-compensation by coupling passive part, **a** adaptive $V_{\mathrm{dc1}_U} = V_{\mathrm{dc1}_L}$, **b** Q_{sxf} of phase *b*, **c** DPF of phase *b* before and after HAPF starts operation and **d** DPF of phase *b* before and after the 2nd loading is connected

Table 4.6 Simulation results before and after HAPF reactive power compensation with an adaptive dc-link voltage control (Over-compensation by coupling passive part, $L_{c1} = 6$ mH, $C_{c1} = 190$ μF)

Before compensation				After compensation			
Different cases	Q_{Lxf} (var)	DPF	i_{sx} (A)	Q_{sxf} (var)	DPF (A)	i_{sx} (A)	THDi_{sx} (%)
1st inductive loading	150.4	0.729	4.01	−10.8	0.998	2.97	3.7
1st and 2nd inductive loading	200.0	0.810	6.25	3.2	1.000	5.08	3.2

Table 4.7 Experimental results before and after HAPF reactive power compensation with an adaptive dc-link voltage control (Over-compensation by coupling passive part, $L_{c1} = 6$ mH, $C_{c1} = 190$ μF)

Before compensation					After compensation			
Different cases		Q_{Lxf} (var)	DPF	i_{sx} (A)	Q_{sxf} (var)	DPF	i_{sx} (A)	THDi_{sx} (%)
1st inductive loading	A	148.5	0.763	4.06	−13.4	0.990	3.10	4.3
	B	146.4	0.742	3.90	−16.8	0.989	3.15	5.5
	C	145.1	0.746	4.01	−13.8	0.990	3.03	5.3
1st and 2nd inductive loading	A	188.7	0.805	6.03	−3.4	0.999	5.01	1.9
	B	184.5	0.815	5.87	−2.9	0.999	4.99	2.5
	C	183.6	0.822	5.94	−0.8	0.999	4.91	2.7

4.5.3 Comparison Between Fixed and Adaptive DC-Link Voltage Control

During under-compensation by coupling passive part case ($L_{c1} = 6$ mH, $C_{c1} = 140$ μF), with a fixed dc-link voltage of V_{dc1_U}, $V_{\mathrm{dc1}_L} = 30$ V, Figs. 4.10 and 4.11 show the HAPF whole simulated and experimental dynamic compensation process for the same loading situations as shown in Fig. 4.5. Comparing Figs. 4.10 and 4.11 with Figs. 4.6 and 4.7, the fixed and adaptive dc-link voltage control can achieve more or less the same steady-state reactive power compensation results. However, the adaptive control scheme just requires a lower dc-link voltage of V_{dc1_U}, $V_{\mathrm{dc1}_L} = 10$ V for compensating the 1st loading as shown in Figs. 4.6a and 4.7a. For the adaptive dc-link voltage control of the HAPF, due to its final reference dc-link voltage level V^*_{dc1} can be varied according to different loading conditions, the compensation performance will be influenced during each changing of the dc voltage level. Compared with the fixed dc-link voltage control, the adaptive control scheme will have a longer settling time during the load and dc voltage level changing situation, which can be verified by the compensated Q_{sx_f} as shown in Figs. 4.6, 4.7, 4.10, and 4.11.

Figures 4.12 and 4.13 show the HAPF simulated and experimental compensating current i_{cx} of phase b and their spectra with: a a fixed dc-link voltage of

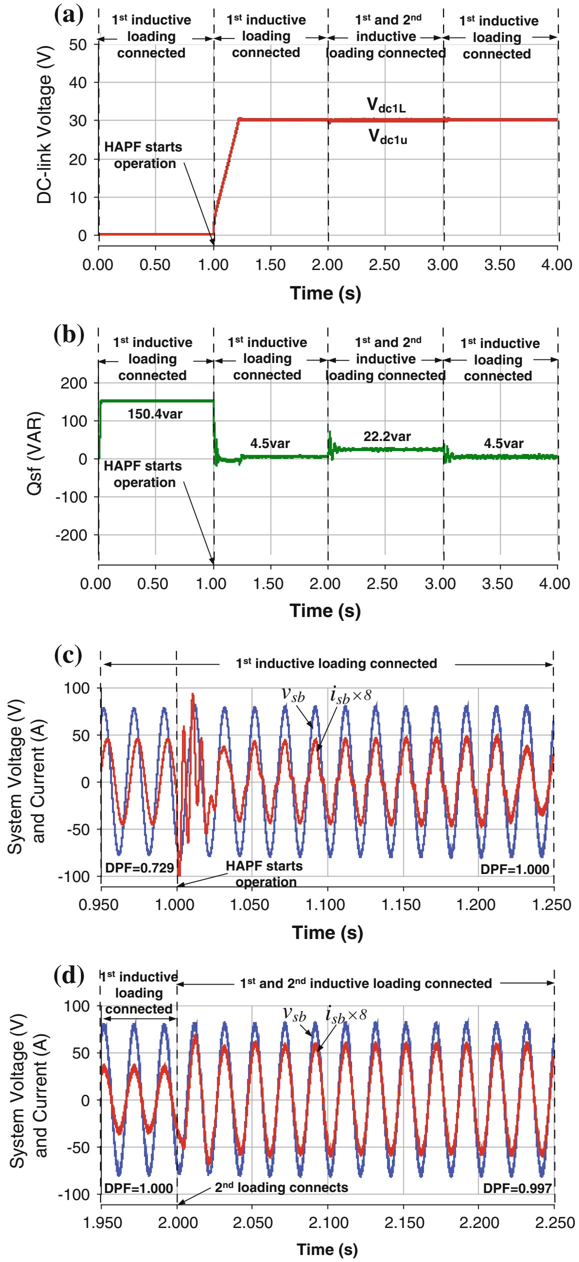

Fig. 4.10 HAPF whole simulated dynamic process during under-compensation by coupling passive part, **a** fixed $V_{\mathrm{dc1}_U} = V_{\mathrm{dc1}_L} = 30\,\mathrm{V}$, **b** Q_{sxf} of phase *b*, **c** DPF of phase *b* before and after HAPF starts operation and **d** DPF of phase *b* before and after the 2nd loading is connected

V_{dc1_U}, V_{dc1_L} = 30 V, and b adaptive dc-link voltage control during the 1st loading connected case. As the reactive power consumption of the 1st inductive loading can almost be fully compensated by the coupling passive part as shown in

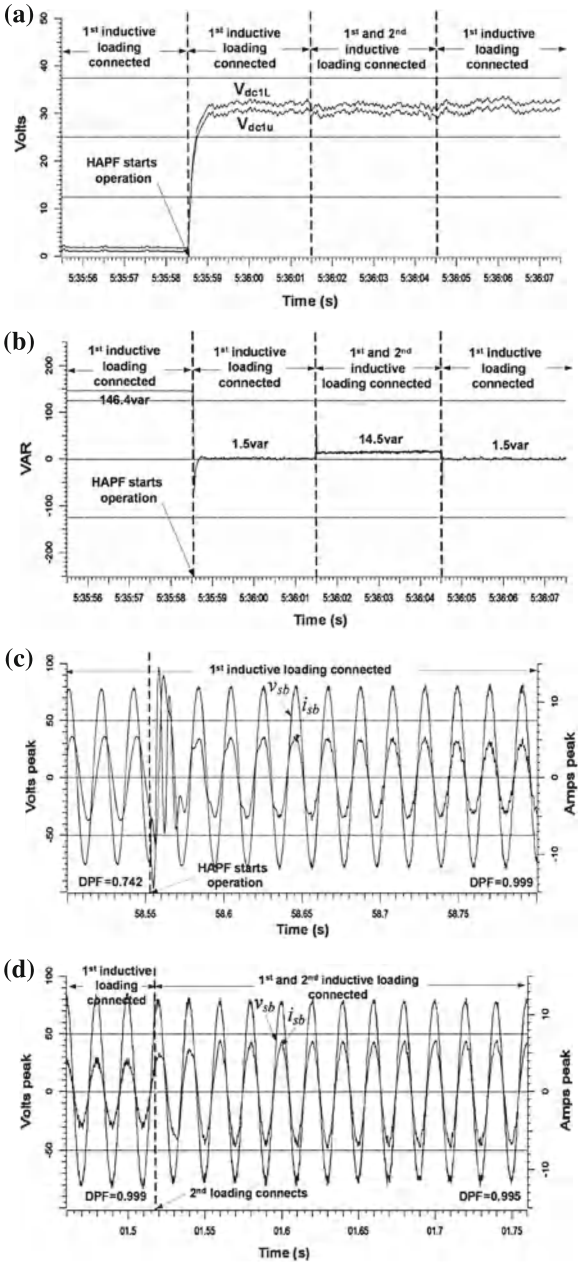

Fig. 4.11 HAPF whole experimental dynamic process during under-compensation by coupling passive part, **a** fixed $V_{\mathrm{dc1}_U} = V_{\mathrm{dc1}_L} = 30\,\mathrm{V}$, **b** Q_{sxf} of phase *b*, **c** DPF of phase *b* before and after HAPF starts operation and **d** DPF of phase *b* before and after the 2nd loading is connected

Table 4.3, it is clearly illustrated in Figs. 4.12 and 4.13 that the adaptive dc control scheme can effectively reduce the switching noise compared with the fixed V_{dc1_U}, $V_{\mathrm{dc1}_L} = 30$ V.

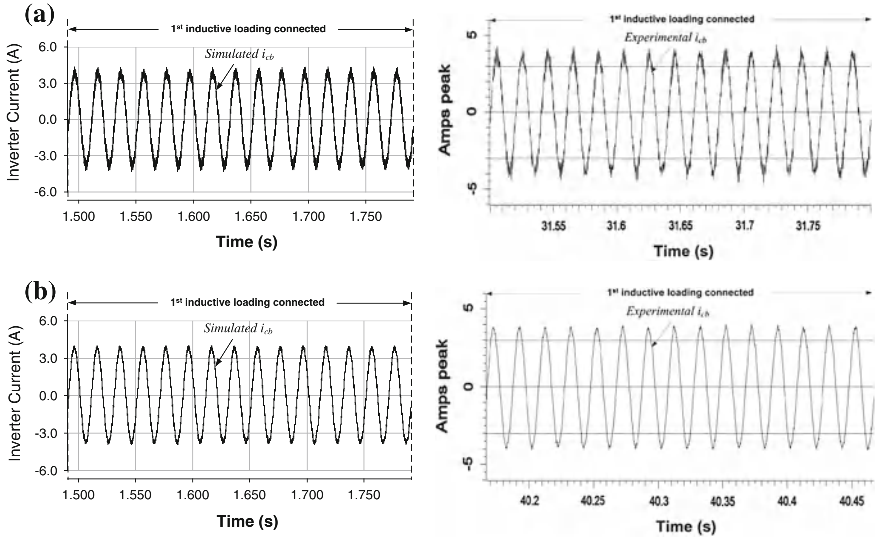

Fig. 4.12 Simulated and experimental i_{cx} of phase b with, **a** fixed $V_{\mathrm{dc1}_U} = V_{\mathrm{dc1}_L} = 30\,\mathrm{V}$ and **b** adaptive dc-link voltage control during under-compensation by coupling passive part case

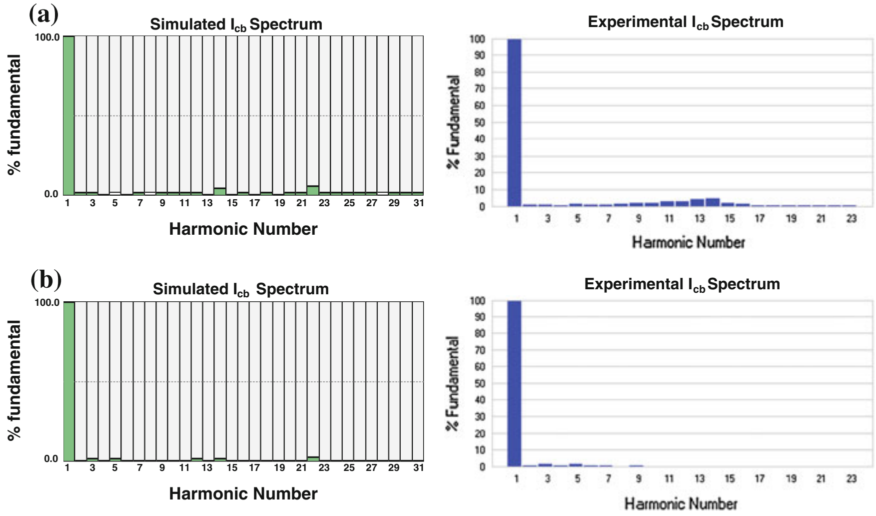

Fig. 4.13 Simulated and experimental frequency spectrum for i_{cx} of phase b with **a** fixed $V_{\mathrm{dc1}_U} = V_{\mathrm{dc1}_L} = 30\,\mathrm{V}$ and **b** adaptive dc-link voltage control during under-compensation by coupling passive part case

Therefore, the adaptive dc control method for the HAPF can reduce the switching loss and switching noise compared with the traditional fixed dc-link voltage case. During over-compensation by coupling passive part case, the similar simulated and experimental results can be obtained when both the 1st and 2nd loadings are connected.

From Figs. 4.5–4.13, and Tables 4.4–4.7, they verify that the adaptive dc-link voltage controlled HAPF can obtain good dynamic reactive power compensation performance and reduce the system switching loss and switching noise, compared with the traditional fixed dc-link voltage controlled HAPF.

4.6 Summary

An adaptive dc-link voltage control technique for the HAPF in dynamic reactive power compensation is proposed in this chapter. In order to implement the adaptive dc-link voltage control algorithm, the HAPF required minimum dc-link voltage for compensating different reactive power is deduced and its adaptive control block diagram is also built. The final reference dc-link voltage is classified into certain levels for selection, so that the impact on the compensation performances by the fluctuation of the adaptive dc-link voltage in the practical case can be reduced. Then the viability and effectiveness of the adaptive dc-link voltage control for the three-phase four-wire HAPF have been proved by both simulation and experimental results, in which it can achieve a good dynamic reactive power compensation performance as well as reducing the switching loss and switching noise compared with the traditional fixed dc-link voltage controlled HAPF. Therefore, the adaptive dc-link voltage controlled HAPF is a cost-effective solution for reactive power compensation in practical situations. Nevertheless, this adaptive control method would not reduce the initial cost of the HAPF because its maximum compensation range is merely determined by its specifications.

References

1. H. Akagi, S. Srianthumrong, and Y. Tamai, Comparisons in circuit configuration and filtering performance between hybrid and pure shunt active filters. in *Conference Rec. IEEE-IAS Annual Meeting*, vol. 2, pp. 1195–1202, (2003)
2. S. Srianthumrong, H. Akagi, A medium-voltage transformerless AC/DC Power conversion system consisting of a diode rectifier and a shunt hybrid filter, IEEE Trans. Ind. Applicat. **39**(3), 874–882, (2003)
3. W. Tangtheerajaroonwong, T. Hatada, K. Wada, H. Akagi, Design and performance of a transformerless shunt hybrid filter integrated into a three-phase diode rectifier. IEEE Trans. Power Electron. **22**(5), 1882–1889 (2007)
4. H. -L. Jou, K. -D. Wu, J.- C. Wu, C. -H. Li, M. -S. Huang, Novel power converter topology for three phase four-wire hybrid power filter, IET Power Electron. **1**(1), 164–173, (2008)

5. R. Inzunza, H. Akagi, A 6.6-kV transformerless shunt hybrid active filter for installation on a power distribution system. IEEE Trans. Power Electron. **20**(4), 893–900 (2005)
6. V.-F. Corasaniti, M.-B. Barbieri, P.-L. Arnera, M.-I. Valla, Hybrid power filter to enhance power quality in a medium voltage distribution. IEEE Trans. Ind. Electron. **56**(8), 2885–2893 (2009)
7. S. Rahmani, A. Hamadi, N. Mendalek, K. Al-Haddad, A new control technique for three-phase shunt hybrid power filter. IEEE Trans. Ind. Electron. **56**(8), 2904–2915 (2009)
8. S. –U. Tai, Power quality study in Macau and virtual power analyzer. Master thesis, University of Macau, 2012
9. S.-U. Tai, M.-C. Wong, M.-C. Dong, Y.-D. Han, Some findings on harmonic measurement in Macao, in *Proceeding of the 7th Internatinal Conference on Power Electronics and Drive Systems, PEDS. 07*, pp. 405–410, 2007
10. M.-C. Wong, J. Tang, Y.-D. Han, Cylindrical coordinate control of three-dimensional PWM technique in three-phase four-wired trilevel inverter. IEEE Trans. Power Electron. **18**(1), 208–220 (2003)
11. C.-S. Lam, M.-C. Wong, Y.-D. Han, Voltage swell and overvoltage compensation with unidirectional power flow controlled dynamic voltage restorer. IEEE Trans. Power Del. **23**(4), 2513–2521 (2008)
12. L.H. Wu, F. Zhuo, P.B. Zhang, H.Y. Li, Z.A. Wang, Study on the influence of supply-voltage fluctuation on shunt active power filter. IEEE Trans. Power Del. **22**(3), 1743–1749 (2007)
13. W.-H. Choi, C.-S. Lam, M.-C. Wong, Y.-D. Han, Analysis of dc-link voltage controls in three-phase four-wire hybrid active power filters. IEEE Trans. Power Electron. **28**(5), 2180–2191 (2013)
14. X.-X. Cui, C.-S. Lam, N.-Y. Dai, W.-H. Choi, M.-C. Wong, Study on dc voltage control of hybrid active power filters, *in the 6th IEEE Conference on Industrial Electronics and Applications, ICIEA2011*, pp. 856–861, (2011)
15. M. Aredes, J. Hafner, K. Heumann, Three-phase four-wire shunt active filter control strategies. IEEE Trans. Power Electron. **12**(2), 311–318 (1997)
16. N.Y. Dai, M.C. Wong, Y.D. Han, Three-dimensional space vector modulation with DC voltage variation control in a three-leg centre-split power quality compensator. IEE Proc. Electr. Power Appl. 151(2), 98–204, (2004)

Chapter 5
Minimum Inverter Capacity Design for HAPF

Abstract This chapter presents a minimum inverter capacity design for three-phase four-wire center-split hybrid active power filter (HAPF) in dynamic reactive power and current harmonics compensation. Based on HAPF equivalent circuit models in d-q-0 coordinate, the coupling part filtering characteristics of the HAPF without or with neutral inductor can be illustrated. According to the current quality data, the minimum dc-link voltage expressions for the HAPF without and with neutral inductor are deduced and compared. Conventionally, the coupling inductor and capacitor (LC) is usually tuned at a higher fifth or seventh order harmonic frequency to reduce its cost and size compared with the third order case. When triplen harmonic currents exist significantly, the HAPF with a small tuned neutral inductor can further reduce its minimum dc-link voltage requirement. Thus, the initial cost, switching loss and switching noise of the HAPF can be lowered. Representative simulation and experimental results of the three-phase four-wire HAPF with neutral inductor are presented to verify the filtering characteristics analysis and minimum dc-link voltage expressions, to show the effectiveness of reducing its inverter capacity, switching loss and switching noise in dynamic reactive power and current harmonics compensation compared with the conventional HAPF without neutral inductor.

Keywords Coupling Neutral Inductor · Current Harmonics · d-q-0 Coordinate · Hybrid Active Power Filter · Minimum DC-Link Voltage · Reactive Power · Switching Loss · Switching Noise

5.1 Introduction

Nowadays, because of the rapid growth of advanced power conversion devices and power electronic equipments, their full wave rectifier front ends make the current quality issues become more serious in three-phase four-wire system, especially in harmonic current (3rd, 5th, 7th, 9th, etc.) [1, 2]. In addition, the triplen harmonic currents (especially third order) drawn by these rectifier front ends will accumulate

C.-S. Lam and M.-C. Wong, *Design and Control of Hybrid Active Power Filters*, SpringerBriefs in Electrical and Computer Engineering,
DOI: 10.1007/978-3-642-41323-0_5, © The Author(s) 2014

in the neutral conductor, which results in increasing the risk for stray voltage complaints especially near substations and the electromagnetic field (EMF) levels near three-phase distribution feeders, etc. [3]. Moreover, excess neutral current will overheat and even burn the neutral conductor. Conventionally, the coupling LC of the HAPF is tuned at the fifth or seventh order harmonic frequencies [4–8] to reduce the system's initial cost and size. To compensate the dominant triplen harmonic current, the HAPF requires either a higher dc-link voltage requirement or an extra LC branch to filter that triplen harmonic current. However, the first method may raise the system cost by increasing the voltage rating requirement of the switching devices and dc-link capacitor. Moreover, a higher dc-link operating voltage will increase the switching loss and switching noise. And the second method will directly increase the system initial cost and size.

To filter the triplen harmonic current without tuning the LC at triplen harmonic frequency or adding any extra LC branches, the authors in [9] has presented an analysis for the HAPF with a coupling neutral inductor. Through the generic filter structure under positive, negative, and zero-sequence analysis, instead of having only one filtering resonant frequency from the coupling LC, the HAPF with a tuned coupling neutral inductor can provide two different resonant frequencies simultaneously in order to predominantly drain harmonic current away at these two frequencies [9]. However, the coupling part filtering improvement analysis based on the generic filter structure is not as obvious and comprehensible as the deduced equivalent circuit models in d-q-0 coordinate in this chapter. Moreover, because of the limitations among the existing literatures [4–8], there is still no mathematical deduction for the design of HAPF minimum dc-link voltage in reactive power and current harmonics compensation. Therefore, this chapter aims to investigate the minimum dc-link voltage design for a three-phase four-wire HAPF without and with neutral inductor. So that the inverter capacity reduction analysis by adding a neutral inductor can be mathematically found.

In the following, a three-phase four-wire center-split HAPF with a coupling neutral inductor and its corresponding equivalent circuit models in d-q-0 coordinate are initially introduced. Based on these circuit models, its coupling LC filtering characteristics without and with coupling neutral inductor are analyzed and discussed. According to the current quality of the loading and the HAPF single-phase equivalent circuit models in a-b-c coordinate, the required minimum dc-link voltage expressions for the HAPF without and with coupling neutral inductor will be proposed. Finally, representative simulation and experimental results of the HAPF with coupling neutral inductor are given to verify its filtering characteristics and the minimum dc-link voltage design expressions, to show the effectiveness of reducing its dc-link voltage requirement, switching loss and switching noise in reactive power and current harmonics compensation compared with the conventional HAPF without coupling neutral inductor. Given that most of the loadings in the distribution power systems are inductive, the following analysis and discussion only focus on inductive nonlinear loads [10].

5.2 Mathematical Modeling of A Three-Phase Four-Wire Center-Split HAPF in D-Q-0 Coordinate

5.2.1 Equivalent Circuit Models of a Three-Phase Four-Wire HAPF in D-Q-0 Coordinate

A three-phase four-wire center-split HAPF with a coupling neutral inductor is shown in Fig. 5.1a, in which the nonlinear loads are modeled as three single-phase full bridge diode rectifiers. The corresponding equivalent circuit model of HAPF in a-b-c coordinate is shown in Fig. 5.1b, where the subscript 'x' denotes phase a, b, c, n.v_x is the load voltage, i_{sx}, i_{Lx} and i_{cx} are the system, load and inverter current for each phase. C_{c1} and L_{c1} are the coupling capacitor and inductor for each leg of the three-phase VSI. v_{Cc1x} and v_{Lc1x} are the coupling capacitor voltage and inductor voltage. L_{cn} and v_{Lcn} are the coupling neutral inductor and neutral inductor voltage of the three-phase VSI. C_{dc1} and $0.5V_{dc1}$ are the dc capacitor, upper and lower dc capacitor voltages. The dc-link voltage is assumed as an ideal voltage source of V_{dc1}, and $v_{\mathrm{inv}1x}$ is the inverter output voltage.

From Fig. 5.1b, the differential equations of the coupling inductor L_{c1} and capacitor C_{c1} can be expressed as:

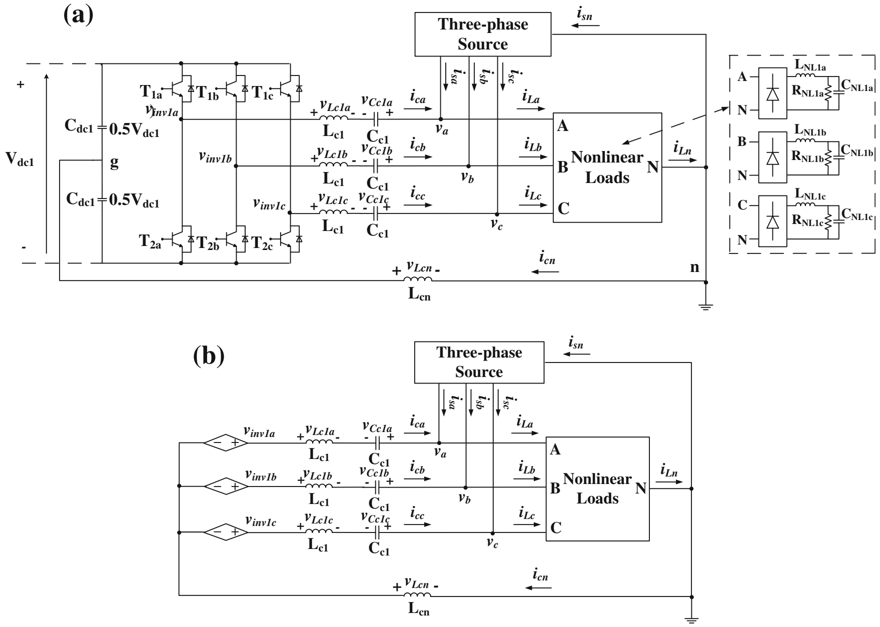

Fig. 5.1 A three-phase four-wire center-split HAPF with L_{cn}: **a** circuit configuration and **b** equivalent circuit model in a-b-c coordinate

$$L_{c1}\frac{d}{dt}\begin{bmatrix} i_{ca} \\ i_{cb} \\ i_{cc} \end{bmatrix} = \begin{bmatrix} v_{\text{inv1}a} \\ v_{\text{inv1}b} \\ v_{\text{inv1}c} \end{bmatrix} + L_{cn}\frac{d}{dt}\begin{bmatrix} i_{cn} \\ i_{cn} \\ i_{cn} \end{bmatrix} - \left(\begin{bmatrix} v_a \\ v_b \\ v_c \end{bmatrix} - \begin{bmatrix} v_{Cc1a} \\ v_{Cc1b} \\ v_{Cc1c} \end{bmatrix} \right) \tag{5.1}$$

$$C_{c1}\frac{d}{dt}\begin{bmatrix} v_{Cc1a} \\ v_{Cc1b} \\ v_{Cc1c} \end{bmatrix} = -\begin{bmatrix} i_{ca} \\ i_{cb} \\ i_{cc} \end{bmatrix} \tag{5.2}$$

With the help of [11, 12], after applying Park transformation, (5.1) and (5.2) in the d-q-0 rotating coordinate can be expressed as:

$$\begin{aligned} \omega L_{c1}\begin{bmatrix} -i_{cq} \\ i_{cd} \\ 0 \end{bmatrix} + L_{c1}\frac{d}{dt}\begin{bmatrix} i_{cd} \\ i_{cq} \\ i_{c0} \end{bmatrix} = \begin{bmatrix} v_{\text{inv1}d} \\ v_{\text{inv1}q} \\ v_{\text{inv1}0} \end{bmatrix} - 3L_{cn}\frac{d}{dt}\begin{bmatrix} 0 \\ 0 \\ i_{c0} \end{bmatrix} \\ - \left(\begin{bmatrix} v_d \\ v_q \\ v_0 \end{bmatrix} - \begin{bmatrix} v_{Cc1d} \\ v_{Cc1q} \\ v_{Cc10} \end{bmatrix} \right) \end{aligned} \tag{5.3}$$

$$\omega C_{c1}\begin{bmatrix} -v_{Cc1q} \\ v_{Cc1d} \\ 0 \end{bmatrix} + C_{c1}\frac{d}{dt}\begin{bmatrix} v_{Cc1d} \\ v_{Cc1q} \\ v_{Cc10} \end{bmatrix} = -\begin{bmatrix} i_{cd} \\ i_{cq} \\ i_{c0} \end{bmatrix} \tag{5.4}$$

where ω is the angular frequency of the d-q-0 rotating coordinate frame, and is synchronized with the line frequency. When HAPF does not contain coupling neutral inductor ($L_{cn} = 0$), (5.3) and (5.4) becomes:

$$\omega L_{c1}\begin{bmatrix} -i_{cq} \\ i_{cd} \\ 0 \end{bmatrix} + L_{c1}\frac{d}{dt}\begin{bmatrix} i_{cd} \\ i_{cq} \\ i_{c0} \end{bmatrix} = \begin{bmatrix} v_{inv1d} \\ v_{\text{inv1}q} \\ v_{\text{inv1}0} \end{bmatrix} - \left(\begin{bmatrix} v_d \\ v_q \\ v_0 \end{bmatrix} - \begin{bmatrix} v_{Cc1d} \\ v_{Cc1q} \\ v_{Cc10} \end{bmatrix} \right) \tag{5.5}$$

$$\omega C_{c1}\begin{bmatrix} -v_{Cc1q} \\ v_{Cc1d} \\ 0 \end{bmatrix} + C_{c1}\frac{d}{dt}\begin{bmatrix} v_{Cc1d} \\ v_{Cc1q} \\ v_{Cc10} \end{bmatrix} = -\begin{bmatrix} i_{cd} \\ i_{cq} \\ i_{c0} \end{bmatrix} \tag{5.6}$$

According to (5.3)–(5.6), the equivalent circuit models of the three-phase four-wire center-split HAPF without and with coupling neutral inductor in d-q-0 coordinate are shown in Fig. 5.2.

5.2.2 Coupling Part Filtering Characteristics Analysis of the HAPF without or with Coupling Neutral Inductor

From Fig. 5.2a, b, and d, L_{cn} will not influence the d, q-coordinate circuit models of the HAPF, but it will influence the 0-coordinate circuit model only. Compared with the 0-coordinate circuit model without L_{cn} as shown in Fig. 5.2c, when L_{cn} is

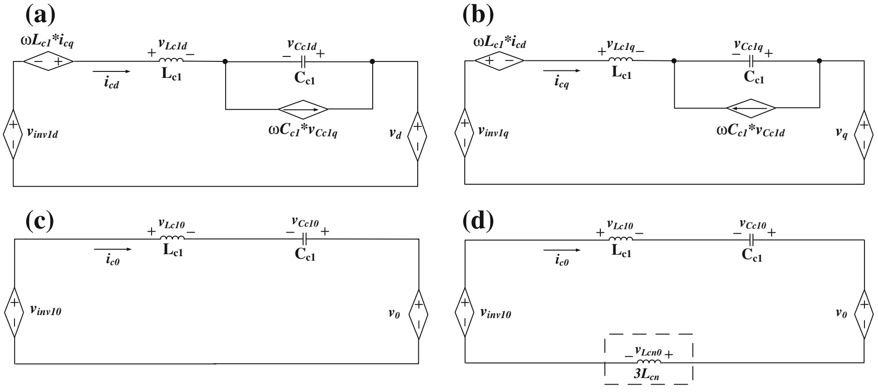

Fig. 5.2 Equivalent circuit models of the three-phase four-wire center-split HAPF without and with L_{cn} in d-q-0 coordinate: **a** d-coordinate circuit model without or with L_{cn}, **b** q-coordinate circuit model without or with L_{cn}, **c** 0-coordinate circuit model without L_{cn} and **d** 0-coordinate circuit model with L_{cn}

added, there is actually an added inductor of $3L_{cn}$ to the 0-coordinate circuit model, as shown in Fig. 5.2d.

From Fig. 5.2, without L_{cn}, the resonant frequency of the coupling part of the HAPF in d, q, and 0-coordinate circuit models are the same:

$$f_{dq\_NL} = f_{0\_NL} = \frac{1}{2\pi\sqrt{L_{c1}C_{c1}}} \tag{5.7}$$

where f_{dq_NL} and f_{0_NL} are the coupling part resonant frequencies for the HAPF d, q-coordinate circuit models and 0-coordinate circuit model without L_{cn} situation, the subscript ''*_NL*'' denotes the system without L_{cn}. This result implies that the coupling part can only possess one resonant frequency for filtering current harmonics.

From Fig. 5.2, with L_{cn}, the resonant frequency of the coupling part of the HAPF in d, q, and 0-coordinate circuit models can be expressed as:

$$f_{dq\_L} = \frac{1}{2\pi\sqrt{L_{c1}C_{c1}}} \tag{5.8}$$

$$f_{0\_L} = \frac{1}{2\pi\sqrt{(3L_{cn} + L_{c1})C_{c1}}} \tag{5.9}$$

where f_{dq_L} and f_{0_L} $\left(f_{0\_L} < f_{dq\_L}\right)$ are the coupling part resonant frequencies for the HAPF d, q-coordinate circuit models and 0-coordinate circuit model with L_{cn} situation, the subscript ''*_L*'' denotes the system with L_{cn}. From (5.8) and (5.9), it is clearly illustrated that the HAPF can have two different resonant frequencies for filtering current harmonics after the addition of L_{cn}.

The above analysis clearly shows that the three-phase four-wire center-split HAPF without and with L_{cn} will have the same d, q-coordinate but different 0-coordinate circuit models. Moreover, the HAPF with L_{cn} can have two different resonant frequencies for harmonic current filtering as indicated by (5.8) and (5.9), whereas the HAPF without L_{cn} can only have one as indicated by (5.7), in which the deduced results based on the equivalent circuit models in d-q-0 coordinate are equivalent as those deduced through the generic filter structure under positive, negative and zero-sequence analysis [9]. In the following, the resonant frequency selection for the coupling LC without or with L_{cn} will be discussed.

5.2.3 Resonant Frequency Selection for Coupling LC without or with Coupling Neutral Inductor

Under balanced nonlinear loadings consideration, the filtering characteristics and resonant frequency selection for the coupling LC without or with L_{cn} can be determined as follows.

1. When the loading contains $3k$th $(k = 1,\ 2 \ldots \infty)$ order harmonic current only: Since $3k$th order harmonic current presents in the 0-coordinate circuit model only, the coupling LC without and with L_{cn} can both be tuned at the dominant $3k$th order harmonic frequency (f_{0_NL} and f_{0_L}). From (5.7) and (5.9), for $f_{0\_NL} = f_{0\_L}$ consideration, a small L_{cn} can already significantly reduce the size of the three coupling inductor L_{c1}, which benefits for lowering the system initial cost. Therefore, it has a merit to add a L_{cn} to the HAPF under this loading situation. Moreover, the coupling LC without and with L_{cn} can only provide one $3k$th order resonant frequency for harmonic current filtering, as indicated by Fig. 5.2.
2. When the loading contains $3k \pm 1$th order harmonic current only: Since $3k \pm 1$th order harmonic current presents in the d, q-coordinate circuit models only, from Fig. 5.2a, b, L_{cn} cannot help to improve the coupling part filtering performances under this loading situation. As a result, it is not necessary to add a L_{cn} to the HAPF and the coupling LC can be tuned at the dominant $3k \pm 1$th order harmonic frequency (f_{dq_NL} and f_{dq_L}). Moreover, the coupling LC without and with L_{cn} can only provide one $3k \pm 1$th order resonant frequency for harmonic current filtering, as indicated by Fig. 5.2.
3. When the loading contains any order harmonic current. Since $3k$th and $3k \pm 1$th order harmonic currents can only present in the 0-coordinate and d, q-coordinate circuit models respectively, the coupling LC with L_{cn} can provide two resonant frequencies for eliminating one $3k$th and one $3k \pm 1$th order harmonic currents, as indicated by Fig. 5.2. Therefore, the coupling LC with L_{cn} can be tuned at one dominant $3k$th and one dominant $3k \pm 1$th order harmonic frequency (f_{dq_L} and f_{0_L}), where the $3kth$ order must be smaller than $3k \pm 1$th order.

4. When the loading contains unknown harmonic current. Owing to widely usage of the personal computers, uninterruptible power supplies, high frequency fluorescent lights, air-conditioning system, various office and consumer electronics equipments in residential, commercial and office buildings, both $3k$th and $3k \pm 1$th order harmonic currents are usually present in those three-phase four-wire distribution power systems, thus it is recommended to add a L_{cn} to the HAPF.

Under unbalanced nonlinear loadings consideration, both $3k$th and $3k \pm 1$th order harmonic currents can present in the d, q, 0-coordinate circuit models, the coupling LC with L_{cn} can be tuned at two dominant harmonic frequencies $\left(f_{dq\_L}, f_{0\_L}\right)$ and $\left(f_{0\_L} < f_{dq\_L}\right)$. In the following, the minimum dc-link voltage expressions for the HAPF without and with L_{cn} will be proposed and presented.

5.3 Minimum Inverter Capacity Analysis of A Three-Phase Four-Wire Center-Split HAPF

From the previous analysis results, Fig. 5.3 shows the HAPF single-phase equivalent circuit models in a-b-c coordinate without and with L_{cn}. In the following analysis, all parameters are in RMS value. From Fig. 5.3, the required inverter fundamental output voltages $\left(V_{\text{inv}1xf\_NL}, V_{\text{inv}1xf\_L}\right)$ and inverter harmonic output voltages $\left(V_{\text{inv}1xn\_NL}, V_{\text{inv}1xn\_L}\right)$ at each harmonic order can be found, where the subscripts 'f' and 'n' denote the fundamental and harmonic frequency components. As $V_{\text{inv}1xf\_NL}, V_{\text{inv}1xn\_NL}, V_{\text{inv}1xf\_L}, V_{\text{inv}1xn\_L}$ are in RMS values, their corresponding peak values can be obtained by multiplying a $\sqrt{2}$. Then their peak values will be treated as the minimum dc-link voltage values at the DC side. Thus, the minimum dc-link voltage values $\left(V_{dc1xf\_NL}, V_{dc1xn\_NL}, V_{dc1xf\_L}, V_{dc1xn\_L}\right)$ for compensating the phase fundamental reactive current component and each harmonic current component are calculated as the peak values of the required inverter fundamental and harmonic output voltages, in which $V_{dc1xf\_NL} = \sqrt{2}V_{\text{inv}1xf\_NL}$, $V_{dc1xn\_NL} = \sqrt{2}V_{\text{inv}1xn\_NL}$, $V_{dc1xf\_L} = \sqrt{2}V_{\text{inv}1xf\_L}$, $V_{dc1xn\_L} = \sqrt{2}V_{\text{inv}1xn\_L}$ respectively.

In order to provide sufficient dc-link voltage for compensating load reactive and harmonic currents, the minimum dc-link voltage requirement $\left(V_{dc1x\_NL}, V_{dc1x\_L}\right)$ of the HAPF single-phase circuit models without and with L_{cn} as shown in (5.10) and (5.11) are deduced by considering the worst phase relation between each harmonic component, in which their corresponding peak voltages of the VSI at AC side are assumed to be superimposed.

$$V_{dc1x\_NL} = \sqrt{\left|V_{dc1xf\_NL}\right|^2 + \sum_{n=2}^{\infty} \left|V_{dc1xn\_NL}\right|^2} \tag{5.10}$$

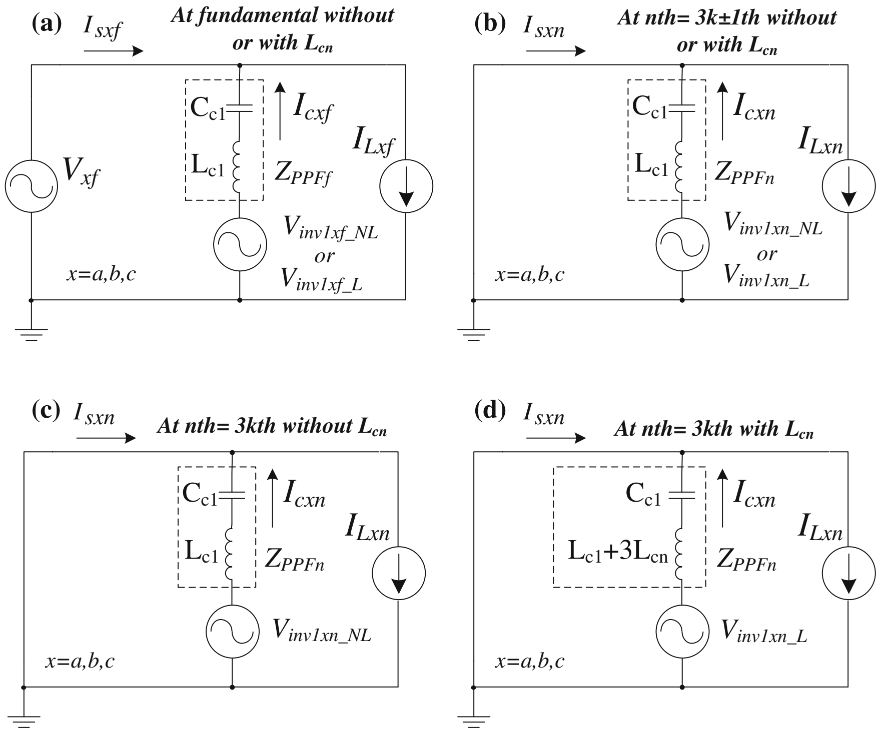

Fig. 5.3 HAPF single-phase equivalent circuit models in a-b-c coordinate: **a** at fundamental frequency without or with L_{cn}, **b** at nth = $3k \pm 1$th harmonic order frequency without or with L_{cn}, **c** at nth = $3k$th harmonic order frequency without L_{cn} and **d** at nth = $3k$th harmonic order frequency with L_{cn}

$$V_{dc1x\_L} = \sqrt{\left|V_{dc1xf\_L}\right|^2 + \sum_{n=2}^{\infty} \left|V_{dc1xn\_L}\right|^2} \tag{5.11}$$

From Fig. 5.3, as the L_{cn} affects only the $3kth$ order harmonic impedance of the coupling part, the HAPF without and with L_{cn} obtain the same fundamental impedance of the coupling part as shown in Fig. 5.3a. From Fig. 5.3a, when the load voltage V_x is pure sinusoidal without harmonic components, $V_x = V_{xf}$, the inverter fundamental output voltage of the HAPF single-phase circuit models without and with L_{cn} can be expressed as:

$$V_{\mathrm{inv}1xf\_NL} = V_{\mathrm{inv}1xf\_L} = V_x + Z_{\mathrm{PPFf}} \times I_{\mathrm{cxf}} \tag{5.12}$$

As most of the loadings in the distribution power systems are inductive, the fundamental impedance of the coupling capacitor C_{c1} should be larger than that of the coupling inductor L_{c1}, that yields $Z_{\mathrm{PPFf}} = |Z_{\mathrm{PPFf}}|e^{j\varphi f}$, $\left(\varphi f = -90^{\circ}\right)$. When the HAPF operates at ideal case, the fundamental compensating current I_{cxf} contains the pure reactive component I_{cxfq} only without the active current component I_{cxfp}, therefore (5.12) can be rewritten as:

$$V_{\mathrm{inv}1xf\_NL} = V_{\mathrm{inv}1xf\_L} = V_x - \left|\omega L_{c1} - \frac{1}{\omega C_{c1}}\right| \left|I_{\mathrm{cxfq}}\right| \qquad \omega = 2\pi f \tag{5.13}$$

When the HAPF does not contain L_{cn}, from Fig. 5.3b and c, the inverter harmonic output voltage $V_{\mathrm{inv}1xn\_NL}$ at nth $= 3k \pm 1$th or $3k$th ($k = 1, 2 \ldots \infty$) harmonic order can be expressed as:

$$V_{\mathrm{inv}1xn\_NL} = \left|n\omega L_{c1} - \frac{1}{n\omega C_{c1}}\right| \left|I_{\mathrm{cxn}}\right| \qquad n = 2,\ 3 \ldots \infty \tag{5.14}$$

where I_{cxn} is the nth order harmonic compensating current.

When the HAPF contains L_{cn}, from Fig. 5.3b and d, the inverter harmonic output voltage $V_{\mathrm{inv}1xn\_L}$ at $nth = 3k \pm 1$th or $3k$th harmonic order can be expressed as:

$$V_{\mathrm{inv}1xn\_L} = \begin{cases} V_{\mathrm{inv}1x3k\pm1\_L} = \left|(3k \pm 1)\omega L_{c1} - \dfrac{1}{(3k \pm 1)\omega C_{c1}}\right| \left|I_{cx3k\pm1}\right| \\ V_{\mathrm{inv}1x3k\_L} = \left|3k\omega(L_{c1} + 3L_{cn}) - \dfrac{1}{3k\omega C_{c1}}\right| \left|I_{cx3k}\right| \end{cases} \quad \begin{matrix} k = 1,\ 2 \ldots \infty \\ n = 2,\ 3 \ldots \infty \end{matrix} \tag{5.15}$$

When the HAPF is performing compensation, the absolute reactive and nth order harmonic compensating current should be equal to those of the loading, this yields:

$$\left|I_{\mathrm{cxfq}}\right| = \left|I_{\mathrm{Lxfq}}\right|, \quad \left|I_{\mathrm{cxn}}\right| = \left|I_{\mathrm{Lxn}}\right| \tag{5.16}$$

where I_{Lxfq} and I_{Lxn} are the reactive and nth order harmonic current of the loading.

From (5.12)–(5.16), the inverter fundamental and each nth harmonic order output voltages of the HAPF single-phase circuit model without and with $L_{cn}\left(V_{\mathrm{inv}1xf\_NL}, V_{\mathrm{inv}1xn\_NL}, V_{\mathrm{inv}1xf\_L}, V_{\mathrm{inv}1xn\_L}\right)$ can be calculated. Then the minimum dc-link voltage requirement $(V_{dc1x\_NL}, V_{dc1x\_L})$ for the HAPF single-phase circuit models can be found by (5.10) and (5.11).

As the HAPF discussed in this book aims to compensate reactive power and current harmonics, the generalized single-phase pq theory as discussed in Appendix A.2 is chosen in this chapter. By using the single-phase pq theory, the reactive power and current harmonics in each phase can be compensated independently, thus the final required minimum dc-link voltage for the three-phase four-wire center-split HAPF without and with $L_{cn}(V_{dc1\_NL}, V_{dc1\_L})$ will be the maximum one among the calculated minimum value of each phase $(V_{dc1x\_NL}, V_{dc1x\_L})$, which are expressed in (5.17) and (5.18).

$$V_{dc1\_NL} = V_{dc1\_\min} = \max(2V_{dc1a\_NL}, 2V_{dc1b\_NL}, 2V_{dc1c\_NL}) \tag{5.17}$$

$$V_{dc1\_L} = V_{dc1\_\min} = \max(2V_{dc1a\_L}, 2V_{dc1b\_L}, 2V_{dc1c\_L}) \tag{5.18}$$

From (5.17) and (5.18), the inverter capacity of the HAPF without and with L_{cn} $(S_{\mathrm{inv}\_NL}, S_{\mathrm{inv}\_L})$ can be expressed as:

$$S_{\mathrm{inv}\_NL} = 3\frac{V_{dc1\_NL}}{\sqrt{2}} I_c \tag{5.19}$$

$$S_{\mathrm{inv}\_L} = 3\frac{V_{dc1\_L}}{\sqrt{2}} I_c \tag{5.20}$$

where $I_c = \max(I_{ca}, I_{cb}, I_{cc})$. From (5.19) and (5.20), the inverter capacity of the HAPF without and with L_{cn} is proportional to their corresponding dc-link voltage. Thus, the dc-link voltage level can reflect the inverter capacity of the HAPF. Table 5.1 lists the minimum dc-link voltage deduction steps of the HAPF without and with L_{cn}.

From Table 5.1, the minimum dc-link voltage values can be calculated only when the spectra of the load currents are known. If the load current spectra cannot be measured (unknown loads) before the installation of the HAPF system, via Fast Fourier Transform (FFT), the load current spectra can also be figured out by using the DSP of the HAPF after installation. Then the minimum dc-link voltage value can be calculated by using the DSP via the deduction steps in Table 5.1. Once the

Table 5.1 Minimum dc-link voltage deduction steps of the HAPF without and with L_{cn}

1	Inverter fundamental output voltage without and with L_{cn}: $V_{\mathrm{inv}1xf\_NL} = V_{\mathrm{inv}1xf\_L} = V_x - \left\lvert \omega L_{c1} - \frac{1}{\omega C_{c1}} \right\rvert \lvert I_{\mathrm{cxfq}} \rvert$ where $\lvert I_{\mathrm{cxfq}} \rvert = \lvert I_{\mathrm{Lxfq}} \rvert$, where $\omega = 2\pi f$	(5.13)
2	Inverter *nth* harmonic order output voltage without and with L_{cn}: $V_{\mathrm{inv}1xn\_NL} = \left\lvert n\omega L_{c1} - \frac{1}{n\omega C_{c1}} \right\rvert \lvert I_{\mathrm{cxn}} \rvert$	(5.14)
	$V_{\mathrm{inv}1xn\_L} = \begin{cases} V_{\mathrm{inv}1x3k\pm1\_L} = \left\lvert (3k\pm1)\omega L_{c1} - \frac{1}{(3k\pm1)\omega C_{c1}} \right\rvert \lvert I_{cx3k\pm1} \rvert \\ V_{\mathrm{inv}1x3k\_L} = \left\lvert 3k\omega(L_{c1} + 3L_{cn}) - \frac{1}{3k\omega C_{c1}} \right\rvert \lvert I_{cx3k} \rvert \end{cases}$ where $\lvert I_{\mathrm{cxn}} \rvert = \lvert I_{\mathrm{Lxn}} \rvert$, nth $= 3\ k \pm 1$th or $3k$th, $k = 1,\ 2 \ldots \infty$, $n = 2,\ 3 \ldots \infty, \quad \omega = 2\pi f$	(5.15)
3	Minimum dc-link voltage without L_{cn}: $V_{dc1\_NL} = V_{dc1\_\min} = \max(2V_{dc1a\_NL}, 2V_{dc1b\_NL}, 2V_{dc1c\_NL})$	(5.17)
	Where $V_{dc1x\_NL} = \sqrt{\lvert V_{dc1xf\_NL} \rvert^2 + \sum_{n=2}^{\infty} \lvert V_{dc1xn\_NL} \rvert^2}$ $V_{dc1xf\_NL} = \sqrt{2} V_{\mathrm{inv}1xf\_NL}$, $V_{dc1xn\_NL} = \sqrt{2} V_{\mathrm{inv}1xn\_NL}$, where $n = 2,\ 3 \ldots \infty$	(5.10)
	Minimum dc-link voltage with L_{cn}: $V_{dc1\_L} = V_{dc1\_\min} = \max(2V_{dc1a\_L}, 2V_{dc1b\_L}, 2V_{dc1c\_L})$	(5.18)
	Where $V_{dc1x\_L} = \sqrt{\lvert V_{dc1xf\_L} \rvert^2 + \sum_{n=2}^{\infty} \lvert V_{dc1xn\_L} \rvert^2}$ $V_{dc1xf\_L} = \sqrt{2} V_{\mathrm{inv}1xf\_L}$, $V_{dc1xn\_L} = \sqrt{2} V_{\mathrm{inv}1xn\_L}$, where $n = 2,\ 3 \ldots \infty$	(5.11)

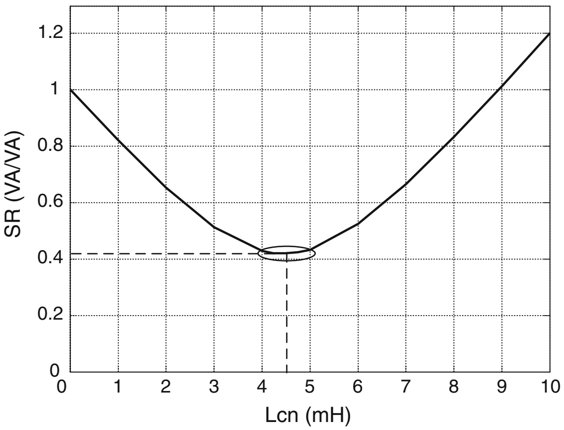

Fig. 5.4 Inverter capacity ratio S_R between the HAPF without and with different L_{cn} values

minimum dc-link voltage value is known, the HAPF system can start operation. Through the dc-link voltage control method, the dc-link voltage of HAPF can be controlled to reach this minimum reference value.

For the three single-phase full bridge rectifier loadings as shown in Fig. 5.1a are approximately balanced, from (5.19)–(5.20), the inverter capacity ratio S_R between the HAPF with and without L_{cn} can be expressed as:

$$S_R = \frac{S_{\text{inv}\_L}}{S_{\text{inv}\_NL}} = \frac{V_{dc1\_L}}{V_{dc1\_NL}} = \frac{V_{dc1x\_L}}{V_{dc1x\_NL}} \tag{5.21}$$

As the load harmonic currents are mainly contributed by the third, fifth, seventh, and ninth harmonic orders, the coupling part (L_{c1}, C_{c1}) with the L_{cn} can be tuned at the fifth and third harmonic orders, respectively. For the simulated HAPF system parameters and balanced loading situations as shown in Tables 5.3 and 5.4, Fig. 5.4 shows the S_R between the HAPF without and with different L_{cn} values. From Fig. 5.4, when L_{cn} is chosen at around 4.5mH, the minimum inverter capacity of the HAPF can be achieved. Moreover, the inverter capacity of the HAPF with L_{cn} (L_{cn} = 4–5 mH) can be reduced by more than 50 % of that without L_{cn} (L_{cn} = 0 mH).

From the above analysis, when the 3kth and 3k ± 1th order harmonic contents dominate the load harmonic current in a three-phase four-wire power system, through appropriate design of the coupling part (L_{c1}, C_{c1}) and L_{cn}, the HAPF with L_{cn} can reduce its inverter capacity compared with the HAPF without L_{cn}. The coupling LC is required to be tuned at 3k ± 1th order harmonic frequency because the coupling LC with L_{cn} can only eliminate the *3kth* order harmonic current. Moreover, 3kth harmonic order should be smaller than 3k ± 1th harmonic order.

Although the use of L_{cn} increases one passive component of the HAPF, it may effectively reduce the minimum dc-link voltage requirement, so as to lower the HAPF system initial cost. Moreover, as the switching loss is directly proportional to the dc-link voltage [13], the HAPF with L_{cn} will obtain less switching loss if a

Table 5.2 Characteristics of the HAPF without and with L_{cn}

HAPF	No. of resonant frequency order for filtering harmonics	No. of LC components		Capacity of the inverter
		L	C	
Without L_{cn}	1	3	3	Larger
With L_{cn}	2	4	3	Smaller

lower dc-link voltage is used, and vice versa. Besides, the system can also obtain less switching noise, so as to improve its compensation performances. Table 5.2 summarizes the characteristics of the HAPF without and with L_{cn}.

5.4 Simulation and Experimental Verifications for Inverter Capacity Reduction Analysis of the Three-Phase Four-Wire HAPF with Coupling Neutral Inductor

In order to verify the filtering characteristics and minimum dc-link voltage analysis in previous sections, representative simulation and experimental results of the three-phase four-wire center-split HAPF system without and with L_{cn} as shown in Fig. 5.1a will be given. To simplify the verification in this chapter, the dc-link is supported by external dc voltage source and the simulated and experimental three-phase loadings are approximately balanced. Table 5.3 lists the simulated and experimental system parameters for the HAPF. From Table 5.3, the coupling L_{c1} and C_{c1} are designed basing on the load fundamental reactive power consumption and tuned at the fifth order harmonic frequency, and the coupling LC with L_{cn} are tuned at the third order harmonic frequency. As the simulated and experimental loadings are approximately balanced, only phase *a* compensation diagrams will be illustrated.

The HAPF reactive and harmonic reference compensating current is determined by using the single-phase instantaneous *pq* theory as discussed in Appendix A.2.

Table 5.3 HAPF system parameters for simulations and experiments

System parameters		Physical values
System source-side	V_x	220 V
	f	50 Hz
HAPF	L_{c1}	8 mH
	C_{c1}	50 uF
	V_{dc1}	45, 65, 90 V
	L_{cn}	5 mH
Nonlinear rectifier load	R_{NL1x}	43.2 Ω
	L_{NL1x}	34.5 mH
	C_{NL1x}	392.0 uF

Then the corresponding control block diagram of the three-phase four-wire HAPF is also illustrated in Appendix A.2 . And hysteresis PWM is applied for generating the required compensating current. Thus, the compensating current error Δi_{cx} together with hysteresis band H will be sent to the current PWM control part for generating the trigger signals to control the switching devices of the VSI. In the following, as the load harmonic current contents beyond the ninth order are small, for simplicity, the required minimum dc-link voltage calculation will be taken into account up to ninth harmonic order only.

Simulation studies were carried out by using Matlab. In order to verify the simulation results, a 220 V, 10 kVA three-phase four-wire center-split HAPF prototype is implemented in the laboratory. IGBTs are employed as the switching devices for the active inverter part. And the control system of the prototype is a DSP TMS320F2812 and the analog-to-digital (A/D) sampling frequency of the HAPF system is set at 40 μs (25 kHz). And the details of the 220 V, 10 kVA experimental prototype can be found in Chap. 6.

5.4.1 Simulation Results

Figure 5.5a illustrates the simulated load current i_{Lx} waveform and its spectrum of phase *a*, in which its corresponding fundamental reactive current, third, fifth, seventh, and ninth order harmonic current in RMS values are shown in Table 5.4. From Fig. 5.5a and Table 5.6, the total harmonic distortion of the load current $(THD_{i_{Lx}})$ is 32.1 % and the load neutral current (i_{Ln}) is 5.35 A, in which the 3rd (3*k*th) and 5th (3*k* ± 1th) order harmonic contents dominate the load harmonic current. With the help of Tables 5.1, 5.5 shows the required minimum dc-link voltage values $(V_{dc1xf\_NL}, V_{dc1xn\_NL}, V_{dc1xf\_L}, V_{dc1xn\_L})$ for compensating the fundamental reactive current, 3rd, 5th, 7th, and 9th harmonic current components and the minimum dc-link voltages (V_{dc1_NL}, V_{dc1_L}) of the HAPF without and with L_{cn}, in which $V_{dc1\_NL} = 79.24$ V and $V_{dc1\_L} = 34.22$ V respectively. The dc-link voltage for the HAPF is chosen as $V_{dc1} = 45, 65, 90$ V three levels for performing compensation respectively. After compensation by the HAPF without and with L_{cn}, Fig. 5.5b–e show the simulated system current i_{sx} waveforms and their spectra of phase *a* at different dc-link voltage levels. Moreover, their corresponding results are summarized in Table 5.6.

Table 5.4 Simulated and experimental fundamental reactive current, third, fifth, seventh, and ninth orders harmonic current values of the loading

	Fundamental reactive current (A)	Third order harmonic current (A)	Fifth order harmonic current (A)	Seven order harmonic current (A)	Ninth order harmonic current (A)
Simulation results	3.72	1.96	0.53	0.23	0.16
Experimental results	3.41	1.92	0.45	0.20	0.12

Fig. 5.5 Simulated i_{sx} and its spectrum of phase *a* before and after HAPF compensation: **a** before compensation, **b** after compensation with $V_{dc1} = 45$ V ($L_{cn} = 0$), **c** after compensation with $V_{dc1} = 65$ V ($L_{cn} = 0$), **d** after compensation with $V_{dc1} = 90$ V ($L_{cn} = 0$) and **e** after compensation with $V_{dc1} = 45$ V ($L_{cn} = 5$ mH)

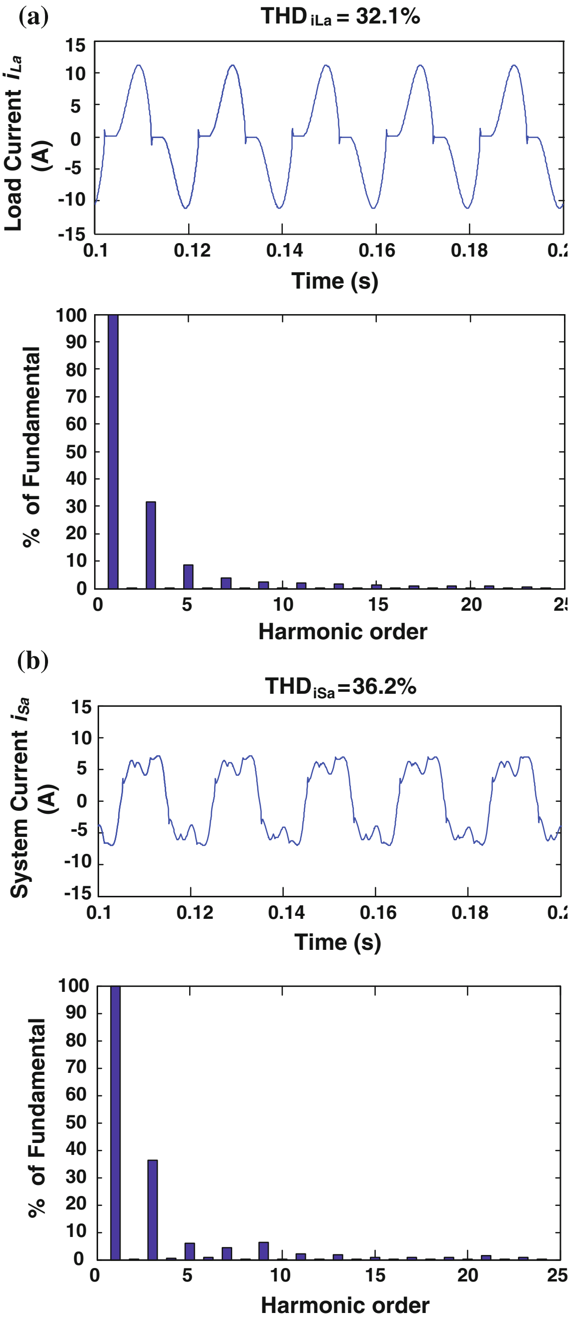

Fig. 5.5 continued

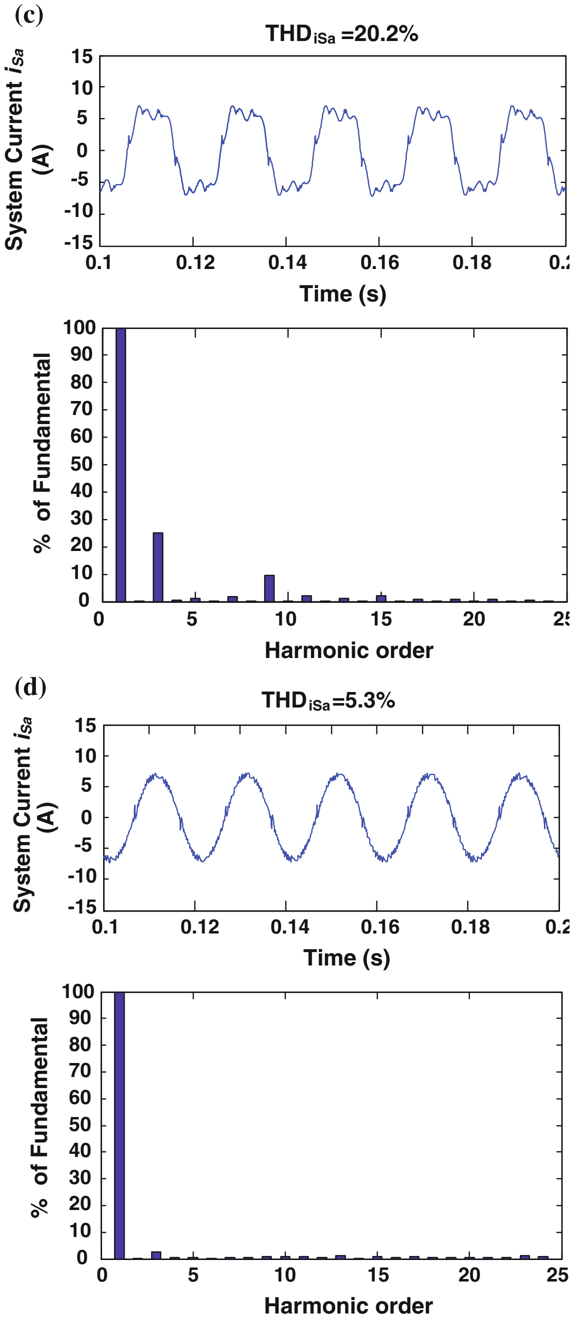

Fig. 5.5 continued

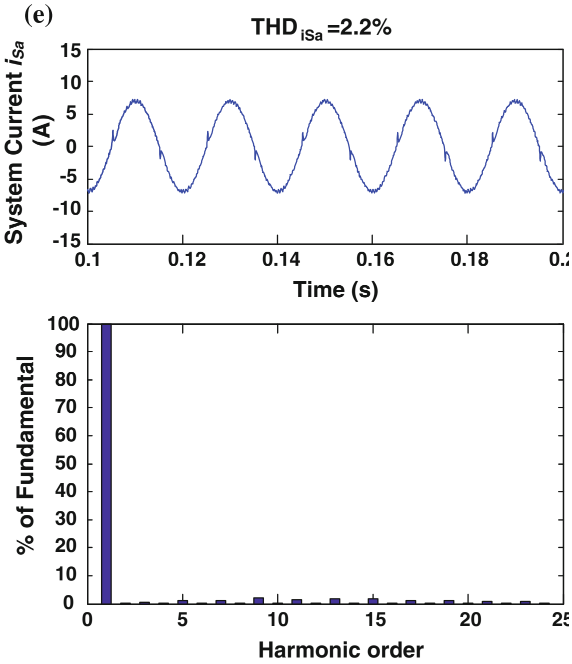

From Tables 5.5 and 5.6, when the HAPF is operating without L_{cn}, the coupling LC of the HAPF mainly eliminates the fifth order harmonic current. From Fig. 5.5b–e and Table 5.6, with the dc-link voltage of $V_{dc1} = 45$ V ($< V_{dc1\_NL} = 79.24$ V), the HAPF cannot perform current compensation effectively. After compensation, the THD of phase *a* system current is $THD_{i_{sx}} = 36.2\ \%$ and the system neutral current (i_{sn}) is 5.85 A, in which the compensated $THD_{i_{sx}}$ does not satisfy the international standards ($THD_{i_{sx}} < 20\ \%$ for IEEE, $THD_{i_{sx}} < 16\ \%$ for IEC) [14, 15]. When the dc-link voltage increases to $V_{dc1} = 65$ V, as this value is closer to the required $V_{dc1\_NL} = 79.24$ V, the HAPF can obtain better compensating performances with $THD_{i_{sx}} = 20.2\ \%$ and $i_{sn} = 3.60$ A, in which the compensated $THD_{i_{sx}}$still does not satisfy the international standards [14, 15]. When the dc-link voltage increases to $V_{dc1} = 90$ V, the HAPF

Table 5.5 Simulated and experimental required dc-link voltage of the HAPF without and with L_{cn}

	HAPF (mH)	V_{dc1xf_NL}, V_{dc1xf_L} (V)	V_{dc1x3_NL}, V_{dc1x3_L} (V)	V_{dc1x5_NL}, V_{dc1x5_L} (V)	V_{dc1x7_NL}, V_{dc1x7_L} (V)	V_{dc1x9_NL}, V_{dc1x9_L} (V)	V_{dc1_NL}, V_{dc1_L} (V)
Simulation results	$L_{cn} = 0$	10.56	37.92	0.13	2.77	3.52	79.24
	$L_{cn} = 5$	10.56	1.26	0.13	2.76	13.11	34.22
Experimental results	$L_{cn} = 0$	16.42	37.15	0.10	2.40	2.64	81.54
	$L_{cn} = 5$	16.42	1.24	0.10	2.40	9.83	38.66

Table 5.6 Summary of simulated and experimental results before and after HAPF compensation during balanced loading situation

HAPF		V_{dc1} (V)	3rd harmonic (%)	5th harmonic (%)	DPF	THD_{isx} (%)	i_{sn} (A)
Simulation results	Without comp.	–	31.5	8.6	0.80	32.1	5.35
	HAPF ($L_{cn} = 0$ mH)	45	36.2	6.1	1.00	36.2	5.85
		65	25.2	1.1	1.00	20.2	3.60
		90	2.7	0.6	1.00	5.3	0.86
	HAPF ($L_{cn} = 5$ mH)	45	0.5	1.0	1.00	2.2	0.34
Experimental results	Without comp.	–	31.4	7.3	0.83	32.7	5.77
	HAPF ($L_{cn} = 0$ mH)	45	23.8	3.2	1.00	25.3	3.51
		65	14.8	2.4	1.00	17.2	2.45
		90	6.3	1.1	1.00	8.0	1.30
	HAPF ($L_{cn} = 5$mH)	45	2.4	1.5	1.00	5.6	0.74

can effectively track the reference compensating current and achieve the best compensation performances with $THD_{i_{sx}} = 5.3\ \%$ and $i_{sn} = 0.86$ A among the three cases. From Tables 5.5 and 5.6, when the HAPF is operating with L_{cn}, the coupling LC together with L_{cn} already eliminates the two dominant third and fifth orders harmonic current. Therefore, the dc-link voltage of $V_{dc1} = 45$ V ($>V_{dc1\_L} = 34.22$ V) is already sufficient for the HAPF to obtain very good compensating performances with $THD_{i_{sx}} = 2.2\ \%$ and $i_{sn} = 0.34$ A, as verified by Fig. 5.5e and Table 5.6, in which the compensated $THD_{i_{sx}}$ satisfies the international standards [14, 15].

5.4.2 Experimental Results

Figure 5.6a illustrates the experimental i_{Lx} waveform and its spectrum of phase *a*, in which its corresponding fundamental reactive current, third, fifth, seventh, and ninth order harmonic current in RMS values of the loading are shown in Table 5.4. From Fig. 5.6a and Table 5.6, the $THD_{i_{Lx}}$ is 32.7 % and the i_{Ln} is 5.77A, in which the 3rd (3*k*th) and 5th (3*k* ± 1th) orders harmonic contents dominate the load harmonic current. With the help of Tables 5.1, 5.5 shows the required V_{dc1xf_NL}, V_{dc1xn_NL}, V_{dc1xf_L}, V_{dc1xn_L} and V_{dc1_NL}, V_{dc1_L} of the HAPF without and with L_{cn}, in which $V_{dc1\_NL} = 81.54$ V and $V_{dc1\_L} = 38.66$ V respectively. Similar as simulation part, the dc-link voltage for the HAPF is chosen as $V_{dc1} = 45$ V, 65 V, 90 V three levels for performing compensation respectively. After compensation by the HAPF without and with L_{cn}, Fig. 5.6b–e show the experimental i_{sx} waveforms and their spectra of phase *a* at different dc-link voltage levels. Moreover, their corresponding experimental results are summarized in Table 5.6.

From Tables 5.5 and 5.6, when the HAPF is operating without L_{cn}, the coupling LC of the HAPF mainly eliminates the fifth order harmonic current. From

Fig. 5.6 Experimental i_{sx} and its spectrum of phase *a* before and after HAPF compensation: **a** before compensation, **b** after compensation with $V_{dc1} = 45$ V ($L_{cn} = 0$), **c** after compensation with $V_{dc1} = 65$ V ($L_{cn} = 0$), **d** after compensation with $V_{dc1} = 90$ V ($L_{cn} = 0$) and **e** after compensation with $V_{dc1} = 45$ V ($L_{cn} = 5$ mH)

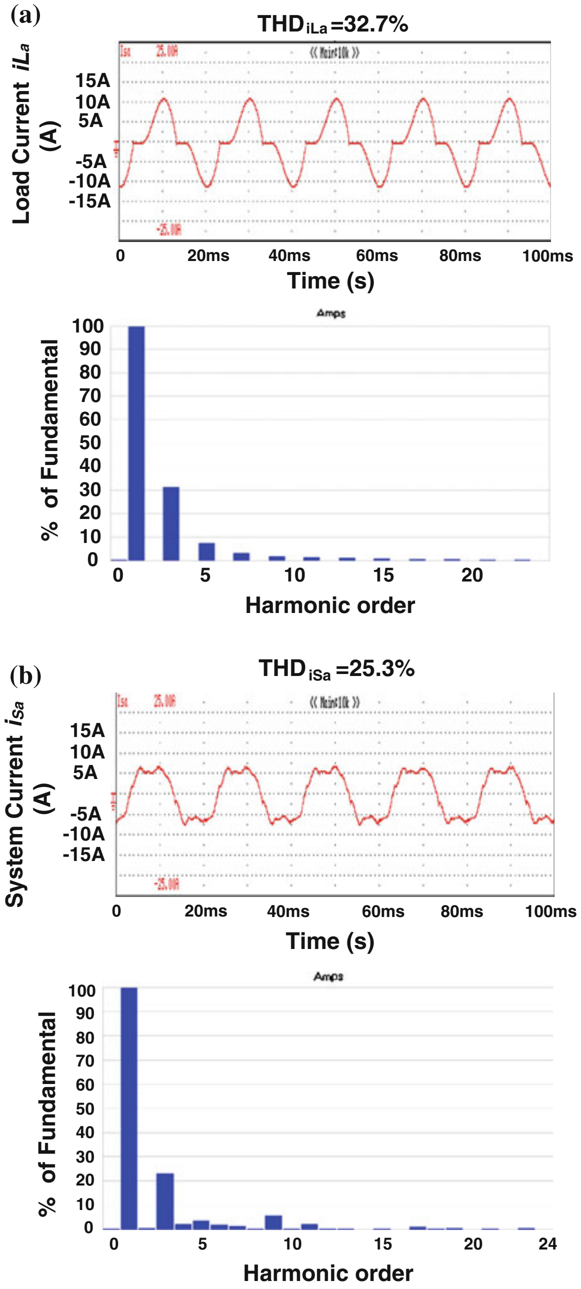

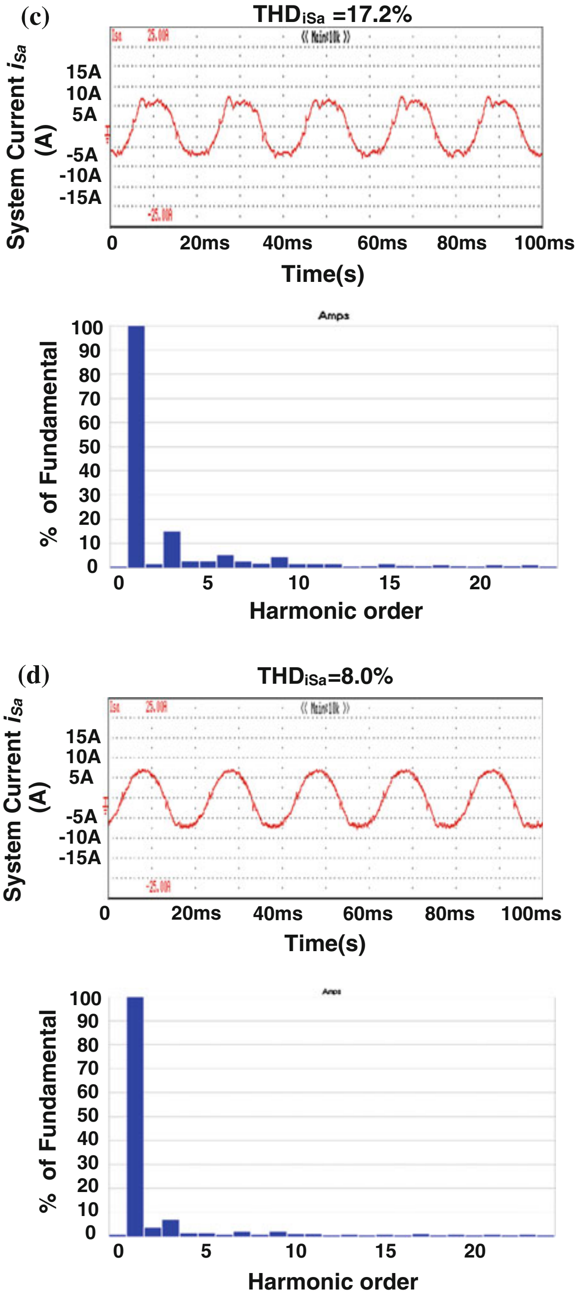

Fig. 5.6 continued

Fig. 5.6 continued

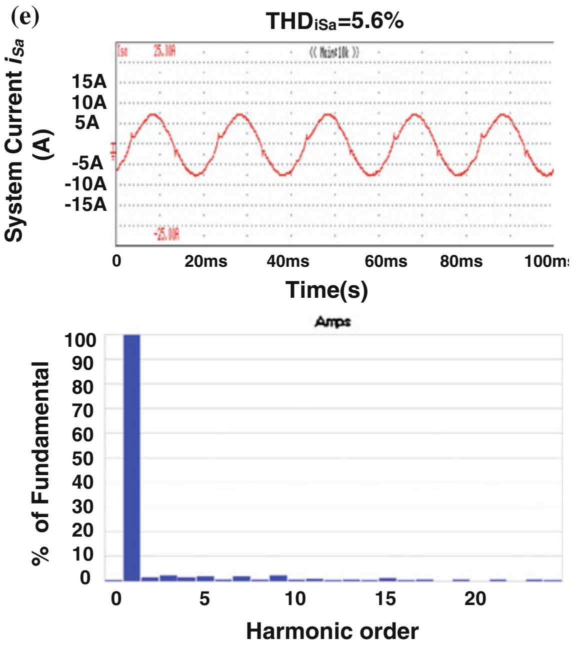

Fig. 5.6b–e, with $V_{dc1} = 45$ V ($<V_{dc1\_NL} = 81.54$ V), the HAPF cannot perform current compensation effectively. After compensation, the $THD_{i_{sx}}$ of phase a is 25.3 % and the i_{sn} is 3.51 A, in which the compensated $THD_{i_{sx}}$ does not satisfy the international standards [14, 15]. When the dc-link voltage increases to $V_{dc1} = 65$ V, as this value is closer to the required $V_{dc1\_NL} = 81.54$ V, the HAPF can obtain better compensating performances with $THD_{i_{sx}} = 17.2\ \%$ and $i_{sn} = 2.45$ A, in which the compensated $THD_{i_{sx}}$ still does not satisfy the international standards [14, 15]. When the dc-link voltage increases to $V_{dc1} = 90$ V, the HAPF can achieve the best compensation performances with $THD_{i_{sx}} = 8.0\ \%$ and $i_{sn} = 1.30$ A among the three cases. From Tables 5.5 and 5.6, when the HAPF is operating with L_{cn}, the coupling LC together with L_{cn} already eliminates the two dominant third and fifth orders harmonic current. Therefore, the dc-link voltage of $V_{dc1} = 45$ V ($>V_{dc1\_L} = 38.66$ V) is already sufficient to obtain very good compensating performances with $THD_{i_{sx}} = 5.6\ \%$ and $i_{sn} = 0.74$ A, as verified by Fig. 5.6e and Table 5.6, in which the compensated $THD_{i_{sx}}$ satisfies the international standards [14, 15].

Figures 5.7–5.8 show the HAPF simulated and experimental compensating current i_{cx} waveforms and their spectra of phase a with $V_{dc1} = 90$ V (without L_{cn}) and $V_{dc1} = 45$ V (with $L_{cn} = 5$ mH). As the i_{ca} harmonic contents above 15th harmonic order (switching noise) shows a significant reduction by adding a L_{cn}, thus the HAPF with L_{cn} can effectively reduce the switching noise and also improve the compensation performances as verified by Table 5.6, in comparison

Fig. 5.7 Simulated i_{cx} waveform and its spectrum of phase a: **a** $V_{dc1} = 90$ V ($L_{cn} = 0$) and **b** $V_{dc1} = 45$ V ($L_{cn} = 5$ mH)

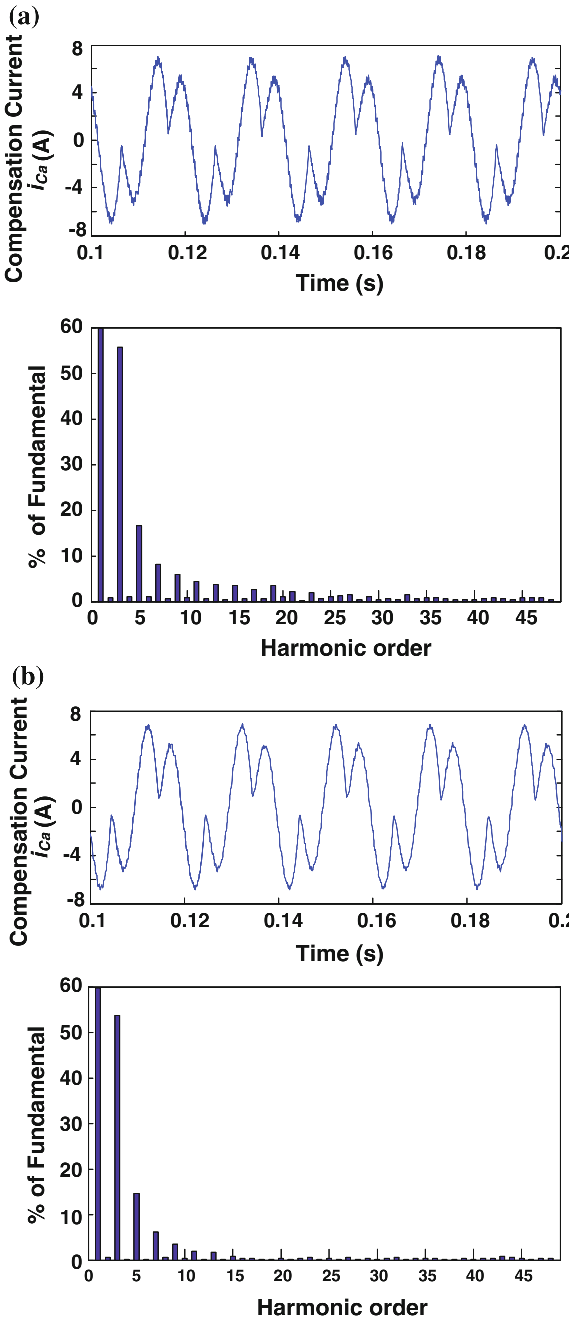

Fig. 5.8 Experimental i_{cx} waveform and its spectrum of phase a: **a** $V_{dc1} = 90$ V ($L_{cn} = 0$) and **b** $V_{dc1} = 45$ V ($L_{cn} = 5$ mH)

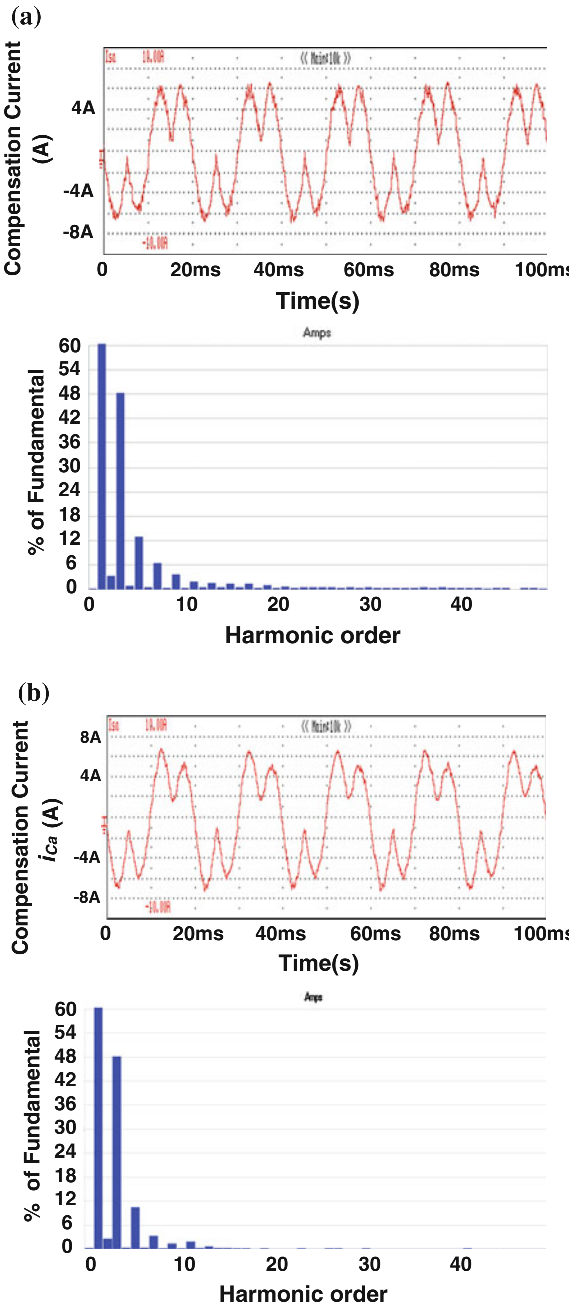

with the conventional HAPF without L_{cn}, because it just requires a lower dc-link voltage requirement for performing compensation.

Without L_{cn} case, if the coupling L_{c1} and C_{c1} are tuned at third order harmonic frequency instead of fifth order, the dc-link voltage reduction with L_{cn} may not be so significant. Unfortunately, by tuning L_{c1} and C_{c1} at third order harmonic frequency, it will significantly increase the initial cost and size of the HAPF, because the required three coupling L_{c1} will be increased from 8 to 22.5 mH, compared with the coupling L_{c1} and C_{c1} tuned at fifth order with a L_{cn} of 5 mH only.

If $3k$th order load harmonic current exists, by concerning about: (i) initial costs of both the coupling part (L_{c1} and C_{c1}) and inverter part (dc-link voltage) and (ii) switching loss and switching noise, it is cost effective for the coupling LC of the HAPF with coupling neutral inductor to be tuned at one dominant $3k$th and one dominant $3k \pm 1$th order harmonic currents ($3k\text{th} < 3k \pm 1\text{th}$).

5.5 Summary

This chapter aims to investigate the minimum inverter capacity design for three-phase four-wire center-split HAPF in reactive power and current harmonics compensation. First, the equivalent circuit models of three-phase four-wire center-split HAPF in d-q-0 coordinate are built and proposed. Based on the circuit models, the filtering performance of the HAPF can be improved by adding a tuned coupling neutral inductor. After that, the minimum dc-link voltage expressions for the HAPF without and with coupling neutral inductor are also deduced. According to the current quality of the loading and the minimum dc-link voltage expressions, the dc-link voltage reduction analysis for the HAPF with coupling neutral inductor can be mathematically obtained. Thus, the initial cost, switching loss, and switching noise of the HAPF can be lowered by the additional neutral inductor. Finally, simulation and experimental results of the three-phase four-wire center-split HAPF with coupling neutral inductor are presented to verify its filtering characteristics and the deduced minimum dc-link voltage expressions, to show the effectiveness of reducing its dc-link voltage requirement (inverter capacity), switching loss, switching noise, and improving the system performances in reactive power and current harmonics compensation compared with the conventional HAPF without coupling neutral inductor.

References

1. J.S. Subjek, J.S. Mcquilkin, Harmonics-causes, effects, measurements and analysis. IEEE Trans. Ind. Electron. **26**(6), 1034–1042 (1990)
2. L.H.S. Duarte, M.F. Alves, The degradation of power capacitors under the influence of harmonics, in *Proceedings IEEE 10*th *International Conference on Harmonics and Quality of Power*, vol. 1 (2002), pp. 334–339

3. T.Q. Tran, L.E. Conrad, B.K. Stallman, Electric shock and elevated EMF levels due to triplen harmonics. IEEE Trans. Power Del. **11**(2), 1041–1049 (1996)
4. H. Akagi, S. Srianthumrong, Y. Tamai, Comparisons in circuit configuration and filtering performance between hybrid and pure shunt active filters, in *Conference Record IEEE-IAS Annual Meeting,* vol. 2 (2003), pp. 1195–1202
5. S. Srianthumrong, H. Akagi, A medium-voltage transformerless AC/DC Power conversion system consisting of a diode rectifier and a shunt hybrid filter. IEEE Trans. Ind. Applicat. **39**(3), 874–882 (2003)
6. W. Tangtheerajaroonwong, T. Hatada, K. Wada, H. Akagi, Design and performance of a transformerless shunt hybrid filter integrated into a three-phase diode rectifier. IEEE Trans. Power Electron. **22**(5), 1882–1889 (2007)
7. R. Inzunza, H. Akagi, A 6.6 kV transformerless shunt hybrid active filter for installation on a power distribution system. IEEE Trans. Power Electron. **20**(4), 893–900 (2005)
8. V.-F. Corasaniti, M.-B. Barbieri, P.-L. Arnera, M.-I. Valla, Hybrid power filter to enhance power quality in a medium voltage distribution. IEEE Trans. Ind. Electron. **56**(8), 2885–2893 (2009)
9. J.I. Rodriguez, A. Candela, L. Luna, R. Asiminoaei, R. Teodorescu, F. Blaabjerg, Current harmonics cancellation in three-phase four-wire systems by using a four-branch star filtering topology. IEEE Trans. Power Electron. **24**(8), 1939–1950 (2009)
10. C.-S. Lam, M.-C. Wong, Y.-D. Han, Voltage swell and overvoltage compensation with unidirectional power flow controlled dynamic voltage restorer. IEEE Trans. Power Del. **23**(4), 2513–2521 (2008)
11. S. Hiti, D. Boroyevich, C. Cuadros, Small-signal modeling and control of three-phase PWM conver1ters, in *Conference Record of the Industry Applications Society Annual Meeting*, vol. 2 (1994), pp. 1143–1150
12. R. Zhang High performance power converter systems for nonlinear and unbalanced load/source", Ph.D. thesis, Virginia Polytechnic Institute and State University, 1998
13. M.-C. Wong, J. Tang, Y.-D. Han, Cylindrical coordinate control of three-dimensional PWM technique in three-phase four-wired trilevel inverter. IEEE Trans. Power Electron. **18**(1), 208–220 (2003)
14. *IEEE Recommended Practice on Monitoring Electric Power Quality*, 1995, IEEE Standard 1159:1995
15. *Electromagnetic Compatibility (EMC), Part 3: Limits, Section 2: Limits for Harmonics Current Emissions (Equipment Input Current $\leq$ 16A Per Phase)*, IEC Standard 61000-3-2, 1997

Chapter 6
Design and Performance of A 220 V 10 kVA Adaptive Low DC-Link Voltage Controlled HAPF with a Coupling Neutral Inductor Experimental System

Abstract This chapter presents the design and performance of a 220 V, 10 kVA adaptive low dc-link voltage-controlled hybrid active power filter (HAPF) with a coupling neutral inductor experimental system, which can compensate both dynamic reactive power and current harmonics in the three-phase four-wire distribution power systems. Owning to its adaptive low dc-link voltage characteristic, it can obtain the least switching loss and switching noise and the best compensating performances, compared with the conventional fixed and newly adaptive dc-link voltage-controlled HAPFs. Initially, the design procedures of the adaptive dc-link voltage controller are discussed, so that the proportional and integral (PI) gains can be designed accordingly. Then the design of the passive power filter (PPF) and active power filter (APF) parts are introduced in details. And the general design procedures for the adaptive dc voltage-controlled HAPF with neutral inductor are also given. Finally, the validity and effectiveness of the 220 V, 10 kVA adaptive dc-link voltage-controlled HAPF with neutral inductor experimental system are confirmed by experimental results compared with the conventional fixed and adaptive dc-link voltage-controlled HAPFs without neutral inductor.

Keywords 220 V · 10 kVA · Three-Phase Four-Wire Center-Split HAPF · Adaptive DC-Link Voltage Control · Coupling Neutral Inductor · Current Harmonics · Digital Signal Processor · IGBT · Reactive Power · Signal Conditioning Board

6.1 Introduction

The linear operation requirements of hysteresis PWM control for a three-phase four-wire HAPF have been investigated and discussed in Chap. 3. To reduce the switching loss and switching noise without adding-in the soft-switching circuit and implement the dynamic reactive power compensation capability, an adaptive dc-link voltage control technique for HAPF in reactive power compensation has been proposed in Chap. 4. In Chap. 5, by adding a small tuned coupling neutral inductor

C.-S. Lam and M.-C. Wong, *Design and Control of Hybrid Active Power Filters*,
SpringerBriefs in Electrical and Computer Engineering,
DOI: 10.1007/978-3-642-41323-0_6, © The Author(s) 2014

to the HAPF, its minimum dc-link voltage requirement can be further reduced, thus further reducing its switching loss, switching noise, and improving the system compensating performances. However, (i) the adaptive dc control technique proposed in Chap. 4 did not include current harmonics consideration, (ii) the HAPF with neutral inductor discussed in Chap. 5 is operating at a fixed dc-link voltage and its adaptive dc voltage control algorithm is still absent, and (iii) the important proportional and integral (PI) gains design procedures for the adaptive dc-link voltage controller including stability study and dynamic performance analysis have not been considered and analyzed in the previous chapters.

In this chapter, the adaptive dc-link voltage controller for the HAPF with coupling neutral inductor in both reactive power and current harmonics compensation will be first proposed and described. And the PI gains design procedures for the controller are also included. Then the system configuration, the design of the PPF part and APF part of the 220 V, 10 kVA HAPF experimental system will be introduced. And the general design procedures for the adaptive dc voltage-controlled HAPF with neutral inductor are also given. Finally, a 220 V, 10 kVA adaptive low dc-link voltage-controlled HAPF with neutral inductor laboratory prototype is tested, representative experimental results are given in comparison with the conventional fixed and adaptive dc-link voltage-controlled HAPFs without neutral inductor. Given that most of the loads in the distribution power systems are inductive, the following analysis and discussion will only focus on inductive loads [1].

6.2 Adaptive DC-Link Voltage Controller for A HAPF without and with L_{cn}

The switching loss of the switching device can be classified as turn-on and turn-off losses. Equation (6.1) is the total turn-on and turn-off power loss [2], where V_{dc}, I_{CM}, I_{CN}, t_{rN}, t_{fN}, and f_{sw} are the dc-link voltage, maximum collector current, rated collector current, rated rise time, rated fall time, and switching frequency. Thus, the higher the dc-link voltage of the HAPF, the higher the switching loss obtained, and vice versa.

$$P_{Loss} = V_{dc}\, I_{CM} f_{sw} \left(\frac{1}{8} t_{rN} \frac{I_{CM}^2}{I_{CN}} + t_{fN} \left(\frac{1}{3\pi} + \frac{1}{24} \frac{I_{CM}}{I_{CN}} \right) \right) \tag{6.1}$$

In addition, the current tracking speed of the HAPF is directly proportional to the voltage difference between its dc-link voltage and load voltage, and inversely proportional to its coupling LC impedance. For each reference compensating current, there is an optimum dc voltage to get balance between the performances and suppressing switching noise [3]. If the minimum dc-link voltage is found, it can optimize the HAPF performances, switching loss and switching noise.

Table 6.1 Minimum dc-Link voltage deduction steps of the three-phase four-wire HAPF without and with L_{cn}

(1) Fundamental Frequency	Minimum dc-link voltage without and with L_{cn} for compensating reactive power: $V_{dc1xf\_NL} = V_{dc1xf\_L} = \sqrt{2}\,V_{inv1xf\_NL} = \sqrt{2}\,V_{inv1xf\_L}$ $= \sqrt{2}\,V_x \left\lvert 1 - \frac{Q_{Lx_f}}{\lvert Q_{cx_{f\_PPF}}\rvert} \right\rvert$ (6.2) where Q_{Lxf} is loading fundamental reactive power, Q_{cxf_PPF} is the reactive power provided by coupling *LC*.
(2) Harmonic Frequencies	Minimum dc-link voltage without and with L_{cn} for compensating each *nth* order current harmonic: $V_{dc1xn\_\mathrm{NL}} =$ $\sqrt{2}V_{inv1xn\_\mathrm{NL}} = \sqrt{2}\left\lvert n\omega L_{c1} - \frac{1}{n\omega C_{c1}} \right\rvert \lvert I_{cxn}\rvert$ (6.3) $V_{dc1xn\_L} = \sqrt{2}V_{inv1xn\_L} =$ $\begin{cases} \sqrt{2}V_{inv1x3k\pm1\_L} = \sqrt{2}\left\lvert (3k\pm1)\omega L_{c1} - \frac{1}{(3k\pm1)\omega C_{c1}} \right\rvert \lvert I_{cx3k\pm1}\rvert \\ \sqrt{2}V_{inv1x3k\_L} = \sqrt{2}\left\lvert 3k\omega(L_{c1}+3L_{cn}) - \frac{1}{3k\omega C_{c1}} \right\rvert \lvert I_{cx3k}\rvert \end{cases}$ (6.4) where $\lvert I_{cxn}\rvert = \lvert I_{Lxn}\rvert$, *n*th = 3 *k* ± 1th or *3kth*, $k = 1, 2\ldots\infty$, $n = 2, 3\ldots\infty$, $\omega = 2\pi f$
(3) All Frequencies	Minimum dc-link voltage without and with L_{cn}: $V_{dc1\_NL} = V_{dc1\_\min} = \max(2V_{dc1a\_\mathrm{NL}}, 2V_{dc1b\_\mathrm{NL}}, 2V_{dc1c\_\mathrm{NL}})$ (6.5) where $V_{dc1x\_\mathrm{NL}} = \sqrt{\lvert V_{dc1xf\_\mathrm{NL}}\rvert^2 + \sum_{n=2}^{\infty} \lvert V_{dc1xn\_\mathrm{NL}}\rvert^2}$ (6.6) $V_{dc1\_L} = V_{dc1\_\min} = \max(2V_{dca\_L}, 2V_{dcb\_L}, 2V_{dcc\_L})$ (6.7) where $V_{dc1x\_L} = \sqrt{\lvert V_{dc1xf\_L}\rvert^2 + \sum_{n=2}^{\infty} \lvert V_{dc1xn\_L}\rvert^2}$ (6.8) where $n = 2, 3\ldots\infty$

From Chap. 4 and Chap. 5, the required minimum dc-link voltage for compensating reactive power (V_{dc1xf_NL}, V_{dc1xf_L}) and each *nth* current harmonic order (V_{dc1xn_NL}, V_{dc1xn_L}) without and with L_{cn} case can be summarized by (6.2–6.4) as shown in Table 6.1. Then the minimum dc-link voltage requirements (V_{dc1x_NL}, V_{dc1x_L}) for the HAPF single-phase equivalent circuit models can be obtained by (6.6) and (6.8) in Table 6.1. To compensate both the reactive power and current harmonics of the loading, the final minimum dc-link voltage for the three-phase four-wire HAPF without and with L_{cn} (V_{dc1_NL}, V_{dc1_L}) will be the maximum one among the calculated minimum value of each phase indicated by (6.5) and (6.7) in Table 6.1. Therefore, the calculated dc-link voltage must be sufficient for all three phases. Based on the results in Table 6.1, the adaptive dc-link voltage controller for the three-phase four-wire HAPF without and with L_{cn} will be proposed in the following.

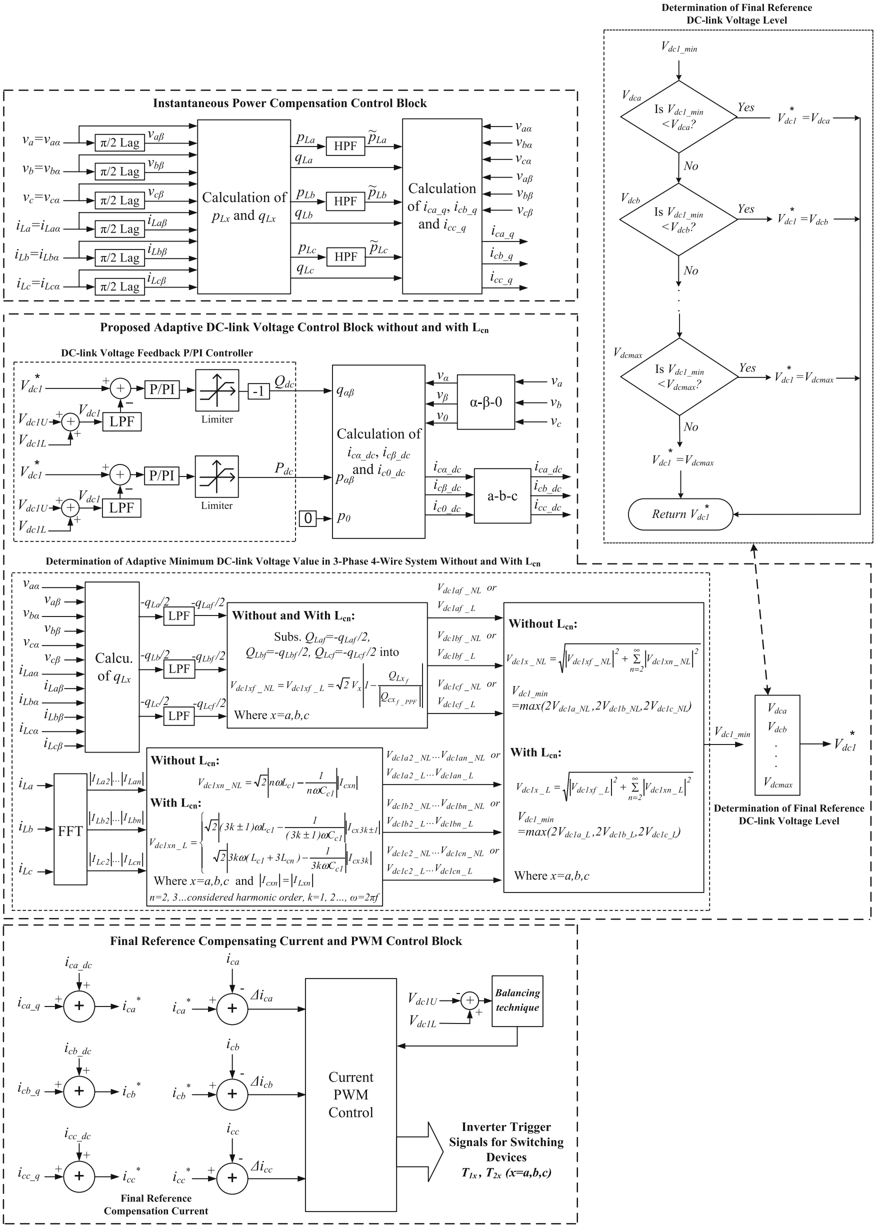

Fig. 6.1 Proposed adaptive dc-link voltage control block diagram for the three-phase four-wire HAPF without and with L_{cn} for reactive power and current harmonics compensation

Figure 6.1 shows the adaptive dc-link voltage control block diagram for the three-phase four-wire HAPF without and with L_{cn} for reactive power and current harmonics compensation, in which it consists of three main control blocks: instantaneous power compensation control block, proposed adaptive dc-link voltage control block, and final reference compensating current and PWM control block.

6.2.1 Instantaneous Power Compensation Control Block

For the instantaneous power compensation control block, the reference reactive and harmonic compensating currents for HAPF (i_{cx_q}, the subscript $x = a, b, c$ for three phases) are determined by the single-phase instantaneous *pq* theory as discussed in Appendix A.2.

6.2.2 Proposed Adaptive DC-Link Voltage Control Block

The adaptive dc-link voltage control block consists of three parts: (1) determination of adaptive minimum dc-link voltage V_{dc1_min}, (2) determination of final reference dc-link voltage level V^*_{dc1}, and (3) dc-link voltage feedback P/PI controller.

(1) *Determination of Adaptive Minimum DC-Link Voltage*: The loading instantaneous fundamental reactive power in each phase q_{Lxf} is calculated by using single-phase instantaneous *pq* theory as discussed in Appendix A.2 and low-pass filters. Usually, $-q_{Lxf}/2$ can keep as a constant value for more than one cycle, thus loading fundamental reactive power consumption Q_{Lxf} in each phase can be approximately treated as $Q_{Lxf} \approx -q_{Lxf}/2$. Then the required minimum dc-link voltage for compensating each phase Q_{Lxf} can be calculated by using (6.2). With the help of FFT, the load current spectra $|I_{Lxn}|$ up to the considered current harmonic order n can be calculated, the required minimum dc-link voltage for compensating each *nth* order current harmonic can be calculated by using (6.3) and (6.4). With the help of (6.6) and (6.8), the adaptive minimum dc-link voltage V_{dc1_min} for the three-phase four-wire HAPF without and with L_{cn} can be determined by (6.5) and (6.7) accordingly. To implement the adaptive dc voltage control function for the HAPF, V_{dc1_min} can be simply treated as the final reference dc voltage V^*_{dc1}. It is obvious that when the loading is changing, the system adaptively yields different V_{dc1_min} value.

(2) *Determination of Final Reference DC-Link Voltage Level*: However, this adaptive control scheme may frequently change the dc voltage reference V^*_{dc1} in practical situation, as the loading is randomly determined by electric users (different Q_{Lxf} and I_{Lxn}). Then this frequent change would cause a rapid dc voltage fluctuation, resulting in deterioration of the HAPF operating performances. To alleviate this problem, a final reference dc-link voltage level determination process proposed in Chap. 4 is added, so that V^*_{dc1} can be

maintained as a constant value within a specific compensation range. If V_{dc1_min} is greater than the maximum level V_{dcmax}, $V^*_{dc1} = V_{dcmax}$.

(3) *DC-Link Voltage Feedback P/PI Controller*: The HAPF can effectively control the adaptive dc-link voltage level by feedback the dc voltage-controlled signal as both reactive and active current reference components (Q_{dc}, P_{dc}) [4]:

$$Q_{dc} = -K_q \cdot (V^*_{dc_1} - V_{dc_1}) - K_I \int (V^*_{dc_1} - V_{dc_1})\,dt \tag{6.9}$$

$$P_{dc} = K_p \cdot (V^*_{dc_1} - V_{dc_1}) + K_{II} \int (V^*_{dc_1} - V_{dc_1})\,dt \tag{6.10}$$

where Q_{dc} aims to change the dc-link voltage level due to adaptive dc control and start-up dc-link self-charging function, while P_{dc} aims to maintain the dc-link voltage due to the system loss. K_q and K_p are the proportional gains, while K_I and K_{II} are the integral gains of the controllers. With the help of the three-phase instantaneous *pq* theory as discussed in Appendix A.1 and Q_{dc} and P_{dc} terms, the dc-link voltage V_{dc1} can track its reference V^*_{dc1} by changing the three-phase dc voltage control reference compensating currents i_{cx_dc} in *a*-*b*-*c* coordinates, in which the calculation details are discussed in both [4] and Sect. 4.4.2. In the following, the design process for K_q, K_p, K_I , and K_{II} will be discussed.

Figure 6.2 shows the dc-link voltage control block diagram during adaptive dc control and start-up dc-link self-charging function, and Fig. 6.3 shows the dc-link voltage control block diagram during compensating system loss, where $V_{inv1xfp} = |V_x - |I_{cxfq}|\ |X_{PPFf}||$ and $V_{inv1xfq} = |I_{cxfp}||X_{PPFf}|$ are the inverter fundamental active and reactive voltages, I_{cxfp} and I_{cxfq} are the fundamental compensating active and reactive currents.

When PI controller is applied, from Figs. 6.2 and 6.3, their close-loop transfer functions can be expressed as:

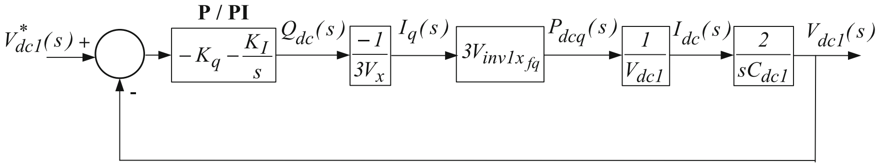

Fig. 6.2 Block diagram of dc-link voltage control during adaptive dc voltage control and start-up dc-link self-charging function

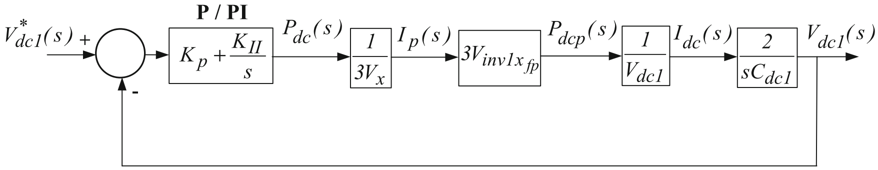

Fig. 6.3 Block diagram of dc-link voltage control during compensating system loss

Fig. 6.4 Stability and dynamic response of dc-link voltage controller in Fig. 6.2 when $K_I = 50$ and K_q varies from 5 to 50: **a** bode diagram and **b** step response

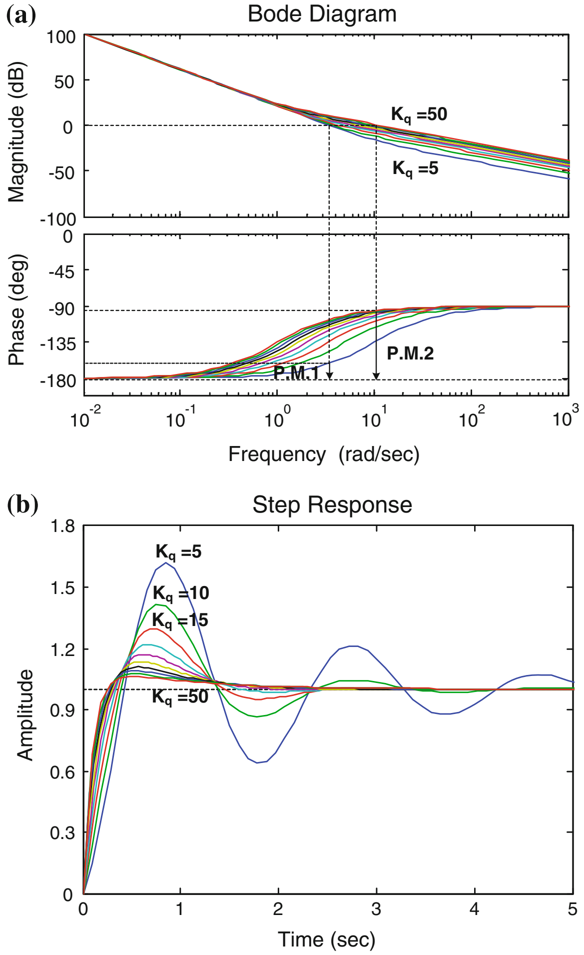

$$\frac{V_{dc1}(s)}{V_{dc1}^{*}(s)} = \frac{\dfrac{2V_{inv1xfq}K_q}{V_x V_{dc1} C_{dc1}} s + \dfrac{2V_{inv1xfq}K_I}{V_x V_{dc1} C_{dc1}}}{s^2 + \dfrac{2V_{inv1xfq}K_q}{V_x V_{dc1} C_{dc1}} s + \dfrac{2V_{inv1xfq}K_I}{V_x V_{dc1} C_{dc1}}} \tag{6.11}$$

$$\frac{V_{dc1}(s)}{V_{dc1}^{*}(s)} = \frac{\dfrac{2V_{inv1xfp}K_p}{V_x V_{dc1} C_{dc1}} s + \dfrac{2V_{inv1xfp}K_{II}}{V_x V_{dc1} C_{dc1}}}{s^2 + \dfrac{2V_{inv1xfp}K_p}{V_x V_{dc1} C_{dc1}} s + \dfrac{2V_{inv1xfp}K_{II}}{V_x V_{dc1} C_{dc1}}} \tag{6.12}$$

By ROUTH-HURWITZ criterion, the Routh tables for (6.11) and (6.12) can be obtained. As K_q, K_p, K_I , and $K_{II} > 0$, the dc-link voltage controllers will be stable. From the HAPF experimental system parameters in Table 6.5, $C_{c1} = 50$ μF,

Fig. 6.5 Stability and dynamic response of dc-link voltage controller in Fig. 6.3 when $K_{II} = 50$ and K_p varies from 5 to 50: **a** bode diagram and **b** step response

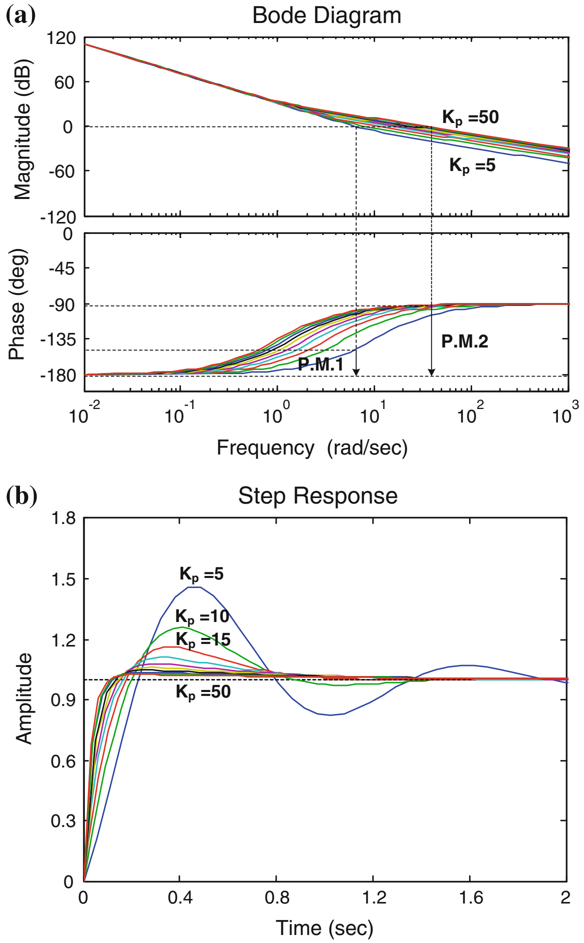

$L_{c1} = 8$ mH, $C_{dc1} = 3.3$ mF, and $V_x = 220$ V. For the dc-link maximum operating voltage is $V_{dc1} = 150$ V, fundamental compensating active and reactive currents are $|I_{cxfp}| = 0.2$ A and $|I_{cxfq}| = 4.2$ A, when $K_I = K_{II} = 50$, the effect of K_q and K_p to the controller's stability and dynamic response are shown in Figs. 6.4 and 6.5. From Figs. 6.4 and 6.5, when K_q and K_p are varying from 5 to 50, their phase margins (P.M.) are increasing from P.M.1 to P.M.2, which enhance the controllers' stability. Moreover, a larger K_q and K_p value will yield a faster dynamic response for the controllers.

When only P controller is applied, that is $K_I = K_{II} = 0$ in Figs. 6.2 and 6.3, their close-loop transfer functions can be deduced from (6.11) and (6.12). By Routh tables, as K_q and $K_p > 0$, the dc-link voltage controllers will be stable. If the proportional gains K_q and K_p are set too large, they produce a large fluctuation during steady-state. On the contrary, if they are set too small, a long settling time

Fig. 6.6 Stability and dynamic response of dc-link voltage controller in Fig. 6.2 when K_q varies from 5 to 50: **a** bode diagram and **b** step response

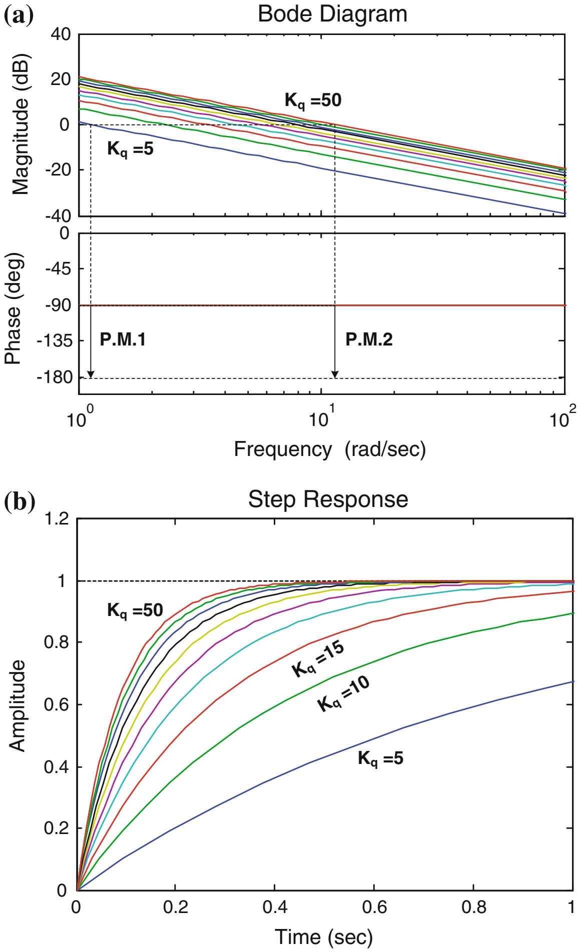

and a large steady-state error will occur. In addition, the effect of K_q and K_p to the controllers' stability and dynamic response are shown in Figs. 6.6 and 6.7. From Figs. 6.6 and 6.7, when K_q and K_p are varying from 5 to 50, their phase margins (P.M.1 and P.M.2) do not change at all, and the controllers obtain good stability. And a larger K_q and K_p value will yield a faster dynamic response.

To simplify the control process, Q_{dc} and P_{dc} in (6.9) and (6.10) can be calculated by the same controller, i.e., $K_q = K_p$, and $K_I = K_{II}$. Even though the P controller yields a steady-state error, it is chosen in this work because of its simplicity and memory resource saving in the DSP, therefore it can yield a faster response than the PI controller, as verified by Figs. 6.4b, 6.5b, 6.6b, and 6.7b. And $K_q = K_p = 40$ is selected. If the dc-link voltage with zero steady-state error is taken into consideration, PI controller is appreciated, $K_q = K_p = 40$ and $K_I = K_{II} = 50$ can be chosen. A limiter is also applied to avoid the overflow problem of the controllers.

Fig. 6.7 Stability and response dynamic of dc-link voltage controller in Fig. 6.3 when K_p varies from 5 to 50: **a** bode diagram and **b** step response

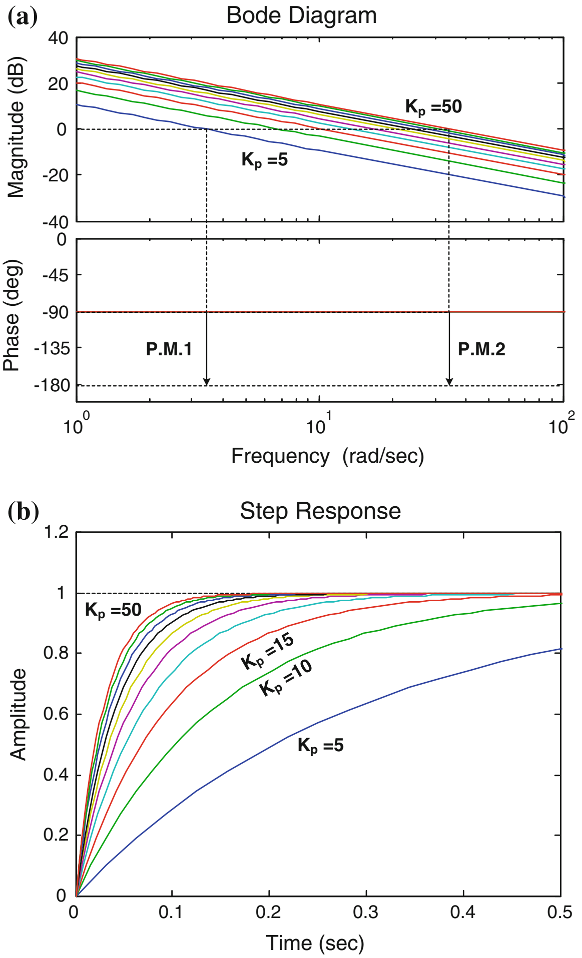

6.2.3 Final Reference Compensating Current and PWM Control Block

Both the hysteresis PWM and triangular carrier-based sinusoidal PWM method can be applied for the PWM control part. After the process of instantaneous power compensation and adaptive dc-link voltage control blocks as shown in Fig. 6.1, the final reference compensating current i_{cx}^{*} can be obtained by summing up the i_{cx_q} and i_{cx_dc}. Then the final reference and actual compensating currents i_{cx}^{*} and i_{cx} will be sent to the PWM control part, and the PWM trigger signals for the switching devices can then be generated. If the three-phase loadings are unbalanced, the dc capacitor voltage imbalance may occur, the dc capacitor voltage balancing concepts and techniques in [5] can be applied to balance the V_{dc1U} and V_{dc1L} under the adaptive dc voltage control method.

In the following, the system configuration, the parameters design of the PPF and APF parts of the 220 V, 10 kVA three-phase four-wire center-split HAPF experimental system will be introduced in details.

6.3 A 220 V 10kVA Three-Phase Four-Wire Center-Split HAPF Experimental Prototype

6.3.1 System Configuration of Three-Phase Four-Wire Center-Split HAPF

The experimental prototype of the 220 V, 10 kVA three-phase four-wire center-split HAPF has been developed and built. The system configuration of the three-phase four-wire HAPF experimental prototype is shown in Fig. 6.8, where the subscript '*x*' denotes phase *a*, *b*, *c*, and *n*. v_x is the load voltage, i_{sx}, i_{Lx}, and i_{cx} are the system, load, and inverter current for each phase. C_{c1} and L_{c1} are the coupling capacitor and inductor, L_{cn} is the coupling neutral inductor. C_{dc1}, V_{dc1U}, and V_{dc1L} are the dc capacitor, upper, and lower dc capacitor voltages with $V_{dc1U} = V_{dc1L} = 0.5\ V_{dc1}$. S_{source}, S_{HAPF}, S_{APF}, S_{PPF}, S_R, and $S_{\text{discharge}}$ are controllable switches for controlling different parts of the circuit. VTSC and CTSC

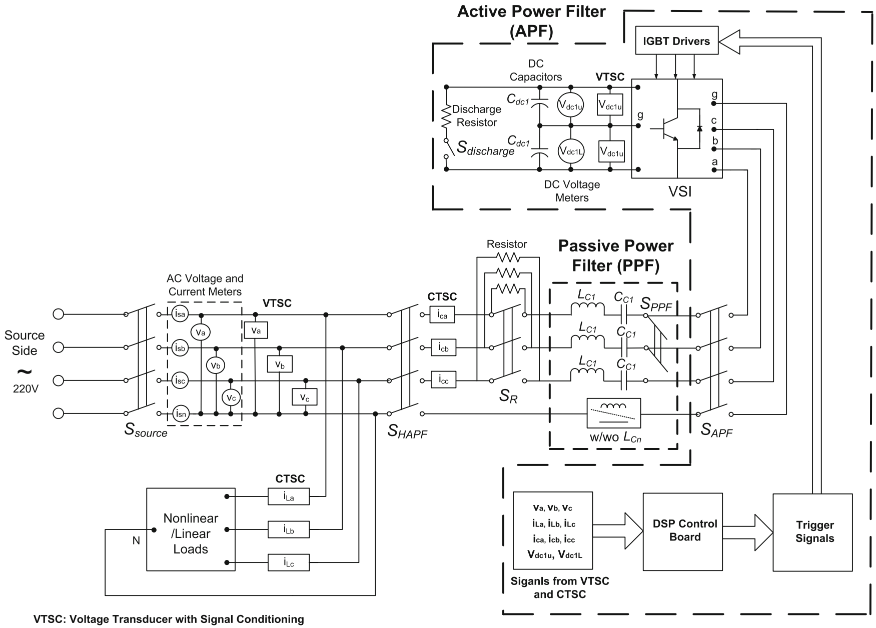

VTSC: Voltage Transducer with Signal Conditioning
CTSC: Current Transducer with Signal Conditioning

Fig. 6.8 System configuration of the 220 V, 10 kVA HAPF experimental prototype

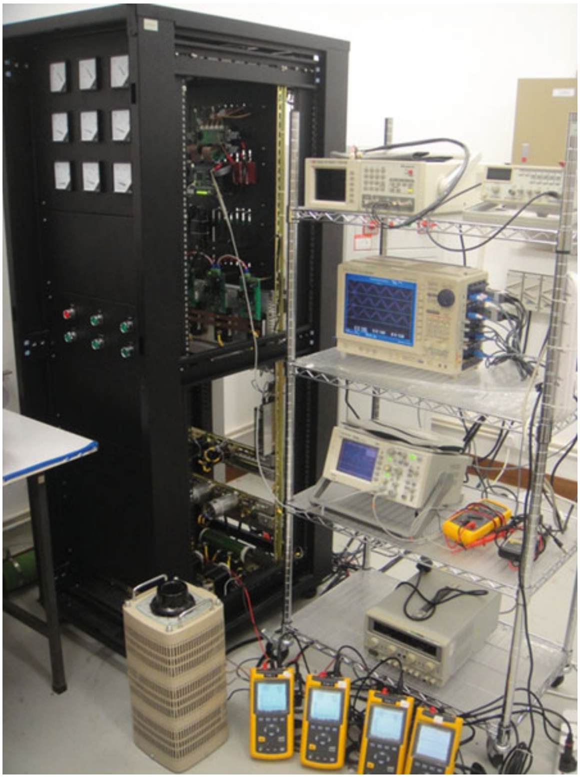

Fig. 6.9 The 220 V, 10 kVA HAPF experimental prototype testing environment

represent voltage and current transducer with signal conditioning board. The load is a nonlinear load, a linear load, or their combination. And the HAPF experimental prototype testing environment is shown in Fig. 6.9.

6.3.2 Experimental Testing Loads

The 220 V, 10 kVA three-phase four-wire center-split HAPF experimental prototype has been tested under the loadings as shown in Fig. 6.10. And their corresponding parameters' values are summarized in Table 6.2.

6.3.3 Design of PPF Part of HAPF

The coupling C_{c1} and L_{c1} of the HAPF are designed basing on the average fundamental reactive power consumption and the $n_I = 3\,k \pm 1$th harmonic current of the loading, $k = 1, 2\ldots\infty$. The reactance of C_{c1} and L_{c1} can be expressed as:

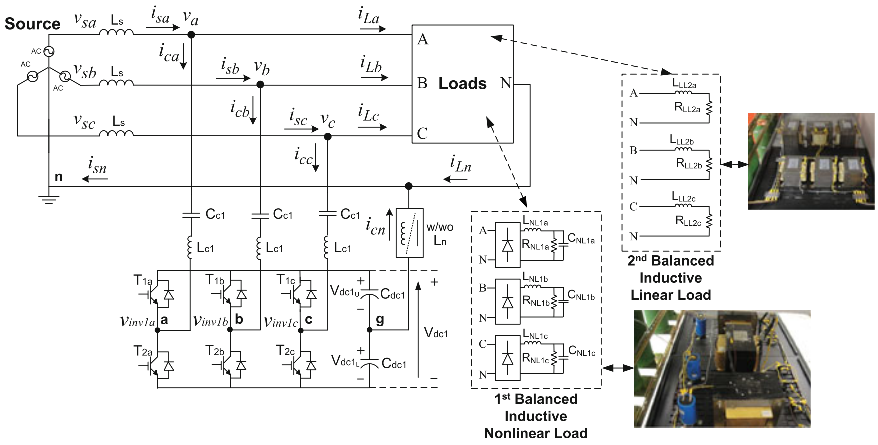

Fig. 6.10 The 220 V, 10 kVA HAPF experimental prototype under testing loads situation

$$X_{Cc1} = \frac{V_{\mathrm{x}}^2}{\left|\bar{Q}_{Lx_f}\right|} + X_{\mathrm{Lc1}},\ X_{\mathrm{Lc1}} = \frac{1}{n_1^2} X_{\mathrm{Cc1}} \tag{6.13}$$

where V_x is the RMS load voltage, $\bar{Q}_{Lx_f}$ is the phase average fundamental reactive power consumption of the loading. From (6.13), C_{c1} can be found:

$$C_{c1} = \left(\frac{n_1^2 - 1}{n_1^2}\right) \frac{\left|\bar{Q}_{Lx_f}\right|}{2\pi f \cdot V_{\mathrm{x}}^2} \tag{6.14}$$

Then the coupling L_{c1} can be expressed as:

$$L_{c1} = \frac{1}{(n_1 \cdot 2\pi f)^2 \cdot C_{c1}} \tag{6.15}$$

where L_{c1} can also smooth the inverter output current ripple. And the coupling neutral inductor L_{cn} can be obtained as:

$$L_{cn} = \frac{1}{3}\left(\frac{1}{(n_2 \cdot 2\pi f)^2 \cdot C_{c1}} - L_{c1}\right) \tag{6.16}$$

where n_2 is a *3kth* harmonic current order, and $n_1 > n_2$.

For the full bridge diode rectifier loading as shown in Fig. 6.10, the 3rd and 5th order harmonic currents will be the two dominant harmonic current contents. From Table 6.2, when designing the passive part parameters based on $\bar{Q}_{Lx_f} = 790.0\,\mathrm{var}$, $n_1 = 5$, and $n_2 = 3$, the coupling capacitor, inductor, and neutral inductor are: $C_{c1} \approx 50$ uF, $L_{c1} \approx 8$ mH and $L_{cn} \approx 5$ mH, respectively. The PPF hardware circuit diagram of the 220 V, 10 kVA HAPF experimental system is shown in Fig. 6.11.

Table 6.2 Experimental parameters for testing loads situation

System parameters			Physical values
V_x			220 V
f			50 Hz
1st inductive nonlinear rectifier load	A B C	R_{NL1x}, L_{NL1x}, C_{NL1x}	43.2 Ω, 34.5 mH, 392.0 μF ($Q_{Lxf} \approx$ 720.0 var)
2nd inductive linear load	A B C	R_{LL2x}, L_{LL2x}	60 Ω, 70 mH ($Q_{Lxf} \approx$ 200.0 var)

6.3.4 Design of APF Part of HAPF

The APF part of the HAPF is composed of a dc-to-ac center-split VSI with dc-link capacitors, which includes IGBT power switches with drivers, transducers with signal conditioning boards, and digital controller. In the following, the design of the following three components of the APF part will be presented.

(1) IGBT power switches with drivers,
(2) Transducer with signal conditioning boards,
(3) Digital controller and its software design.

6.3.4.1 IGBT Power Switches with Drivers

For the switching frequency range from a few kHz up to 20 kHz and the allowable maximum voltage of 400 V, IGBT is chosen as the power switching devices of the APF part of the HAPF system. Moreover, IGBT has the merit of low switching losses and require very little drive power at the gate. IGBT module can cover a power range up to about 1 megawatt and is now having a major impact on the

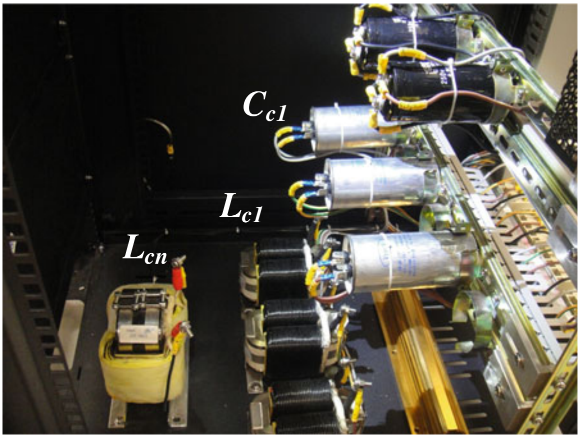

Fig. 6.11 Hardware circuit diagram for PPF part of the 220 V, 10 kVA HAPF

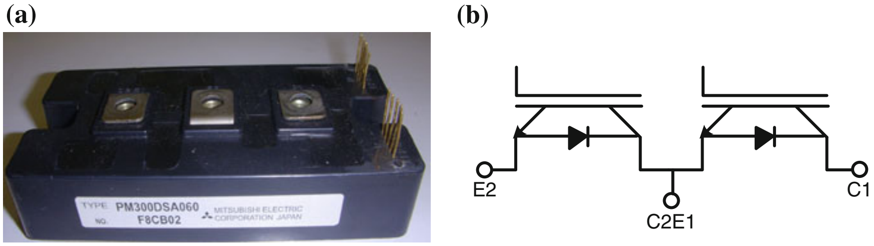

Fig. 6.12 Dual IPM module: **a** photo and **b** circuit diagram

power electronic systems in the low to medium power range for industrial and consumer applications. The Mitsubishi third generation IGBT PM300DSA60 dual intelligent power module (IPM) is selected, with maximum rated current and voltage of 300 A and 600 V, respectively [6]. The IPM provides the user with the additional benefits of equipment miniaturization and reduced time to market as they include gate drive circuit and protection circuits [7, 8]. The photo and circuit diagram of the selected dual IPM is shown in Fig. 6.12, in which this module can be used as one leg of the VSI, which provides great convenience to the hardware implementation.

The schematic diagram of the IGBT driver board is shown in Fig. 6.13, which is used to drive one dual IPM. The IGBT driver board is designed to control the switching state of IGBT with the trigger signals generated by the digital controller.

The followings are some key information for the IGBT driver with the input/output (I/O) requirement of the digital controller.

(1) M57140-01 is an isolated dc-to-dc converter designed to drive IPMs. With an input DC 20 V, the module supplies four 15 V outputs with total 3 W maximum power. Isolation is provided from primary to secondary and also between the secondaries [9].
(2) The SN74HCT08 AND Gate is used to protect the I/O of digital controller. It works as a buffer since the current of the I/O is recommended to within 1.67 mA per pin for 3.3 V-tolerance [10]; while the typical working current of HCPL4504 optocoupler is 16 mA [11].
(3) PC817 is a photocoupler that works for fault signal “FO”. +VL, R7, and R8 are combined as resistor divider to pull up the fault signal “FO” and limit the voltage within 3.3 V.
(4) The RC low-pass filter is adopted to filter the noise which could probably be on the fault signal. The selection of R1 should consider the current of digital controller I/O, “FO” pull up potential, and RC low-pass filter’s loading effect.

The final hardware connection between the IGBT power switches and drivers are shown in Fig. 6.14.

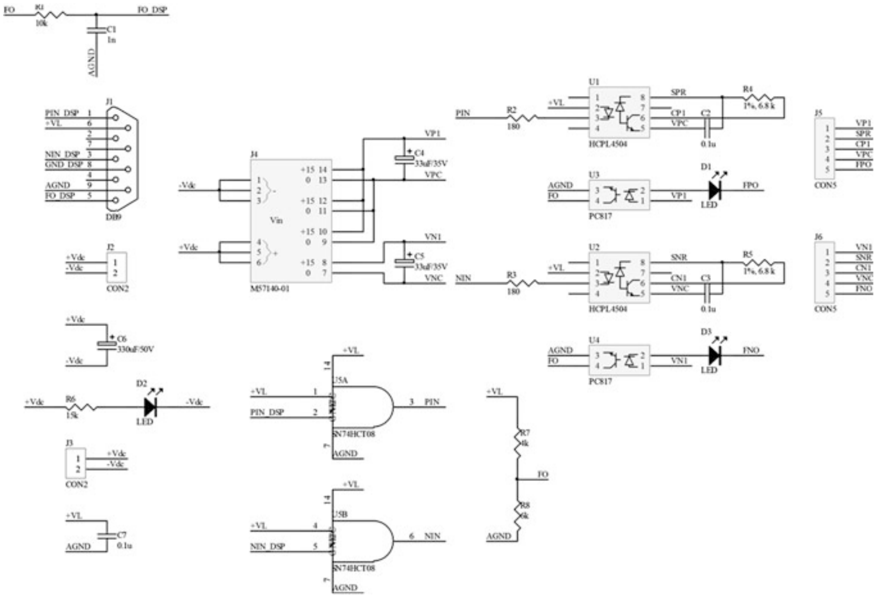

Fig. 6.13 Schematic diagram of IGBT driver board

6.3.4.2 Transducers with Signal Conditioning Boards

The three-phase load voltages, load currents, compensating currents, and dc-link voltages of the HAPF are measured by transducers with signal conditioning boards. The adopted transducers are based on the Hall-Effect transducer, which provides an isolated measurement for dc and ac voltage and current. The voltage and current signal conditioning boards can transfer the large electrical signals into small analog signals in order to be adopted as the A/D converter inputs of the

Fig. 6.14 Hardware connection between IGBT power switches and drivers of the 220 V, 10 kVA HAPF

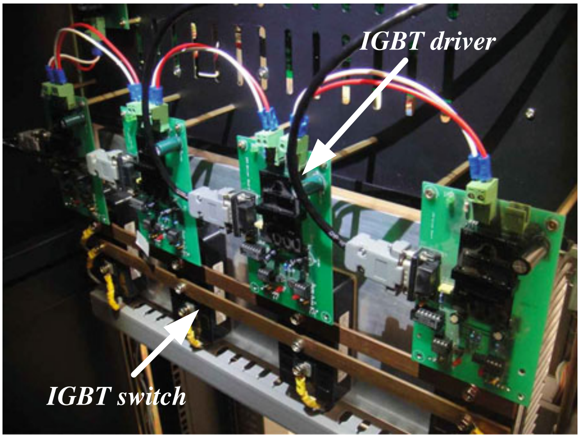

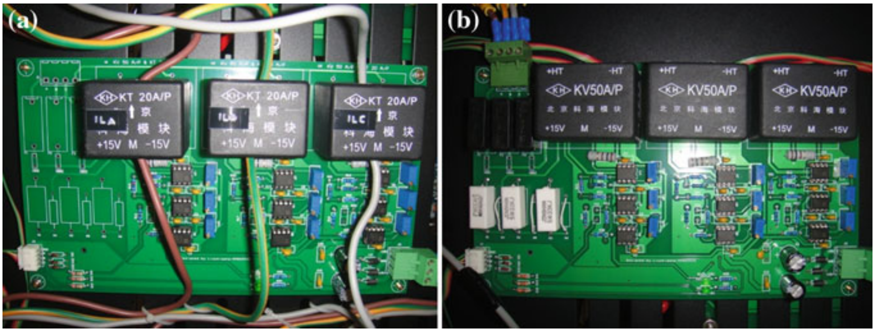

Fig. 6.15 Transducers with signal conditioning boards: **a** current board and **b** voltage board

digital control system. The measured output signals from the signal conditioning boards are sent to the A/D converter and converted into digital signals in the digital controller. These signals are required to calculate the reference compensating currents. The photos of the voltage and current transducers with signal conditioning boards are shown in Fig. 6.15. And the schematic diagram of the signal conditioning circuit is shown in Fig. 6.16. From Fig. 6.16, the signal conditioning circuit mainly includes one voltage follower and two negative gain amplifiers. The voltage follower can provide a high input impedance to avoid loading effect, while the two negative gain amplifiers can provide an appropriate positive output electrical signal to A/D input of the digital controller. A 3.3 V zener diode is implemented at the output side to limit the input voltage level to a 3.3 V digital controller.

In order to synthesize parameters of the signal conditioning circuit, the R1 of KT 20 A/P (current transducer) indicated in Fig. 6.16 is selected as 50 Ω, while that of KV 50 A/P (voltage transducer) is selected as 100 Ω [12]. Therefore, the current and voltage transducer output voltage (V_{in}) will have the same range between −5 to 5 V_{peak}.

The selected A/D converter of the digital controller has an input range of $0 \sim 3.3$ V. Therefore, the output voltage (V_o) of the signal conditioning circuits

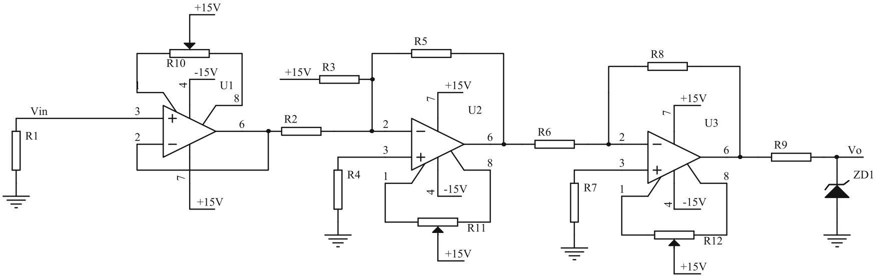

Fig. 6.16 Schematic diagram of the signal conditioning circuit

Table 6.3 Parameters of the signal conditioning boards (in peak value)

Max. measurement range (A_{peak}/V_{peak})			V_{in} (V_{peak})	V_o (V_{peak})	R_2 (kΩ)	R_3 (kΩ)	R_5 (kΩ)
Current	i_{Lx}	$-20 \sim 20$	$-5 \sim 5$	$0.309 \sim 2.991$	8.2	20	2.2
	i_{cx}	$-20 \sim 20$	$-5 \sim 5$	$0.309 \sim 2.991$	8.2	20	2.2
Voltage	v_x	$-330 \sim 330$	$-5 \sim 5$	$0.309 \sim 2.991$	8.2	20	2.2
	V_{dc1U}, V_{dc1L}	$0 \sim 200$	$0 \sim 5$	$0.330 \sim 2.991$	8.2	100	2.2

Note: $R_4 = 1.5$ kΩ, $R_7 = 5$ kΩ, $R_6 = R_8 = 10$ kΩ, and R_{10}, R_{11}, R_{12} are 20 kΩ adjustable resistor

should be consistent with ($0 \sim 3.3$ V). To avoid the unsteady state when the input voltage approaches 3.3 V, the peak output voltage is changed to the range of $0.3 \sim 3.0$ V. According to the schematic diagram as shown in Fig. 6.16, the signal conditioning board output voltage can be expressed as:

$$V_o = \frac{R_5}{R_2} V_{in} + \frac{R_5}{R_3} \times 15 \tag{6.17}$$

For ac measurement, a dc offset should be provided for the input analog signals because a negative voltage is not compatible for a $0 \sim 3.3$ V digital controller. Set $R_5 = 2.2$ kΩ and $R_3 = 20$ kΩ, then $V_o = \frac{2.2k}{R_2} V_{in} + 1.65$.

According to the experimental loading conditions as listed in Tables 6.2 and 6.4, the maximum measurement ranges for load currents and compensating currents are set as ±20 and ±20 A_{peak}, respectively. And the maximum measurement range of the load voltages and dc-link capacitor voltages are set as ±330 and +200 V_{peak}, respectively. Table 6.3 shows the design parameters of the signal conditioning boards. And the photo of the overall current and voltage transducers with signal condition boards for the HAPF experimental prototype is shown in Fig. 6.17.

6.3.4.3 Software Design of Digital Controller DSP-TMS320F2812

The reference compensating current calculation is achieved by a digital signal processor (DSP). The high speed DSP-TMS320F2812 is chosen which has high performances in the real-time control and motor/machine control. There are a total of 16 multiplexed analog inputs of 12-bit analog-to-digital converter (ADC) core with built-in sample and hold (S/H) in the DSP-TMS320F2812. The 12-bit ADC module is operating with a fast conversion rate of 80 ns at 25 MHz ADC clock. The ADC sequencer consists of two independent 8-state sequencers that can also be cascaded together to form one 16-state sequencer [10]. After conversion, the digital value of the selected channel is stored in the appropriate result register. The results will be transformed into the corresponding format and values by bit shift operation on the result registers.

There are two Event Managers (EV), EVA and EVB, embedded in TMS320F2812. And each EV module contains two general-purpose (GP) timers [10]. The GP timers can be used as the timer to activate the A/D conversion, to

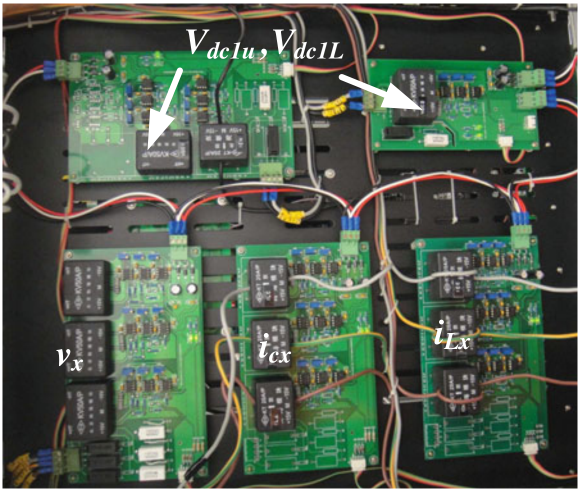

Fig. 6.17 Overall current and voltage transducers with signal conditioning boards of the 220 V, 10 kVA HAPF

provide a time base for the operation of the full compare units, or to calculate the reference current. There are six PWM outputs with programmable deadband and output logic for each EV created by the intrinsic three full compare units. These PWM signals are generated by using EV module, Timer 1 (EVA), and Timer 3 (EVB). The deadband unit is used to implement the deadtime of the inverter in each of the compare units. When the deadband unit is enabled for the compare unit, the transition edges of the two signals are separated by a time interval determined by the inverter switch limitation. A deadband can be provided to avoid the short-circuit case between the upper and lower switches in one leg. The deadband is designed as 4.27 μs, which is larger than the recommended condition (≥3.5 μs) of the PM300DSA60 IPM.

For the 220 V, 10 kVA HAPF experimental prototype, Timer 2 (EVA) is used to define the sample rate of ADC module, in which the sampling frequency is set to 25 kHz. For every 1/25 kHz(s) period, the Timer 2 will provide a trigger signal to process A/D conversion and the corresponding interrupt. And there are totally 4 groups with 12 channel signals (3 load voltages v_x, 3 load currents i_{Lx}, 3 compensating currents i_{cx}, and 2 dc-link capacitor voltages V_{dc1U}, V_{dc1L}) are converted into digital values. Timer 1 (EVA) is responsible for generating PWM. The frequency of Timer 1 is determined by the switching frequency limitation of the IGBT; Timer 1 is set to have a maximum switching frequency of 12.5 kH. And there is only one interrupt activated, in which the A/D interrupt has the highest priority. In the following, the program flowchart for the DSP-TMS320F2812 in performing A/D signal sampling, reference compensating current calculation, adaptive dc-link voltage control, and generating the PWM signals for controlling the VSI output is shown in Fig. 6.18. And the DSP controller of the 220 V, 10 kVA HAPF experimental prototype is shown in Fig. 6.19, in which there is a signal connection printed circuit board (PCB) for convenient connection between the peripherals I/O ports of the DSP and other physical devices.

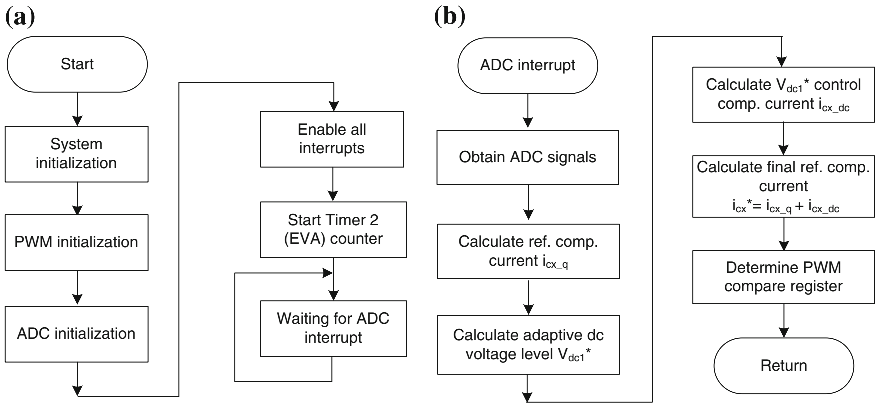

Fig. 6.18 DSP program flowchart of the HAPF: **a** main program and **b** interrupt service routine

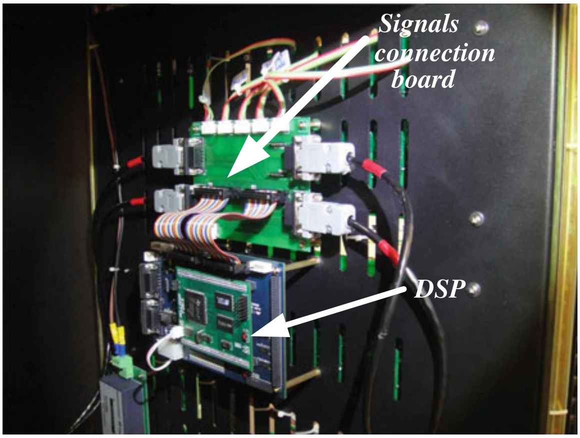

Fig. 6.19 The DSP controller of the 220 V, 10 kVA HAPF

6.3.5 *General Design Procedures for Adaptive DC-Link Voltage Controlled HAPF with L_{cn}*

The general design procedures for the adaptive dc-link voltage-controlled HAPF with L_{cn} will be summarized in the following steps:

(1) From the average $\bar{Q}_{Lxf}$ and the dominant $n_1 = 3\ k \pm 1$th and $n_2 = 3\ k$th, $n_1 > n_2$, C_{c1}, L_{c1}, and L_{cn} can be designed by (6.13–6.16).
(2) V_{dcmax} is designed according to HAPF's specification; $V_{dcmax}/3$ or $V_{dcmax}/4$ can be treated as each dc-link voltage level step size.
(3) PI gains of dc-link voltage controller can be designed by plotting bode and step response plots of (6.11, 6.12).
(4) According to Fig. 6.1, the proposed adaptive dc-link voltage controller for the HAPF with L_{cn} can be implemented by using a DSP.

(5) Sampling frequency, switching frequency, and hysteresis band of the HAPF can be designed refer to [13].

In next section, the adaptive dc-link voltage-controlled HAPF with L_{cn} experimental compensation results will be given, compared with the conventional fixed and adaptive dc-link voltage-controlled HAPF without L_{cn}.

6.4 Experimental Verifications of A 220 V 10 KVA Low Adaptive DC-Link Voltage-Controlled HAPF with L_{cn} Experimental Prototype

In this section, the proposed adaptive dc-link voltage-controlled HAPF without and with L_{cn} for dynamic reactive power and current harmonics compensation will be verified by experiments on a 220 V, 10 kVA HAPF experimental prototype. The control system is a DSP TMS320F2812 and its sampling frequency is set at 25 kHz. Hysteresis current PWM is applied for the experimental prototype with hysteresis band of $H = 0.0625$A and maximum switching frequency is 12.5 kHz, in which the hysteresis band and sampling frequency satisfy the HAPF linearization requirement [13]. Moreover, the Mitsubishi IGBT IPMs PM300DSA60 are employed as the switching devices of the inverter, and their switching frequency limitation are at 20 kHz. Figure 6.1 shows the adaptive dc-link voltage-controlled HAPF without and with L_{cn} control block diagram for experiments.

For the experimental testing loads as shown in Fig. 6.10 and Table 6.2, as its harmonic current contents beyond the 9th order are small, for simplicity, the required minimum dc-link voltage for current harmonics compensation will be calculated up to 9th harmonic order only. Table 6.4 shows the 3rd, 5th, 7th, and 9th order harmonic current in RMS values. From Tables 6.2 and 6.4 and the reactive power provided by the coupling passive part $Q_{cxf\_\mathrm{PPF}} \approx -777.0$ var ($V_x = 218$ V) ~ -806.0var ($V_x = 222$ V), the final reference V^*_{dc1} is designed to have three adaptive dc voltage levels (V_{dc1U}, $V_{dc1L} = 25$, 50, and 75 V) for the experimental verification. Table 6.5 lists the system parameters for the 220 V, 10 kVA HAPF with L_{cn} experimental prototype. From Tables 6.1, 6.2, and 6.4, the final minimum adaptive levels V_{dc1U}, V_{dc1L} for the experiments are illustrated in Table 6.6.

Table 6.4 Experimental 3rd, 5th, 7th, and 9th orders load harmonic current values under testing loads situation

Different situations		Harmonic current order			
		3rd order (A)	5th order (A)	7th order (A)	9th order (A)
1st loading	A, B, C	1.92	0.45	0.20	0.12
1st and 2nd loadings	A, B, C	1.90	0.46	0.23	0.12

Table 6.5 System parameters of the 220 V, 10 kVA HAPF

System parameters		Physical values
System source-side	V_x, f	220 V, 50 Hz
Passive part ($Q_{cxf\_\mathrm{PPF}} \approx -790.0$ var)	L_{c1}, C_{c1}, L_{cn}	8 mH, 50 uF, 5 mH
DC capacitor	C_{dc1}	3.3 mF
DC-link voltage levels	V_{dc1U}, V_{dc1L}	25 V, 50 V, 75 V

Table 6.6 HAPF experimental minimum dc-link voltage levels (25, 50, and 75 V) without or with L_{cn}

Different situations			Required $V_{dc1\_min}/2$ (V)	Final minimum adapt. level V_{dc1U},V_{dc1L} (V)
$L_{cn} = 0$mH	1st loading	A, B, C	44.0	50
	1st and 2nd loadings	A, B, C	58.3	75
$L_{cn} = 5$mH	1st loading	A, B, C	25.3	25
	1st and 2nd loadings	A, B, C	46.3	50

6.4.1 *Power Quality Data of the Experimental Loadings*

Before the HAPF performs compensation, Fig. 6.20 shows the experimental reactive power at system source-side Q_{sxf}, load voltage v_x, and system current i_{sx} waveforms of phase *a*. As the experimental loadings are approximately balanced, only v_x and i_{sx} waveforms of phase *a* will be illustrated. Table 6.7 summarizes the power quality parameters for the testing loadings. When the 1st inductive loading is connected, the three-phase Q_{sxf} are 723.0, 718.5, and 721.2 var with power factor (PF) = 0.804, 0.805, and 0.804, respectively, and the total harmonic distortion (THD_{isx}) of i_{sx} are 32.5, 31.5, and 31.6 %, in which the THD_{isx} do not satisfy the international standards ($\mathrm{THD}_{isx} < 20$ % for IEEE and 16 % for IEC) [14, 15]. When both the 1st and 2nd inductive loadings are connected, the three-phase Q_{sxf} increase to 921.3, 920.1, and 921.9 var with PF = 0.870, 0.872, and 0.870, respectively, and the THD_{isx} become 21.3, 20.5, and 20.7 %, in which the THD_{isx} do not satisfy the standards [14, 15]. In the following, the experimental compensation results by three different HAPFs: (i) conventional fixed dc-link voltage-controlled HAPF, (ii) adaptive dc-link voltage-controlled HAPF, and (iii) adaptive dc-link voltage-controlled HAPF with L_{cn}, will be given and compared.

6.4.2 *Experimental Results of Conventional Fixed DC-Link Voltage-Controlled HAPF*

With conventional fixed dc-link voltage reference (V_{dc1U}, $V_{dc1L} = 75$ V) for the HAPF, Fig. 6.21a shows that the V_{dc1U}, V_{dc1L} level can be controlled as its reference 75 V no matter when the 1st loading or 1st and 2nd loadings are connected.

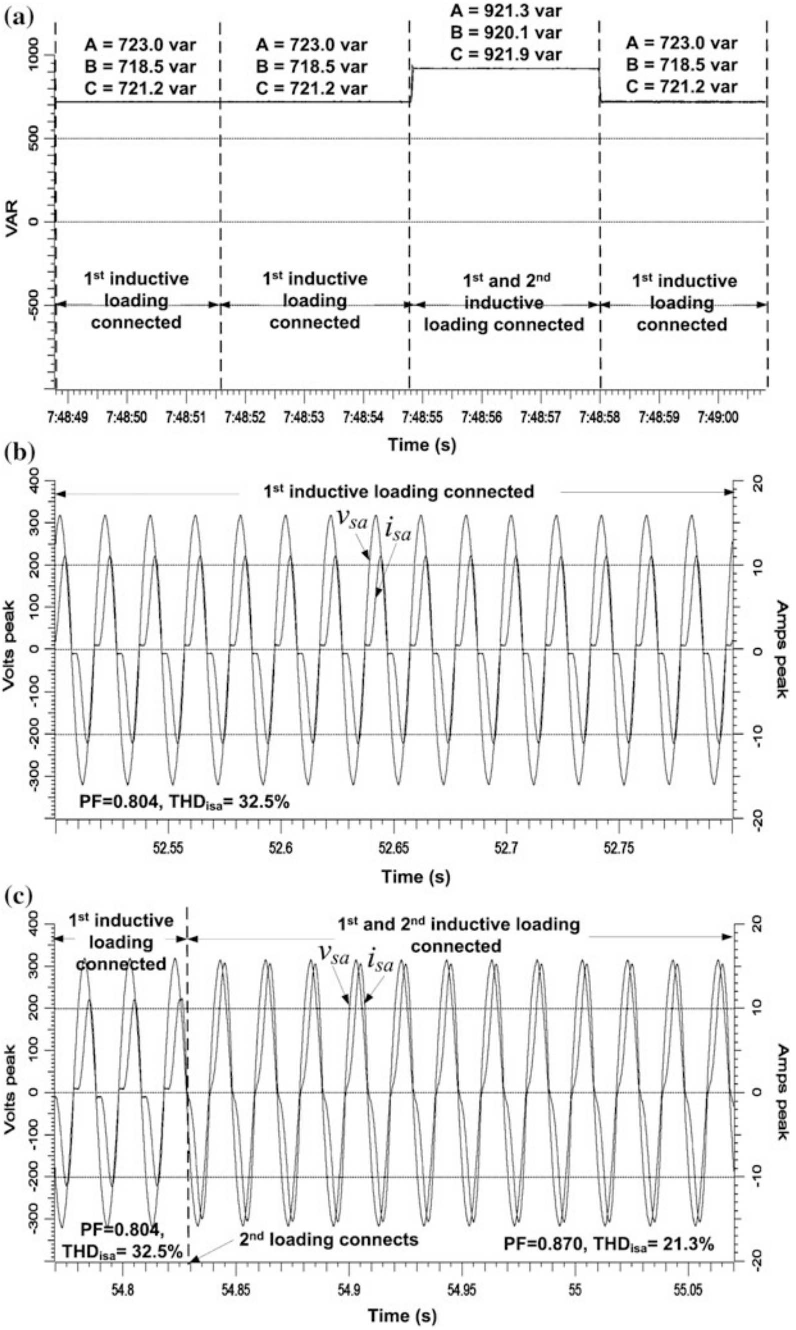

Fig. 6.20 Before HAPF compensation: **a** Q_{sxf}, **b** v_x and i_{sx} of phase a when the 1st loading is connected and **c** v_x and i_{sx} of phase a when the 1st and 2nd loadings are connected

Table 6.7 Experimental results before HAPF compensation

Before HAPF compensation for testing loading							
Different cases		Q_{sxf} (var)	PF	THD_{isx} (%)	THD_{vx} (%)	i_{sx} (A)	i_{sn} (A)
1st inductive loading	A	723.0	0.804	32.5	1.7	6.506	5.808
	B	718.5	0.805	31.5	1.9	6.467	
	C	721.2	0.804	31.6	1.5	6.444	
1st and 2nd inductive loading	A	921.3	0.870	21.3	1.6	9.520	5.659
	B	920.1	0.872	20.5	1.8	9.539	
	C	921.9	0.870	20.7	1.5	9.493	

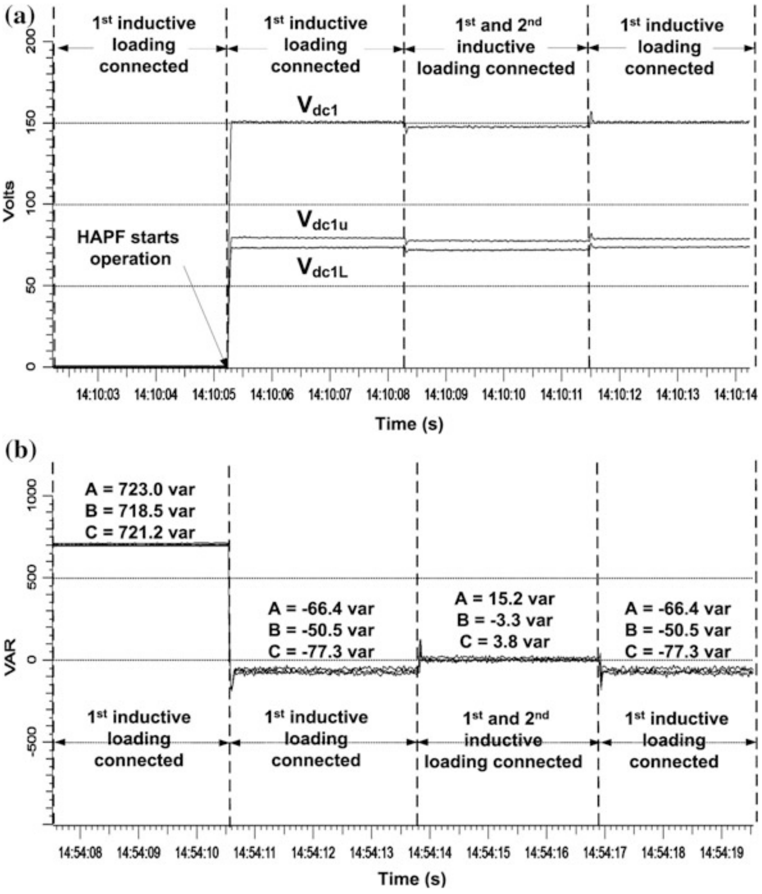

Fig. 6.21 HAPF whole experimental dynamic compensation process with conventional fixed dc-link voltage control scheme: **a** V_{dc1U}, V_{dc1L}, **b** Q_{sxf}, **c** v_x and i_{sx} of phase *a* after HAPF starts operation, and **d** v_x and i_{sx} of phase *a* after the 2nd loading is connected

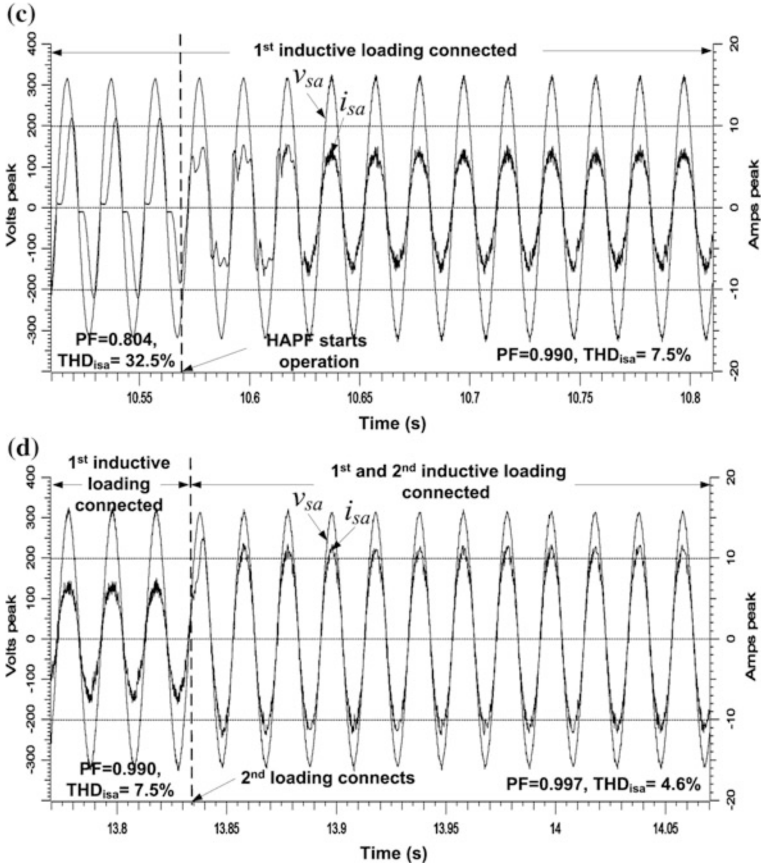

Fig. 6.21 continued

Table 6.8 Experimental results after HAPF compensation with conventional fixed dc-link voltage control

After HAPF compensation with conventional fixed dc-link voltage control								
Different cases		Q_{sxf} (var)	PF	THD$_{isx}$ (%)	THD$_{vx}$ (%)	i_{sx} (A)	i_{sn} (A)	V_{dc1U}, V_{dc1L} (V)
1st inductive loading	A	−66.4	0.990	7.5	1.3	4.943	1.347	75
	B	−50.5	0.990	8.7	1.2	5.024		
	C	−77.3	0.989	9.0	1.1	5.108		
1st and 2nd inductive loading	A	15.2	0.997	4.6	1.1	8.071	1.324	75
	B	−3.3	0.997	5.2	1.0	8.036		
	C	3.8	0.997	5.8	1.1	8.023		

From Fig. 6.21b, the experimental Q_{sxf} can be approximately compensated close to zero for both loadings case, compared with Fig. 6.20a. Figure 6.21c shows the PF and THD$_{isx}$ of phase *a* can be improved from 0.804 to 0.990 and 32.5 to 7.5 % at

1st loading case. From Fig. 6.21d, the PF and THD_{isx} of phase a become 0.997 and 4.6 % when the 2nd loading is connected. Table 6.8 summarizes the results of the HAPF with the conventional fixed dc-link voltage control.

6.4.3 Experimental Results of Adaptive DC-Link Voltage-Controlled HAPF

With the adaptive dc-link voltage control for the HAPF, Fig. 6.22a shows that the V_{dc1U}, V_{dc1L} can be adaptively changed (V_{dc1U}, $V_{dc1L} = 50$ V for the 1st loading,

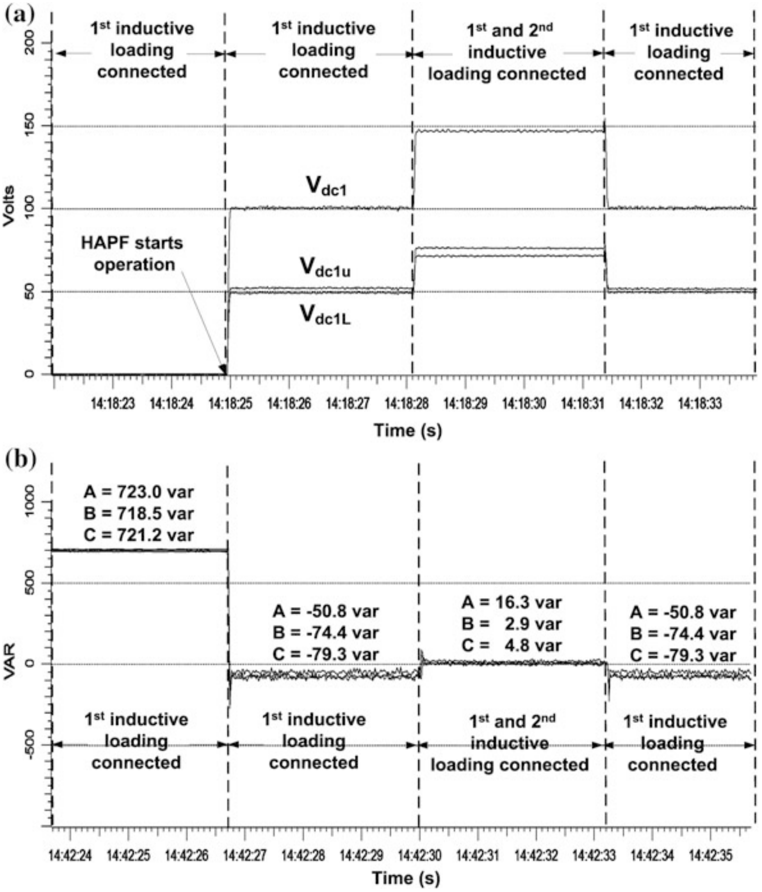

Fig. 6.22 HAPF whole experimental dynamic compensation process with adaptive dc-link voltage control scheme: **a** V_{dc1U}, V_{dc1L}, **b** Q_{sxf}, **c** v_x and i_{sx} of phase a after HAPF starts operation, and **d** v_x and i_{sx} of phase a after the 2nd loading is connected

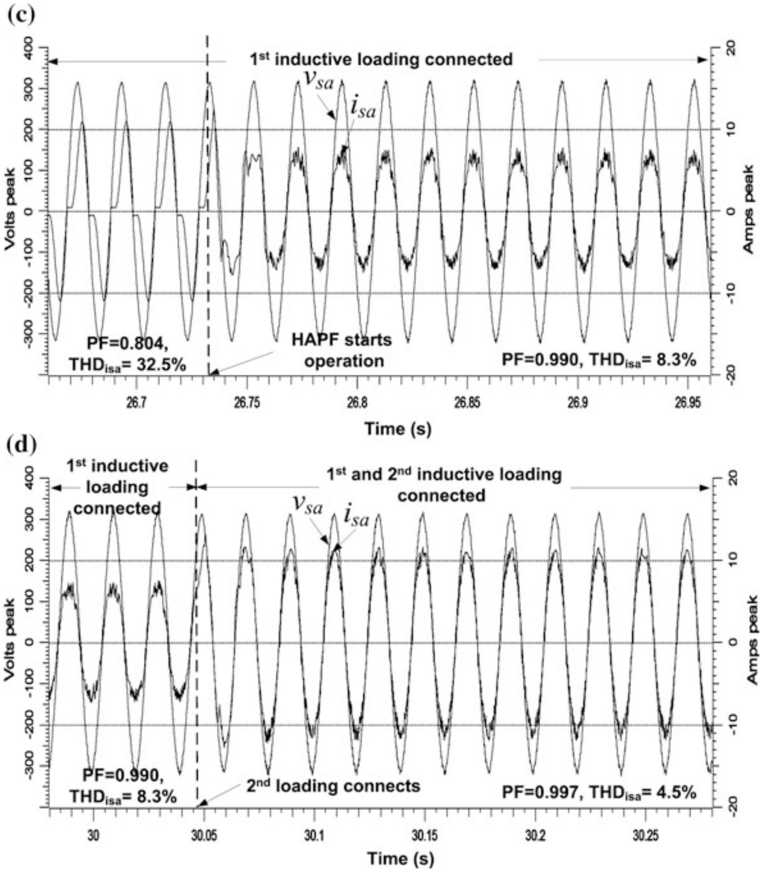

Fig. 6.22 continued

Table 6.9 Experimental results after HAPF compensation with adaptive dc-link voltage control

After HAPF compensation with adaptive dc-link voltage control								
Different cases		Q_{sx} (var)	PF	THD$_{isx}$ (%)	THD$_{vx}$ (%)	i_{sx} (A)	i_{sn} (A)	V_{dc1U}, V_{dc1L} (V)
1st inductive loading	A	−50.8	0.990	8.3	1.0	5.023	1.500	50 V
	B	−74.4	0.989	10.3	1.1	5.044		
	C	−79.3	0.989	10.7	1.0	5.058		
1st and 2nd inductive loading	A	16.3	0.997	4.5	1.0	8.085	1.414	75 V
	B	2.9	0.997	5.0	1.0	8.047		
	C	4.8	0.997	5.9	1.0	8.008		

V_{dc1U}, V_{dc1L} = 75 V for the 1st and 2nd loadings) according to different loading cases. From Fig. 6.22b, the experimental Q_{sxf} can be compensated close to zero for both loadings case. Figure 6.22c shows that the PF and THD$_{isx}$ of phase a can be

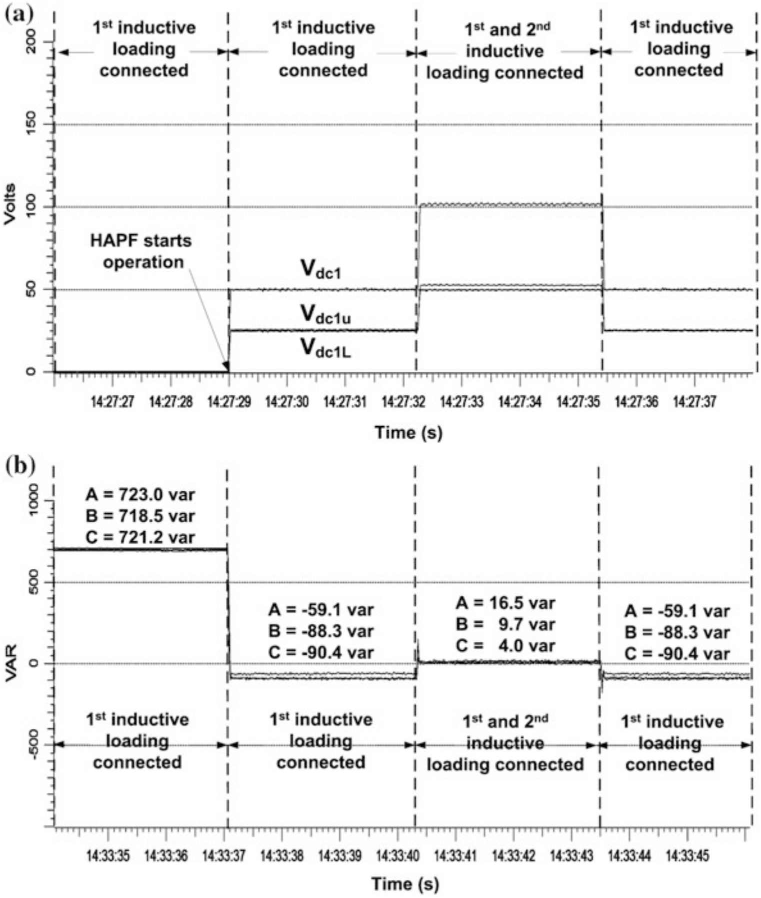

Fig. 6.23 HAPF whole experimental dynamic compensation process with adaptive dc-link voltage control scheme and L_{cn}: **a** V_{dc1U}, V_{dc1L}, **b** Q_{sxf}, **c** v_x and i_{sx} of phase *a* after HAPF starts operation, and **d** v_x and i_{sx} of phase *a* after the 2nd loading is connected

improved from 0.804 to 0.990 and 32.5 to 8.3 % at 1st loading case. From Fig. 6.22d, the PF and THD$_{isx}$ of phase *a* become 0.997 and 4.5 % when the 2nd loading is connected. Table 6.9 summarizes the results of the HAPF with the adaptive dc-link voltage control scheme.

6.4.4 Experimental Results of Adaptive DC-Link Voltage-Controlled HAPF with L_{cn}

With the adaptive dc-link voltage control for the HAPF with L_{cn}, Fig. 6.23a shows that the V_{dc1U}, V_{dc1L} can be adaptively changed (V_{dc1U}, $V_{dc1L} = 25$ V for the 1st

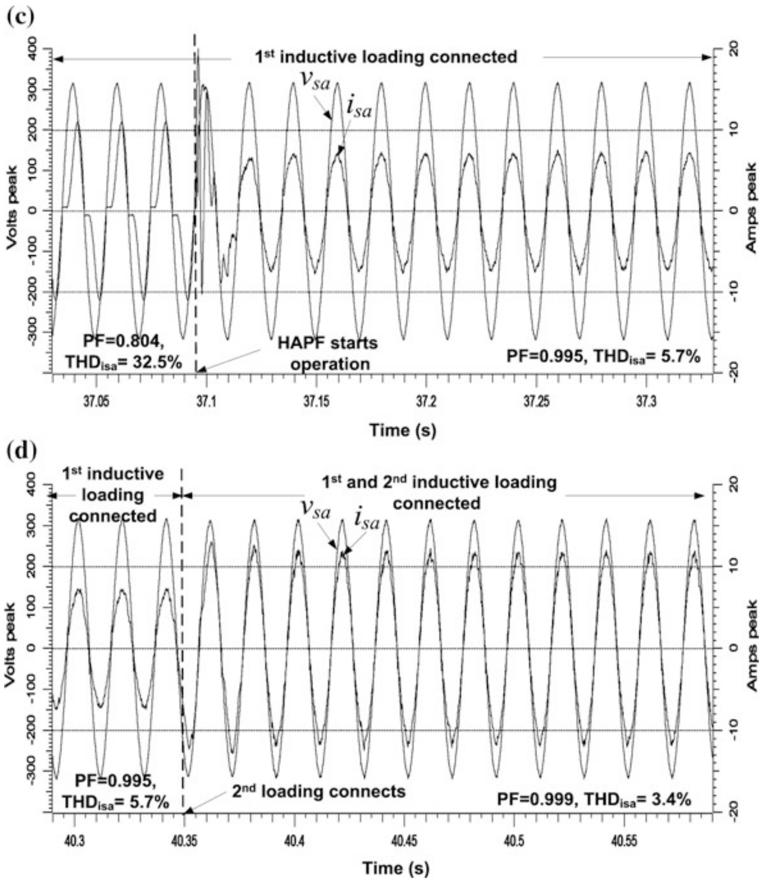

Fig. 6.23 continued

loading, V_{dc1U}, $V_{dc1L} = 50$ V for the 1st and 2nd loadings) according to different loading cases. From Fig. 6.23b, the experimental Q_{sxf} can be compensated close to zero for both loadings case. Figure 6.23c shows that the PF and THD$_{isx}$ of phase *a* can be improved from 0.804 to 0.995 and 32.5 to 5.7 % at 1st loading case. From Fig. 6.23d, the PF and THD$_{isx}$ of phase *a* become 0.999 and 3.4 % when the 2nd loading is connected. Table 6.10 summarizes the results of the HAPF with the adaptive dc-link voltage control scheme and L_{cn}.

6.4.5 Comparison

From Figs. 6.21, 6.22, and 6.23 and Tables 6.8, 6.9, and 6.10, the three different HAPFs can achieve more or less the same steady-state reactive power

Table 6.10 Experimental results after HAPF compensation with adaptive dc-link voltage control and L_{cn}

After HAPF compensation with adaptive dc-link voltage control and L_{cn}								
Different cases		Q_{sxf} (var)	PF	THD_{isx} (%)	THD_{vx} (%)	i_{sx} (A)	i_{sn} (A)	V_{dc1U}, V_{dc1L} (V)
1st inductive loading	A	−59.1	0.995	5.7	0.9	5.052	0.815	25
	B	−88.3	0.994	5.9	0.9	5.011		
	C	−90.4	0.994	6.4	0.9	4.962		
1st and 2nd inductive loading	A	16.5	0.999	3.4	0.9	8.073	0.839	50
	B	9.7	0.998	3.6	0.8	8.017		
	C	4.0	0.998	4.3	0.9	8.031		

Table 6.11 Experimental inverter power loss of HAPF with fixed V_{dc1u}, $V_{dc1L} = 75$ V, adaptive dc-link voltage control, and adaptive dc-link voltage control with L_{cn}

Inverter power loss of HAPF		Fixed V_{dc1U}, $V_{dc1L} = 75$ V	Adaptive dc	Adaptive dc with L_{cn}
Power loss (W)	1st inductive loading	41 W	37 W (50 V) ~ 10 %↓	35 W (25 V) ~ 15 %↓
	1st and 2nd inductive loading	59 W	59 W (75 V)	54 W (50 V) ~ 9 %↓

compensation results, and their compensated THD_{isx} and THD_{vx} satisfy the international standards [14–16]. Moreover, the system current i_{sx} and neutral current i_{sn} can be significantly reduced after compensation. From Table 6.11, during 1st loading case, the adaptive dc control scheme (V_{dc1U}, $V_{dc1L} = 50$ V) can reduce the switching loss compared with the conventional fixed V_{dc1U}, $V_{dc1L} = 75$ V control, because the switching loss is directly proportional to the dc-link voltage [2]. And the adaptive dc-link voltage-controlled HAPF with L_{cn} can obtain the least switching loss because it just requires the lowest dc-link voltage levels for compensating both loadings case. The lowest dc-link voltage also leads the HAPF to obtain the best current harmonics and neutral current reduction.

Fig. 6.24 shows the experimental compensating currents i_{cx} of phase a with: (a) fixed V_{dc1U}, $V_{dc1L} = 75$ V; (b) adaptive dc-link voltage control; and (c) adaptive dc-link voltage control with L_{cn} at 1st loading case. Figure 6.24 illustrates that the adaptive dc voltage control scheme can reduce the switching noise (~20 %↓ in current ripple) compared with the fixed dc voltage case. And the adaptive dc voltage-controlled HAPF with L_{cn} can further reduce the switching noise (~70 %↓ in current ripple). Figure 6.25 shows the experimental neutral inverter currents i_{cn}, which also verifies the switching noise reduction by the adaptive dc-link voltage control and L_{cn}.

Fig. 6.26a shows the performances comparison between the HAPF with and without L_{cn}. With L_{cn} case, its compensating current tracking ability can be enhanced, thus the HAPF can obtain a low THD_{isx} value under low V_{dc1U},

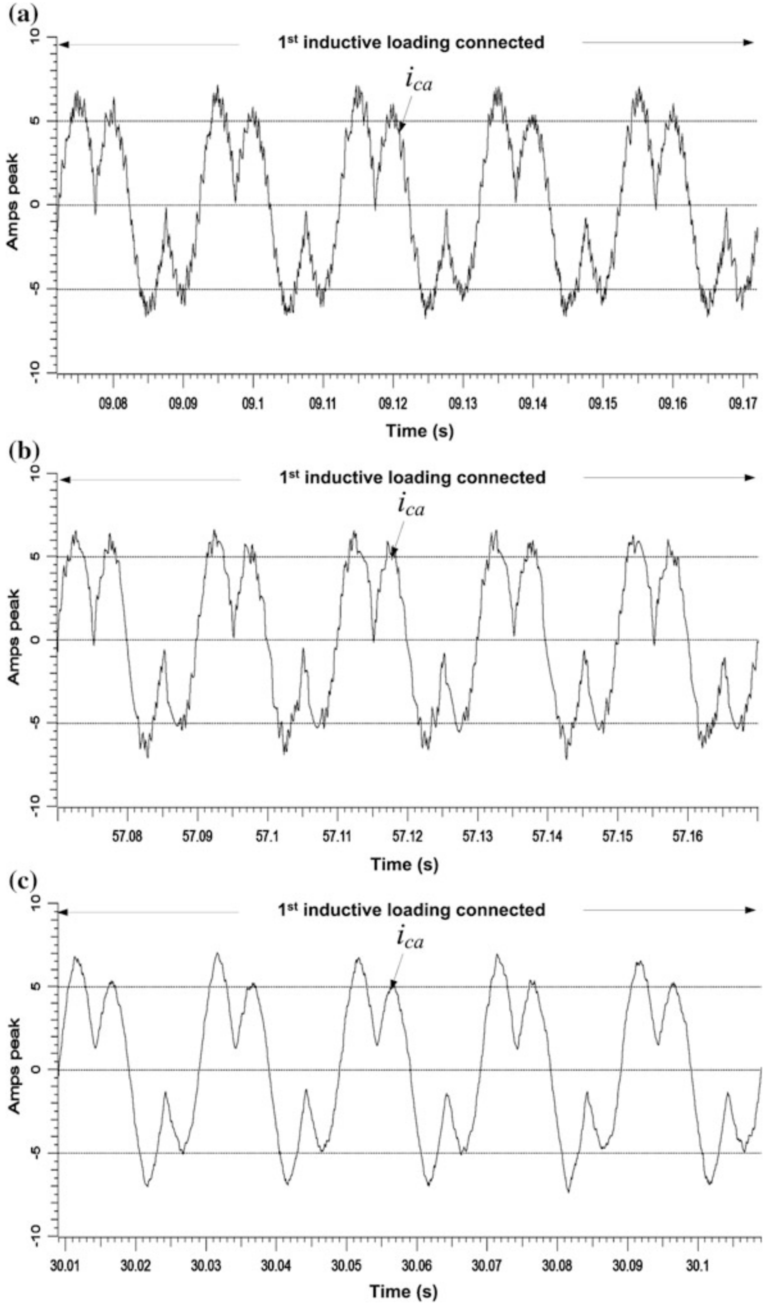

Fig. 6.24 Experimental i_{cx} of phase a with: **a** a fixed V_{dc1U}, $V_{dc1L} = 75$ V, **b** adaptive dc-link voltage control, and **c** adaptive dc-link voltage control with L_{cn}

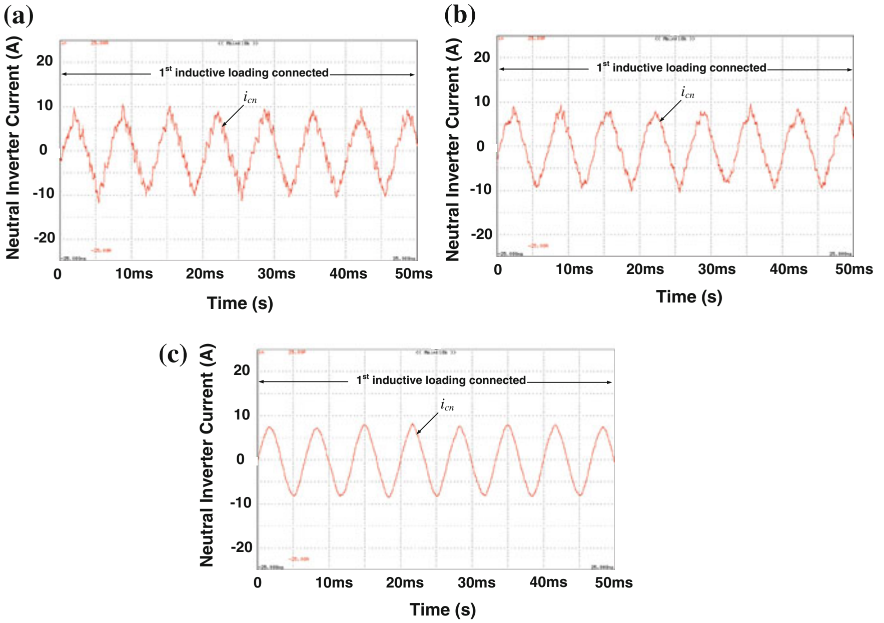

Fig. 6.25 Experimental i_{cn} with: **a** a fixed V_{dc1U}, $V_{dc1L} = 75$ V, **b** adaptive dc-link voltage control, and **c** adaptive dc-link voltage control with L_{cn}

$V_{dc1L} = 25$ V. Without L_{cn} case, a sufficient dc-link voltage (V_{dc1U}, $V_{dc1L} \geq 50$ V) should be applied to ensure its current tracking ability. To obtain similar THD$_{isx}$ value, the HAPF with L_{cn} can have a much lower dc operating voltage. In addition, the inverter power loss curve of HAPF under different dc voltage level is shown in Fig. 6.26b. From Fig. 6.26b, it clearly indicates that a lower inverter power loss can be obtained for the HAPF with L_{cn}.

For the adaptive dc-link voltage-controlled HAPF with or without L_{cn}, due to its reference dc voltage V_{dc1}^{*} can be varied according to different loading conditions, its compensating performance will be influenced during each changing of the dc voltage level. Compared with the fixed dc voltage control, the adaptive dc control scheme will have a longer settling time during the load and dc voltage level changing situation.

The adaptive dc-link voltage-controlled HAPF with L_{cn} can obtain the least switching loss and switching noise and the best compensating performances among the three different HAPFs. As the switching loss is directly proportional to the dc-link voltage and switching frequency [2], applying the fixed frequency triangular PWM scheme will also yield the same trends of loss reduction results.

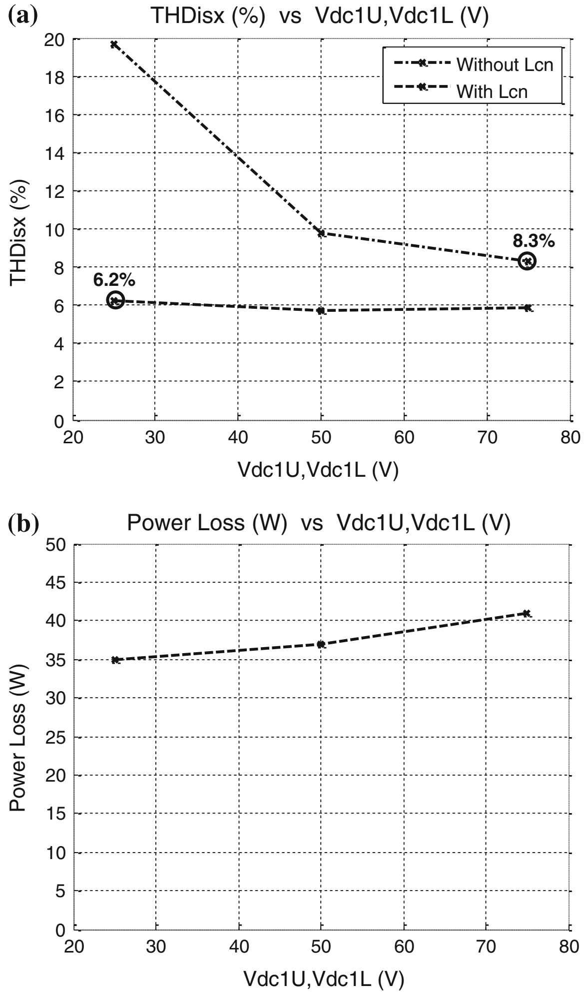

Fig. 6.26 Experimental results of (**a**) THD_{isx} and (**b**) inverter power loss with different V_{dc1U}, V_{dc1L} level under balanced 1st loading situation

6.5 Summary

In this chapter, a 220 V, 10 kVA adaptive low dc-link voltage-controlled HAPF with coupling neutral inductor experimental prototype was developed and built, which can compensate both dynamic reactive power and current harmonics in three-phase four-wire distribution power systems. Initially, its adaptive dc-link voltage controller's design procedures are discussed, so that the PI gain values can be designed accordingly. Then the parameters design of the PPF part, the design of transducers with signal conditioning circuits, IGBT drivers, and digital control system for the APF part of the HAPF experimental system are introduced. And the general design procedures for the adaptive dc-link voltage-controlled HAPF with coupling neutral inductor are also given. Finally, the 220 V, 10 kVA adaptive low dc-link voltage-controlled HAPF with neutral inductor laboratory prototype has been tested to verify its viability and effectiveness, in which it can obtain the least switching loss and switching noise and the best compensating performances compared with the conventional fixed and newly adaptive dc-link voltage-controlled HAPF without neutral inductor. Moreover, it can significantly decrease the three-phase and neutral currents to enhance the power network efficiency.

References

1. C.-S. Lam, M.-C. Wong, Y.-D. Han, Voltage swell and overvoltage compensation with unidirectional power flow controlled dynamic voltage restorer. IEEE Trans. Power Delivery **23**(4), 2513–2521 (2008)
2. M.-C. Wong, J. Tang, Y.-D. Han, Cylindrical coordinate control of three-dimensional PWM technique in three-phase four-wired trilevel inverter. IEEE Trans. Power Electron. **18**(1), 208–220 (2003)
3. N.-Y. Dai, M.-C. Wong, Design considerations of coupling inductance for active power filters, in *The 6th IEEE Conference on Industrial Electronics and Applications (ICIEA)*, Beijing, China, 21–23 Jun. 2011, pp. 1370–1375
4. W.-H. Choi, C.-S. Lam, M.-C. Wong, Y.-D. Han, Analysis of dc-link voltage controls in three-phase four-wire hybrid active power filters. IEEE Trans. Power Electron. **28**(5), 2180–2191 (2013)
5. M. Aredes, J. Hafner, K. Heumann, Three-phase four-wire shunt active filter control strategies. IEEE Trans. Power Electron. **12**(2), 311–318 (1997)
6. Datasheet of Mitsubishi Third generation IGBT PM300DSA60 Dual Intelligent Power Module
7. J. D. Van Wyk, and Fred C. Lee, Power electronics technology at the dawn of the new millennium-status and future" in *Proceeding of IEEE Power Electronics Specialists Conference*, vol. 1, (June-July 1999), pp. 3–12
8. *Featured projects technology and trend*, *Mitsubishi Electric.*, Japan, 1998
9. Datasheet of M57140-01 Isolated Dc-to-DC Converter
10. Datasheet of DSP-TMS320F2812
11. Datasheet of HCPL4504 Optocoupler
12. Datasheets of Voltage and Current Transducer of Ke Hai Module "KT 20 A/P" and "KV 50 A/P"
13. C.-S. Lam, M.-C. Wong, Y.-D. Han, Hysteresis current control of hybrid active power filters. IET Power Electron. **5**(7), 1175–1187 (2012)
14. *IEEE Recommended Practices and Requirements for Harmonic Control in Electrical Power Systems*, (1992), IEEE Standard 519-1992
15. *Electromagnetic Compatibility (EMC)*, *Part 3: Limits*, *Section 2: Limits for Harmonics Current Emissions (Equipment Input Current* $\leq$ *16A Per Phase)*, IEC Standard 61000-3-2, 1997
16. *IEEE recommended practice on monitoring electric power quality*, 1995, IEEE Standard 1159:1995

Chapter 7
Conclusions and Prospective for Future Work

Abstract In this final chapter, conclusion remarks for the proposed design and control methods of a low-cost and low loss hybrid active power filter (HAPF) system for dynamic reactive power and current harmonics compensation in three-phase four-wire distribution power system are presented. Some possible future research works are also provided.

Keywords Adaptive DC-Link Voltage Control · Coupling Neutral Inductor · Current Harmonics · Hybrid Active Power Filter · Hysteresis PWM · Reactive Power · Switching Loss · Switching Noise

7.1 Conclusions

This book presents and discusses the design and control of a low-cost HAPF system for dynamic reactive power and current harmonics compensation in three-phase four-wire distribution power system, which can also minimize the switching loss and switching noise purposes. Moreover, the HAPF is capable to prevent the resonance phenomena inherent in the pure PPF part and enhances the system robustness. Two experimental prototypes (55, 1.65, and 220 V, 10 kVA) are designed and tested to show its validity and effectiveness. The key contributions of this book are summarized below:

1. The HAPF good resonance phenomena prevention capability, filtering performance, and system robustness have been investigated and verified by simulations in Chap. 2.
2. The nonlinear characteristics and linear slope requirements of hysteresis PWM control for the HAPF are investigated and discussed in Chap. 3. Representative simulation and experimental results of HAPF system are also given to prove the validity of the hysteresis linearization study.

C.-S. Lam and M.-C. Wong, *Design and Control of Hybrid Active Power Filters*,
SpringerBriefs in Electrical and Computer Engineering,
DOI: 10.1007/978-3-642-41323-0_7,

3. An adaptive dc-link voltage control technique for the HAPF in dynamic reactive power compensation is proposed in Chap. 4, so that the system switching loss and switching noise can be reduced. Moreover, the proposed control technique can achieve the initial start-up dc-link self-charging function, in which its validity and effectiveness are verified by both simulation and experimental results compared with the conventional fixed dc-link voltage control.
4. The minimum inverter capacity analysis of the HAPF is carried out in Chap. 5, in which the minimum dc-link operating voltage requirement for the HAPF in reactive power and current harmonics compensation has been mathematically deduced. Through the HAPF equivalent circuit models in d-q-0 coordinate analyses, if two dominant current harmonics (3 kth and 3 k ± 1th, 3 kth $<$ 3 k ± 1th) existed in the loading, the dc-link voltage requirement for the HAPF can be further reduced by adding a tuned coupling neutral inductor, thus possibly to further reduce the system initial cost, switching loss, and switching noise, in which the analyses are verified by both simulations and experiments.
5. A 220 V 10 kVA adaptive low dc-link voltage-controlled HAPF with or without coupling neutral inductor experimental prototype is developed and reported in Chap. 6, which can compensate dynamic reactive power and current harmonics in three-phase four-wire distribution power system. The design details of the PPF and APF parts of the HAPF experimental system are described. Compared with the conventional fixed and newly adaptive dc-link-controlled HAPF without neutral inductor, the adaptive low dc-link voltage-controlled HAPF with neutral inductor can obtain the least switching loss and switching noise and the best compensating performances. Moreover, it can significantly reduce the three-phase and neutral currents. And the compensated current quality data satisfied the requirements of the international standards.

7.2 Perspectives for Future Work

Based on the research works done in this book, there are numerous issues meriting further exploration in future research:

1. The adaptive dc-link voltage control idea can be further extended into the existing APF, static synchronous compensator (STATCOM), etc., applications, in order to reduce the system switching loss, switching noise, and improve the system performances.
2. The HAPF steady-state performances (resonances, robustness, etc.) with a capacitor bank or PPF originally installed in parallel with the distribution power system can be analyzed.
3. As hysteresis PWM control is simple and widely applied in current quality compensation, the hysteresis PWM control of this HAPF (LC coupling VSI) has been proposed and discussed, in which the other PWM control strategies can be further investigated for this HAPF.

Appendix

A.1 Algorithm for HAPF Reference Reactive and Harmonic Compensating Current Calculation Based on Three-Phase Instantaneous *PQ* Theory

The reference reactive and harmonic compensating current calculation for the HAPF can be achieved by the well-known three-phase instantaneous *pq* theory proposed by H. Akagi et al. [1, 2]. The core of *pq* theory is to convert the instantaneous voltages and currents into instantaneous space vectors.

From [1], the three-phase instantaneous load voltages (v_a, v_b, v_c) and load current (i_{La}, i_{Lb}, i_{Lc}) on the *a-b-c* coordinates can be transformed into those on the *α-β-0* coordinates by the Clarke transformation:

$$\begin{bmatrix} v_0 \\ v_\alpha \\ v_\beta \end{bmatrix} = \sqrt{\frac{2}{3}} \begin{bmatrix} 1/\sqrt{2} & 1/\sqrt{2} & 1/\sqrt{2} \\ 1 & -1/\sqrt{2} & -1/\sqrt{2} \\ 0 & \sqrt{3}/2 & -\sqrt{3}/2 \end{bmatrix} \begin{bmatrix} v_a \\ v_b \\ v_c \end{bmatrix} \tag{A.1}$$

$$\begin{bmatrix} i_{L0} \\ i_{L\alpha} \\ i_{L\beta} \end{bmatrix} = \sqrt{\frac{2}{3}} \begin{bmatrix} 1/\sqrt{2} & 1/\sqrt{2} & 1/\sqrt{2} \\ 1 & -1/\sqrt{2} & -1/\sqrt{2} \\ 0 & \sqrt{3}/2 & -\sqrt{3}/2 \end{bmatrix} \begin{bmatrix} i_{La} \\ i_{Lb} \\ i_{Lc} \end{bmatrix} \tag{A.2}$$

For a three-phase four-wire system, the *pq* theory defines two instantaneous real power p_0 and $p_{\alpha\beta}$, and an instantaneous imaginary powers $q_{\alpha\beta}$ as follows:

$$\begin{bmatrix} p_0 \\ p_{\alpha\beta} \\ q_{\alpha\beta} \end{bmatrix} = \begin{bmatrix} v_0 & 0 & 0 \\ 0 & v_\alpha & v_\beta \\ 0 & -v_\beta & v_\alpha \end{bmatrix} \begin{bmatrix} i_{L0} \\ i_{L\alpha} \\ i_{L\beta} \end{bmatrix} \tag{A.3}$$

The inverse transformation of (A.3) is performed as follows:

$$\begin{bmatrix} i_{L0} \\ i_{L\alpha} \\ i_{L\beta} \end{bmatrix} = \frac{1}{v_0 v_{\alpha\beta}^2} \begin{bmatrix} v_{\alpha\beta}^2 & 0 & 0 \\ 0 & v_0 v_\alpha & -v_0 v_\beta \\ 0 & v_0 v_\beta & v_0 v_\alpha \end{bmatrix} \begin{bmatrix} p_0 \\ p_{\alpha\beta} \\ q_{\alpha\beta} \end{bmatrix} \tag{A.4}$$

C.-S. Lam and M.-C. Wong, *Design and Control of Hybrid Active Power Filters*,
SpringerBriefs in Electrical and Computer Engineering,
DOI: 10.1007/978-3-642-41323-0, © The Author(s) 2014

where $v_{\alpha\beta}^2 = v_\alpha^2 + v_\beta^2$

$$\begin{bmatrix} p_0 \\ p \\ q \end{bmatrix} = \begin{bmatrix} p_0 \\ p_{\alpha\beta} \\ q_{\alpha\beta} \end{bmatrix} = \begin{bmatrix} p_0 \\ \bar{p} + \tilde{p} \\ \bar{q} + \tilde{q} \end{bmatrix} \tag{A.5}$$

where p_0 is the zero-sequence instantaneous power, $\bar{p}$ and $\bar{q}$ are the instantaneous active and reactive power originating from the symmetrical fundamental component (positive-sequence) of the load current, $\tilde{p}$ and $\tilde{q}$ are the instantaneous active and reactive power originating from harmonic and the asymmetrical fundamental component (negative-sequence) of the load current.

Therefore, the reference compensating currents in *α-β-0* coordinates can be calculated as follows:

$$\begin{bmatrix} i_{c0\_q} \\ i_{c\alpha\_q} \\ i_{c\beta\_q} \end{bmatrix} = \frac{1}{v_0 v_{\alpha\beta}^2} \begin{bmatrix} v_{\alpha\beta}^2 & 0 & 0 \\ 0 & v_0 v_\alpha & -v_0 v_\beta \\ 0 & v_0 v_\beta & v_0 v_\alpha \end{bmatrix} \begin{bmatrix} p_0 \\ \tilde{p}_{\alpha\beta} \\ q_{\alpha\beta} \end{bmatrix} \tag{A.6}$$

where the term $\tilde{p}_{\alpha\beta}$ in (A.6) can easily be extracted from $p_{\alpha\beta}$ by using a low pass filter (LPF) or high pass filter (HPF). Finally, the reference compensating currents in *a-b-c* coordinates can be obtained by the inverse matrix of Clarke transformation in *α-β-0* coordinates:

$$\begin{bmatrix} i_{ca\_q} \\ i_{cb\_q} \\ i_{cc\_q} \end{bmatrix} = \sqrt{\frac{2}{3}} \begin{bmatrix} 1/\sqrt{2} & 1 & 0 \\ 1/\sqrt{2} & -1/2 & \sqrt{3}/2 \\ 1/\sqrt{2} & -1/2 & \sqrt{3}/2 \end{bmatrix} \begin{bmatrix} i_{c0\_q} \\ i_{c\alpha\_q} \\ i_{c\beta\_q} \end{bmatrix} \tag{A.7}$$

Figure A.1 shows the control block diagram for the three-phase four-wire HAPF with three-phase instantaneous *pq* theory (without dc-link voltage control). After the instantaneous reference compensating currents i_{cx_q} ($x = a, b, c$) are determined, the final reference compensating current $i_{cx}^* = i_{cx\_q}$ without the dc control. Then the final reference compensating current $i_{cx}^*$and the compensating current i_{cx} will be sent to the PWM control part and the PWM trigger signals for the switching devices can then be generated.

A.2 Algorithm for Reference Reactive and Harmonic Compensating Current Calculation Based on Single-Phase Instantaneous *PQ* Theory

The instantaneous *pq* theory was originally developed for three-phase three-wire and three-phase four-wire systems [1, 2]. Recently, the *pq* theory was developed and expanded for single-phase systems [3]. In addition, this generalized single-phase *pq* theory proposed by V. Khadkikar et al. [3] can also be well applied to

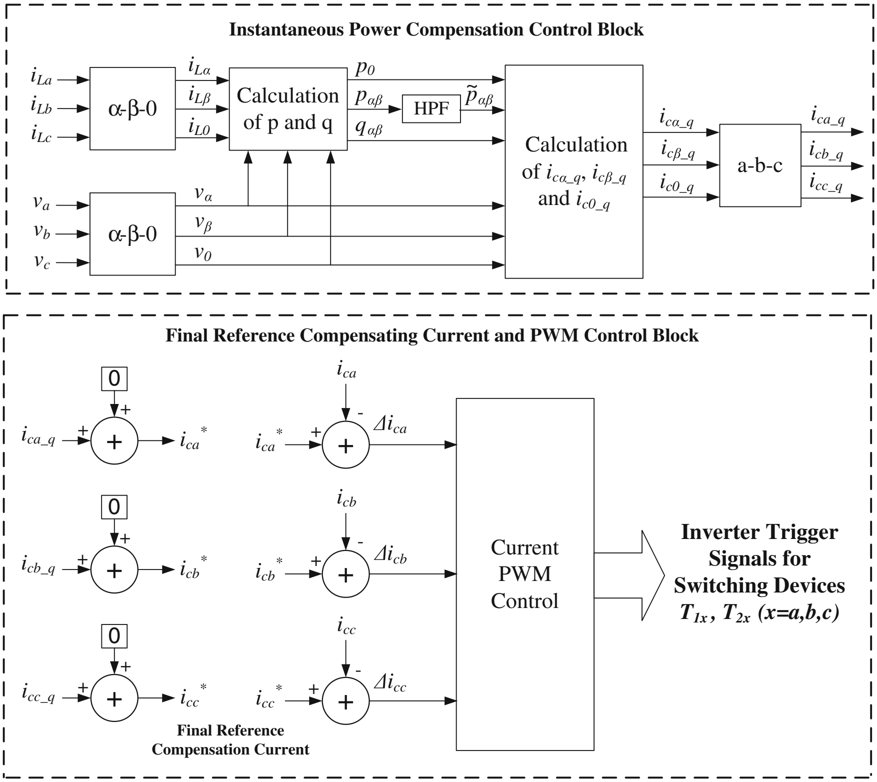

Fig. A.1 Control block diagram for the three-phase four-wire HAPF with three-phase instantaneous *pq* theory (without dc control)

three-phase or even multiphase systems. Thus, the reference reactive and harmonic compensating current calculation for the HAPF can be also achieved by the single-phase instantaneous *pq* theory.

The single-phase *pq* theory is based on an instantaneous $\pi/2$ lag or $\pi/2$ lead of voltage and current to define the original system as a pseudo two-phase system. Thus, the overall system can then be easily represented in α-β coordinates. The phase load voltage v_x and load current i_{Lx} ($x = a, b, c$) are considered as quantities on the α-axis, whereas β-axis quantities are obtained by a $\pi/2$ lag or $\pi/2$ lead of the phase load voltage and load current [3]. The phase load voltage v_x and current i_{Lx} representation in α-β coordinates with a $\pi/2$ lag can be expressed as:

$$\begin{bmatrix} v_{x\alpha} \\ v_{x\beta} \end{bmatrix} = \begin{bmatrix} v_x \\ v_x e^{-j\pi/2} \end{bmatrix} \tag{A.8}$$

$$\begin{bmatrix} i_{Lx\alpha} \\ i_{Lx\beta} \end{bmatrix} = \begin{bmatrix} i_{Lx} \\ i_{Lx} e^{-j\pi/2} \end{bmatrix} \tag{A.9}$$

The phase instantaneous active power p_{Lx} and reactive power q_{Lx} can be expressed as:

$$\begin{bmatrix} p_{Lx} \\ q_{Lx} \end{bmatrix} = \begin{bmatrix} v_{x\alpha} & v_{x\beta} \\ -v_{x\beta} & v_{x\alpha} \end{bmatrix} \cdot \begin{bmatrix} i_{Lx\alpha} \\ i_{Lx\beta} \end{bmatrix} \tag{A.10}$$

The p_{Lx} and q_{Lx} can also be expressed as

$$p_{Lx} = \bar{p}_{Lx} + \tilde{p}_{Lx} \tag{A.11}$$

$$q_{Lx} = \bar{q}_{Lx} + \tilde{q}_{Lx} \tag{A.12}$$

where $\bar{p}_{Lx}$ and $\bar{q}_{Lx}$ represent the DC components responsible for instantaneous fundamental active and reactive power, whereas $\tilde{p}_{Lx}$ and $\tilde{q}_{Lx}$ represent the AC components responsible for harmonic power.

To compensate the reactive power and current harmonics generated by the load, the reference compensating current i_{cx_q} for each phase of the HAPF can be calculated by:

$$i_{cx\_q} = \frac{1}{A_x}\left[-v_{x\alpha} \cdot \tilde{p}_{Lx} + v_{x\beta} \cdot q_{Lx}\right] \tag{A.13}$$

where $A_x = v_{x\alpha}^2 + v_{x\beta}^2$. The term $\tilde{p}_{Lx}$ in (A.13) can easily be extracted from p_{Lx} by using a low pass filter (LPF) or high pass filter (HPF).

Figure A.2 shows the control block diagram for the three-phase four-wire HAPF with single-phase instantaneous *pq* theory (without dc-link voltage control). After the instantaneous reference compensating currents i_{cx_q} ($x = a, b, c$) are determined, the final reference compensating current $i_{cx}^* = i_{cx\_q}$ without the dc control. Then the final reference compensating current i_{cx}^* and the compensating current i_{cx} will be sent to the PWM control part and the PWM trigger signals for the switching devices can then be generated.

A.3 Quasi-linear Limit T_{limit} and Linear Limit T_{linear} for HAPF Inverter Current Slope

Combining (3.4) and (3.6), the complete response of coupling capacitor voltage $v_{Cc1x}(t)$ can be derived. Then the HAPF inverter current i_{cx} can be deduced by taking derivative of $v_{Cc1x}(t)$ via (3.6). After that, taking derivative of i_{cx} will yield the rate of change of inverter current ($\mathrm{d}i_{cx}/\mathrm{d}t$). As the initial condition of i_{cx}will not affect the nonlinear nature of the inverter current slope, it can be simply treated as zero. Substitute this initial condition into $\mathrm{d}i_{cx}/\mathrm{d}t$ during each switching interval, this yields:

$$\frac{\mathrm{d}i_{cx}(t)}{\mathrm{d}t} = -\omega_r^2 C_{c1} B_1 A \tag{A.14}$$

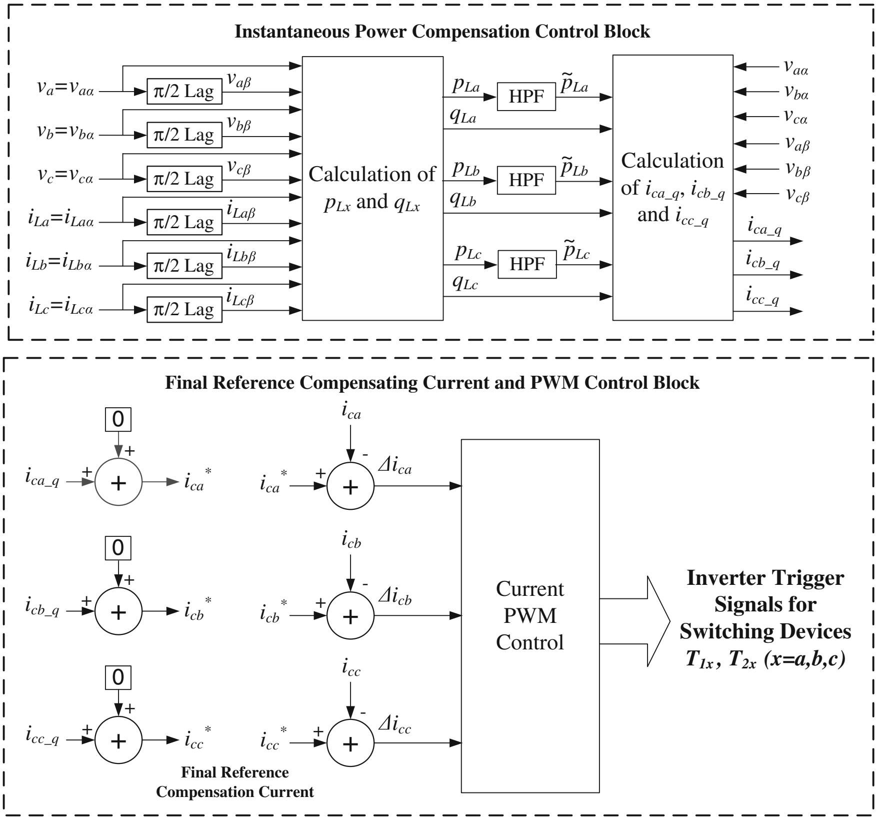

Fig. A.2 Control block diagram for the three-phase four-wire HAPF with single-phase instantaneous *pq* theory (without dc control)

where t represents each switching on or off interval ($t = \mathrm{t_{on}}\,\mathrm{or}\,\mathrm{t_{off}}$), $\omega_r = 1/\sqrt{L_{c1}C_{c1}}$, B_1 is a real number and kept constant at each switching interval, and $A = \cos\omega_r t$. To prevent the current slope from being nonlinear, the polarity of (A.14) should be kept unchanged within each switching interval as shown in Fig. 3.3. However, due to the nonlinear term $A = \cos\omega_r t$, its polarity may have interchanging within each switching on or off interval. In addition, the nonlinear term is mainly affected by the coupling part (C_{c1}, L_{c1}) and the switching frequency f_{sw}. As the coupling part is designed basing on the reactive power consumption and the dominant harmonic current of the loading, the effect of changing the coupling part values will not be studied. As a result, only the effect of changing the switching frequency will be investigated in this work. In the following, the quasi-linear limit T_{limit} and linear limit T_{linear} that divides the HAPF into nonlinear, quasi-linear and linear regions will be determined based on a constant reference inverter current i^*_{cx} ($\mathrm{d}i^*_{cx}/\mathrm{dt} = 0$) assumption. Then the quasi-linear limit H_{limit} and linear limitH_{linear} for the hysteresis band can be obtained correspondingly.

From Fig. 3.3, the quasi-linear limit T_{limit} and linear limit T_{linear} will be deduced based on one switching interval ($\mathrm{t_{on}}$ or $\mathrm{t_{off}}$) analysis. As the hysteresis control method yields asymmetric switching on and off intervals during operation, by choosing the switching frequency $f_{sw} = 1/(\mathrm{t_{on}} + \mathrm{t_{off}}) \geq 1/2T_{\text{limit}}$ or $f_{sw} \geq 1/2T_{\text{linear}}$, it is still possible that either switching on or off interval cannot satisfy the limit T_{limit} or T_{linear}. As a result, in order to ensure that each switching interval satisfies the limit, the switching frequency should be chosen as $f_{sw} \geq 1/T_{\text{limit}}$ or $f_{sw} \geq 1/T_{\text{linear}}$. As a result, once the limits are determined, the inverse of these limits are treated as the quasi-linear limit and linear limit for the switching frequency f_{sw}.

Figure A.3a illustrates the graphs of nonlinear term A at different time t. From Fig. A.3a, in order to prevent the HAPF current slope from being nonlinear, the switching frequency f_{sw} and sampling time T can be chosen as:

$$f_{\text{sw}} \geq \frac{1}{T_{\text{limit}}},\ T \leq T_{\text{limit}} \text{ and } T \leq \frac{1}{f_{sw}} \tag{A.15}$$

where T_{limit} is the quasi-linear limit for each switching on or off interval.

From (A.14), the absolute error of the HAPF inverter current slope $|\mathrm{d}i_{cx}/\mathrm{d}t|_{\text{error}}$ compared with a linear one can be expressed as:

$$\left|\frac{\mathrm{d}i_{cx}}{\mathrm{d}t}\right|_{\text{error}} = |1 - \cos\omega_r t| \tag{A.16}$$

From Fig. 3.3c, once $|\mathrm{d}i_{cx}/\mathrm{d}t|_{\text{error}} \leq \varepsilon\%$ is satisfied, the inverter current slope can be approximately treated as linear. From Fig. A.3b, if each switching interval is less than T_{linear}, it can satisfy the HAPF linear region definition $\left|\frac{\mathrm{d}i_{cx}}{\mathrm{d}t}\right|_{\text{error}} \leq \varepsilon\,\%$. In order to obtain a linear inverter current slope, the switching frequency f_{sw} and sampling time T can be chosen as:

$$f_{sw} \geq \frac{1}{T_{\text{linear}}},\ T \leq T_{\text{linear}} \text{ and } T \leq \frac{1}{f_{sw}} \tag{A.17}$$

where T_{linear} is the linear limit for each switching on or off interval.

From Fig. 3.3, if the current slope error limit ε is set to be large, the HAPF will result in low switching frequency and loss, but with a large operational error. When ε is set close to zero, it is impractical due to a high switching frequency requirement for the switching devices. Figure A.3c shows the switching frequency f_{sw} requirement in respect to different absolute percentage error ($|\mathrm{d}i_{cx}/\mathrm{d}t|_{\text{error}}$) of the current slope. From Fig. A.3c, when $|\mathrm{d}i_{cx}/\mathrm{d}t|_{error}$ is desired to be decreased a little bit more from 5 %, the switching frequency requirement will exponentially increase a lot. In this book, ε is set at 5 % because its corresponding switching frequency is within limitation of the switching devices. Moreover, the HAPF compensation performances under $\varepsilon = 5\,\%$ consideration are acceptable as verified by the simulation and experimental results in Chap. 3.

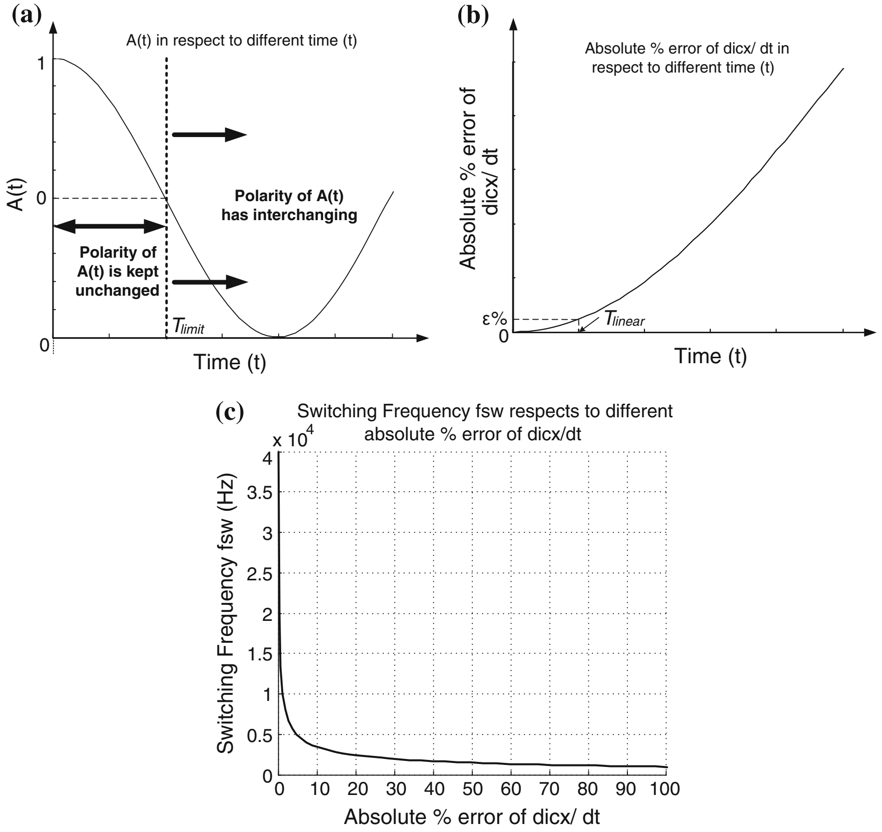

Fig. A.3 Graphs of: **a** $A = cos\ \omega_r t$ at different time t, **b** $|di_{cx}\ /\ dt|_{error}$ at different time t and **c** f_{sw} versus $|di_{cx}\ /\ dt|_{error}$

A.4 Relationship Among Hysteresis Band *H*, Switching Frequency f_{sw}, and DC-Link Voltage V_{dc1} of Linearized HAPF

Figure A.4 shows the hysteresis current-controlled PWM for HAPF: (a) switching scheme block diagram for one phase and (b) current and voltage waveforms before and after linearization. From Fig. A.4, the relationship among the switching frequency f_{sw}, hysteresis band H, dc-link voltage V_{dc1} under HAPF linear region can be derived. After simplification, the hysteresis band H value under a fixed switching frequency f_{sw} can be approximately expressed as:

$$H \approx \frac{V_{\mathrm{dc1}}}{8L_{c1}f_{\mathrm{sw}}}\left[1 - \frac{4L_{c1}^2}{V_{\mathrm{dc1}}^2}m^2\right] \tag{A.18}$$

where $m = di_{\mathrm{cx}}^{*}\big/dt$ is the slope of the reference inverter current i_{cx}^{*}.

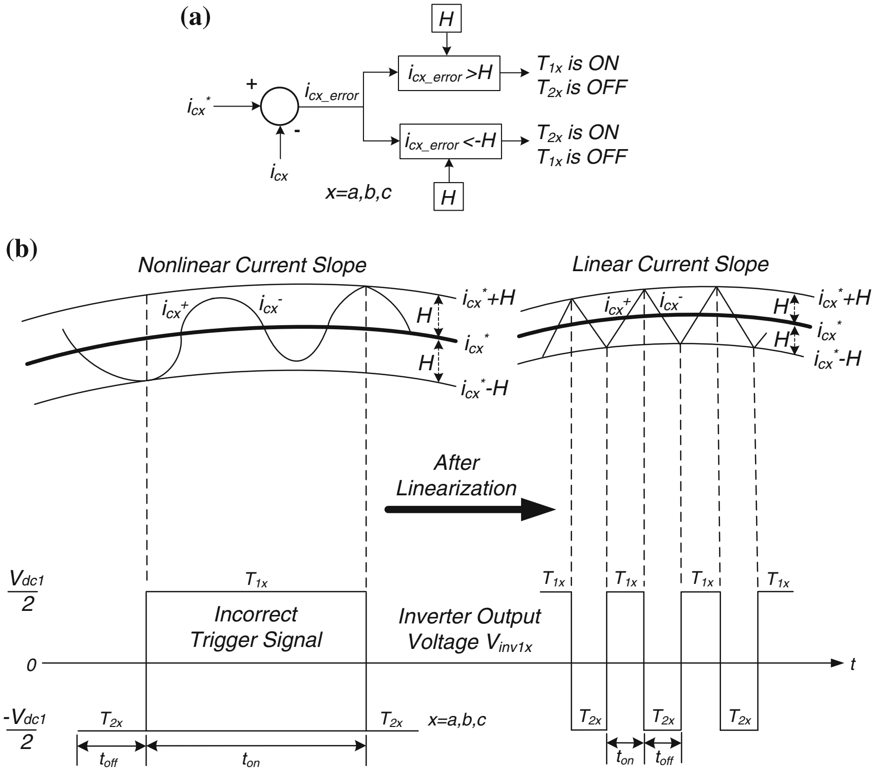

Fig. A.4 Hysteresis current-controlled PWM for HAPF: **a** switching scheme block diagram for one phase and **b** current and voltage waveforms before and after linearization

As the reference inverter current is assumed to be a constant value during the linearization analysis in previous Sect. A.3, (A.18) becomes:

$$H = \frac{V_{\mathrm{dc1}}}{8L_{c1}f_{\mathrm{sw}}} \tag{A.19}$$

Substituting $f_{\mathrm{sw}} = {}^{1}\!/T_{\mathrm{limit}}$ or ${}^{1}\!/T_{\mathrm{linear}}$ into (A.19), this yields the quasi-linear limit H_{limit} or linear limit H_{linear} for the hysteresis band. Under constant reference inverter current i^{*}_{cx} assumption, the system operating switching frequency under H_{limit} or H_{linear} will be fixed. When i^{*}_{cx} is not a constant value, (A.19) will yield the HAPF maximum operating switching frequency under a fixed hysteresis band.

A.5 Photo and System Parameters of A 55V 1.65kVA HAPF Experimental Prototype

(Fig. A.5, Table 1)

Fig. A.5 A 55V 1.65kVA HAPF experimental prototype

Table 1 A 55V 1.65kVA HAPF experimental system parameters

System parameters		Physical values
System source-side	V_x	55 V
	f	50 Hz
Passive part	L_{c1}	6 mH
	C_{c1}	70/140/190 uF
DC capacitor	C_{dc1}	5 mF
DC-link voltage levels	V_{dc1u}, V_{dc1L}	10 V
		20 V
		30 V
		40 V

References

1. H. Akagi, Y. Kanazawa, A. Nabae, Generalized theory of the instantaneous reactive power in three-phase currents, *International Conference on Power Electronics*, 1983, pp. 1375–1386
2. H. Akagi, S. Ogasawara, H. Kim, The theory of instantaneous power in three-phase four-wire systems: a comprehensive approach, *in Conference of Record IEEE-34th IAS Annual Meeting*, vol. 1, 1999, pp. 431–439
3. V. Khadkikar, A. Chandra, B.N. Singh, Generalized single-phase pq theory for active power filtering: simulation and DSP-based experimental investigation. IET Power Electron. **2**, 67–78 (2009)

Biography of Authors

Chi-Seng Lam, received his B.Sc., M.Sc., and Ph.D. degrees in Electrical and Electronics Engineering from University of Macau (UM), Macao, China, in 2003, 2006, and 2012 respectively. From 2006 to 2009, he was an Electrical and Mechanical Engineer in the Campus Development and Engineering Section at UM. In 2009, he returned to the Power Electronics Laboratory (PELab) of UM to work as a Technician and pursue his Ph.D. degree at the same time. In 2013, he was a Postdoctoral Fellow in The Hong Kong Polytechnic University, Hong Kong, China. He is currently an assistant professor in the State Key Laboratory of Analog and Mixed-Signal VLSI, University of Macau, Macao, China. His research interests include integrated power electronics controller, power electronics converters, energy saving, power quality compensators, smart grid technology, electric vehicle charger, and renewable energy.

Dr. Lam has co-authored one book: *Design and Control of Hybrid Active Power Filters* (Springer, in press) and more than 30 technical journals and conference papers. He holds 1 patent in China and has submitted the other 2 patents application in China and U.S.A respectively.

Dr. Lam was the recipient of the Macao Scientific and Technological R&D Award for Postgraduates (Ph.D. level) in 2012. He also received Ph.D. Research Scholarship, Government of Macao in 2009–2012, Macao Foundation Postgraduate Research Scholarship in 2003–2005, the 3rd Regional Inter-University Postgraduate Electrical and Electronic Engineering Conference (RIUPEEEC) Merit Paper Award in 2005, as well as Award of Dean Honor List of UM, in 1999–2000, 2000–2001, 2001–2002, 2002–2003, respectively. In 2007, he was the GOLD Officer of IEEE Macau Section. In 2008, he was the Student Branch Officer of IEEE Macau Section. Since 2009, he is also a certified Facility Management Professional (FMP) (with Highest Score Prize awarded by Labour Affairs Bureau, Macao SAR, and Macau Institute of Management) of International Facility Management Association (IFMA).

C.-S. Lam and M.-C. Wong, *Design and Control of Hybrid Active Power Filters*,
SpringerBriefs in Electrical and Computer Engineering,
DOI: 10.1007/978-3-642-41323-0,

Man-Chung Wong, received his B.Sc., and M.Sc., degrees in Electrical and Electronics Engineering from University of Macau, Macao at 1993 and 1997, respectively and Ph.D. degree in Electrical Engineering from Tsinghua University in 2003. He is working as an associate professor in University of Macau, China. His research interests are power electronics converters, pulse with modulation, active power filters, hybrid active power filters, and hybrid power quality compensator for high speed railway power supply system.

Prof. Wong received several awards based on his research results such as Macao Young Scientific Award from Macau International Research Institute at Year 2000, Young Scholar Award of University of Macau at Year 2001, second prize for Tsinghua University Excellent Ph.D. thesis Award at 2003 and third class Award of Macao Science and Technology **Awards—Technological Invention Award** at Year 2012, respectively. He supervised several students to receive merit paper awards in conferences and champions in student project competitions.

Prof. Wong is one of pioneers, who have significantly advanced the development of innovative principle of three-dimensional pulse width modulation to control 3-phase 4-wire power quality compensators. Besides, he supervised his research students to apply Hybrid Active Power Filter for dynamic reactive power compensation as well as adaptive DC linked voltage to reduce total power loss. All the results are published in world top journals such as IEEE transactions and IET journals. Since 1999 and up to 2013, he published more than 90 papers in the area of power electronics. Up to 2013, three patents were granted in China and other 4 patents are in application in China and U.S.A.